Density Functional Theory Studies of O_2, H_2O, OH^- and Xanthates Adsorption on Platinum Antimony ($PtSb_2$) Surfaces

by

Samuel Seshupo Mangoejane

THESIS

Submitted in fulfilment of the requirements for the degree of

DOCTOR OF PHILOSOPHY (PhD)

in

PHYSICS

in the

FACULTY OF SCIENCES & AGRICULTURE

(School of Physical & Mineral Sciences)

at the

UNIVERSITY OF LIMPOPO

SUPERVISOR: Prof. P.E. Ngoepe

CO- SUPERVISOR: Dr P.P.Mkhonto

2020

Declaration

I declare that the thesis "Density Functional Theory Studies of O_2, H_2O, OH^- and Xanthates Adsorption on Platinum Antimony ($PtSb_2$) Surfaces" hereby submitted to the University of Limpopo for the degree of Doctor of Philosophy (PhD) in Physics has not previously been submitted by me for a degree at this or any other university; that this is my work in design and in execution, and that all material contained herein has been duly acknowledged.

Samuel Seshupo Mangoejane 27/05/2020 **Date**

Dedication

This thesis is dedicated to my siblings (Steve, Ngebi, Mmanoka and Nunu), sons (Moatlhodi and Omaatla) and aunt (Kenyaditswe) for having been there for me during the most trying times in the writing of this manuscript.

Acknowledgements

I would like to send my gratitude to my project Leader and Advisor, Prof P.E. Ngoepe for giving the opportunity to explore the wonderful spectacle of materials modelling in the field of minerals. He inspired a lot of dedication in what was to be uncovered and also inculcated a sense of being oneself. Also in the team that oversaw the completion of the work was the sterling collaboration with Dr P.P. Mkhonto for his outstanding and excellent exposition of what I lacked when faced with difficult questions surrounding surfaces and their reactions. I would also like to thank Professor S.C. Parker, University of Bath, UK, for valuable inputs in the early stages of the work.

Furthermore, the institution, University of Limpopo (Library Services, HR personnel), has been my home for pursuing this research and Materials Modelling Centre is the incubation of what came out of this connection. Members of the centre (MMC) are duly acknowledged and the MMC server group, K.M. Kgatwane, K.W. Phoshoko, M. Mashamaite and D. Hlungwani for their unswerving and tireless assistance offered when systems were down.

My gratitude is extended to the funders of the study NRF, CSIR through CHPC for the computational muscle afforded to get through.

My friends and family who stood by be through thick and thin are duly acknowledged for not forsaking me, I am grateful to all.

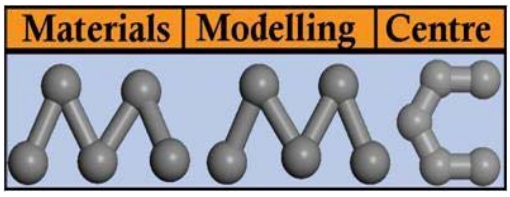

Abstract

The effects of O_2, H_2O and OH^- and collectors are the major factors that determine the flotability behaviour of minerals. In particular, the influence of the chain length variation on xanthate collectors gives rise to increased recovery rates, and are still the most versatile collector for most minerals. This study explores the bonding behaviour, adsorption energies and electronic properties directly related to the reactivity of O_2, H_2O and OH^-, ethyl xanthates (EX), normal propyl-xanthate (nPX), normal-butyl-xanthate (nBX$^-$) and amyl-xanthate (AX) with the platinum antimony mineral surfaces: (100), (110) and (111) surfaces. We employed the *ab-initio* quantum mechanical density functional theory to investigate their adsorption and their electronic properties.

In order to attain precise calculations, the cut-off energy of 500 eV was used for the bulk $PtSb_2$, which was also transferred to the surfaces. To obtain accurate results the k-point used for both the bulk and surfaces were 6x6x6 and 4x4x1, respectively. The bulk relaxation was found to give final lattice parameter of 6.531 Å. The DOS (Density Of States) indicated that both bulk and surfaces of $PtSb_2$ had a metallic character, thereby indicating semiconducting behaviour. In cleaving the surfaces, all possible terminations were considered and the slab thickness was varied to obtain the desired stable surfaces. Their relaxed surface energies were 0.807 $J.m^{-2}$, 1.077 $J.m^{-2}$ and 1.074 $J.m^{-2}$ for the (100), (111) and (110), respectively. These indicated that the (100) surface was the most stable and dominant plane for the platinum antimony. This fact is also observed in other minerals in general that low-index surfaces with lower surface energies indicates structural stability. The DOS showed stability with the E_F (Fermi level/ Fermi energy) falling deep into the pseudo gap for all surface. The valence electrons on the surface were $5d^96s^1$ for Pt and $5s^25p^3$ for Sb as depicted from the Mulliken population charges and these electrons were actively involved in the hybridisation.

The oxidation showed that the oxygen molecules preferred interacting with the Sb atoms than the Pt atoms for all surfaces. For the (100) surface we found that the Pt-O_2 peroxide adsorption site gave the strongest adsorption, while for the (110) surface we noted that the Sb2-O-O-Sb3 bridging gave the most exothermic adsorption. The case of the (111) surface showed the Sb2-O-O-Sb2 bridging to give the strongest exothermic adsorption, which dissociated and resulted in atomic bonding. Their atomic charges indicated that the oxygen molecules gain charges from the Pt and Sb atoms. In all cases,

the O_2 interacting with Sb gained more charges, thus showing preferential adsorption to the Sb atoms. In addition, the Sb/Pt-bonded oxygens were more negative than the terminal or end-bonded oxygen atom for superoxide modes. These suggested that the 2p-orbital spin-down unoccupied orbital (LUMO) of O_2 is fully occupied.

The case of H_2O molecules adsorptions on the three $PtSb_2$ mineral surfaces indicated that the H_2O adsorbed through van der Waals forces, in particular for multi adsorptions by physisorption process for the (100) and the (110) surfaces. However, on the (111) surface we observed chemisorption adsorption. For the (100) surface we found that the H_2O-Pt was exothermic, while the H_2O-Sb was endothermic and only showed exothermic from 5/8-8/8 H_2O/Sb. The case of the (110) surface showed stronger adsorption of H_2O on Pt than on Sb atoms, with a weaker adsorption on Sb2 atoms, while the adsorption on the (111) surface was stronger on Sb3 and weaker on Sb2 atoms. The full-coverage for the (110) surface gave –35.00 kJ/mol per H_2O molecule, which is similar to the full-coverage on the (100) surface (–38.19 kJ/mol per H_2O molecule). Furthermore, the full-monolayer adsorption on Sb2 and Sb3 for the (111) surface gave much stronger adsorption (–55.54 kJ/mol per H_2O). In addition, the full-coverage on the (111) surface (i.e. on Pt1 and all Sb atoms) gave adsorption energy of –54.95 kJ/mol per H_2O molecule.

The adsorption of hydroxide on the surfaces showed stronger affinity than the water molecules. This suggested that they will bind preferentially over the water molecules. We also found that the OH^- preferred the Sb atoms on the (100) surface, with a greater adsorption energy of –576.65 kJ/mol per OH^- molecule for full-surface coverage. The (110) surface adsorption energy on full-surface coverage was –541.98 kJ/mol per OH^- molecule. The (111) surface full-coverage yielded adsorption energy of –579.53 kJ/mol per OH^- molecule. The atomic charges related to both hydration and hydroxide adsorption showed charge depletion on both Pt/Sb and O atoms of the H_2O and OH^-. This suggested that there is a charge transfer into other regions within the orbitals.

The adsorption of collectors on the $PtSb_2$ surfaces to investigate their affinity with surfaces were performed considering different adsorption sites in order to find the most stable exothermic preferred site. In respect of the (100) surface, we noted that the bridging on Pt and Sb atoms by the collector involved the S atoms for all xanthates. Their adsorption energies showed that EX had strong affinity with the surface and the order was as: EX ≈ AX > nBX > nPX. In the case of the (110) surface the bridging on Pt atoms were

the most preferred sites for EX, nPX, nBX and AX. The order of adsorption energies was: nBX > nPX ≈ AX > EX. The (111) surface was observed to have the bridging on Sb2 and Sb3 atoms most exothermic for EX, nBX and AX, while the nPX showed the bridging on Pt1 and Sb3 atoms. The adsorption energies were found to have the nPX more stronger on the surface, with EX weaker and the order decreased as: nPX > nBX > AX > EX. This gave insights in the recovery of the minerals during flotation, that the use of EX or AX may float the platinum antimonide better based on the adsorption trends on the (100) surface, which is the most stable surface plane cleavage for platinum antimonide.

The analysis of the electronic structures of the collector on the surface from density of states showed stability bonding of the collector on the surface, due to the E_F falling deep into the pseudo gap for collector S atoms and surface Pt and Sb PDOS. The atomic charges computed indicated that the collectors behave as electron donors and acceptors to the Pt and Sb on the surface, respectively for the (100) surface. Interestingly for the (110) surface we observed that both surface Pt and Sb atoms lost charges, with a loss of charges on the collector S atoms. These observations suggested that the collectors S atoms offer their HOMO electrons to Pt and Sb atoms to form bond and simultaneously the Pt and Sb atoms donate their d-orbital and p-orbitals electrons to the LUMO of the collectors to form a back donation covalent bond, respectively. The (111) surface clearly showed that the surface Pt and Sb atoms lose charges to the collector S atoms, suggested a back donation covalent bonds.

Table of contents

List of figures

List of tables

List of abbreviations

PGEs	Platinum Group Elements

PGMs	Platinum Group Minerals
BMS	Base Metal Sulphides
XPS	X-ray Photoelectron Spectroscopy
AES	Auger Electron Spectroscopy
CEMS	Conversion Electron Mossbauer Spectroscopy
DFT	Density Functional Theory
GGA	Generalised Gradient Approximations
GGA	Generalised Gradient Approximations
PBE	Perdew-Burke-Ernzerhof
LDA	Local Density Approximation
PW	Plane-Wave
H-K	Hohenberg-Kohn
K-S	Kohn-Sham
SCF	Self-Consistent Functional
MD	Molecular Dynamics
SEX	Sodium Ethyl Xanthate
EX	Ethyl Xanthate
SNPX	Sodium n-Propyl Xanthate
SNBX	Sodium n-Butyl Xanthate
IBX	Isobutyl Xanthate
SIBX	Sodium Isobutyl Xanthate
AX	Amyl Xanthate

PAX	Potassium Amyl Xanthate
DTP	Dithiophosphate
DOS	Density of States
PDOS	Partial Density of States
TDOS	Total Density of States
VB	Valence Band
CB	Conduction Band
HOMO	Highest Occupied Molecular Orbital
LUMO	Lowest Un-occupied Molecular Orbital
E_F	Fermi Energy
eV	Electron Volt
Å	Angstrom

CHAPTER 1

Introduction

In this thesis, we reported the structural and surfaces properties of the geversite mineral ($PtSb_2$). The oxidation, hydration, hydroxide and effect of xanthate collectors of different alkyl chain length on the $PtSb_2$ mineral surfaces (100), (110) and (111) were discussed. These properties have been investigated using a density functional theory (DFT), *ab-initio* methods. In this introductory chapter, we review briefly from literature the previous theoretical and experimental studies and related methods that were used to study the $PtSb_2$ mineral. Furthermore, the flotation process necessary for platinum antimonide extraction was discussed. The crystal structure of the geversite mineral was reviewed and finally, the rationale and objectives of this study were stated.

1.1 Historical overview

The platinum antimonide ($PtSb_2$) mineral is one of the mostly mined in the Driekop mine, Sekhukhune, Burgersfort, Limpopo, South Africa. The platinum mineralization at Driekop occurs in a pipe-like body of dunite which cuts the norites of the critical zone of the Bushveld Complex [Stumpfl 1961, Scoon et al. 2004, O'Connor et al. 2013]. The mine was in operation until 1961 and was dormant [Stumpfl 1961], but new mines have opened and are in operation in extraction of platinum ores.

In 1957 a study was conducted to examine the minerals in the Driekop mine using microscopic investigation of the platinum concentrates and revealed the presence of a number of unknown minerals as well as a wide range of sulphides and other established members of the platinum paragenesis. The unknown minerals were found to occur in very fine intergrowths, which made the separation of individual phases for analytical purposes or X-ray work impossible. This was solved by using the X-ray microanalyser that determined the chemical composition of the minerals [Stumpfl 1961]. The different minerals extracted in the Driekop mines approximated to the formulae $PtSb_2$, PtSb, Pt(Sb,Bi), $(Pt,Ir)As_2$, $Pt(Ir,Os)_2As_4$, Pd_2CuSb, Pd(Sb,Bi), Pd_8CuSb_3, $Pt_4Sn_3Cu_4$, and $(Fe,Ni)_2S$ which have been discovered as fine intergrowths in platinum concentrates. The $PtSb_2$ is widespread, occurring in small isolated grains as well as intergrown with other members of the paragenesis. The name geversite was proposed for the phase $PtSb_2$, which has a pyrite type of structure [Stumpfl 1961]

The Platreef has similar minerals with the same structure such as sperrylite ($PtAs_2$) and there are about 21% of arsenides in the reef. Since the arsenic and antimony are in

the same group, they may have similar characters in the mineral structure. The $PtSb_2$ mineral under investigation is dominant in the reefs and is of crucial significance that could unlock the extraction of the arsenides. The high concentration of the $PtSb_2$ minerals in the Burgersfort mines makes it necessary to explore opportunities to maximise its recovery by flotation process.

$PtSb_2$ (geversite), which has an extremely narrow band gap, is a potential material for cryogenic Peltier cooling applications because of its semi-metal character with a high Seebeck coefficient and low electrical resistivity [Spencer et al. 2015]. This material has the pyrite structure and reportedly melts at 1226 ºC. The pyrite ($PtSb_2$) structure was derived from the NaCl structure by retaining the cations and replacing the anions (Sb_2) groups disposed along threefold axes, and in this fashion, six S atoms octahedrally coordinate the Pt atoms and Sb_2 groups have six octahedrally disposed Fe neighbours. Elliott et al. [1968], gave the thermal energy gap as 0.112 eV, and Zhang et al. [2017], which suggested that the $PtSb_2$ is a narrow band-gap semiconductor with a approximately 80.0 meV [Emtage 1965].

The filled Pt^{4+} t_{2g}-orbital ($5d^6$ low-spin state) is similar to the Co^{3+} orbital ($3d^6$ low-spin state) of Na_xCoO_2, sharing the semiconducting nature. The bulk $PtSb_2$ can be both metallic and semiconducting for deviations from the ideal stoichiometry. The pyrite-type platinum-group dipnictides are attractive for their good thermal and electronic conductivity [Nishikubo et al. 2002]. These materials also have novel magnetism in a low carrier density environment and high electrocatalytic activity for fuel-cell applications [Qazilbash et al. 2009, Casado-Rivera et al. 2003, Innocente [2006] and Zhang et al. 2006]. Other related compounds of the Platinum Group of Minerals include sulphides, arsenides and selenides of Osmium, Iridium, Ruthenium, Rhodium and Palladium naturally occurring in most parts of the world in ores mixed with other metals. These groups of minerals are important in many industrial and commercial applications as they are being used in catalytic converters in car emission systems and in medical circles (treatment of certain forms of cancers, Pt-based drugs, e.g., cisplatin) and aerospace industries where metals that can withstand high temperatures and pressures are a requirement.

1.2 Literature review

Oxidation is often associated with the unwanted corrosion of materials. Nevertheless, under controlled conditions, oxidation may assist the production of catalyst, semiconductor devices, or protective and functional oxide films. In terms of flotation oxidation and hydration play as significant role in that they can make minerals react easily with collectors. as this has an effect on the pH of the adsorbates (deleted)

The investigation of the collector strength of affinity with mineral surface can be achieved at an atomic level where the adsorptions of collector ligands are studied at mineral surfaces through computational simulations. However, the modelling of such complex systems has its own challenges, but offers platform to benchmark the results obtained against experimental study, which is extremely desirable [Waterson et al. 2016]. A wide range of studies have been carried out on other minerals of the surface oxidation such as FeS_2 (pyrite) [Sun et al. 2004, Russo et al. 1999, Chandra and Gerson 2010], pentlandite [Mkhonto et al. 2015, Legrand et al. 2005:Part1, Legrand et al. 2005:Part2], $CuFeS_2$ (chalcopyrite) [Wei et al 2019, Aneesuddin et al. 1983, Todd et al. 2003], but not on the platinum chalcogenides. An understanding of chemical bonding and electronic structure in sulphide minerals is central to any attempt at understanding their crystal structures, stabilities and physical properties. It is also an essential precursor to understanding reactivity through modelling surface structure at the molecular scale. In recent decades, there have been remarkable advances in first principles (*ab-initio*) methods for the quantitative calculation of electronic structure [Hohenberg et al. 1965]. These advances have been made possible by the very rapid development of high performance computers [Vaughan et al. 2006]. Such studies have also been conducted on metals due to catalysis for the motor industry in a bid to curb pollution by toxic emissions of gases. Studies for adsorption of xanthates on the FeS_2 surfaces have been carried out [Li Quan et al. 2007]. The oxidation of pyrite, the most abundant of all metal sulphide minerals, is the dominant process giving rise to acidification of natural waters [Rimstidt et al. 2003].

In the absence of previous work reported on the $PtSb_2$ mineral study, we analysed the related structure of $PtAs_2$ that has recently been given much attention [Waterson 2016]. The computational report for sperrylite study adsorbed with xanthate, dithiocarbamate (DTC) and dithiophospinate (DTPi) showed that the binding strength of

ethyl xanthate (EX^-) was stronger than that of diethyl dithiocarbamate (DEDTC) and diisobutyl dithiophospinate (DTPi). In the same study it was found that the OH^- had stronger affinity than the collectors, which indicated that at higher pH the collector may not be able to displace the coverage of OH^- on the mineral surface of sperrylite.

Previously the xanthate adsorption was also carried out on FeS_2 low-index surfaces (i.e., (100), (110) and (111)) for investigation of froth flotation, a case of separation and concentration of valuable transition metal sulphide minerals [Hung et al. 2003, 2004]. Also, in another article, Hung et al. [2003] showed using DFT calculations that the xanthates readily undergo dissociation at the fourfold coordinated surface Fe (iron) on the (110) surface, and the bridging S (sulphur) of the (111) surface. Their results suggested that xanthate may undergo chemisorption at defect sites on real FeS_2 surfaces, which contain low-coordinate Fe sites in proximity to cleaved S-S bonds [Hung et al. 2003].

1.3 Structural properties

The $PtSb_2$ has a space group of, a pyrite structure, which is Pa-3 (205), where the four metal atoms are located at 4(a) positions and the eight antimony atoms are in 8(c) positions. The internal parameter of $PtSb_2$ is u = 0.375 and the lattice parameter of the unit cell a = 6.440 Å [Emtage et al. 1965, Brese et al. 2004] which was obtained from experimental measurements.

Table 1.1: The atomic positions of $PtSb_2$ crystal structure.

Property			**Value**	
Formula			$PtSb_2$	
Z			4	
Unit cell length (a=b=c)			6.440 Å	
Cell angles (α=β=γ)			90˚	
Space-group			Pa-3 (#205)	
Atoms	**Position**	**x**	**y**	**Z**
Pt	(4a)	0.000	0.000	0.000
Sb	(8c)	0.375	0.375	0.375

Pt denote the octahedral Pt(O) and Sb denote the tetrahedral Sb(T) atoms.

The Pt–Sb (1) and the closest Sb–Sb (2) bond lengths for $PtSb_2$ are as follows:, 2.671(1), 2.782(2) Å [Brese et al. 1994]. The melting point of $PtSb_2$ is estimated to be around 1500K, which indicated that it takes significant energy to dissociate. The melting temperature gives a guide as to the strength of the material and therefore its crystal or lattice energy.

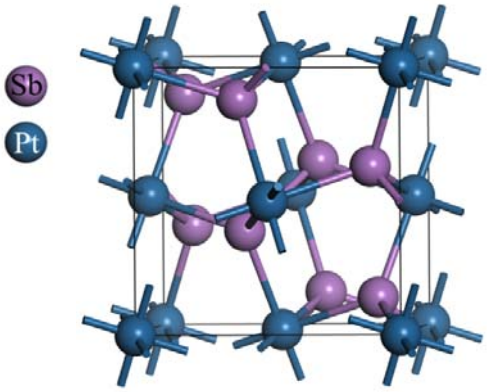

Figure 1.1: The crystal structures of (geversite) mineral ($PtSb_2$).

1.4 Significance/Application of the study

1.4.1 Mineral extraction

For the recovery of valuable elements from their ores, a process of froth flotation is to be utilised, but in our studies there is a computational means of employing Density Functional Theory (DFT). This is also important as some of the valuable elements are left in mine tailings during the recovery of other ores which are in abundance and the less valuable are left behind. The recovery process should be effected by using methods which are cost effective and economical, hence computational methods need to be employed. There is a need for more effective processes that are being exploited around the world which have the potential of being studied, as described in the chapters to follow.

Also, knowledge of the interaction of the surfaces of minerals with water gives an understanding of crystal growth and dissolution processes and is useful for the recovery of the mineral from the ore deposits. It is important to know the reactivity of the surfaces with water, collectors and any surfactants used for extraction since this is critical in the design of an efficient flotation scheme.

1.4.2 Flotation Process

Froth flotation is a process for selectively separating hydrophobic materials from hydrophilic materials and it is a physio-chemical process which exploits the differences in the electrochemical properties of mineral surfaces [Muzenda et al. 2011]. It has been reported that the hydrophobic character of a variety of base-metal sulphides were

examined in the presence of ligands such as potassium ethyl xanthate [Walker. et al. 1986]. The flotation method is used in several processing industries and historically this was first used in the mining industries. This method is one of the most versatile and flexible of all mineral separation processes due to the fact that reasonable outcomes are fairly easy to obtain. However, the flotation processes are complex and thus a better understanding of these processes may lead to higher yields and less damage to the environment. An outstanding performance is achieved by a frequent monitoring of the process and the understanding of the mineral ore. Some of the variables that affect the operation and control of a flotation process are chemical components such as collectors, frothers, activators, depressants and pH modifier together with the operation components such as mineralogy, particle size, pulp density and temperature [www.jmeech.mining.ubc.ca].

For froth flotation to be carried out, a number of steps have to be performed. Firstly, the grinding of the ore should be fine enough so that valuable mineral particles become liberated from the waste rock and to a size range suitable to be floated (10 - 200 microns). Secondly, mixing the grinded ore with water is done because water is a medium in which many processes easily take place, however the ratio of water to solids is very important [Muzenda E. et al. 2011]. Thirdly, the conditions must be made favourable for the desired mineral particles to adhere to air bubbles; this is done by stage-adding of collectors. The collector should attach through its polar sulphur atoms to only valuable mineral particles so that water is repelled and air bubbles can become attached upon collision [www.jmeech.mining.ubc.ca/MINE290/Froth%20Flotation.pdf, 2012]. Lastly, a rising current must be created, and this is done by blowing air into the flotation cell which creates air bubbles that act like 'hot-air balloons' providing the necessary buoyancy to carry selected minerals to the pulp surface [www.jmeech.mining.ubc.ca]. When all theses are done it results in formation of a mineralized froth on the surface of the ore pulp which is skimmed off from the flotation cell or vessel. A typical flotation cell and the processes that occur in it are presented in Figure 1.1.

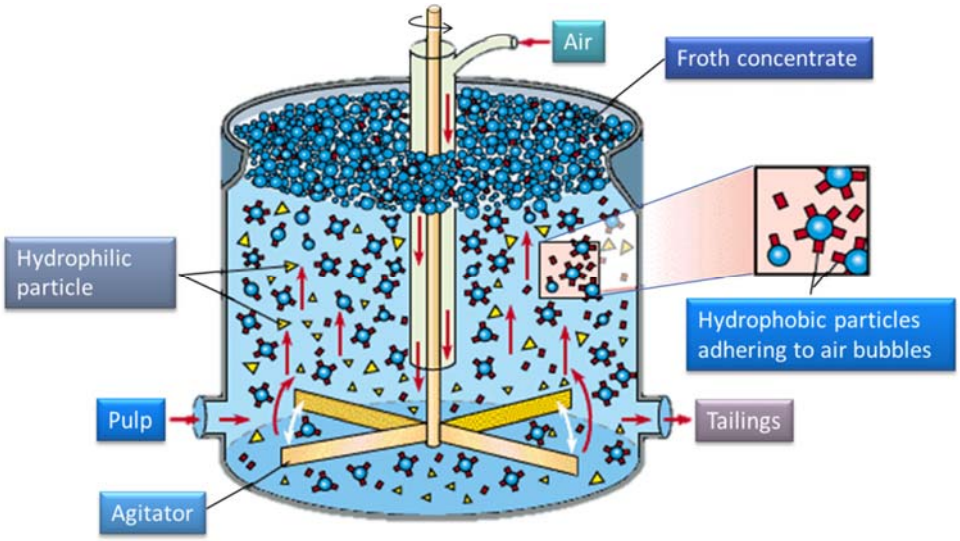

Figure 1.2: Flotation cell displaying the processes of froth floatation [Flotation 2010].

The polar (ionic) sulphur atoms on the non-polar (hydrophobic) hydrocarbon thiol collector interact with the metals on the surface; surrounding the metals in a vertical orientation with the tails of the collectors being hydrophobic. This causes the mineral to adhere to the air bubble which causes the mineral to move to the pulp surface [Muzenda et al. 2011]. In order to understand the physical and chemical properties at the (geversite) mineral surface, it is necessary to know the properties of the bulk material; the former is merely a breach of the translational symmetry of the latter.

Performing flotation using xanthate collectors is still a challenge, even though xanthate collectors are known as low-cost, easy-to-produce collectors which usually give good flotation efficiency. The continued use of xanthate however, has raised ever increasing environmental concern as carbon disulphide is readily emitted from xanthate decomposition, thus engineers and scientists have embarked on looking for the replacement of xanthate collectors [Dong et al. 2011]. The attempt to partially and completely replace the xanthate collector by dithiocarbamate have been performed and it was found that the mixture of xanthate and dithiocarbamate yield high recoveries. However, it was observed that pure xanthate is more efficient than pure dithiocarbamate alone, thus dithiocarbamate may not be able to fully replace xanthate. Moreover, the dithiocarbamates are economically problematic as they are more expensive than xanthates [Ngobeni et al. 2013]. Furthermore, the dithiophosphate was also found not suitable to

replace the xanthate on the flotation of (geversite) containing ore (Ngobeni W. et al. 2013). In order to mimic the problems encountered with mineral extraction, we seek to imitate the flotation process by using computational technique (DFT). In this instance we study the oxidation (naturally oxidation), hydroxide adsorption (pH dependence) and hydration (addition of water) in the (geversite) surfaces. Furthermore, the collectors such as, ethyl xanthate (EX), n-propyl xanthate (nPX), n-butyl xanthate (nBX) and amyl xanthate (AX) will be investigated on the mineral (100), (110) and (111) surfaces.

1.5 Rationale and objectives

1.5.1 Rationale

Investigation of $PtSb_2$ has not been extensively studied and thus limited literature is available on this mineral both experimentally and computationally. The recent technology of computation algorithms that has been developed offers hope to investigate complex surfaces with low cost and efficiency. The first principle calculations are able to give some better reactive properties of the mineral surfaces that experiments might not easily accomplish, for example the hydration and influence of collectors on surfaces which are limited in literature computationally. There is a growing demand for improving platinum recovery, in particular those that are hosted in hard to float arsenide and antimony minerals. Thus the extraction of $PtSb_2$ mineral requires knowledge and understanding of the reactivity of the surface/collector interaction. The proposed study will employ first principles method to investigate the geversite ($PtSb_2$). The surface study will include the surface orientation and termination to better understand the surface reaction of this mineral for flotation and extraction. This study will focus on the surface properties of $PtSb_2$, their interaction with oxygen and water, hydroxide and the influence of xanthate collector of different chain lengths.

The surface interaction will be investigated from the surface and adsorption energies on different surface slab orientations and terminations. More importantly, the electronic signature and behaviour of DOS and atomic charges will be investigated. These are important to distinguish the preference of surface as well as the adsorption site for possible maximum recovery. Studies of $PtSb_2$ surfaces have not been carried out experimentally (especially surfaces interactions with collectors). As such this study

explores and investigates the interaction of oxygen, water, hydroxide and xanthate of different chain lengths (C2, C3, C4, C5) with the platinum antimonide ($PtSb_2$) surfaces: (100), (110) and (111) using computational methods. The study will begin with exploring the bulk and the surfaces before adsorptions.. The electronic properties such as density of states (DOS) and Mulliken atimic charges describe the chemistry of interaction of the O_2, H_2O, OH^- and xanthates with the surface. In addition the DOS and atomic charges will be computed for the bulk and clean surfaces.

1.5.2 Objectives

First principle objectives of the study are to:

i. Determine the suitable cut-off energy and k-point mesh parameters for $PtSb_2$ mineral.
ii. Perform full geometry optimisation of bulk and surface structures.
iii. Determine the lattice constants: lattice parameters and bond lengths,
iv. Cleave the low index (100), (110) and (111) surfaces at different terminations.
v. Determine the most stable surface termination that is less reactive (surface energy).
vi. Calculate electronic structures for the stable surface termination.
vii. Determine the effects of oxidation, hydration, hydroxide on (100), (110) and (111) surfaces
viii. Investigate the influence of xanthate collectors (EX, nPX, nBX and AX) on the low index mineral surfaces
ix. Describe the bonding behaviour of the adsorbates on the surfaces in terms of adsoption energies, electronic structures of surfaces, with DOS and Mulliken atomic charge.

1.6 Outline of the thesis

The following chapters will look into discussions and results obtained while doing the project and the interpretation thereof.

This thesis gives a report on the study of surfaces and electronic properties of the platinum antimonide, using first principles DFT methods.

The thesis is partitioned into seven chapters:

Chapter 1 deals with the historical overview based on the theory and different techniques that have been used previously on studies of these groups of transition metal sulphides. We also review the crystal structure analysis of the $PtSb_2$ mineral. Finally, rationale and objectives of this work were stated.

Chapter 2 deals with the methods that have been used in the current study: DFT, plane-wave pseudopotential method and Cambridge Serial Total Energy Package (CASTEP) code. Firstly, the chapter introduces various first principle techniques; secondly, the DFT for calculating geometry optimisation is described; thirdly, approximation method such as LDA and GGA are described, fourthly, density of states and lastly the plane-wave pseudopotential method, and population charges and the CASTEP code.

Chapter 3 is concerned with optimization of the bulk and surfaces and their electronic structures.

Chapter 4 is concerned with the results and discussions for oxidation of low index surfaces and their electronic structures.

Chapter 5 is concerned with the results and discussions for hydration and hydroxide adsorption on the surfaces and their electronic structures.

Chapter 6 is concerned with the results and discussions for xanthates adsorption onto the three surfaces and their electronic structures and comparison of xanthate and OH^- adsorption energies and xanthates adsorption in the presence of water molecules

Chapter 7 gives the summary, conclusion, recommendations, future work and Appendix.

Finally, the bibliography which helps give insight to the analysis of the work is listed and papers presented in conferences are given in Appendices.

CHAPTER 2

Density Functional Theory Methodology

This chapter is concerned with the methods of calculations employed in this study. Computational simulations offer alternative means of investigating various structural, electronic and surface properties of materials alongside experiment and theory. This approach has been widely used in solid-state physics, chemistry and materials science, to predict the real situation by presenting physical systems as models.

The newly developed computer algorithm of high performance computers has made modelling of surface chemistry studies possible. There are three types of computational approaches that can be used to study surfaces properties of materials. Firstly, the quantum mechanical methods, which take into account the motions and the interactions of electrons in a material. Secondly, the empirical potential methods (atomistic method), consider the interactions of atoms in Quasi-classical form and avoids the electronic interactions. Lastly, semi-empirical methods, these act as a bridge between quantum and atomistic methods. This method incorporates both quantum mechanical and the atomistic methods, where the electron and atom interaction in quasi-classical can be obtained.

In this study we have used *ab initio* quantum mechanical density functional theory [Hohenberg et al. 1965], to study surface properties of geversite mineral ($PtSb_2$). The theory solves Schrödinger equation and applies the plane-wave (PW) pseudopotential method. The plane-wave pseudopotential method is necessary for performing full geometry optimisation of the structures. In the next section we discuss the DFT for describing the many-body problem by approximation methods, using electron density (n).

2.1 Density functional theory

Density functional theory is a quantum mechanical based method used in physics and chemistry to investigate the electronic structure of many-body systems, in particular atoms, molecules, and the condensed phases [Vignale 1979]. Within the DFT, the properties of a many electron systems can be determined by using functional, i.e. function of another function, which in this case is the spatially dependent electron density. DFT is among the most popular and versatile methods available in condensed-matter physics, computational physics, and computational chemistry. It is used for calculations in solid state physics. Although DFT has its theoretical backgrounds in the Thomas-Fermi model, the theoretical basis were confirmed by the two Hohenberg-Kohn (H-K) theorems [Hohenberg et al. 1965]. The first H-K theorem demonstrates that the ground state

properties of a many-electron system are uniquely determined by an electron density that depends on only three spatial coordinates. This gives the possibility for reducing the many-body problem of N electrons with 3N spatial coordinates to 3 spatial coordinates, through the use of functionals of the electron density. This theorem can be extended to the time-independent domain to develop time-dependent density functional theory, which can be used to describe excited states [Hohenberg et al. 1965].

The second H-K theorem defines energy functional for the system and proves that the correct ground-state electron density minimizes this energy functional. Within the framework of Kohn-Sham (K-S) DFT, the intractable many-body problem of interacting electrons in static potentials is reduced to a tractable problem of non-interacting electrons moving in an effective potential [Kohn et al. 1965]. The effective potential includes the external potential and the effects of the Coulomb interactions between the electrons, that is the exchange and correlation interactions. Modelling the latter two interactions is impossible within K-S DFT. The LDA is based upon exact energy for a uniform electron gas, which can be obtained from the Thomas-Fermi model, and from fits to the correlation energy for a uniform electron gas. Non-interacting systems are relatively easy to solve as the wave function can be represented as a Slater determinant of orbitals (Slater et al. 1929). Further, the kinetic energy functional of such a system is known exactly. The exchange-correlation part of the total-energy functional remains unknown and must be approximated. The Kohn-Sham total energy functional for a set of doubly occupied electronic states can be written as:

$$E = \{\psi_i\} = 2\sum_i \left(\frac{-\hbar}{2m}\right)\nabla^2\psi_i d^3r + \int V_{ion}(r)n(r)d^3r + \frac{e^2}{2}\int \frac{n(r)n(r')}{|r-r'|}d^3r d^3r' + E_{xc}[n(r)] + E_{ion}(\{R_I\}), \quad 2.1$$

where E_{ion} is the Coulomb energy associated with interactions among the nuclei (or ions) at positions $\{R_I\}$, V_{ion} is the static total electron-ion potential, n(r) is the electronic density given by

$$n(r) = 2\sum_i |\psi_i(r)|^2, \quad 2.2$$

and E_{XC} [n(r)] is the exchange-correlation functional. Only the minimum value of the Kohn-Sham energy functional has physical meaning. At the minimum, the Kohn-Sham

energy functional is equal to the ground-state energy of the system of electrons with the ions in positions $\{R_I\}$. It is necessary to determine the set of wave functions ψ_i that minimizes the Kohn-Sham energy functional. These are given by the self-consistent solutions to the Kohn-Sham equations:

$$\left[\frac{-\hbar}{2m}\nabla^2 + V_{ion}(r) + V_H(r) + V_{xc}(r)\right]\psi_i(r) = \varepsilon_i\psi_i(r), \qquad 2.3$$

where ψ_i is the wave function of electronic state i, ε_i is the Kohn-Sham eigen value and V_H is the Hartree potential of the electrons [Payne et al. 1992]. DFT calculations are normally used to solve K-S equations self consistently. Within the framework of Kohn and Sham DFT, the intractable electrons in a static external potential is reduced to tractable of non-interacting electrons moving in an interacting effective potential. The effective potential includes the external potential and the effects of the coulomb interactions between electrons. K-S DFT shows that only exchange-correlation as a function of the electron spin (up and down) density n(r) must be approximated [Hohenberg et al. 1965].

2.1.1 Local density approximation

The Hohenberg-Kohn theorem provides some motivation for using approximate methods to describe the exchange-correlation energy as a function of the electron density. The simplest method of describing the exchange-correlation energy of an electronic system is to use the LDA [Payne et al. 1992]. In local density approximation the exchange-correlation energy of an electronic system is constructed by assuming that the exchange-correlation energy per electron at a point r in the electron gas, $\varepsilon_{XC}(r)$, is equal to the exchange-correlation energy per electron in a homogeneous electron gas that has the same density as the electron gas at point r, thus

$$E_{xc}[n(r)] = \int \varepsilon_{xc}(r)n(r)d^3r, \qquad 2.4$$

The local density approximation assumes that the exchange-correlation energy functional is purely local. The local density approximation, in principle, ignores correction to the exchange-correlation energy at a point r due to nearby in homogeneities in the electron density. The LDA is a first-principle approach in the sense that the

quantum mechanical problem is solved without any adjustable, arbitrary or system dependent parameters [Kudoh et al. 1986]. For any many-electron system, the function for total energy has a minimum equal to the ground state energy at the ground state density.

2.1.2 Generalized gradient approximation

The generalized gradient approximation is still local but it also takes into account the gradient of the density at the density at the same coordinates as follows;

$$E_{xc}[n_{\uparrow}, n_{\downarrow}] = \int \varepsilon_{xc}(n_{\uparrow}, n_{\downarrow}, \nabla n_{\uparrow}, \nabla n_{\downarrow})\rho(r)d^3r, \qquad 2.5$$

GGA for the exchange-correlation energy improves upon the local spin density approximations (LSDA) description of atoms and solids. It tends to improve total energies and structural energy differences and it expands and weakens the bonds, an effect that corrects the LSDA prediction [Perdew et al. 1992]. The GGA functions are accurate, give very good results for molecular geometries and ground-state energies, and are expressed in terms of Perdew-Wang, however potentially more accurate than the GGA functional and meta-GGA functions [Perdew et al. 1986]. These functionals include further terms in expansion depending on the density, the gradient of the density and the Laplacian second derivatives of the density. There are other important functionals of DFT such as hybrid Meta GGA, hybrid and double functional. There are different GGA exchange-correlation functionals important for calculating solids, such as GGA-PBE, GGA-rPBE, GGA-PW91, GGA-WC and GGA-PBEsol.

2.1.3 Ultrasoft pseudopotentials method

Ultrasoft pseudopotential (USP) covers a wide range of atoms including the transition metals. In 1990, Vanderbilt developed a pseudopotential known as ultrasoft pseudopotentials. Many of the modern pseudopotential calculations use the generalisation of the Kleinman-Bylander [Vanderbilt 1990]. The approach is a radical departure from norm-conserving pseudopotentials discussed below, since ultrasoft pseudopotential attaining much smoother pseudo wavefunctions. In this approach, the pseudo wavefunctions are required to be equal to all electron wavefunctions outside the radius, as with the norm-conserving pseudopotentials, but inside the radius are allowed to be as

soft as possible. Again the norm conserving constraint is removed, but this also introduces some complications. However, the ultrasoft pseudopotential still be able to reduce the plane cut-off needed in calculations, particularly since large values of radius can be used in their scheme.

The complications that result are two-fold. First, since the pseudo wavefunctions are equal to all-electron wavefunctions (and have the same norm) in the interstitial, but have a different norm inside the topological complexity they are necessarily not normalised. Secondly, the pseudo charge density is not obtained by computing $\sum \varphi^* \varphi$ as with norm-conserving pseudopotential, this will lead to the incorrect total charge. A third, but less important complication is that, by relating the norm-conservation, the resulting pseudopotentials can become less transferrable. However, Vanderbilt pseudopotentials were proposed for use in large-scale calculations, for which the costs of generating pseudopotentials are negligible as compared to the cost of the calculations [Vanderbilt 1990]. The electron density is subdivided into a smooth part that extends throughout the unit cell and a hard part localised in the core region. The ultrasoft pseudopotential has advantage over the norm-conserving pseudopotential.

2.1.4 k-points sampling

Electronic states are allowed at asset of *k*-points determined by the boundary conditions that apply to the bulk solid. The density of allowed *k*-points is proportional to the volume of the solid. The infinite numbers of electrons in the solid are accounted for by an infinite number of k-points and only a finite number of electronic states are occupied at each *k*-point.

The Bloch theorem changes the problem of calculating an infinite number of electronic wavefunctions to one of calculating a finite number of *k*-points. The occupied states at each *k*-point contribute to the electronic potential in the bulk solid so that in principle an infinite number of calculations are needed to compute this potential. Furthermore, the electronic wavefunctions at *k*-points that are very close are identical. Hence it is possible to represent the electronic wavefunctions over a region of *k* space by the wavefunctions at a single *k*-point. In this case the electronic states at only a finite number of *k*-points are required to calculate the electronic potential and hence determine the total energy of the solid.

Methods have been devised for obtaining very accurate approximations to the electronic potential from a filled electronic band by calculating the electronic wavefunctions at special sets of *k*-points. The two most common methods are those of Chadi and Cohen [Chadi et al. 1973] and Monkhorst and Pack [Monkhorst et al. 1976]. Using these methods, the electronic potential and the total energy of an insulator can be obtained by calculating the electronic states at a very small number of *k*-points. A denser set of k-points are required to calculate the electronic potential and the total energy of a metallic system in order to define the Fermi surface precisely.

However, the computational costs of performing a very dense sampling of *k* space increase linearly with the number of k-points in the Brillouin zone (BZ). Density functional codes approximate these *k* space integrals with a finite sampling of *k*-points. Special *k*-points schemes have been developed to use the fewest possible *k*-points for a given accuracy, thereby reducing the computational cost. The most commonly used scheme is that of Monkhorst and Pack [Monkhorst et al. 1976].

2.2 Plane-wave pseudopotential method

The plane-wave pseudopotential technique is a good method used to calculate with accuracy, the variational self-consistent solution to the density functional theory. It is applicable in large systems that are subject to 3D periodic boundary condition. In this method the wave function is expressed in terms of plane-wave basis and a good pseudopotential representation of the ions in the crystal is given.

2.2.1 Plane-wave basis

An infinite plane-wave basis set is required to expand the electronic wave functions of the system. The Plane-wave pseudopotential method is a powerful and reliable tool to study the properties of materials. This method is designed for periodic solids but again is used for problems such as atoms and surfaces. The key of this method is Bloch's theorem which allows the electronic wave functions to be expanded in terms of a discrete set of plane waves as follows:

$$\psi_i(\mathrm{r}) = \mathrm{e}^{[\mathrm{ik.r}]}\mathrm{F_i}(\mathrm{r}) \qquad 2.6$$

This expression has a wavelike and cell periodic part where,

$$F_i(r) = \sum_{\vec{G}} C_{i,G} e^{[iG.r]}, \quad 2.7$$

where G is the reciprocal lattice vectors of the periodic cell. Thus each electronic wave function can be written as follows:

$$\psi k_i(r) = \sum_{G} C_{i,K+G}\, e^{[i(k+g).r]}, \quad 2.8$$

where $C_{i,K+G}$ are the coefficients of plane waves and depend entirely on the specific kinetic energy,

$$\left(\frac{\hbar^2}{2m}\right)|K + G_c|^2. \quad 2.9$$

The plane wave's basis set is limited by including all plane waves whose kinetic energies are less than some particular cut-off energy (E_{cut}) as follows:

$$\left(\frac{\hbar^2}{2m}\right)|K + G_c|^2 < E_{cut} \quad 2.10$$

The cut-off energy is chosen by increasing its magnitude until the total energy is converged to require accuracy [Perdew et al. 1992]. However, when the number of plane wave is increased one can describe more rapidly varying features and an infinitely large number of basis set could be achieved. Thus finite bases set are obtained when finite cut-off energy is introduced to the discrete plane-wave basis set. This may lead to some errors in the computation of the total energy; cut-off energy should be increased until the calculated energy has converged. Also one needs to use a much denser set of k-points to reduce errors and ensure good convergence.

2.2.2 Pseudopotentials

Although Bloch's theorem states that the electronic wave functions can be expanded using a discrete set of plane waves, a plane-wave basis set is usually very poorly suited to expanding electronic wave functions because a very large number of plane waves are needed to expand the tightly bound core orbitals and to follow the rapid oscillations of the wave functions the valence electrons in the core region. It is well known that most

physical properties of solids are dependent on the valence electrons largely than on the core electrons. The pseudopotential approximation exploits this by removing the core electrons and by replacing them and the strong ionic potential by a weaker pseudopotential that acts on a set of pseudo wave functions. An ionic potential, valence wave function and the corresponding pseudopotential and pseudo wave function are illustrated schematically in the Figure 2.1.

The valence wave functions oscillate rapidly in the region occupied by the core electrons due to the strong ionic potential in this region. These oscillations maintain the orthogonality between the core wave functions and the valence wave functions, which is required by the exclusion principle. The pseudopotential is constructed ideally, so that its scattering properties or phase shifts for the pseudo wave functions are identical to the scattering properties of the ion and the core electrons for the valence wave functions, but in such a way that the pseudo wave functions have no radial nodes in the core region. In the core region, the total phase shift produced by the ion and the core electrons will be greater by π, for each node that the valence functions had in the core region, than the phase shift produced by the ion and the valence electrons. Outside the core region the two potentials are identical, and the scattering from the two potentials is indistinguishable. The phase shift produced by the ion core is different for each angular momentum component of the valence wave function, and so the scattering from the pseudopotential must be angular momentum dependent. The most general form for pseudopotential is:

$$V_{NL} = \sum_{lm} |lm > V_i < lm| \qquad 2.11$$

where |lm> is the spherical harmonics and V_i is the pseudopotential for angular momentum l, acting on the electronic wave function with this operator decomposes the wave function into spherical harmonics, each of which is then multiplied by the relevant pseudopotential(V_i)

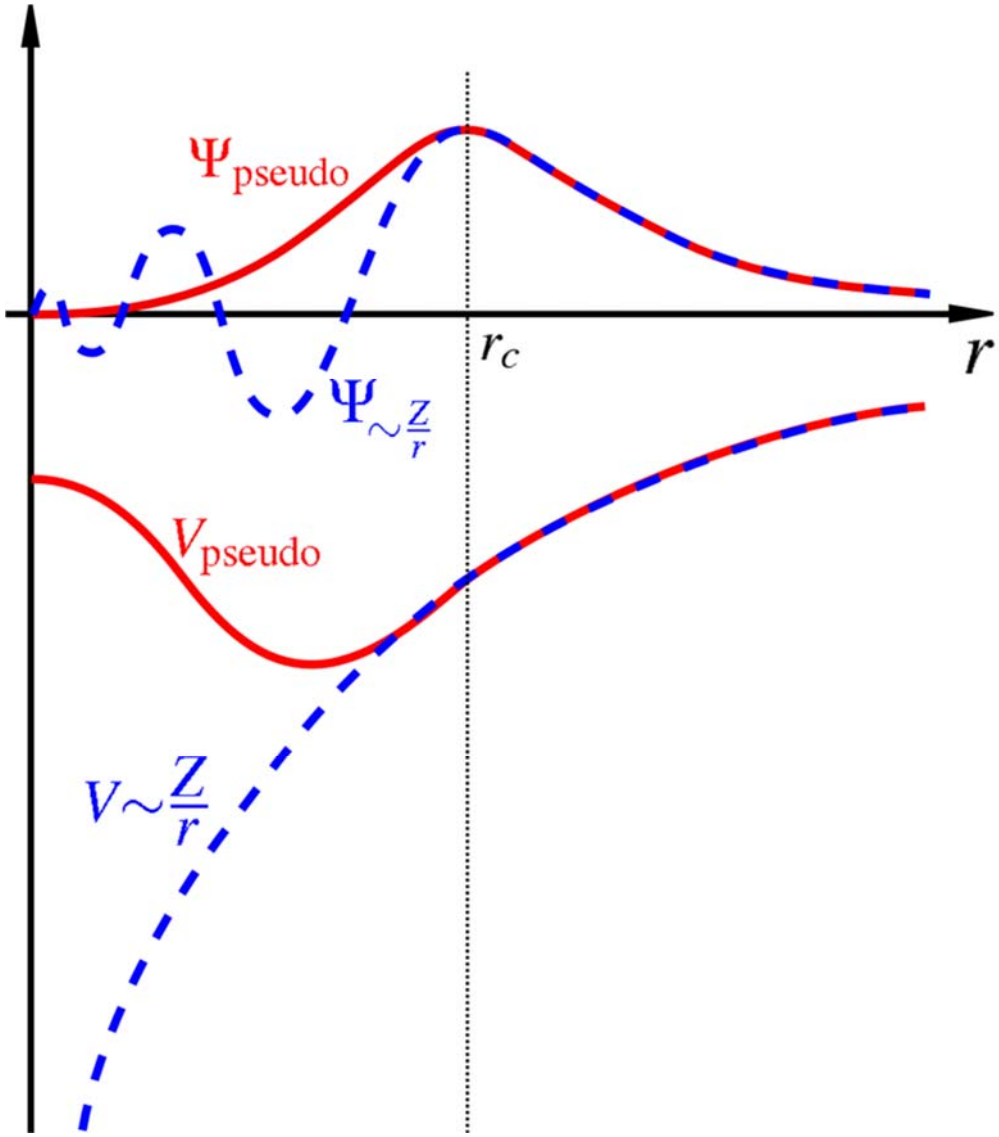

Figure 2.1: The all electron potential (dashed lines) and pseudopotential (solid lines) with the corresponding valence wave function and pseudo-wave functions [Meyer 2006].

The one electron Schrodinger equation is replaced by pseudopotential equation as follows:

$$\frac{P^2}{2m} + V_{pseudo}(r)\psi_{pseudo}(r) = \varepsilon\psi_{pseudo}(r), \qquad 2.12$$

where $\psi_{pseudo}(r)$ is the pseudo wave function and $V_{pseudo}(r)$ is the exact pseudopotential.

2.2.3 CASTEP implementation

The Cambridge Serial Total Energy Package (CASTEP) [Clark et al. 2005] is a first principles quantum mechanical code that explores the properties of crystals and surfaces. Within density functional formalism, it can be used to simulate wide range of materials that include surfaces, crystalline solids, molecules, liquids and amorphous materials. The CASTEP code was originally developed by Payne and Co-workers in the late 1980's and early 1990's [Payne et al. 1992]. The code became widely used for electronic structure calculations. In addition, the new CASTEP code has been designed for parallel computers, allowing much larger problems to be approached.

The code is capable of calculating the physical properties of materials including: total energies: calculations of total energies, forces, stresses and elastic constants; electronic structures: electronic charge densities, orbitals, electrostatic potentials, band structures, total and partial density of states, Mulliken population analysis and optical properties; geometry optimisation: optimisation of atomic position and unit cell parameters, either constrained or unconstrained and under external pressure and stresses; transition states: the LST/QST methods are utilized when finding transition states and exchange and correlation: the well-known LDA and GGA functionals are included (such as PW91, PBE and RPBE functionals), furthermore non-local functionals such as the weighted density approximation (WDA), Hartree-Fock and screened exchange are also available and many other physical properties of materials.

2.3 Density of states

The density of states (DOS) of a system describes the number of states per interval of energy at each energy level that are available. The DOS indicates how densely packed quantum states are in a system. Integration of DOS over a range of energy yields a number of states;

$$N(E) = \int_{E}^{\Delta E} g(E)dE \qquad 2.16$$

where N(E) denotes the carrier density and g(E)dE represents the number of states between E and dE. The density of states permits integration to be done with respect to the electron energy instead of the integration over the Brillouin zone. It is often used for quick visual analysis of the electronic structure. Characteristics such as the width of the valence band, the energy gab in insulators and the number of intensity of the main features are helpful in interpreting experimental spectroscopic data. The most accurate methods used are based on linear or quadratic interpolations of band energies between the reference points in the Brillouin zone. The most popular and reliable technique is based on the tetrahedron interpolation. However, it is not well suited to the Monkhorst-Pack grid of special points. The method is based on linear interpolation in parallelepipeds formed by the points of the Monkhorst-Pack set, which is followed by the histogram sampling of the resultant set of band energies.

In the study of complex minerals there can be a formation of pseudo gap in the electronic density of states at the Fermi energy (E_F) and the relation of this feature to the stability of the particular structure. Pierce et al. [Pierce et al. 1994] and Matsuda et al. [Matsuda et al. 2001] have suggested the role of pseudo gap in the structural stability by the experimental observation of very high resistivity in structurally well-ordered stable quasicrystals. Several contexts have proposed the direct relations between the formation of a pseudo gap and stability of the structure. In oxygen molecule (O_2), water molecule (H_2O), thiol collectors and ferromagnetic Fe and Ni the partial filling of narrow orbitals following Hund's rules and high electron density of states near the E_F result in a spin polarised valence band [Bartell 1968]. Literature reveals that densities of states are also essential in determining the stability trend of structures with same composition with respect to the E_F. The theory suggests that the element with highest density of states around the E_F is considered the least stable, while the element with the lowest density of states is most stable. Moreover, the element with greater contribution at the E_F is the most active or reactive element.

2.4 Charge population analysis

The properties of chemicals and materials are often described in terms of charge transfer between atoms and the presence of ionic charges or electric multipoles on atoms or molecules. Theoretical calculations producing estimates of the electronic charge distribution in the system can, in principle, provide this type of information but it is not clear how to extract it. The atomic charges in molecules or solids are not observables and therefore not defined by quantum mechanical theory. The output of quantum mechanical calculations is a continuous electronic charge density and it is not clear how one should partition electrons amongst fragments of the system such as atoms or molecules. Many different schemes have been proposed, some are based on electronic orbitals (such as Mulliken Population Analysis) and others based on only the charge density such as Bader's atoms in molecules method.

The Mulliken analysis is the most commonly used orbital based method. It can be applied when basis functions centred on atoms are used in the calculation of the electronic wavefunction of the system. The charge associated with the basis functions centred on a particular atom is then assigned to that atom. This can be a fast and useful way of determining partial charges on atoms but it has the major drawback that the analysis is sensitive to the choice of basis set.

CHAPTER 3

Bulk and Surface Modelling

Bulk and surface relaxation of $PtSb_2$

In this chapter, we discussed the DFT results of the bulk structure and surface relaxation for $PtSb_2$ (geversite) mineral. Firstly, the bulk convergence test variation of cut-off and k-points will be discussed. The bulk structures construction and relaxation are shown and their electronic structures were explored. Secondly, different terminations of the surface were investigated from the relaxed bulk structure and variation of slab layers (thickness) convergence was inspected. Thirdly, we showed comparison of the three low index surfaces, ((100), (110) and (111)) for surface stability. Lastly, the electronic structures of surfaces will also be presented.

3.1 Convergence of cut-off energy and k-points sampling

3.1.1 $PtSb_2$ bulk Cut-off energy

Within the plane-wave pseudopotential method (CASTEP) [Clark et al. 2005], before any properties of the system were calculated, it was important to determine the kinetic energy cut-off for the material that gives accurate wave functions and total energy. The kinetic energy cut-off established for $PtSb_2$ structure was determined from a plot of the total energy against kinetic energy cut-off. The structural optimization energy calculations were performed at different kinetic energy cut-off within GGA-PBE [Perdew et al. 1996]. Calculations were repeated for different cut-off energies until a constant minimum energy was reached and the total energies corresponding to particular cut-off energies were noted. The plot of total energy against kinetic energy cut-off for $PtSb_2$ is represented in Figure 3.1. The plot showed almost a zero slope starting from cut-off energy of 450eV, indicating that the variation of total energy with cut-off was negligible at this point. Thus, the kinetic energy cut-off of 500 eV was chosen which corresponds to the minimum total energy and will be used in all calculations for the $PtSb_2$ structures under study.

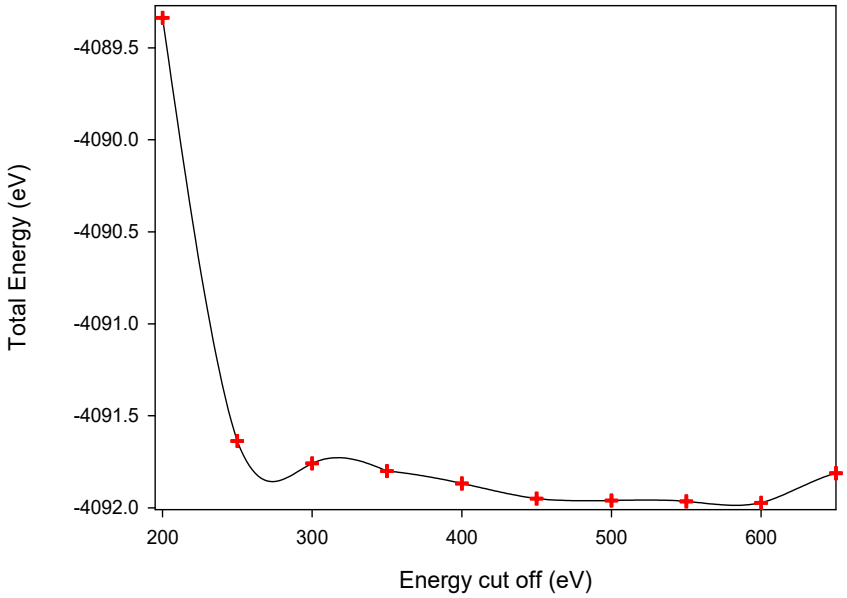

Figure 3.1: Total energy against kinetic energy cut-off for $PtSb_2$ structures.

3.1.2 $PtSb_2$ bulk k-points sampling

After a suitable kinetic cut-off energy has been obtained, it was crucial to also determine the appropriate number of k-points to use in plane-wave pseudopotential calculations. Several methods have been suggested for special k-points sampling in the Brillouin zone [Chadi et al. 1973, Monkhorst et al. 1976]. Such methods helped in obtaining the accurate approximation for the total energy by calculating the electronic state at a very small number of k-points. The Monkhorst-Pack scheme [Monkhorst et al. 1976] of the k-points sampling was used to select an optimal set of special k-points of the Brillouin zone such that the greatest possible accuracy was achieved. Different values of k-points mesh parameters were varied from 2x2x2 to 8x8x8 until the total energy change was negligible. Appropriate k-points mesh parameters were found to be 6x6x6. At this point it was observed that the total energy between two consecutive points converged to within 1.0 meV, which indicated that the energy change was negligible (Figure 3.2).

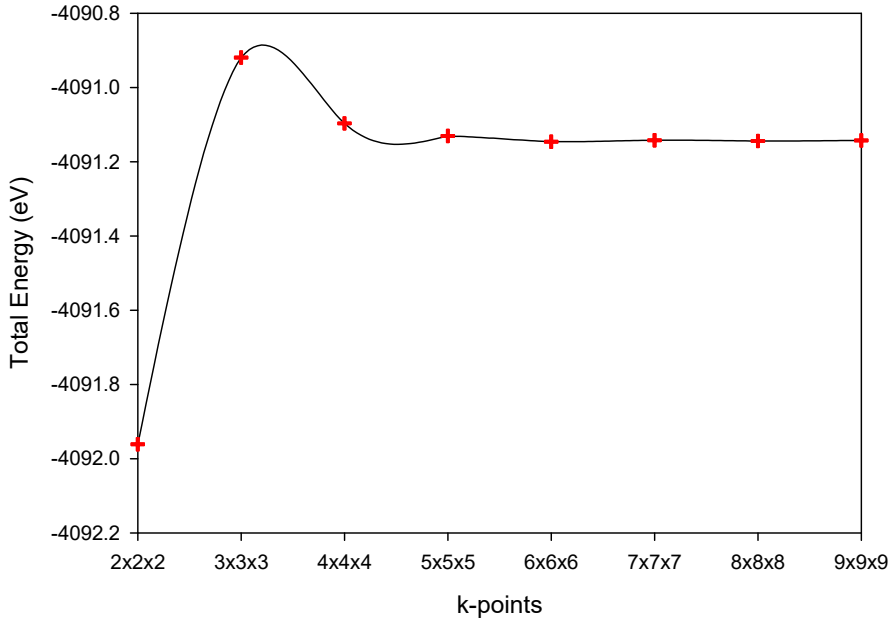

Figure 3.2: Total energy against k-points mesh for $PtSb_2$ bulk structure.

3.1.3 PtSb$_2$ surface k-points sampling

After a suitable kinetic energy cut-off and k-points for the bulk has been obtained, it was crucial to also determine the appropriate number of k-points to use in plane-wave pseudopotential for the surface calculations. The special k-points for surfaces were dependent on the crystal structure that is for a cubic the x and y directions are equal, while the z direction takes the unity value (1) (e.g. 2x2x1). This sampling orders that along the z direction there would be no compression force since it is the vacuum slab site, if the z direction was given a higher value than unity it would mean that the vacuum slab would be ignored. This will enable the adsorbate to interact freely in the vacuum. The Monkhorst-Pack scheme [Monkhorst et al. 1976] of the k-points sampling was used to select an optimal set of special k-points in the Brillouin zone such that the greatest possible accuracy was achieved.

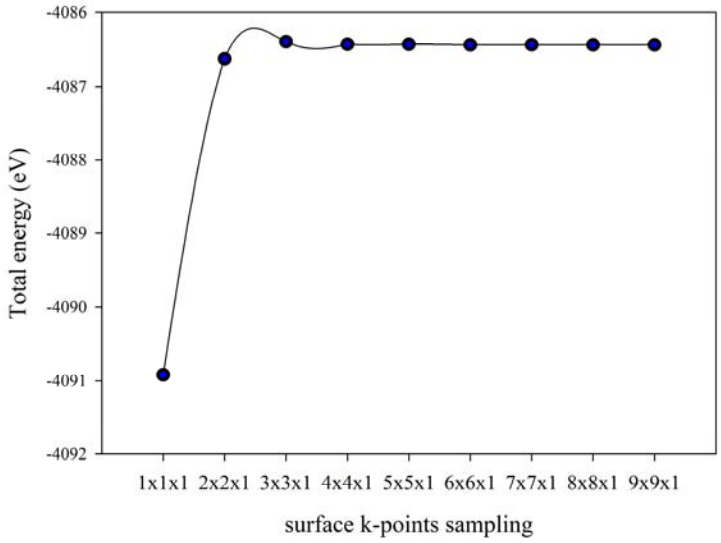

Figure 3.3: Total energy against k-points mesh for $PtSb_2$ surface models.

Different values of k-points mesh parameters were varied from 1x1x1 to 9x9x1 until the total energy change was negligible. Appropriate k-points mesh parameters were found to be 4x4x1. At this point, it was observed that the total energy between two consecutive points converged to within 1meV, which indicated that the energy change was negligible (Figure 3.3). Note that the cut-off energy (500 eV) obtained in the bulk would not change and thus was used in obtaining the special k-points for the surfaces and it will be used throughout the study for both bulk and surfaces.

3.2 Computational details

We have employed the DFT CASTEP code of Materials Studio, using the plane-wave with PBE exchange-correlation functional. The plane-wave basis set with a cut-off energy of 500 eV was set, which demonstrated convergence to within 0.2 meV/atom. We employed the ultrasoft pseudopotentials [Kleinman et al, 1982 and Vanderbilt, 1990] and the electron configurations considered for mineral surface were: Pt: $[Xe]4f^{14}5d^{9}6s^{1}$ and Sb: $[Kr]4d^{10}5s^{2}5p^{3}$ and for adsorbates we focused on the atoms that binds to the surface, which were: S:$[Ne]3s^{2}3p^{4}$, O: $[He]2s^{2}2p^{4}$. A k-point grid of 6x6x6 for the bulk and 4x4x1 for surfaces ware generated using the Monkhorst-Pack [Monkhorst et al. 1976] scheme. The size of the k-point grid used for mineral represents a k-point sampling spacing no greater than 0.05 $Å^{-1}$. The convergence tolerances for force, ionic displacement and energy were 0.05 $eVÅ^{-1}$, 0.001 Å and 0.01 meV/atom, respectively. Slab depth for each

surface model will be listed for each model. The vacuum height (as discussed in the following section) for all surface models in this chapter was set at 20.0 Å in order to avoid the interaction of the adsorbates with the upper repeating slab model. Throughout this work model, total energies (in eV) will be quoted to three(3) decimal places to allow for future in-depth model comparison and optimisation by other researchers, while the surface and adsorption energies will be quoted to three decimal places.

3.3 Bulk $PtSb_2$ optimization and electronic properties

In this section, we present the structural relaxation of the $PtSb_2$ structure. The structural optimizations was performed as discussed in the computational details. We also discussed the density of states (DOS) and Mulliken atomic charges of the $PtSb_2$ bulk structure. These calculated properties were important since they depict the behaviour of the $PtSb_2$ under 0 K conditions.

3.3.1 $PtSb_2$ bulk structure relaxation and electronic properties

We have performed $PtSb_2$ bulk structure relaxation and the optimized structural properties are shown in Table 3.2. The relaxed crystal structure was found to have a = 6.531 Å and the dimer Sb–Sb bond was found to be 2.829 Å as shown in Figure 3.4

Table 3.1: The relaxed atomic positions of $PtSb_2$ crystal structure.

Property			**Value**	
Formula			$PtSb_2$	
Z			4	
Unit cell length (a=b=c)			6.531 Å	
Cell angles (α=β=γ)			90˚	
Space-group			Pa-3 (#205)	
Atoms	**Position**	**x**	**y**	**Z**
Pt	(4a)	0.000	0.000	0.000
Sb	(8c)	0.375	0.375	0.375

Pt denote the octahedral Pt(O) and Sb denote the tetrahedral Sb(T) atoms.

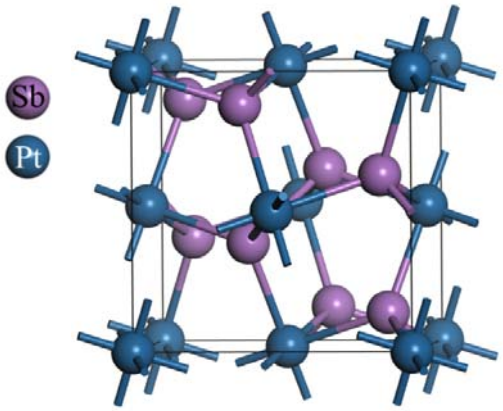

Figure 3.4: $PtSb_2$ bulk structure.

Now we have computed the density of states (DOS) and atomic charges for the bulk structure in order to gain knowledge about its chemistry behaviour. The DOS are shown in Figure 3.4 and showed a metallic behaviour. Furthermore, we observed that the Fermi energy (E_F) fell deep into the pseudo gap suggesting stability. The PDOS indicated that the 5p-orbital of Sb atoms had greater contribution at the E_F than the 5d-orbital and 6p-orbital of Pt atoms. The presence of the 6p-orbital for Pt will be explained below. We observed that the Pt contributed very little at the E_F and at the conduction band (CB). We observed that the pseudo gap was present on both atoms (Pt and Sb), suggesting that stability emanated from both Pt and Sb atoms.

The electron configuration of Pt is a little complicated and it emanates from the relativistic effects, electron correlation, and shielding effects. There is an interplay between the attraction of the nucleus and the electrons, and the electron repulsion between all electrons. The heavier the atoms become, the more important relativistic effects become, since the inner electrons are moving much faster as they are in a stronger electric field from the higher charge of the nucleus. The outer orbitals are less compact than the inner ones, but a stronger effect is that the outer electrons are shielded and therefore the nucleus attraction is weaker. This can be easily solved by the Schrödinger/Dirac equations [https://chemistry.stackexchange.com]. For Pt, the 6s-orbital (outer) and 5d-orbital almost have the same energy as such it is better to have 4 fully filled and 2 half-filled orbitals than having 5 fully filled and 1 empty. The initial configuration of Pt is: $[Xe]4f^{14}5d^{8}6s^{2}$, then one electron is transferred from 6s-orbital to 5d-orbitals, so that all orbitals become stable, either through full filling or half filling, which is better than

having one empty and unstable. This makes the Pt electron configuration to be: $[Xe]4f^{14}5d^{9}6s^{1}$ [https://chemistry.stackexchange.com]. The electron configuration of Sb atoms was considered as $[Kr]4d^{10}5s^{2}5p^{3}$ and the Sb is a poor metal thus its great contribution at the E_F is significant.

The DOS of $PtSb_2$ bulk displayed that there were some electrons transferred into the 6p-orbital from the 5d-orbitals. This was evident since at the E_F, the 6p-orbital was dominant with some empty states of 5d-orbitals just above the E_F. These effects occurred in order to form a stable $PtSb_2$ mineral as we observed E_F falling deep into the pseudo gap. The Sb atoms clearly showed the half-filled 5p-orbital, with some empty states just above the E_F and as such the E_F also fell deep into the pseudo gap for stability.

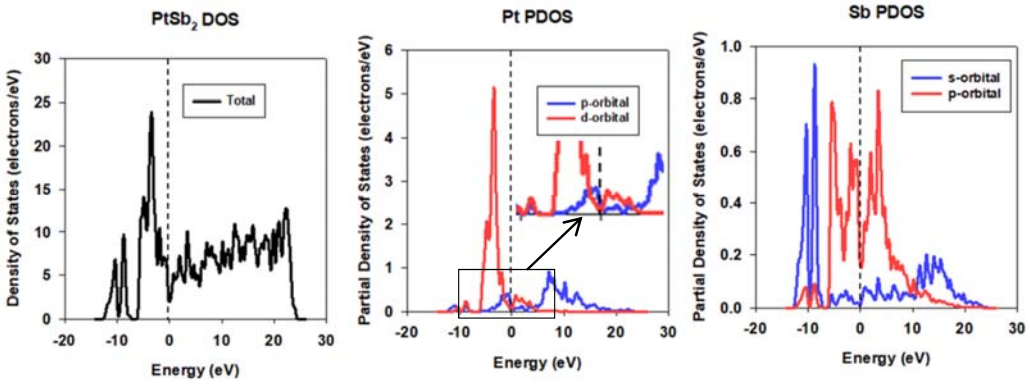

Figure 3.5: The total density of states and partial density for the bulk $PtSb_2$ model.

The atomic charges for the $PtSb_2$ bulk structure was also computed and indicated negative charges for the Pt atoms and positive charges for the Sb atoms as shown in Table 3.1. The presence of 6p-orbital filled can be easier explained from the Mulliken atomic charges. We found that the $4f^{14}$-orbitals of the Pt and $4d^{10}$-orbitals of Sb atoms were shielded and form part of the core electrons thus did not appear on the DOS and on the charges. This indicated that the $5d^{9}6s^{1}$ for Pt and $5s^{2}5p^{3}$ for Sb were the outer shell or valence electrons for these atoms and are actively involved in the hybridisation. The atomic charges clearly displayed these effects with the presence of 6p-orbital for Pt atoms, due to the strong hybridisation of the Pt 5d-orbitals with the 5s-orbital and 5p-orbitals of Sb atoms.

Table 3.2: Calculated Mulliken population atomic charges for the bulk $PtSb_2$.

Atoms	s	p	d	Total	Charges (|e⁻|)
Pt	6s = 1.00	6p = 1.27	5d = 8.99	11.26	–1.26
Sb	5s = 1.47	5p = 2.90	5d = 0.00	4.37	+0.63

The 6s-orbital of Pt, is evident that it is unity (half occupied) as shown in atomic charges (Table 3.1) and this agreed well with the electron configuration of Pt atoms. We found that the 5d-orbital of Pt and the 5s-orbiral and 5p-orbitals of Sb atoms transferred some electrons/charges into the 6p-orbital of the Pt atoms. Thus there was the presence of the 6p-orbital on the Pt atoms. The negative charge on the Pt atoms indicated charge/electron gain from the Sb atoms and the positive charge showed a charge/electron loss on the Sb atom to the Pt atoms. This was evident due to the very little charge loss on the 5d-orbital of Pt atoms (0.01 $|e^-|$). This was in line with the DOS as the Sb dominated the E_F than the Pt atoms.

3.4 Surface modelling

In this section we investigated different surface terminations since these have an effect during adsorption, as a very reactive surface may not give a thermodynamically behaviour of the mineral surface. As such, we considered the most stable surface termination with lowest positive surface energy (less reactive). This was also based on the previous report that during the first stage of flotation where mineral particles are crushed, the minerals will mainly cleave along surfaces that have large inter-planar spacing and few inter-planar bonds, usually low-index surfaces with low surface energies under dry conditions [Mkhonto et al. 2006]. In addition the slab depth was crucial in creating a stable slab and thick enough for adsorption of adsorbate.

3.5 Cleaving of surfaces

The modelling of mineral surfaces is a process of exposing surfaces which is similar to liberation of particles experimentally. Moreover, this emulates the crushing of the rock ore where different surfaces are exposed. In principle different minerals prefer to cleave or break at certain planes which are thermodynamically stable.

Gibbs [1901] developed the concept that the equilibrium structure of a crystal will possess the minimum possible excess energy for a given volume, and as volume and

surface area are inextricably linked, the crystal face with the lowest surface energy will predominate.

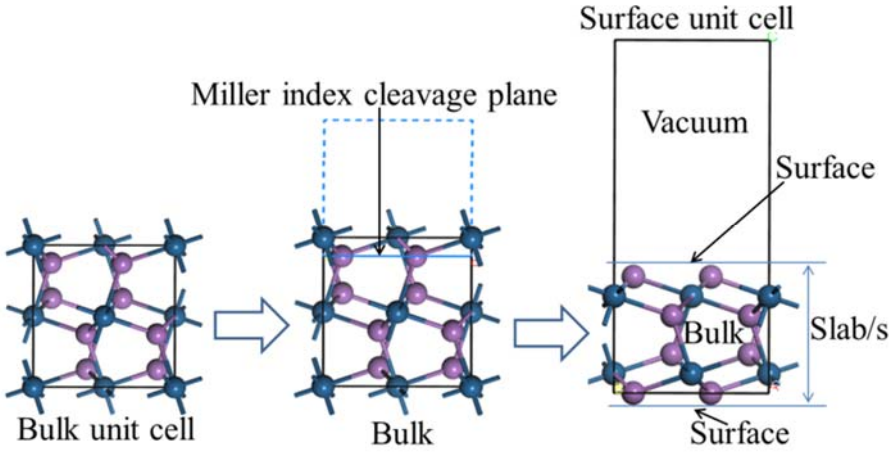

Figure 3.6: The schematics for surface cleavage of $PtSb_2$ slabs.

The surface cleavage of the bulk $PtSb_2$ is shown in Figure 3.6. The initial trial in surfaces cleavage was to obtain the most preferred surfaces termination that possesses no dipole. If a surface termination possessed a dipole, it may be corrected by reconstruction. There are different types of surfaces as discussed by Tasker [Tasker 1979] as shown in Figure 3.7. It is shown that Type I surface has a repeat unit cell where all the anions and cations in the same plane are in stoichiometric ratio. Type II surface has a stacking sequence of charged planes, but the repeat unit consists of several planes, which when considered together have no dipole moment perpendicular to the surface. Type III surface are made up of a stack of alternately charged planes and produce a dipole moment perpendicular to the surface if cut between any planes. In nature, these surfaces are stabilized by defects and/or adsorbed species. To be able to simulate type III the dipole needs to be removed, hence the reconstructed type III surface (Figure 3.7).

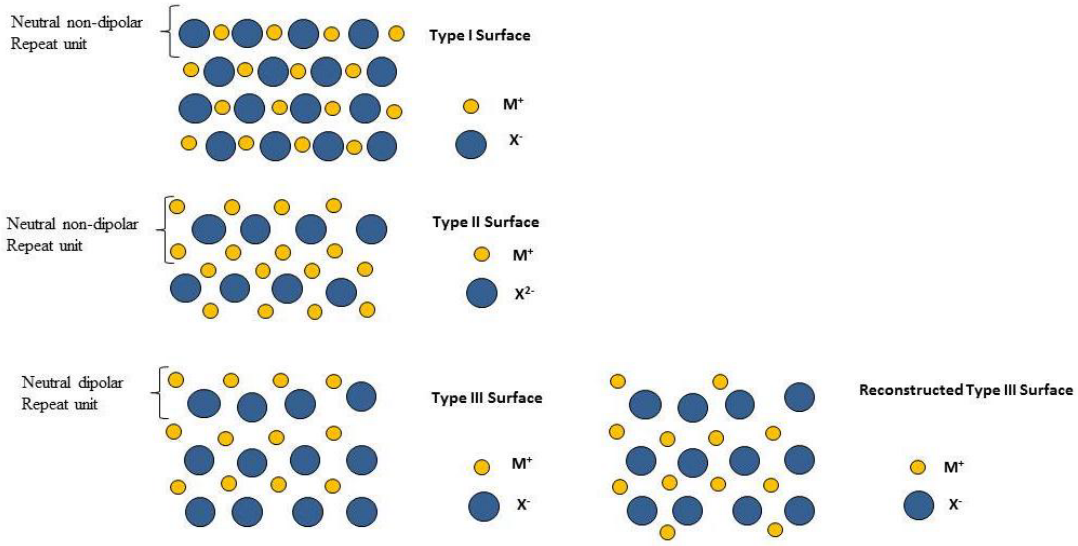

Figure 3.7: The schematics for Tasker type of surfaces

The geometry of the top termination surface was determined by which miller index plane and surface termination was chosen. The bottom termination surface was determined by the slab depth, and must be symmetric to the top termination for a stable surface slab. It was clear that the most stable surface with no dipole were stoichiometric (must be bulk equivalent) and symmetric (both top and bottom must be mirror images).

In addition, the surfaces required a very thick slab to mimic the solid-state interface system of real crystal. This principle insured that the slab depth was sufficient such that both surfaces act as if there is an effectively infinite amount of bulk solid (i.e. the surfaces do not interact with one another through the solid) [Waterson et al. 2015]. However, due to computational costs these were not archived. The stability of the surface terminations and slab thickness can be measured computationally by calculating the surface energy, a measure of the excess energy per unit area induced by cleaving a bulk model, where a small, positive number indicates a stable surface as shown in equation 3.1.

$$E_{surface} = \left(\frac{1}{2A}\right)[E_{slab} - n(E_{bulk})], \qquad 3.1$$

where $E_{(slab)}$ is the energy of the surface, $E_{(bulk)}$/atom is the energy of the bulk per total number of atoms in the bulk and $n_{(slab)}$ is the number of atoms of the surface and A is the surface area. This formula was used in order to account for the number of atoms in the surface and normalize it to the bulk.

Lastly, in order to reduce the search for most stable surfaces to a computationally tractable problem, whilst also ensuring that the most likely surfaces were surveyed, only the bulk terminations on the three low miller index (100), (110) and (111) were considered unless literature suggested otherwise.

3.5.1 $PtSb_2$ Surface terminations

The surface terminations for the $PtSb_2$ (geversite) were prepared in such a way that all mixed and pure metal terminations were considered. In order to achieve the desired terminations precisely, the surfaces were cleaved considering all possible terminations. This exercise had been carried out using the bulk convectional $PtSb_2$ as shown in Figure 3.6. The surface terminations for all the surfaces are shown in Figure 3.8. We found that the (100) and (110) surfaces had three terminations, while the (111) had five possible terminations. We observed that the (100) surface had only one surface that was of Type II with no dipole (Figure 3.8 (100)-B). The other two were similar to Type II. However, they have a layer at the bottom for (100)-A, and a layer for (100)-C, which rendered them to have a dipole perpendicular to the surface. Also the surface energy for (100)-B was lower and indicated that it is the most stable termination.

Table 3.3: Different terminations, number of atoms, number of layers, total energy and surface energy for (100), (110) and (111) surfaces.

Miler Index Plane	Surface Termination	Stoichiometry	Surface energy ($J.m^{-2}$)
			Unrelaxed
(100)	(100)-A	$PtSb_2$	1.569
	(100)-B	***$PtSb_2$***	***0.920***
	(100)-C	$PtSb_2$	1.569
(110)	(110)-A	$PtSb_2$	1.168
	(110)-B	***$PtSb_2$***	***1.194***
	(110)-C	$PtSb_2$	1.170
(111)	(111)-A	$PtSb_2$	1.225
	(111)-B	$PtSb_2$	1.004
	(111)-C	***$PtSb_2$***	***0.939***
	(111)-D	$PtSb_2$	0.992
	(111)-E	$PtSb_2$	1.231

The case of (110) surface, there was also one surface with no dipole (Figure 3.8 (110)-B) which was of Type I, while the other two possessed a dipole. The (111) surface had only one termination which was of Type II with no dipole (Figure 3.8 (111)-C), while the other four were of Type III and required reconstruction. This was similar to pyrite

mineral surfaces as explained elsewhere [Tasker 1979]. All the surfaces were Sb-terminated, suggesting that the $PtSb_2$ cleaves and exposes along the Sb atoms. The computed surface energies for the different terminations indicated that the most stable surface termination with no dipole had the lowest positive surface energy. However, for (110) surface we have used the termination that gave the highest surface energy due to its relaxation after optimization as it will be discussed in section 3.3.3. In addition, similar surface termination has been considered previously for pyrite study [Hung et al. 2002]. It is clear from these preliminary results that the (100) surface had the lowest surface energy compared to the other surfaces.

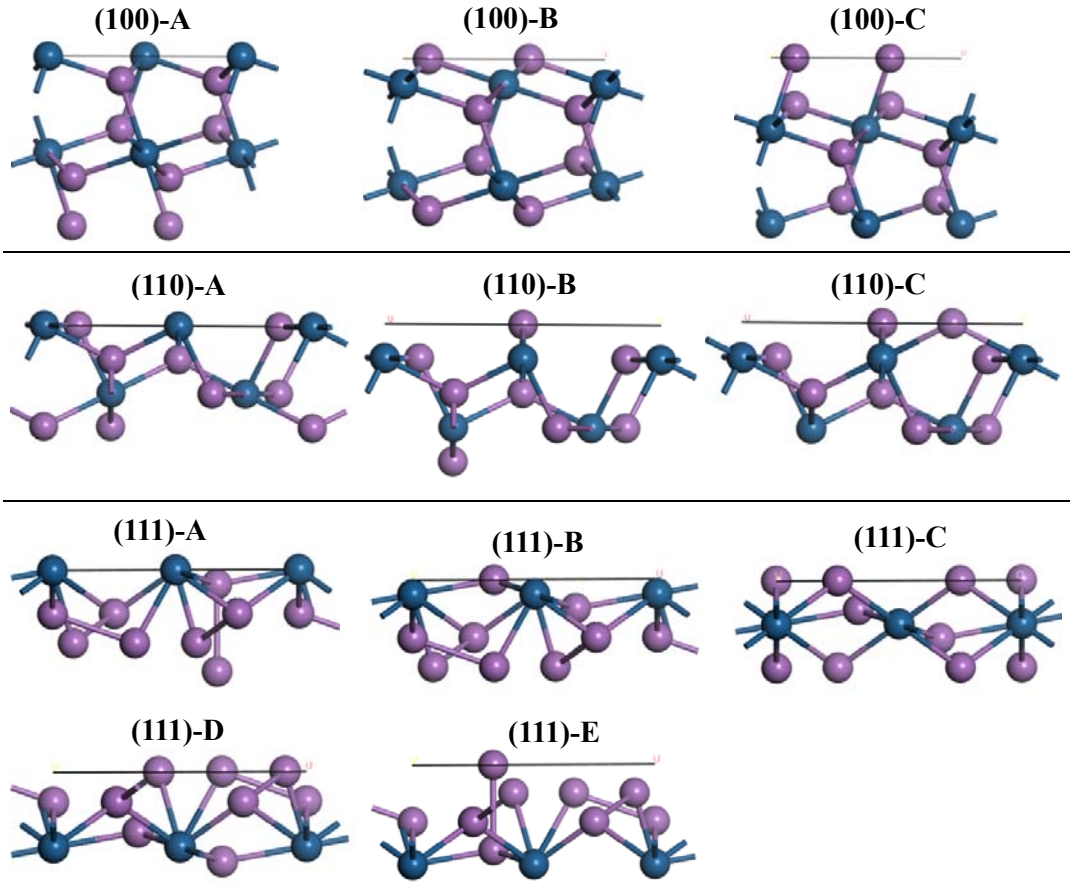

Figure 3.8: The different surface terminations for $PtSb_2$ cleaved from (100), (110) and (111) miller index planes.

3.5.2 $PtSb_2$ Surface slab thickness

Now we have performed slab thickness convergence using the number of slabs on a unit cell. Note that for (100) and (110) surfaces two slabs were equivalent to the bulk, while for (111) surface each slab was equivalent to the bulk and these were unrelaxed calculations. We have plotted a total energy against slab depth and observed a decreasing trend as the slab depth increases, see Figure 3.9, 3.10 and 3.11 for (100) surface slabs, (110) surface slabs and (111) surface slabs, repectively. Furthermore, the surface energies for slabs were computed and these results showed much closer convergence, with values from 5 slabs for (100) and (110) surfaces and from three slabs for (111) surface, agreeing to within 0.01 Jm^{-2}, as shown in Table 3.4, 3.5 and 3.7 for (100), (110) and (111) surface slabs variations respectively. Interestingly, for (111) surface we found that for the four slab the surface energy was very high compared to the other slabs. This may suggest that at this slab there was a high instability of the slab surface. We found that each slab consisted of 3-layers for (100) and (110) surfaces, while for (111) surface each slab consisted of 5-layers. The unit cell may present a problem in adsorptions as such a minimum of a 2x2 supercell for the $PtSb_2$ surfaces were required to permit modelling of collector interactions, otherwise inter-ligand steric interactions may begin to have a significant effect. A 2x2 supercell of five slabs (15-layers) for (100), six slabs (18-layers) for (110) model and 3 slabs (15-layers) for (111) surface were computationally intractable when considering the sheer volume of calculations to be completed as shown in bold in the Table.

Table 3.4: Surface energies for increasing slab depth models of the (100) As terminated $PtSb_2$ surface.

Number of Slabs	Number of Atoms in Model	Total Energy (eV)	Equivalent Bulk Total Energy (eV)	Surface Area ($Å^2$)	Surface Energy ($J.m^{-2}$)
					Unrelaxed
Bulk	12	–4088.4200	–	–	–
2	12	–4083.4675	–4088.4200	0.024	0.930
3	18	–6127.3867	–6132.6301	0.024	0.985
4	24	–8171.5311	–8176.8401	0.024	0.997
5	***30***	***–10215.5824***	***–10221.0501***	***0.024***	***1.027***
6	36	–12259.7939	–12265.2601	0.024	1.027
7	42	–14303.9875	–14309.4701	0.024	1.030
8	48	–16348.1586	–16353.6801	0.024	1.037

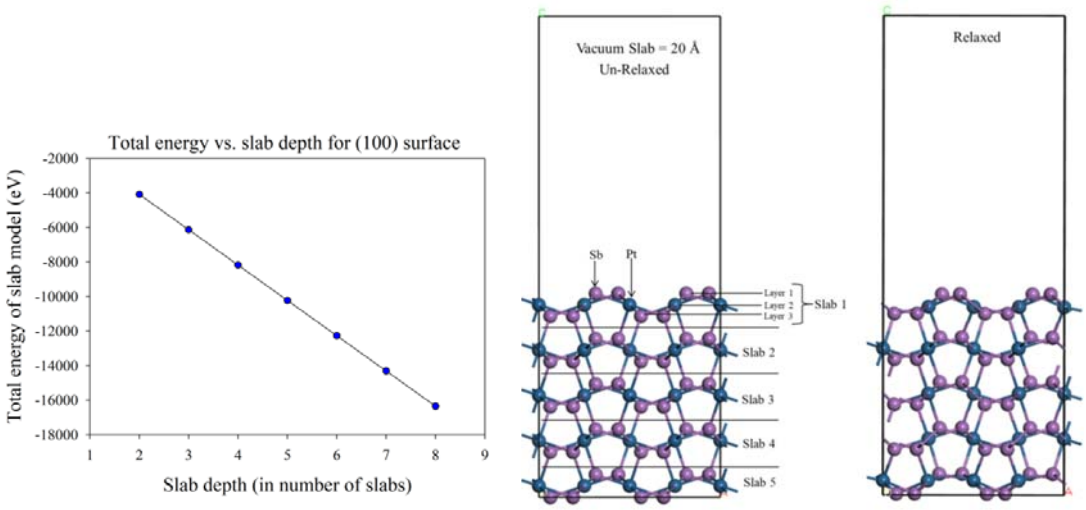

(a) (b) (c)

Figure 3.9: (a) The slab depth against total of slab model; and (b) un-relaxed and (c) relaxed supercell $PtSb_2$ (100) surface models.

Table 3.5: Surface energies for increasing slab depth models of the (110) As terminated $PtSb_2$ surface.

Number of Slabs	Number of Atoms in Model	Total Energy (eV)	Equivalent Bulk Total Energy (eV)	Surface Area (Å²)	Surface Energy (J.m⁻²)
					Unrelaxed
Bulk	12	–4088.4200	–	–	–
2	12	–4079.3130	–4088.4200	0.017	1.209
3	18	–6122.7730	–6132.6301	0.017	1.309
4	24	–8167.0738	–8176.8401	0.017	1.297
5	30	–10211.0912	–10221.0501	0.017	1.323
6	***36***	***–12255.3146***	***–12265.2601***	***0.017***	***1.321***
7	42	–14299.4178	–14309.4701	0.017	1.335
8	48	–16343.6290	–16353.6801	0.017	1.335
9	54	–18387.7665	–18397.8901	0.017	1.344
10	60	–20431.9542	–20442.1002	0.017	1.347

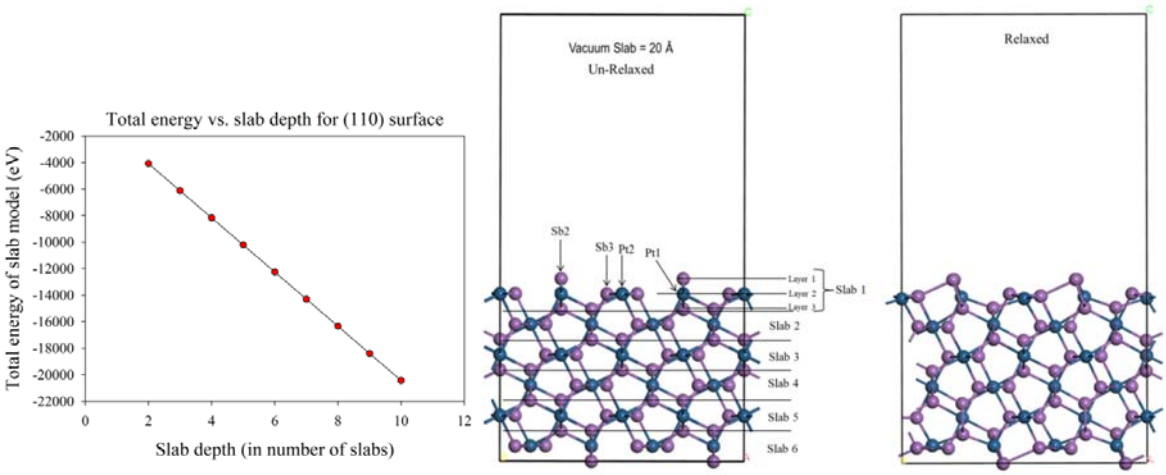

(a) (b) (c)

Figure 3.10: (a) The slab depth against total of slab model; and (b) un-relaxed and (c) relaxed supercell $PtSb_2$ (110) surface models

Table 3.6: Surface energies for increasing slab depth models of the (111) As terminated $PtSb_2$ surface.

Number of Slabs	Number of Atoms in Model	Total Energy (eV)	Equivalent Bulk Total Energy (eV)	Surface Area (Å^2)	Surface Energy (J.m^{-2})
					Unrelaxed
Bulk	12	–4088.4200	–	–	–
1	12	–4078.3193	–4088.4200	0.012	0.949
2	24	–8164.9915	–8176.8401	0.012	1.113
3	***36***	***–12252.9469***	***–12265.2601***	***0.012***	***1.156***
4	48	–16314.2018	–16353.6801	0.012	3.707
5	60	–20429.5271	–20442.1002	0.012	1.181
6	72	–24517.8584	–24530.5202	0.012	1.189

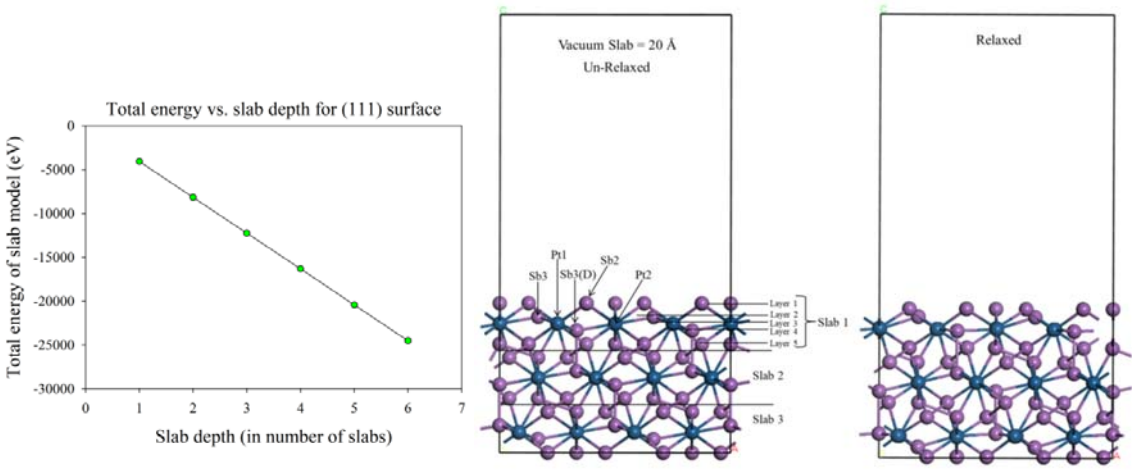

(a) (b) (c)

Figure 3.11: (a) The slab depth against total of slab model; and (b) un-relaxed and (c) relaxed supercell $PtSb_2$ (111) surface models

Table 3.7: Relaxed surface energies for (2x2) supercell of thick slab depth models of the (100), (110) and (111) As terminated $PtSb_2$ surfaces.

Miller Index Plane and Cell	Number of Atoms and slabs in Model	Total Energy (eV)	Equivalent Bulk Total Energy (eV)	Surface Area (Å²)	Surface Energy (J.m⁻²)
					Relaxed
Bulk	12	–4088.4200	–	–	–
(100)-(2x2)	120 (5 slabs)	–40867.0226	–40884.2003	0.006	0.807
(110)-(2x2)	144 (6 slabs)	–49028.6083	–49061.0404	0.004	1.077
(111)-(2x2)	144 (3 slabs)	–49015.2884	–49061.0404	0.003	1.074

Finally, we have performed the surface relaxation and the results are shown in Table 3.7. The computed surface energies showed that the (100) surface was the most stable and the order followed as: (100) < (111) < (110) surfaces. This indicated that the $PtSb_2$ mineral will prefer to cleave along the (100) surface. Both (110) and (111) surfaces have energy which were very close to each other with a difference of 0.003 $J.m^{-2}$. The surface morphology computed using METADISE code [Watson et al. 1996], showed that all three miler index surface planes appear on the crystal morphology as such the mineral crushing will contain all surfaces which is predominantly the (100) surface planes as shown in section 3.3.4. The unrelaxed and relaxed 2x2 supercell surfaces are shown in Figure 3.9, 3.10 and 3.11 for (100), (110) and (111) surfaces, respectively. Their relaxation behaviour are analysed in the next section.

3.5.3 Analysis of the relaxed (100), (110) and (111) surfaces

The $PtSb_2$ surfaces have different coordination and concerning the Pt and the Sb before relaxation and after relaxation as shown in Table 3.8. We found that the Pt and Sb are 5-coordinated and 3-coordinated before after relaxation for (100) surface, respectively. The (110) surface showed that the Pt atoms do not change before and after relaxation, which were 4-coordinated, while the two coordinated Sb atoms changed from 2-coordination to 3-coordination, with the three coordinated Sb atoms changed to 4-coordination. The case of (111) surface did not show any change in coordination (Table 3.8).

Table 3.8: Surface coordination for the top layers atoms for (100), (110) and (111) $PtSb_2$ surfaces.

Surface	**Surface Pt coordination**		**Surface Sb coordination**	
	Unrelaxed	**Relaxed**	**Unrelaxed**	**Relaxed**
(100)	5	5	3	3
(110)	4	4	2, 3	3, 4
(111)	5, 6	5, 6	2, 3	2, 3

Now, the relaxation analysis of the (100) surface was observed to still have the ridge and cleft after relaxation. The Sb atoms in the first layer (1-layer) were observed to relax inwards, while those in the 3-layer relaxed outwards. The Pt atoms relaxed upwards on the surface. However, the surface was still Sb terminated with no creation of new bonds. The case of (110) surface was different, where the Sb atoms reconstructed after relaxation. We observed that the Sb in the 3-layer relaxed outwards, while the Pt atoms relaxed inwards. Interestingly were the Sb in the 1-layer, which relaxed towards and to the left and created new bonds with the 3-coordinated Sb atoms in the 2-layer.

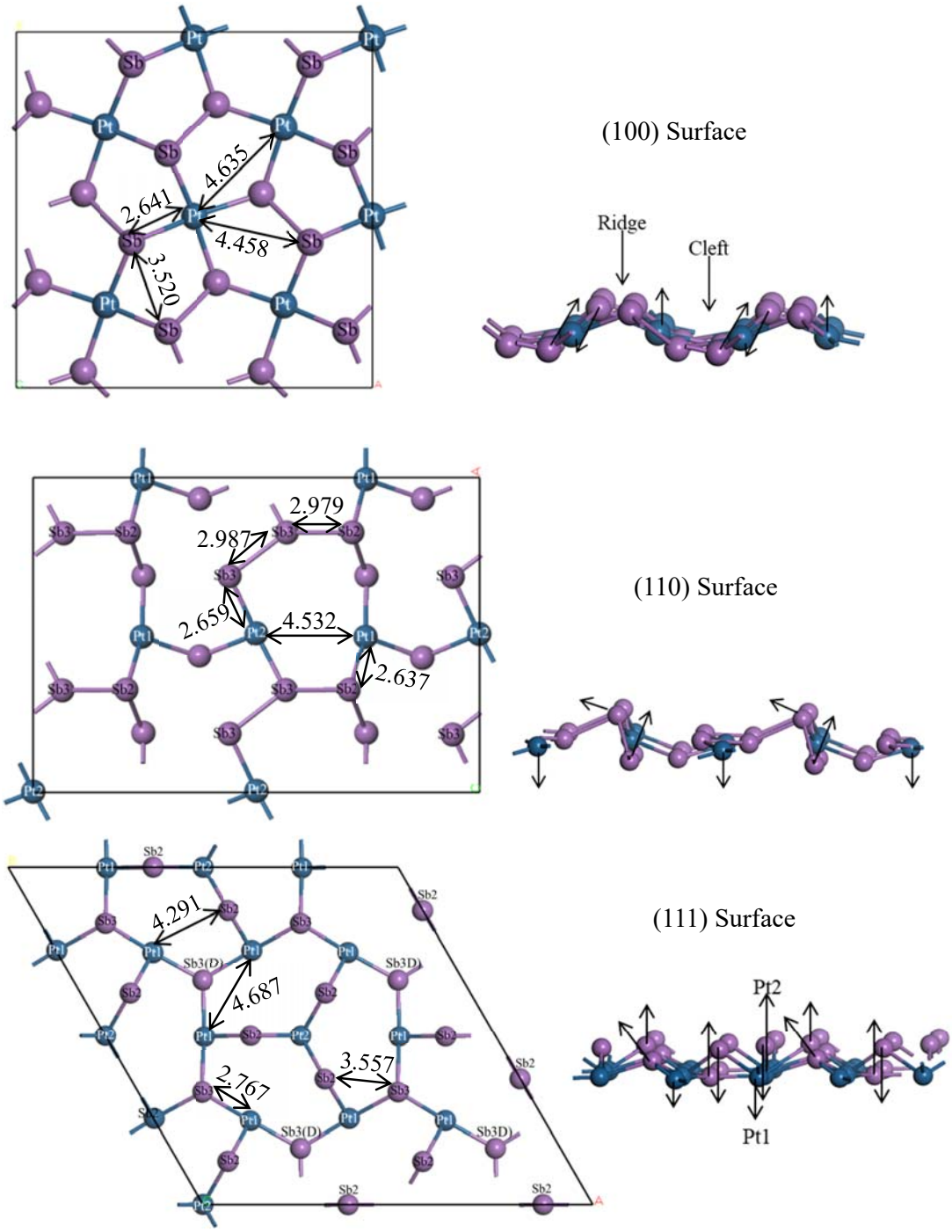

Figure 3.12: The top view and side view of the top most layers for $PtSb_2$ (100), (110) and (111) surface models.

This created a surface termination to change from 2-coordinated to 3-coordinated as such removed the dipole which may have been present on the surface. Although this surface termination had shown high surface energy (least stable) it reconstructed and lowered the

surface energy after relaxation. Thus this surfaces termination was chosen as the working termination and similar surface termination has been reported for pyrite mineral [Hung 2002].

For (111) surface we found an outwards and inwards relaxation of the Pt2 and Pt1 atoms, respectively. The Sb atoms were noted to have some 2-coordinated atoms to relax outwards while others relaxed inwards. The Sb 3-coordinated relaxed outwards, with the dimer Sb3(D) also relaxing outwards aligning to the 3-layer. The (111) surface showed a dominant 2-coordinated Sb-termination surface.

A thorough appreciation of the mineral surface was required in order to understand the collector binding environment. The exposed working surfaces consisted of ridges of Sb atoms, with Pt atoms inhabiting the clefts between ridges, as shown in Figure 3.12. Most importantly, when considering the binding of bridging ligands such as xanthates, which can interact with two surface metals simultaneously is the distance between the metal sites. Considering the Sb lone pairs, it is unlikely that bridging ligands can interact with two Pt atoms in different clefts simultaneously, due to the implicit high steric strain as shown by Waterson et al. [2015]. We found that for (100) surface the Pt-Sb = 2.641 **Å** was the likely bridging site due to its short bond length. For (110) surface the Pt1-Sb3 and Pt2-Sb2 was the likely bridging sites. However, the bridging on Pt1-Pt2 could occur, although the distance is larger, due to the low coordination of these Pt atoms. For (111) surface, the Pt1-Sb3 and Sb2-Sb3 are the most likely bridging sites for xanthate, due to their short distance.

3.5.4 $PtSb_2$ surface morphologies

The crystal morphology defined the cleavage of a mineral during grinding. Experimentally minerals will prefer to cleave along long certain planes and different shapes occur as a result of the most thermodynamically stable surfaces. The breakage of a mineral will contain surface morphology dominanted by the most stable planes. We have computed the surface morphology of $PtSb_2$ to identify the shape of the particle morphology based on the low index surface energies. We found that the (100) surface was cubic, while (110) surface was polyhedron and the (111) surface was octahedron.

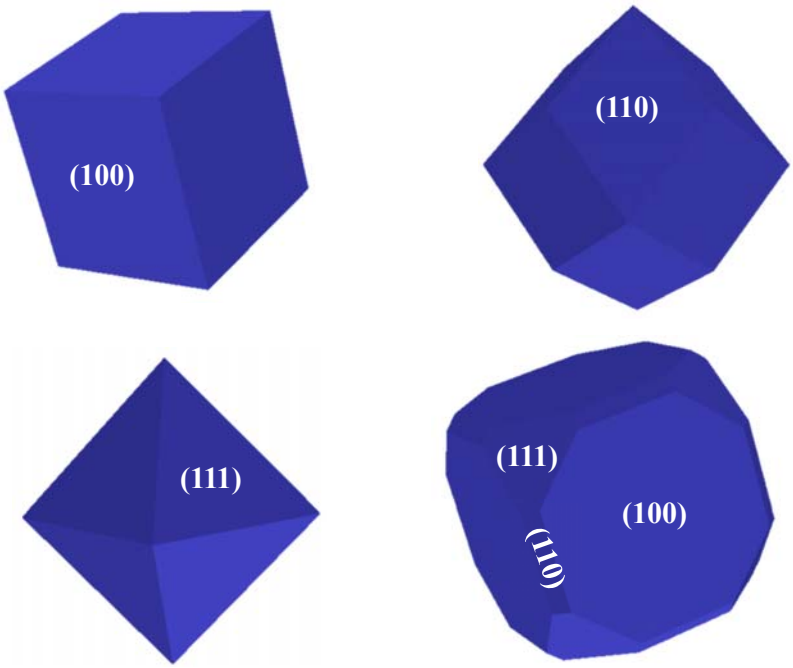

Figure 3.13: The surface morphologies planes for the $PtSb_2$ (100), (110), (111) and combined surface models.

For the combined morphology (i.e. (100), (110) and (111) surfaces), we observed that the (100) surface was dominant at all sides with the presence of the (111) surface at the corner, while the (110) appeared at the edges of the crystal morphology. This indicated that the grinding of the $PtSb_2$ mineral will have the (100) surface dominating, with some (110) and (111) surfaces present. This informed us that all low index surfaces are worth exploring as they may also has an effect in the flotation of the $PtSb_2$ minerals.

3.6 Electronic structures of clean surfaces

In this section we discussed the DOS, Mulliken atomic charges of the three stable clean surfaces. These were important for depicting the nature of bonding behaviour of the surface and interaction of adsorbates.

3.6.1 DOS of (100), (110) and (111) surfaces

The density of states (DOS) for the $PtSb_2$ surfaces have been computed and analysed in order to gain more insight into their chemistry before adsorptions. Generally we observed that all surfaces showed a metallic behaviour. Furthermore, we observed that the Fermi energy (E_F) fell deep into the pseudo gap suggesting stability for (100) and (110) surfaces.

However, for (111) surfaces the pseudo gap was not clearly observed on the total density of states (TDOS). All surfaces showed that for Pt atoms, the 6p-orbital was occupied similar to the bulk structure and it also dominated at the E_F together with the 5d-orbitals. The occupancy of the 6p-orbital will be clearly explained in the Mulliken atoms charges section 3.6.2.

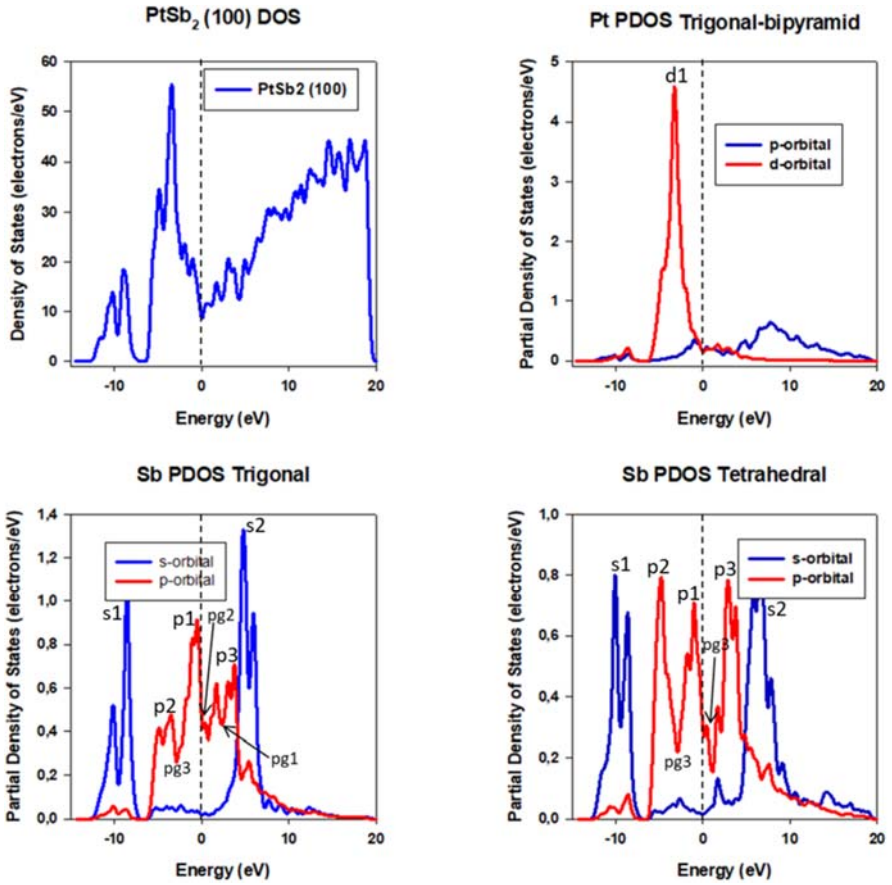

Figure 3.14: The total density of states and partial density of states for the (100) PtSb$_2$ surface.

Now for the case of (100) surfaces as shown in Figure 3.14, we focused and analysed the top Pt and Sb atoms namely Trigonal-bipyramid and Trigonal, respectively. The Tetrahedral Sb atoms were in the third layer on the surface and will not take part in adsorptions. We also observed that at the E_F the Pt atoms dominated very little, with the 6p-orbital and 5d-orbital equal in contribution. Furthermore, the Pt atoms were characterised by a sharp peak (d1) below the E_F. The Sb atoms 5p-orbitals dominated significantly at the E_F and it was characterised by pseudo gaps (pg1, pg2 and pg3) and the

E_F fell into the pseudo gap 2 (pg2). Moreover, it had three dominant 5p-orbital peaks (p1, p2 and p3), with the E_F almost cutting the p1 peak at its highest point. The un-occupied 5p-orbitals states were p3 peaks at the conduction band (CB). We observed that the E_F fell deep into the pseudo gaps of both Pt and Sb atoms, suggesting that both atoms contribute to the stability of the surface. The Sb 5s-orbital were observed to contribute at around –10 eV (s1) at the valence band (VB), while the anti-bonding states (s2) contributed at around 5 eV at the CB.

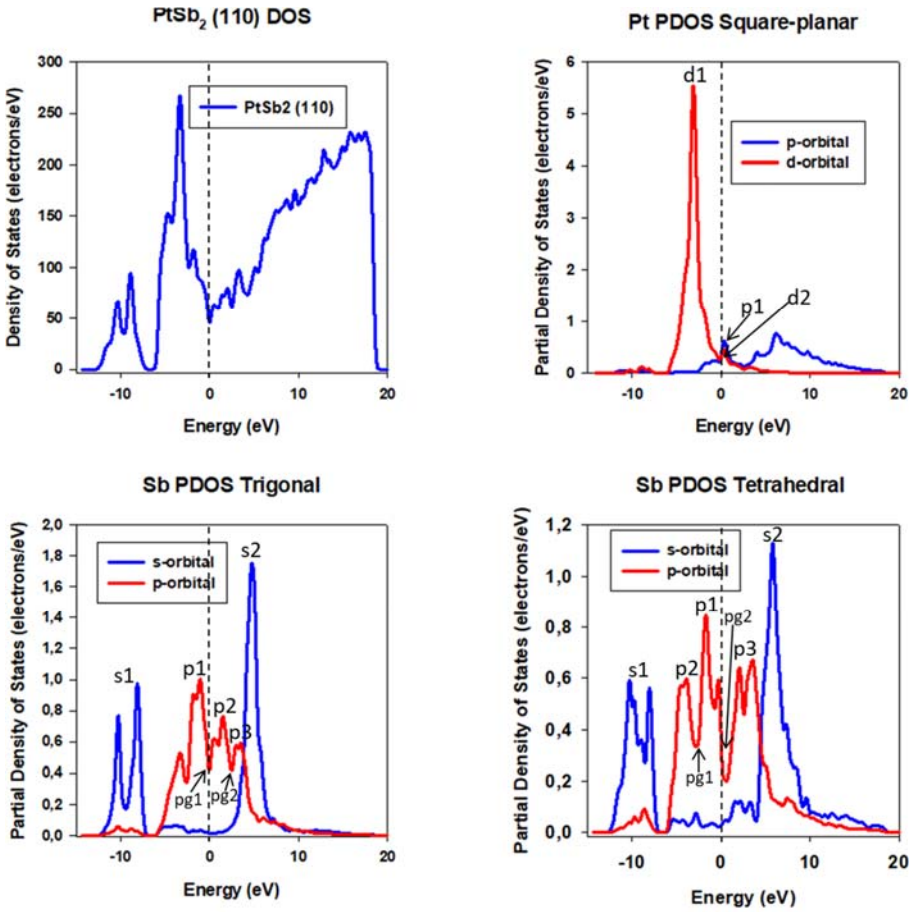

Figure 3.15: The total density of states and partial density of states for the (110) $PtSb_2$ surface

For the (110) surface, we focused on the top Pt and Sb atoms as shown in Figure 3.15. The Tetrahedral Sb atoms were in the second layer on the surface aligned with the Pt atoms (Square-planer). We observed that at the E_F the Pt atoms dominated marginally, with the 6p-orbital having slightly more in states (p1) than the 5d-orbital states (d2). Furthermore, the Pt atoms were characterised by a sharp peak (d1) below the E_F. The Sb

atoms 5p-orbitals dominated significantly at the E_F and it was characterised by pseudo gaps (pg1, pg2 and pg3) and the E_F fell into pseudo gap 1 (pg1). Moreover, it had three dominant 5p-orbital peaks (p1, p2 and p3), with the un-occupied 5p-orbitals states (p2 and p3 peaks) at the conduction band (CB). We observed that the E_F fell deep into the pseudo gaps of mainly the Sb atoms, suggesting that the Sb atoms contribute significantly to the stability of the surface. The Sb 5s-orbital were observed to contribute at around -10 eV (s1) at the valence band (VB), while the anti-bonding states (s2) contributed at around 5 eV at the CB.

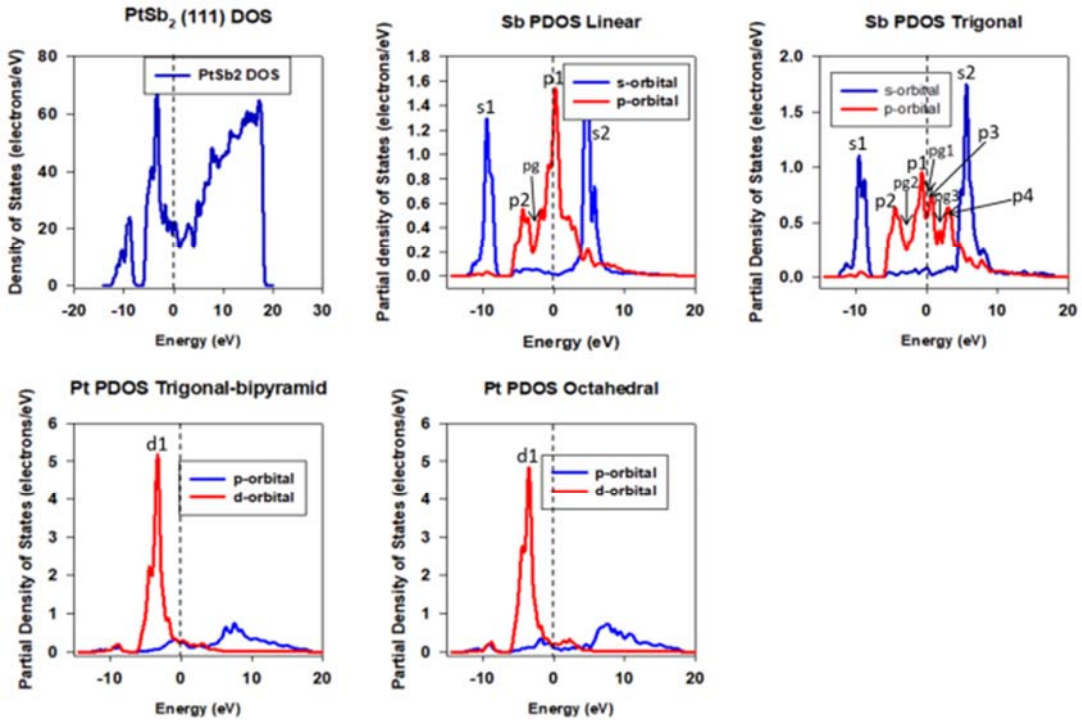

Figure 3.16: The total density of states and partial density of states for the (111) $PtSb_2$ surface

Now, the case of (111) surface is analysed as shown in Figure 3.16 focussing on the top Pt and Sb atoms. The Linear and Trigonal Sb atoms were in the first and second layer on the surface, respectively. The Pt atoms (Trigonal-bipyramid and Octahedral) are in the third layer aligned with the dimer Sb-Sb atoms (Sb3(D). However, we did no show the PDOS for the Sb3(D). We observed that at the E_F the Pt atoms dominated very little, with the 6p-orbital having slightly lower states than the 5d-orbital states for octahedral. For the trigonal-bipyramid the 6p-orbital were equal to the 5d-orbital states at the E_F.

Furthermore, the Pt atoms were characterised by a sharp peak (d1) below the E_F. The Sb atoms 5p-orbitals dominated significantly at the E_F and it was also characterised by pseudo gaps (pg1, pg2 and pg3) for trigonal and only one pseudo gap (pg) for linear Sb atoms. The E_F fell deep into pseudo gap 1 (pg1) of trigonal Sb atoms, while for linear Sb atoms the E_F cuts the p1 peak at its highest point. Furthermore, the trigonal Sb atoms were dominated by four 5p-orbital peaks (p1, p2, p3 and p4), with the un-occupied 5p-orbitals states being the p3 and p4 peaks at the conduction band (CB). The linear Sb atoms were characterised by two 5p-orbital peaks (p1 and p2).

We observed that the E_F fell deep into the pseudo gaps of mainly the trigonal Sb atoms, suggesting that the Sb atoms contributed significantly to the stability of the surface. However, the TDOS did not show any pseudo gap at the E_F. This was due to the linear Sb atoms peak (p1) which was cut by the E_F at its highest point and this also suggested that the linear Sb atoms were more active on the surface. This was also supported by its two-coordination on the surface. The Sb 5s-orbital were observed to contribute at around –10 eV (s1) at the valence band (VB), while the anti-bonding states (s2) contributed at around 5.0 eV at the CB.

3.6.2 Mulliken atomic charges of (100), (110) and (111) surfaces

The atomic charges for the $PtSb_2$ surfaces models were also computed and we noted negative charges for the Pt atoms and positive charges for the Sb atoms as shown in Table 3.9. The interesting presence of 6p-orbital filled can be easier explained from the Mulliken atomic charges. This feature was depicted in the bulk model and the surfaces also showed similar behaviour. The valence electrons on the surface were the $5d^9 6s^1$ for Pt and $5s^2 5p^3$ for Sb and these electrons were actively involved in the hybridisation. The atomic charges clearly displayed these effects with the presence of 6p-orbital for Pt atoms, due to the strong hybridisation of the Pt 5d-orbitals with the 5s-orbital and 5p-orbitals of Sb atoms. As explained in the bulk the 6p-orbital was occupied by electrons from the 5s-orbital and 5p-orbitals of Sb atoms and now for surface the 6s-orbital on (100) and (111) surfaces also lose some electrons. Interestingly, we observed that on all surfaces the 5d-orbital of Pt have the nine electrons ($5d^9$ filled), suggesting that these orbitals are occupied unlike in the bulk model. These effects occurred in order to form a stable surface.

For (100) surface, the Pt 6p-orbital was occupied by electrons from the 5s-orbital and 5p-orbital of the Sb atoms. It is suggested that some electrons may have been transferred from the second slab Pt 5d-orbitals similar to the bulk model behaviour. The (110) surface case indicated that the Pt 6p-orbital was occupied by electrons from the 5s-orbital and 5p-orbital of the Sb atoms and little from the Pt 6s-orbital. Interestingly, the 2-coordinated Sb atom remained with its 3 electrons ($5p^3$ filled), suggesting no loss in electrons. Now, the case of (111) surface showed that the 6-coordinated Pt atoms have more charges into the 6p-orbitals similar to the bulk model behaviour, with no loss in the 6s-orbital. This indicated that the octahedral Pt atoms gained electrons into the 6p-orbital from the Sb atoms. The 5-coordinated Pt atoms showed unity occupancy on the 6p-orbital and with some charges lost in the 6s-orbital.

Table 3.9: Calculated atomic population (Mulliken) charges of $PtSb_2$ surfaces ($|e^-|$).

		Orbital charges				
Surface	**Atom**	**s**	**p**	**d**	**Total**	**Charge |e|**
100	Pt	1.00	0.85	9.08	10.97	–0.97|e⁻|
	Sb	1.84	2.95	0.00	4.79	+0.20|e⁻|
110	Pt1	0.99	0.70	9.09	10.78	–0.78|e⁻|
	Pt2	0.96	0.70	9.11	10.77	–0.77|e⁻|
	Sb2	1.90	3.04	0.00	4.94	+0.06|e⁻|
	Sb3	1.85	2.95	0.00	4.80	+0.20|e⁻|
111	Pt5	0.96	1.00	9.06	11.02	–1.02|e⁻|
	Pt6	1.00	1.16	9.03	11.19	–1.19|e⁻|
	Sb2	1.78	2.91	0.00	4.70	+0.30|e⁻|
	Sb3	1.78	2.91	0.00	4.69	+0.31|e⁻|
	Sb3(D)	1.62	2.93	0.00	4.55	+0.45|e⁻|

These effects showed that the Sb atoms were more actively involved in the 6p-orbital occupancy. The negative charge on the Pt atoms indicated charge/electron gain from the Sb atoms and the positive charge showed a charge/electron loss on the Sb atom to the Pt atoms. This was evident due to no charge loss on the 5d-orbital of Pt atoms. This was in line with the DOS as the Sb dominated the E_F than the Pt atoms, similar to the bulk model.

3.7 Adsorption energies

In this study the models for the adsorbate plus surface, surface, adsorbate and number of adsorbate are referred to as [S + A], [S], [A], and *n*, respectively. The superscript numbers will represent any charged states. The adsorption energies ($E_{ads.}$) of an uncharged adsorbate (H_2O) to a surface was calculated from the difference in total energy between

the neutral adsorbate surface ($[S + A]^0$) and the sum of the neutral adsorbate ($[A]^0$) and neutral surface ($[S]^0$) models, as expressed in:

$$E_{ads.} = [S + A]^0 - ([S]^0 + n[A]^0) \quad (2.14)$$

This equation is applicable for the neutral adsorbate as the atom and electron counts for $[S + A]^0$ and ($[A]^0 + [S]^0$) are the same. However, if [A] carries a formal negative charge, then the [S + A] must also carry a negative charge in order to balance the electrons. This presents a problem, as the periodic-boundary-condition box sizes required to demonstrate effective energy convergence will be prohibitively large as also reported by Waterson et al. [Waterson et al. 2016]. A solution to the problem was reported by Neugebauer and Scheffler [Neugebauer et al. 1992], which utilises the work function (ϕ), to correct the extra electron in the electronic band structure. This was obtained by replacing the total energy of the $[S + A]^-$ system by $[S + A]^0$. We have calculated this correction for the [S + A] system and full details of our results are shown in the sections discussed as reported by Waterson et al [Waterson et al. 2016]. As such the adsorption energies for the charged OH^- and xanthates adsorbate $[A]^-$ to a neutral surface $[S]^0$ is computed from:

$$E_{ads.} = ([S + A]^0 - \phi_{[S+A]^0}) - ([S]^0 + n[A]^-) \quad (2.15)$$

Within these calculation negative adsorption energy corresponds to an exothermic adsorption process and a positive adsorption energy corresponding to an endothermic process. The adsorption energies are given in kJ/mol, a convention by 1.0 (eV) = 96.485 (kJ/mol)/eV.

Table 3.10: The uncorrected total energies (E_0), Makov-Payne (MP) [Makov et al. 1995] correction values, corrected total energies (E_{Corr}) for OH−, EX−, nPX−, nBX− and AX− adsorbate used in the adsorption energy calculations.

Adsorbate	Adsorbate charge	Cell vector a (= b = c) Å	E_0 (eV)	MP (eV)	E_{Corr} (eV)
OH^-	–1	10	–453.689	2.042	–451.647
EX	–1	25	–1539.451	0.817	–1538.634
nPX	–1	25	–1726.760	0.817	–1725.943
nBX	–1	25	–1914.069	0.817	–1913.252
AX	–1	25	–2101.369	0.817	–2100.552

Geometry optimisations for the hydroxide and xanthates collectors were performed in a cubic unit cell α (= β = γ = 90°) with cell size of **a** (= **b** = **c**) = 10 Å for OH^- and **a** (= **b** = **c**) = 25 Å for all collectors. The initial total energy (E_0), Makov-Payne (MP) correction values and corrected total energies (E_{Corr}) are shown in the Tables. The Makov-Payne corrections are calculated using the expression below:

$$E_{corr} = E_0 + (14.39952)\frac{q^2\alpha}{2L} \tag{2.16}$$

where E_0 is the uncorrected total energy, q is the adsorbate molecule charge, α is the Madelung constant (2.8373 for a simple cubic system) [Komsa et al. 2012] and L is the unit cell vector length.

3.8 Summary

In this Chapter, we investigated the bulk and surface relaxation using *ab-initio* CASTEP code. In order to attain precise calculations the cut-off energies were varied for the bulk $PtSb_2$, which were also transferred to the surfaces. The cut-off of 500 eV was chosen as the energy change was converged. In addition to the cu-off energy to obtain accurate results the k-point were sampled for the Brillion zone space for both the bulk and surfaces. The k-point grid of 6x6x6 for the bulk and 4x4x1 for surfaces ware employed. The bulk relaxation was found to give final lattice parameter of 6.531 Å. The DOS indicates that the $PtSb_2$ had a metallic character, even though previous studies suggested that it has a pseudo-gap, thereby insinuating semiconducting behaviour.

The relaxed bulk structure was used to cleave the low-index surfaces, namely (100), (110) and (111) surfaces. In cleaving the surfaces, all possible terminations were considered and it was realised that possible terminations were Type II with no dipole (100)-B, Type I, which was (110)-B and Type II (111)-C where the top few layers of different terminations were shown for clarity. The surface energies were 0.920 $J.m^{-2}$, 0.939 $J.m^{-2}$ and 1.194 $J.m^{-2}$ for (100), (111) and (110), respectively displayed in the order of increasing energy. In the case of slab thicknesses, we observed a trend whereby the surface energies were relatively close to each other, with a deviation of approximately 0.01 $J.m^{-2}$ for (100) and (110). Although this was the case for other surfaces, the (111) showed a drastic departure from the others, and this suggested a degree of instability

insofar as the slab was concerned, regarding adsorption of ligands. We observed from (Table 3.5) the calculated surface energies as per the supercell of 2x2 for all surfaces under scrutiny, and have come to observe the order of surface stability being as: (100) < (111) < (110), with the (110) and (111) being closer to each other by a slim margin. All the surfaces showed some form of coordination with respect to Pt and Sb for the respective surfaces, and Pt coordination did not change whereas for Sb there were changes with regard to the (110) surface relative to unrelaxed and relaxed states. We have also realised that atoms in all the surface re-arrange sideways (laterally), up or down (horizontally), whereby interplanar spacing increased or decreased according to the atomic movements.

The electronic properties of the surfaces showed the chemistry of the surfaces. The DOS showed stability with the E_F falling deep into the pseudo gap for all surface. The valence electrons on the surface were the $5d^9 6s^1$ for Pt and $5s^2 5p^3$ for Sb and these electrons were actively involved in the hybridisation. The atomic charges clearly displayed these effects with the presence of 6p-orbital for Pt atoms, due to the strong hybridisation of the Pt 5d-orbitals with the 5s-orbital and 5p-orbitals of Sb atoms. Interestingly, we observed that on all surfaces, the 5d-orbital of Pt had the nine electrons ($5d^9$ filled), suggesting that these orbitals were occupied unlike in the bulk model, forming a stable surface.

CHAPTER 4

Oxidation of $PtSb_2$ Surfaces

In this chapter we investigated the adsorption geometries of the oxygen molecule/s on the three surfaces ((100), (110) and (111)) of the $PtSb_2$. The adsorption energies of the oxidations on the three surfaces will also be discussed. Firstly, we started by adsorption of the O_2 molecule on the surfaces and examined their bonding geometric behaviour (bond length and angles). Then the Mulliken population charges were analysed and discussed to fully describe the chemistry of the adsorptions.

4.1 Oxidation adsorption geometries and energies

In order to understand the oxidation of the $PtSb_2$ minerals either by weathering or exposure to air, we considered the adsorption of oxygen molecules on mineral surfaces. The adsorption properties will give more insight into the interaction of the oxygen with the atoms on the surface. Generally, minerals are exposed to atmospheric air during crushing or storage. It had been reported previously that oxidation depresses sulphide minerals, resulting in poor grade-recovery performance and the brittle nature of $PtSb_2$ may result in difficulty of its recovery from such ores. Furthermore, it had also been highlighted that the use of oxygen as a bubbling gas, was effective since it increased the pulp potential [Ferihan 2002].

The ground state of isolated O_2 molecule was experimentally found to be a spin triplet state, with the equilibrium bond length of 1.21 Å [Weast 1985]. This corresponded to the current calculated equilibrium oxygen molecule bond length of 1.211 Å. We investigated the preferential oxidation site using DFT on the $PtSb_2$ and described the bonding character of O_2 on the surfaces. On these adsorption we positioned the O_2 on the surface in the vertical orientation. This is in line with previous studies of oxygen-iron/nickel interaction where the superoxide isomers of the iron and nickel favour the vertical orientation [Gutsev et al. 2000].

4.1.1 O_2 adsorptions on $PtSb_2$ (100) surface

We performed oxidation on the $PtSb_2$ (100) surface where O_2 was adsorbed in a peroxo, superoxide and Pt-O-O-Sb bridging on the surface Pt and Sb atoms as shown in Figure 4.1 and 4.2, which also presents the optimised output geometry for these systems. The peroxide adsorption on Pt showed poor adsorption where the oxygen molecule moved up away from the Pt atom. The Sb-superoxide adsorption resulted in a bent geometry of the oxygen molecule (superoxide) as shown in Figure 4.1b.

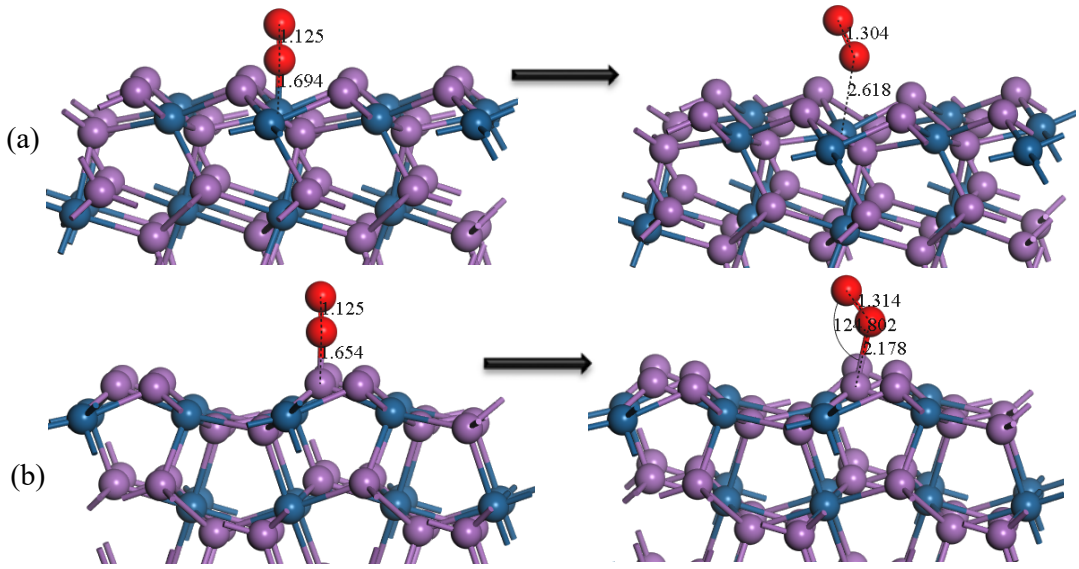

Figure 4.1: The side view of superoxide O_2 molecule adsorption on Pt-top and Sb-top sites on the $PtSb_2$ (100) surface.

We observed that the peroxide adsorption on Pt resulted in migration of oxygen molecule to the Sb atoms forming a Sb-mononuclear bonding (superoxide) and gave a Sb–O–O bond angle of 113.80º. The peroxide adsorption on Sb showed an over stretched O–O bond to 1.541Å, which was due to electron transfer from the Sb atoms to the LUMO p-orbital of the oxygen thus weakening the O–O bond. This is evident from atomic charges in Table 4.4, where the oxygen had more negative charge indicating electron gain. The two Sb–O bond lengths were noted to have one slightly larger than the other and the O–Sb–O was found to be 43.95º. Furthermore, the Sb–O–O–Pt bridging was observed to have poor adsorption on the Pt and thus results in Sb–O–O bonding. The O–O bond was also stretched to O–O = 1.417 Å and the Sb–O–O bond angle was found as 102.88º.

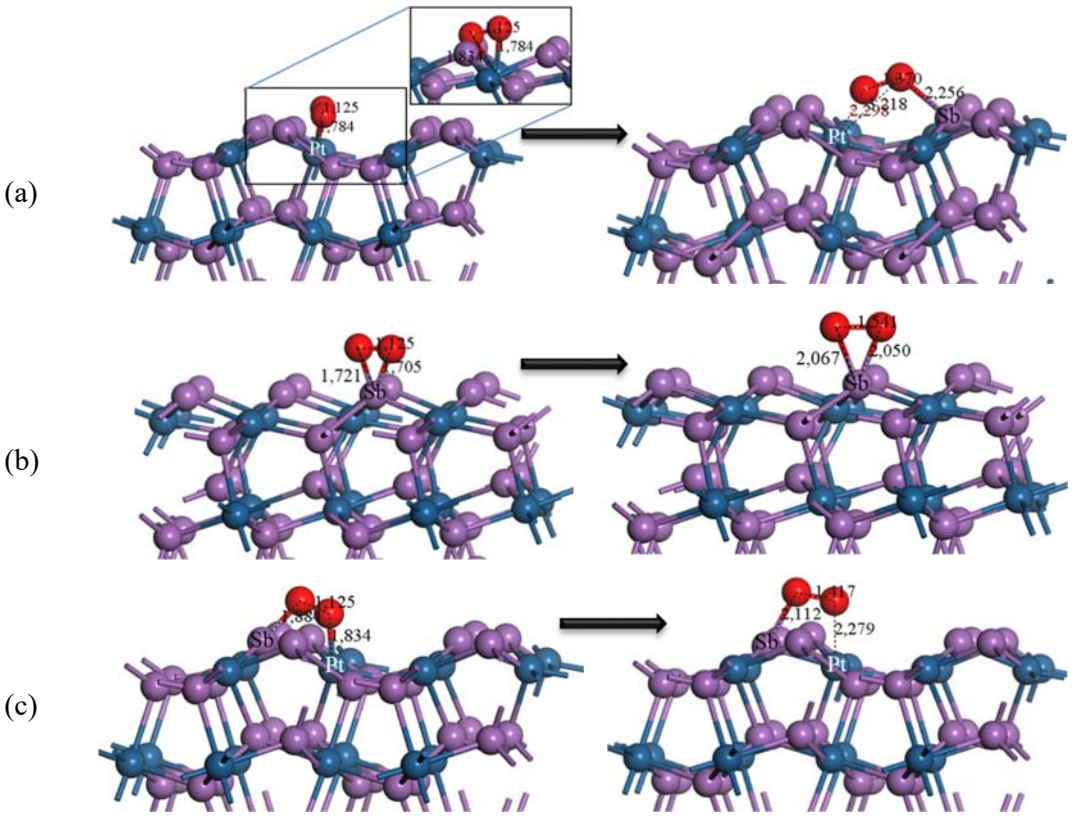

Figure 4.2: The side view of O_2 molecule adsorption on the $PtSb_2$ (100) surface: (a) Pt–O_2 (peroxo), (b) Sb–O_2 (peroxo) and (c) Pt–O_2–Sb (bridge).

Now since both adsorption of Pt–O_2 (peroxo) and Pt–O–O–Sb bridging resulted in a Sb–O–O mononuclear (superoxide) bonding, we found that the superoxide was more exothermic than the peroxide bonding.

Table 4.1: The oxidation adsorption energies of $PtSb_2$ (100) surface, calculated according to equation 2.14.

Adsorption	Atom site	$[S+A]^0$ (eV)	$[A]^0$ (eV)	$[S]^0$ (eV)	Total $E_{ads.}$ (kJ.mol^{-1})
Superoxide	Pt	–41735.311	–868.856	–40867.023	+54.74
	Sb	–41736.065	–868.856	–40867.023	–17.94
Peroxide	Pt	–41736.545	–868.856	–40867.023	–64.29
	Sb	–41736.216	–868.856	–40867.023	–32.56
Bridge	Sb–O–O–Pt	–41736.388	–868.856	–40867.023	–49.12

This is confirmed by the adsorption energies in Table 4.1, which displayed the strength of bonding of the oxygen molecule on the surface. We observed that the peroxide adsorption on Pt gave the most exothermic adsorption energy (–64.29 kJ/mol), while the superoxide adsorption on Pt was endothermic (+54.74 kJ/mol).

4.1.2 O_2 adsorptions on $PtSb_2$ (110) surface

We performed oxidation on the $PtSb_2$ (110) surface where O_2 was adsorbed in a peroxide, superoxide and Pt-O-O-Sb bridging on the surface Pt and Sb atoms as shown in Figure 4.4, 4.3 and 4.4, which also presents the optimised output geometry for these systems. The case of superoxide adsorption on Sb2, Sb3 and Pt1 were observed to relax in a bent fashion of superoxide as shown in Figure 4.3. The bond angle for the superoxide were found as 68.353˚, 67.604˚, 44.043˚ and for Sb2–O–O, Sb3–O–O and Pt1–O–O, respectively.

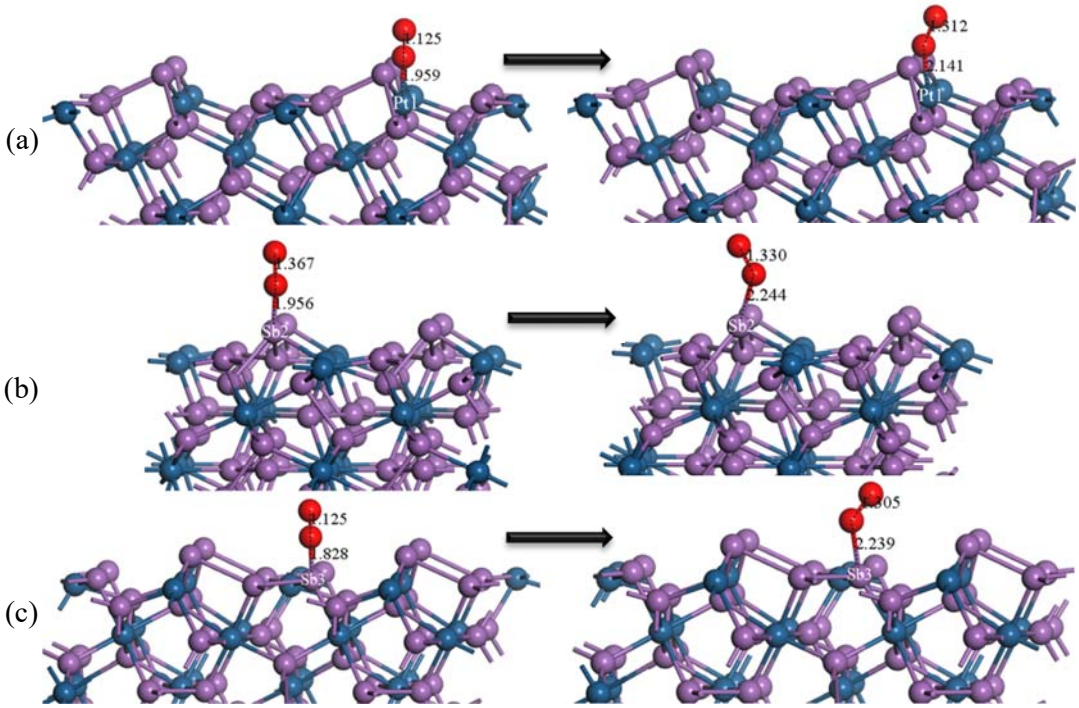

Figure 4.3: The side view of peroxo O_2 molecule adsorption on the $PtSb_2$ (110) surface: (a) Pt1–O_2 (superoxide), (b) Sb2–O_2 (superoxide) and (c) Sb3–O_2 (superoxide).

The peroxide adsorption on Pt2, Sb2 and Sb3 were observed to remain unchanged except for Pt2–O_2 where one bond broke, while on Sb2 and Sb3 the O_2 was tilted sideways. The bond length between Sb, Pt and O_2 were shorter for peroxide than on superoxide, which suggested that the peroxides were preferred compared to the superoxide. The peroxo adsorption on Sb2 and Sb3 showed an over stretched O–O bond of 1.572 Å and 1.552 Å, respectively. This was due to electron transfer from the Sb atoms to the LUMO p-orbital

of the oxygen thus weakening the O–O bond. This was evident from the atomic charges in Table 4.5 where the oxygen has more negative charge indicating electron gain. The two Sb–O bond lengths in both Sb2–O_2 and Sb3–O_2 were noted to have one slightly larger than the other and the O–Sb–O and were found to be 45.59º and 44.04º, respectively.

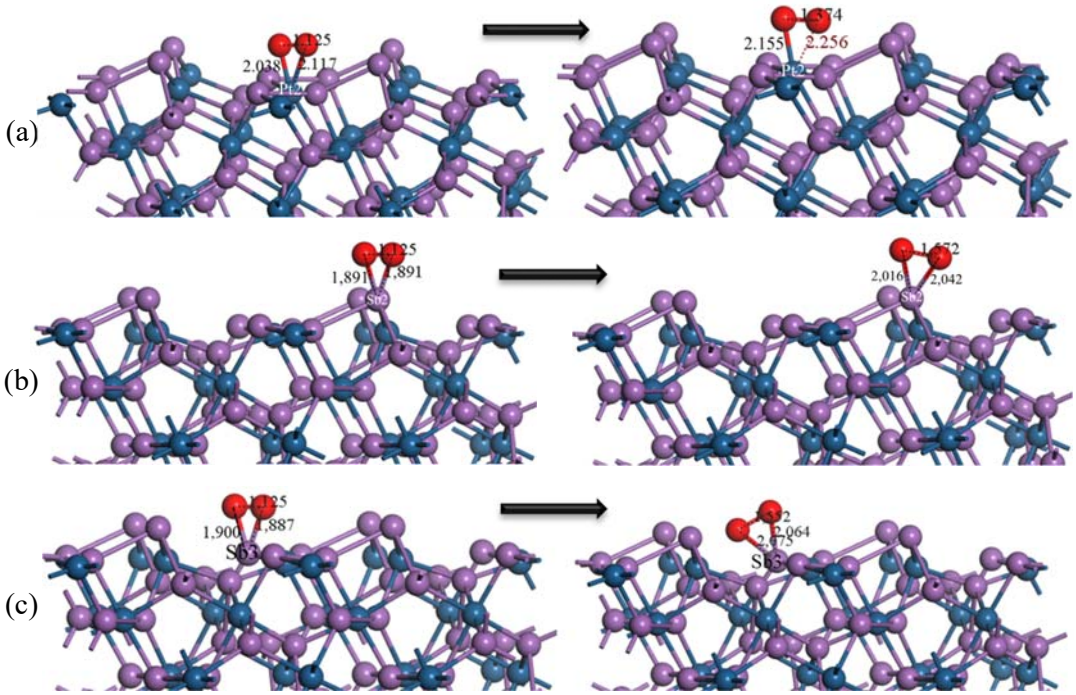

Figure 4.4: The side view of peroxo O_2 molecule adsorption on the $PtSb_2$ (110) surface: (a) Pt2–O_2 (peroxide), (b) Sb2–O_2 (peroxide) and (c) Sb3–O_2 (peroxide).

Furthermore, the Sb2–O–O–Sb3 bridging was observed to have the bond between Sb2 and Sb3 (Sb2–Sb3) stretched and breaking giving a distance of 4.112 Å. The O–O bonds on Sb2–O–O–Sb3 and Sb3–O–O–Pt2 were stretched to 1.453 Å and 1.392 Å, respectively. In addition the Pt–O bond length was shorter than the Sb–O bond. Now in examining the adsorption energies in Table 4.2, we found that amongst the superoxide adsorptions, only Sb3–O–O adsorption was exothermic, while for Sb2–O–O and Pt1–O–O were endothermic. The peroxide were found to be all exothermic, with the Sb3–O_2 more exothermic (–70.16 kJ/mol) than the Sb2–O_2 and Pt2–O_2. The bridging modes were found to have the Sb2–O–O–Sb3 giving the strongest exothermic adsorption energy of –131.79 kJ/mol, while the Pt2–O–O–Sb3 gave –50.89 kJ/mol. These have shown that the peroxide modes were preferred than the superoxide modes, with the bridging on Sb2 and Sb3 more preferred amongst all adsorption modes.

Table 4.2: The adsorption energies of oxidation of $PtSb_2$ (110) surface, calculated according to equation 2.14.

Adsorption	Atom site	$[S+A]^0$ (eV)	$[A]^0$ (eV)	$[S]^0$ (eV)	Total $E_{ads.}$ (kJ.mol^{-1})
Superoxide	Pt1	–49897.441	–868.856	–49028.608	+2.21
	Sb2	–49897.335	–868.856	–49028.608	+12.49
	Sb3	–49897.637	–868.856	–49028.608	–16.63
Peroxide	Pt2	–49897.717	–868.856	–49028.608	–24.38
	Sb2	–49897.910	–868.856	–49028.608	–43.03
	Sb3	–49898.192	–868.856	–49028.608	–70.16
Bridge	Sb3–O–O–Pt2	–49897.992	–868.856	–49028.608	–50.89
	Sb2–O–O–Sb3	–49898.830	–868.856	–49028.608	–131.79

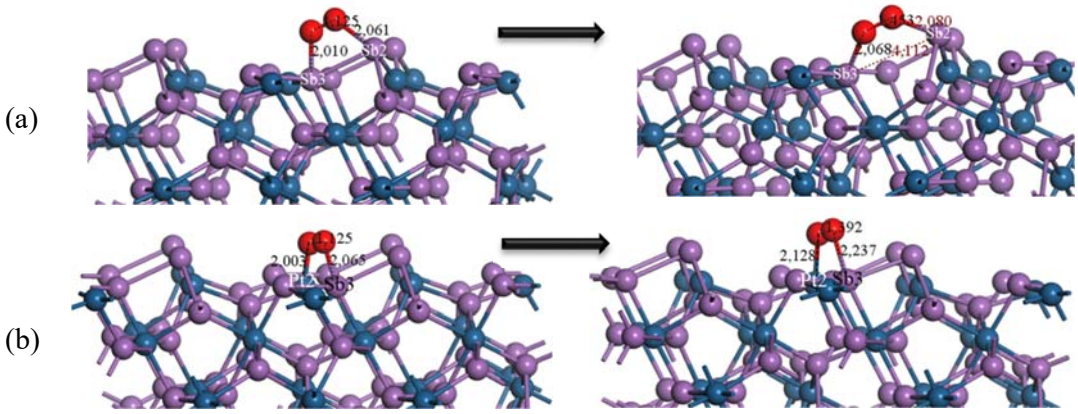

Figure 4.5: The side view of O_2 molecule adsorption on the $PtSb_2$ (110) surface: (a) Sb2–O_2–Sb3 (bridge) and (b) Sb3–O_2–Pt2 (bridge).

4.1.3 O_2 adsorptions on $PtSb_2$ (111) surface

The oxidation of the $PtSb_2$ (111) surface was investigated, where O_2 was also adsorbed in a peroxide, superoxide and Pt–O–O–Sb bridging modes on the surface Pt and Sb atoms as shown in Figure 4.6, 4.7 and 4.8, which also presents the optimised output geometry for these systems. In addition, we have also performed multi adsorptions on Pt atoms in superoxide modes as shown in Figure 4.8f, and 4.8g. We observed that the peroxide adsorption on Pt1 and Sb3 resulted in bridge bonding on the surface, where for Sb3, one oxygen moved and interacted with Sb2 (Sb3–O–O–Sb2) as shown in Figure 4.6c. For Pt1 adsorption, the O_2 migrated and bridged on the Sb2 atoms (Sb2–O–O–Sb2) see Figure 4.6a and 4.6e. Similar behaviour was observed for Pt1–O–O–Sb2 bridging adsorption as shown in Figure 4.7c.

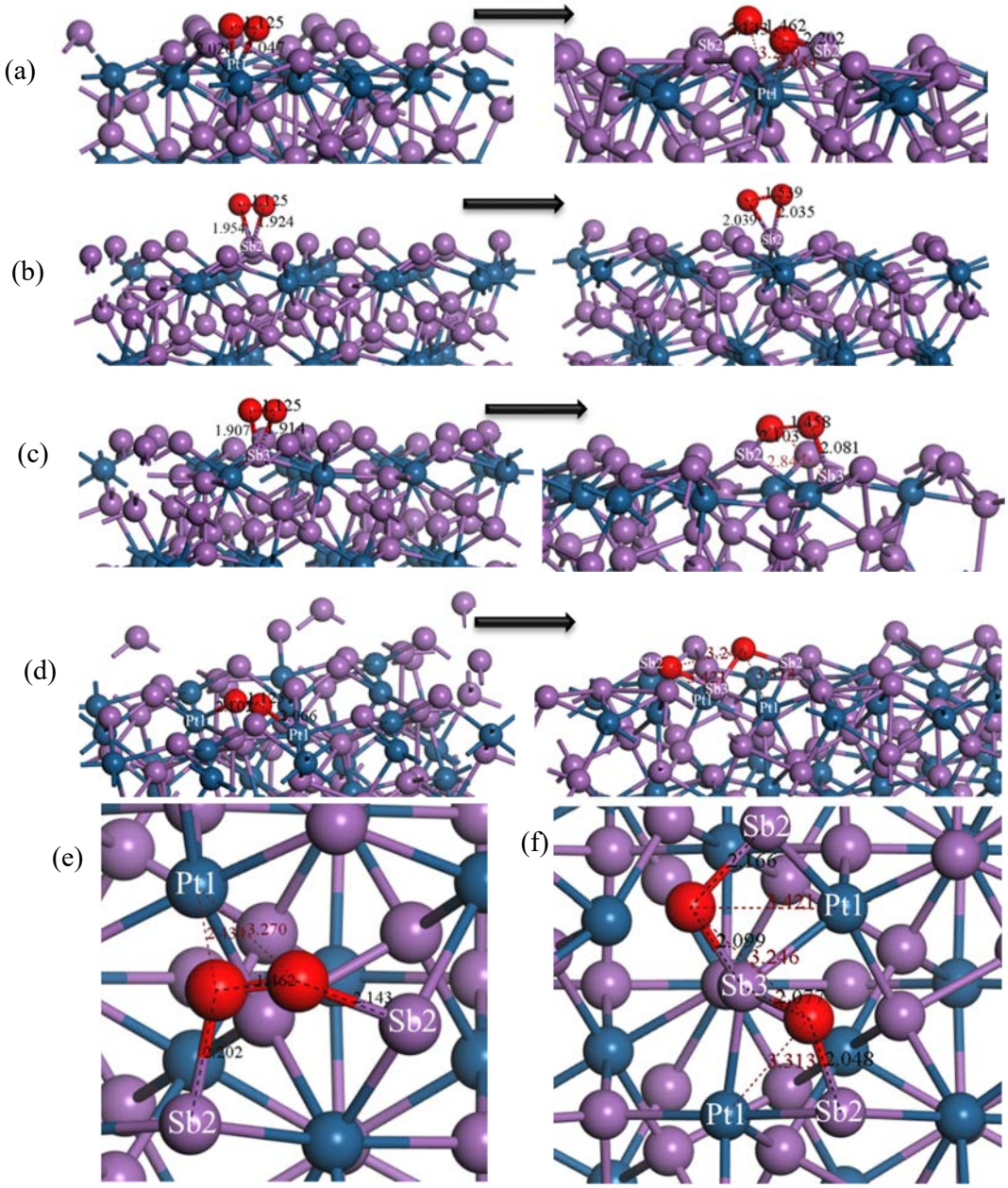

Figure 4.6: The side view of peroxo O_2 molecule adsorption on the $PtSb_2$ (111) surface: (a) Pt1–O_2 (peroxide), (b) Sb2–O_2 (peroxide), (c) Sb3–O_2 (peroxide), (d) Pt1–O–O–Pt1 (bridge), (e) top vies Pt1–O_2 (peroxide) and (f) top view Pt1–O–O–Pt1 (bridge).

Furthermore, on both bridging the O–O bond was overstretched to 1.462 Å and 1.458 Å for Sb2–O–O–Sb2 and Sb3–O–O–Sb2, respectively. The peroxide adsorption on Sb2 showed an over stretched O–O bond to 1.539 Å and gave a Sb2–O_2 bond angle of 44.40º. In all cases, the O–O bond stretch was due to electron transfer from the Sb atoms to the

LUMO p-orbital of the oxygen thus weakening the O–O bond. This was evident from the atomic charges in Table 4.8 and 4.9, where the oxygen had more negative charge indicating electron gain.

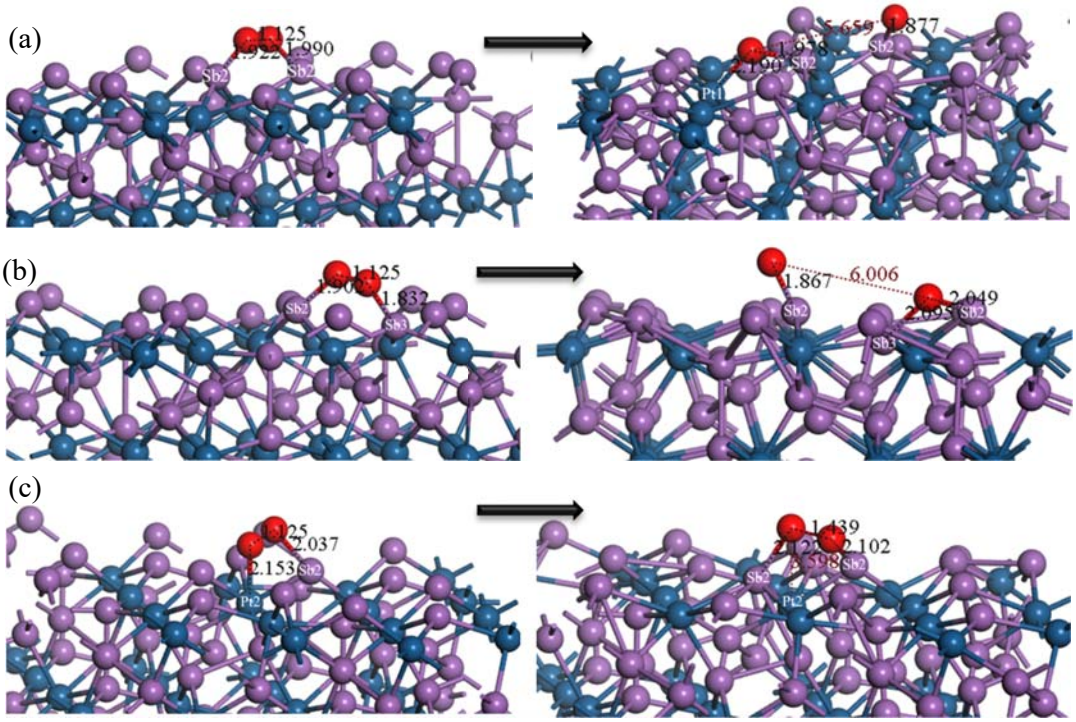

Figure 4.7: The side view and side view of bridging O_2 molecule adsorption on the $PtSb_2$ (111) surface: (a) Sb2–O–O–Sb2, (b) Sb2–O–O–Sb3 and (c) Pt2–O–O–Sb2 bbridging.

The bridge adsorption on Pt1 atoms (Pt1–O–O–Pt1) resulted in dissociation of the oxygen molecule, where each oxygen atom formed a bridge of Sb3–O–Sb2 (see Figure 4.6d and 4.6f). The dissociation of the oxygen molecule was observed for Sb2–O–O–Sb2 and Sb2–O–O–Sb3 bridge adsorption as shown in Figure 4.7a and 4.7b. However, for these bridging, only one oxygen atom dissociated and bridged on Pt1 and Sb2 for Sb2–O–O–Sb2 adsorption and bridged on Sb3 and Sb2 for Sb2–O–O–Sb3 bridge adsorption, while the oxygen atom bond in a mono mode. The dissociation was also due to electron transfer from the Sb atoms to the LUMO p-orbital of the oxygen thus weakening the O–O bond and this adsorption gave the most exothermic adsorption energy. This indicated that the atomic oxygen adsorption was more stable on the (111) surface. Moreover, the strong adsorption energy was associated with the dissociation of the oxygen molecule on the surface.

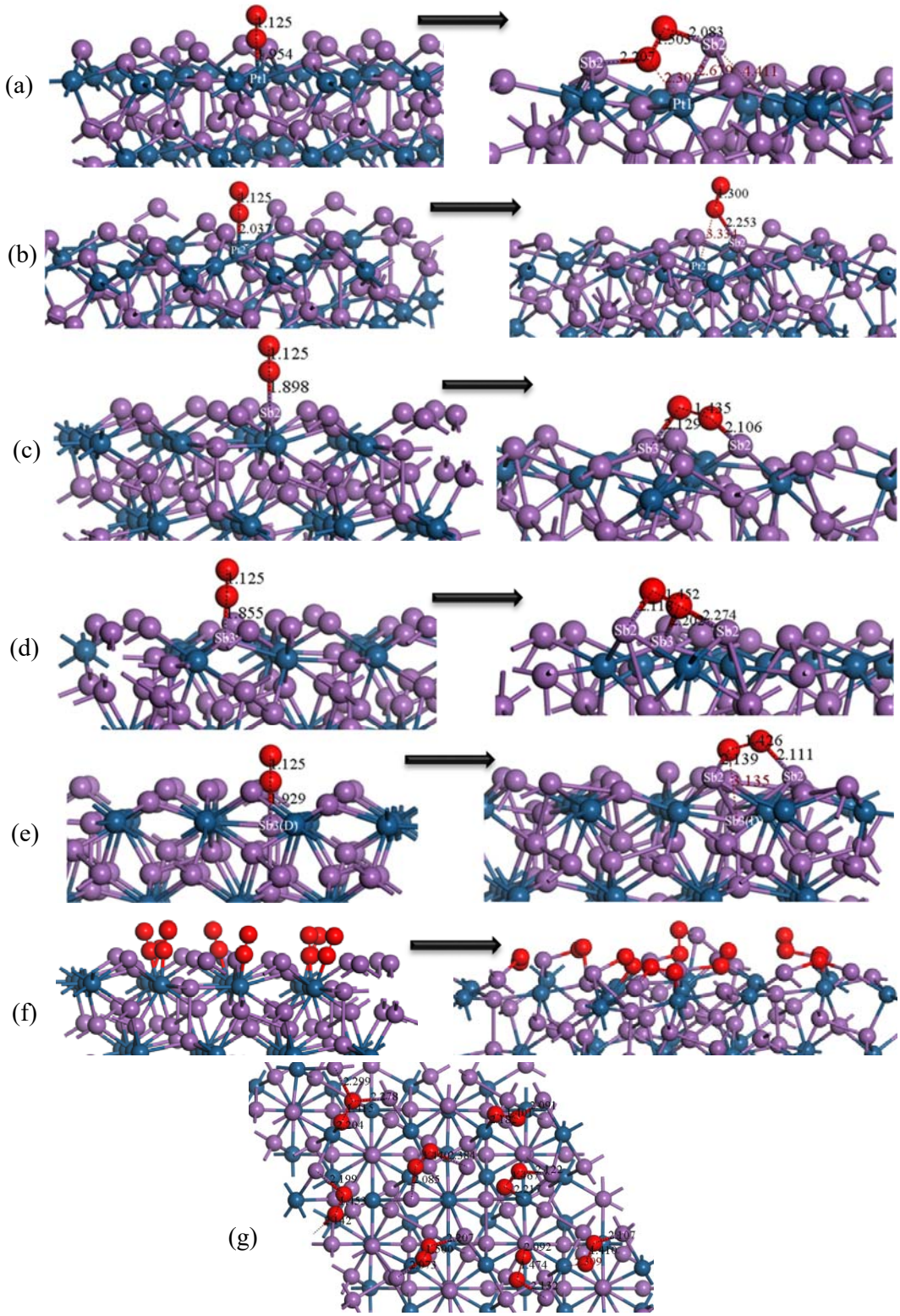

Figure 4.8: The O_2 molecule adsorption on the $PtSb_2$ (111) surface: (a) Pt1–O_2 (superoxide), (b) Pt2–O_2 (superoxide), (c) Sb2–O_2 (superoxide), (d) Sb3–O_2 (superoxide), (e) Sb3(D)–O_2 (superoxide), (f) Pt–O_2 (superoxide) full coverage and (g) Pt–O_2 full coverage top view.

The superoxide bonding adsorption was examined and we noted that for Pt1–O–O and Sb3(D)–O–O resulted in migration of the oxygen molecule to form a Sb2–O–O–Sb2 bridge bond and their O–O bonds were overstretched as shown in Figure 4.8a and 4.8e. The superoxide bonding on Sb3 was observed to have one oxygen bridging between Sb3 and Sb2 atoms, while the other oxygen bonds with Sb2 atom ((Sb3,Sb2)–O–O–Sb2) as shown in Figure 4.8d. Interestingly for the multi adsorption where eight (8) oxygen molecules were adsorbed on Pt1 atoms in a superoxide form (Pt–O–O), we noted different bonding modes after surface relaxation. We observed a Sb2–O–O–Sb2, Pt1–O–O–Sb2, Pt1–O–O– (Sb2, Sb2) bridging bonds as shown in Figure 4.8f and 4.8g.

Table 4.3: The adsorption energies of oxidation of $PtSb_2$ (111) surface, calculated according to equation 2.14.

Adsorption	Atom site	$[S+A]^0$ (eV)	$[A]^0$ (eV)	$[S]^0$ (eV)	Total $E_{ads.}$ (kJ.mol^{-1})
Superoxide	Pt1	–49889.242	–868.856	–49015.288	–491.81
	Pt2	–49888.916	–868.856	–49015.288	–460.36
	Sb2	–49890.123	–868.856	–49015.288	–576.82
	Sb3	–49890.392	–868.856	–49015.288	–602.80
	Sb3(D)	–49888.958	–868.856	–49015.288	–464.42
	Pt–8O_2	–55980.730	–868.856	–49015.288	–1408.00 (–176 per O_2)
Peroxide	Pt1	–49889.874	–868.856	–49015.288	–552.82
	Sb2	–49889.760	–868.856	–49015.288	–541.81
	Sb3	–49890.592	–868.856	–49015.288	–622.06
Bridge	Pt1–O–O–Pt1	–49890.907	–868.856	–49015.288	–652.46
	Sb2–O–O–Sb2	–49891.150	–868.856	–49015.288	–675.92
	Sb2–O–O–Sb3	–49891.027	–868.856	–49015.288	–664.02
	Pt2–O–O–Sb2	–49889.851	–868.856	–49015.288	–550.56

Table 4.3 displayed the adsorption energies for all the bonding modes investigated. We found that for Pt1 and Sb3 interacting in a peroxide mode gave the most exothermic energies compared to the superoxide. For Sb2 interacting in a superoxide gave a strong adsorption compared to the peroxide adsorption. Furthermore, the bridging on Sb2–O–O–Sb2 was more exothermic for a single molecule adsorption with adsorption of –675.92 kJ/mol. The adsorption energy increased as more molecules were adsorbed as found for eight oxygen molecule adsorption, which was –176.0 kJ/mol per O_2 molecule. This suggested that the oxidation of (111) surface is best described under multi O_2 adsorption since the single molecule adsorption gave higher adsorption energies compared to the (100) and (110) surfaces.

4.2 $PtSb_2$ Oxidation Mulliken Population charges

In this section we investigated the electronic properties (Mulliken population charges) for the oxidation adsorption on the $PtSb_2$ (100), (110) and (111) surfaces. These properties will give insights into the chemistry bonding of the oxygen molecule on the surfaces. Moreover, the electron accepting and donation characters of the surface and oxygen will be analysed.

4.2.1 Oxidation of $PtSb_2$ (100) surface DOS and charges

The atomic charges computed for (100) surface were analysed and clearly indicated that the Sb atoms adopted more positive charge (lose charges), while the O_2 molecule adopted more negative charge (gain charges) as shown in Table 4.4. Note that all Sb-peroxide adsorptions resulted in Sb-superoxide bonding mode, except for the Sb–O_2 peroxide which did not change the bonding mode. We found that for all superoxide modes, the Sb-bonded oxygen was more negative than the terminal or end-bonded oxygen atom. This charge distribution behaviour for superoxide has been previously reported [Mkhonto et al. 2015, Uzunova et al. 2008]. The charge on O_2 (i.e., charge sum of O1 and O2), for lowest ground state were as: for Pt–O_2–superoxide (−0.38|e|), for Sb–O_2–superoxide (−0.47|e|), for Pt–O_2–peroxide (−0.60|e|), Sb–O_2–peroxide (−0.91|e|) and Pt–O_2–Sb-bridge (−0.68|e|). It was clear that the Sb–O_2 (peroxide) had more negative charge than all the superoxide modes, suggesting that there was more charge gain on the O_2 molecule. This was due to both oxygen atoms bonded to the Sb atom. For the superoxide, we observed that the O_2 on Pt–O_2–Sb bridge, gained more charge than all other superoxide modes. The negative charge on the oxygen atoms was also confirmed by experiment for superoxide or end-bonded O_2 [Lever et al. 1980].

Table 4.4 clearly indicated that there was a greater loss of electrons in the 5p-orbital of Sb atoms with more gain of electrons in the 2p-orbital of O_2 molecule. This suggested that there was a strong hybridisation of the 5p-orbital of Sb and 2p-orbital of O_2 molecule. These effects may suggest that the Sb atoms take the form $[Kr]5s^25p^2$ electron configurations. However, there was some small charge loss on the 5s-orbital of Sb atoms and these may have been distributed to the 2s-orbital of O_2 molecule.

Table 4.4: The calculated atomic population (Mulliken) charges of superoxide and peroxide O_2 molecule adsorption on $PtSb_2$ (100) surface.

Adsorption	Atom	Adsorptions state	Mulliken population charges (|e⁻|)				
			s	p	d	Total	Charge
Pt–O_2 Superoxide	Pt	Before adsorption	1.00	0.85	9.08	10.97	–0.97|e⁻|
		After adsorption	0.97	0.92	9.02	10.91	–0.91|e⁻|
	O1	Before adsorption	1.88	4.13	0.00	6.00	0.00|e⁻|
		After adsorption	1.88	4.33	0.00	6.21	–0.21|e⁻|
	O2	Before adsorption	1.88	4.13	0.00	6.00	0.00|e⁻|
		After adsorption	1.90	4.27	0.00	6.17	–0.17|e⁻|
Sb–O_2 Superoxide	Sb	Before adsorption	1.84	2.95	0.00	4.79	+0.20|e⁻|
		After adsorption	1.81	2.70	0.00	4.51	+0.49|e⁻|
	O1	Before adsorption	1.88	4.13	0.00	6.00	0.00|e⁻|
		After adsorption	1.87	4.39	0.00	6.27	–0.27|e⁻|
	O2	Before adsorption	1.88	4.13	0.00	6.00	0.00|e⁻|
		After adsorption	1.90	4.30	0.00	6.20	–0.20|e⁻|
Pt–O_2 Peroxo	Sb	Before adsorption	1.84	2.95	0.00	4.79	+0.20|e⁻|
		After adsorption	1.81	2.72	0.00	4.53	+0.47|e⁻|
	O1	Before adsorption	1.88	4.13	0.00	6.00	0.00|e⁻|
		After adsorption	1.90	4.43	0.00	6.33	–0.33|e⁻|
	O2	Before adsorption	1.88	4.13	0.00	6.00	0.00|e⁻|
		After adsorption	1.89	4.38	0.00	6.27	–0.27|e⁻|
Sb–O_2 Peroxo	Sb	Before adsorption	1.84	2.95	0.00	4.79	+0.20|e⁻|
		After adsorption	1.74	2.41	0.00	4.15	+0.85|e⁻|
	O1	Before adsorption	1.88	4.13	0.00	6.00	0.00|e⁻|
		After adsorption	1.94	4.52	0.00	6.47	–0.47|e⁻|
	O2	Before adsorption	1.88	4.13	0.00	6.00	0.00|e⁻|
		After adsorption	1.95	4.50	0.00	6.44	–0.44|e⁻|
Pt–O_2–Sb Bridge	Sb	Before adsorption	1.84	2.95	0.00	4.79	+0.20|e⁻|
		After adsorption	1.80	2.64	0.00	4.43	+0.57|e⁻|
	O1	Before adsorption	1.88	4.13	0.00	6.00	0.00|e⁻|
		After adsorption	1.91	4.74	0.00	6.37	–0.37|e⁻|
	O2	Before adsorption	1.88	4.13	0.00	6.00	0.00|e⁻|
		After adsorption	1.90	4.40	0.00	6.31	–0.31|e⁻|

To justify this we analysed the Sb–O_2 (superoxide) and Pt–O_2 (peroxide) and we observed that the 5p-orbital lost 0.03|e| charge, while the O_2 molecule gained 0.03|e| charge in the 2s-orbital. These findings suggested that the spin-down un-occupied orbital (LUMO) of O_2 was fully occupied as observed by Mkhonto et al. [2015].

4.2.2 Oxidation of $PtSb_2$ (110) surface DOS and charges

Now, the analysis of atomic charges computed for (110) surface, we observed that the Pt and Sb atoms adopted more positive charge (lose charges), while the O_2 molecule adopted

more negative charge (gain charges). Note that O1 was bonded to Sb or Pt atoms, while the O2 was the terminal or end-bonded oxygen atom for the superoxide. We found that for superoxide, the Sb/Pt-bonded oxygen was more negative than the terminal or end-bonded oxygen atom as shown in Table 4.5. The charge on O_2 (i.e., charge sum of O1 and O2), for lowest ground state were as for Pt1–O_2-superoxide (−0.41|e|), for Sb2–O_2-superoxide (−0.44|e|) and for Sb3–O_2–superoxide (−0.45|e|). It was clear that the Sb3–O_2 (superoxide) had more negative charge than all the superoxide modes, suggesting that there was more charge gain on the O_2 molecule. This was attributes to its strong adsorption –16.63 kJ/mol amongst the superoxide adsorption.

Table 4.5: The calculated atomic population (Mulliken) charges of superoxide O_2 molecule adsorption on $PtSb_2$ (110) surface.

			Mulliken population charges (|e⁻|)				
Adsorption	**Atom**	**Adsorptions state**	**s**	**p**	**d**	**Total**	**Charge**
Pt1–O_2 Superoxide	Pt1	Before adsorption	0.99	0.70	9.09	10.78	–0.78|e⁻|
		After adsorption	0.90	0.75	8.96	10.61	–0.61|e⁻|
	O1	Before adsorption	1.88	4.13	0.00	6.00	0.00|e⁻|
		After adsorption	1.84	4.37	0.00	6.22	–0.22|e⁻|
	O2	Before adsorption	1.88	4.13	0.00	6.00	0.00|e⁻|
		After adsorption	1.90	4.29	0.00	6.19	–0.19|e⁻|
Sb2–O_2 Superoxide	Sb2	Before adsorption	1.90	3.04	0.00	4.94	+0.06|e⁻|
		After adsorption	1.93	2.74	0.00	4.66	+0.34|e⁻|
	O1	Before adsorption	1.88	4.13	0.00	6.00	0.00|e⁻|
		After adsorption	1.88	4.39	0.00	6.26	–0.26|e⁻|
	O2	Before adsorption	1.88	4.13	0.00	6.00	0.00|e⁻|
		After adsorption	1.91	4.27	0.00	6.18	–0.18|e⁻|
Sb3–O_2 Superoxide	Sb3	Before adsorption	1.85	2.95	0.00	4.80	+0.20|e⁻|
		After adsorption	1.86	2.68	0.00	4.54	+0.46|e⁻|
	O1	Before adsorption	1.88	4.13	0.00	6.00	0.00|e⁻|
		After adsorption	1.87	4.39	0.00	6.26	–0.26|e⁻|
	O2	Before adsorption	1.88	4.13	0.00	6.00	0.00|e⁻|
		After adsorption	1.90	4.29	0.00	6.19	–0.19|e⁻|

For all peroxide modes, the oxygen atoms did not have equal charges, which were attributed to the different bond length after relaxation. We found that the oxygen on slightly longer bond Sb–O, had more negative charge than the oxygen on slightly shorter bond length Sb–O (Table 4.6). The charge on O_2 (i.e., charge sum of O1 and O2), for lowest ground state were as for Pt–O_2-peroxide (−0.41|e|), for Sb2–O_2-peroxide (−0.94|e|) and Sb3–O_2-peroxide (−0.94|e|). It was clear that the Sb2–O_2 and Sb3–O_2 (peroxide) have equal negative charge and were more negative than the Pt–O_2 (peroxide), suggesting that there was more charge gain on the O_2 molecule on Sb atoms.

Table 4.6: The calculated atomic population (Mulliken) charges of peroxide O_2 molecule adsorption on $PtSb_2$ (110) surface.

Adsorption	Atom	Adsorptions state	Mulliken population charges (|e|)				
			s	p	d	Total	Charge
Pt1–O_2 Peroxide	Pt1	Before adsorption	0.99	0.70	9.09	10.78	–0.78|e⁻|
		After adsorption	0.83	0.77	8.86	10.46	–0.46|e⁻|
	O1	Before adsorption	1.88	4.13	0.00	6.00	0.00|e⁻|
		After adsorption	1.91	4.35	0.00	6.26	–0.26|e⁻|
	O2	Before adsorption	1.88	4.13	0.00	6.00	0.00|e⁻|
		After adsorption	1.91	4.36	0.00	6.27	–0.27|e⁻|
Sb2–O_2 Peroxide	Sb2	Before adsorption	1.90	3.04	0.00	4.94	+0.06|e⁻|
		After adsorption	1.79	2.39	0.00	4.18	+0.82|e⁻|
	O1	Before adsorption	1.88	4.13	0.00	6.00	0.00|e⁻|
		After adsorption	1.95	4.51	0.00	6.46	–0.46|e⁻|
	O2	Before adsorption	1.88	4.13	0.00	6.00	0.00|e⁻|
		After adsorption	1.95	4.53	0.00	6.48	–0.48|e⁻|
Sb3–O_2 Peroxide	Sb3	Before adsorption	1.85	2.95	0.00	4.80	+0.20|e|
		After adsorption	1.79	2.37	0.00	4.16	+0.84|e⁻|
	O1	Before adsorption	1.88	4.13	0.00	6.00	0.00|e⁻|
		After adsorption	1.94	4.55	0.00	6.49	–0.49|e⁻|
	O2	Before adsorption	1.88	4.13	0.00	6.00	0.00|e⁻|
		After adsorption	1.95	4.51	0.00	6.45	–0.45|e⁻|

The bridge bonding as shown in Table 4.7, we observed that the O_2 on Pt1–O_2–Sb3 Bridge, the oxygen bonded to Pt1 had less negative charge than the oxygen bonded to Sb atom. This suggested that Pt lost less charge than the Sb atom. The case of the Sb2–O_2–Sb3 bridging modes, both oxygen had the same charge (−0.44|e|), suggesting that both Sb2 and Sb3 lost equal charges.

Table 4.7: The calculated atomic population (Mulliken) charges of O_2 molecule adsorption on $PtSb_2$ (110) surface.

Adsorption	Atom	Adsorptions state	Mulliken population charges (|e|)				
			s	p	d	Total	Charge
Pt1–O_2–Sb3 Bridge	Pt1	Before adsorption	0.99	0.70	9.09	10.78	–0.78|e⁻|
		After adsorption	0.90	0.74	8.92	10.56	–0.56|e⁻|
	O1	Before adsorption	1.88	4.13	0.00	6.00	0.00|e⁻|
		After adsorption	1.89	4.39	0.00	6.28	–0.28|e⁻|
	O2	Before adsorption	1.88	4.13	0.00	6.00	0.00|e⁻|
		After adsorption	1.90	4.45	0.00	6.35	–0.35|e⁻|
	Sb3	Before adsorption	1.85	2.95	0.00	4.80	+0.20|e⁻|
		After adsorption	1.82	2.80	0.00	4.63	+0.37|e⁻|
Sb2–O_2–Sb3 Bridge	Sb2	Before adsorption	1.90	3.04	0.00	4.94	+0.06|e⁻|
		After adsorption	1.77	2.63	0.00	4.41	+0.59|e⁻|
	O1	Before adsorption	1.88	4.13	0.00	6.00	0.00|e⁻|
		After adsorption	1.91	4.53	0.00	6.44	–0.44|e⁻|
	O2	Before adsorption	1.88	4.13	0.00	6.00	0.00|e⁻|
		After adsorption	1.91	4.53	0.00	6.44	–0.44|e⁻|
	Sb3	Before adsorption	1.85	2.95	0.00	4.80	+0.20|e⁻|
		After adsorption	1.89	2.62	0.00	4.51	+0.49|e⁻|

Furthermore, the charge on O_2 (i.e., charge sum of O1 and O2), for lowest ground state were as: for Pt–O_2–Sb3 (−0.63|e|) and for Sb2–O_2–Sb3 (−0.88|e|), which showed that there was more charge gain on O_2 bridging on Sb2–O_2–Sb3 than on Pt1–O_2–Sb3 (Table 4.7). This was due to the small charge loss on Pt1 atom. The negative charge on the oxygen atoms was also confirmed experimentally [Lever et al. 1980].

Table 4.5, 4.6 and 4.7 clearly indicated that there was a greater loss of electrons in the 5p-orbitals of Sb atoms with more gain of electrons in the 2p-orbitals of O_2 molecule. This suggested that there was a strong hybridisation between the 5p-orbital of Sb and 2p-orbital of O_2 molecule. These effects may suggest that the Sb atoms took the form of [Kr]$5s^2 5p^2$ electron configurations. However, there was some small charge loss on the 5s-orbital of Sb atoms and these may have been distributed to the 2s-orbital of O_2 molecule. These findings also suggested that the 2p-orbital spin-down un-occupied orbital (LUMO) of O_2 were fully occupied as suggested by Mkhonto et al. [2015].

4.2.3 Oxidation of $PtSb_2$ (111) surface DOS and charges

The case of atomic charges computed for (111) surface were analysed and clearly indicated that for all adsorptions the Sb atoms adopted more positive charge (lose charges), while the O_2 molecule adopted more negative charge (gain charges). Note that all adsorptions resulted in Sb-–O–O–Sb bridging mode, except for the Pt–O_2–Pt bridging, which dissociated into atomic bonding mode (see section 4.1.3). We found that for all modes, the O–O bond was stretched due to charge gain into the LUMO 2p-orbital of O_2 thereby weakening the O–O bond. We noted that for Pt2–O_2 superoxide adsorption resulted in Sb2–O_2, where O1 bonds to Sb2, while the O2 was the end-bonded oxygen. As such, we found that the Sb2-bonded oxygen was more negative than the end-bonded oxygen atom. The charge on O_2 (i.e., charge sum of O1 and O2), for lowest ground state were as for Pt1–O_2-superoxide (−0.86|e|), for Pt2–O_2-superoxide (−0.44|e|), for Sb2-O_2-superoxide (−0.81|e|), Sb3–O_2-superoxide (−0.95|e|) and Sb3(D) –O_2-superoxide (−0.83|e|). It was clear that the Sb3–O_2 (superoxide) had more negative charge than all the superoxide modes, suggesting that there was more charge gain on the O_2 molecule. This was due to the oxygen atoms being bridged on three Sb atoms (Sb2–O–O–(Sb2,Sb3)), (see section 4.1.3). The negative charge on the oxygen atoms was also confirmed by experiment for superoxide or end-bonded O_2 [Lever et al. 1980].

Table 4.8: The calculated atomic population (Mulliken) charges of superoxide O_2 molecule adsorption on $PtSb_2$ (111) surface.

			Mulliken population charges (|e|)				
Adsorption	**Atom**	**Adsorptions state**	**s**	**p**	**d**	**Total**	**Charge**
$Pt1–O_2$ Superoxide	Sb2	Before adsorption	1.78	2.91	0.00	4.70	+0.30|e⁻|
		After adsorption	1.93	2.59	0.00	4.51	+0.49|e⁻|
	O1	Before adsorption	1.88	4.13	0.00	6.00	0.00|e⁻|
		After adsorption	1.93	4.54	0.00	6.46	–0.46|e⁻|
	O2	Before adsorption	1.88	4.13	0.00	6.00	0.00|e⁻|
		After adsorption	1.90	4.50	0.00	6.40	–0.40|e⁻|
	Sb2	Before adsorption	1.78	2.91	0.00	4.70	+0.30|e⁻|
		After adsorption	1.89	2.56	0.00	4.45	+0.55|e⁻|
$Pt2–O_2$ Superoxide	Sb2	Before adsorption	1.78	2.91	0.00	4.70	+0.30|e⁻|
		After adsorption	1.89	2.60	0.00	4.49	+0.51|e⁻|
	O1	Before adsorption	1.88	4.13	0.00	6.00	0.00|e⁻|
		After adsorption	1.87	4.38	0.00	6.29	–0.25|e⁻|
	O2	Before adsorption	1.88	4.13	0.00	6.00	0.00|e⁻|
		After adsorption	1.90	4.29	0.00	6.19	–0.19|e⁻|
$Sb2–O_2$ Superoxide	Sb2	Before adsorption	1.78	2.91	0.00	4.70	+0.30|e⁻|
		After adsorption	1.85	2.51	0.00	4.35	+0.65|e⁻|
	O1	Before adsorption	1.88	4.13	0.00	6.00	0.00|e⁻|
		After adsorption	1.91	4.50	0.00	6.40	–0.40|e⁻|
	O2	Before adsorption	1.88	4.13	0.00	6.00	0.00|e⁻|
		After adsorption	1.90	4.50	0.00	6.41	–0.41|e⁻|
	Sb3	Before adsorption	1.78	2.91	0.00	4.69	+0.31|e⁻|
		After adsorption	1.85	2.52	0.00	4.38	+0.62|e⁻|
$Sb3–O_2$ Superoxide	Sb2	Before adsorption	1.78	2.91	0.00	4.70	+0.30|e⁻|
		After adsorption	1.74	2.41	0.00	4.15	+0.85|e⁻|
	O1	Before adsorption	1.88	4.13	0.00	6.00	0.00|e⁻|
		After adsorption	1.91	4.53	0.00	6.44	–0.44|e⁻|
	Sb2	Before adsorption	1.78	2.91	0.00	4.70	+0.30|e⁻|
		After adsorption	1.90	2.59	0.00	4.49	+0.51|e⁻|
	O2	Before adsorption	1.88	4.13	0.00	6.00	0.00|e⁻|
		After adsorption	1.89	4.54	0.00	6.44	–0.44|e⁻|
	Sb3	Before adsorption	1.78	2.91	0.00	4.69	+0.31|e⁻|
		After adsorption	1.83	2.56	0.00	4.40	+0.60|e⁻|
$Sb3(D)–O_2$ Superoxide	Sb2	Before adsorption	1.78	2.91	0.00	4.70	+0.30|e⁻|
		After adsorption	1.92	2.51	0.00	4.43	+0.57|e⁻|
	O1	Before adsorption	1.88	4.13	0.00	6.00	0.00|e⁻|
		After adsorption	1.90	4.52	0.00	6.42	–0.42|e⁻|
	O2	Before adsorption	1.88	4.13	0.00	6.00	0.00|e⁻|
		After adsorption	1.91	4.51	0.00	6.41	–0.41|e⁻|
	Sb2	Before adsorption	1.78	2.91	0.00	4.70	+0.30|e⁻|
		After adsorption	1.89	2.53	0.00	4.42	+0.58|e⁻|

We found that for all peroxide modes adsorption, only the Sb2−O_2 did not change after relaxation. We also found that for Sb2−O_2 (peroxide), although the bond lengths for Sb−O were slightly different the oxygens had equal charges gained (see Table 4.9). The charge on O_2 (i.e., charge sum of O1 and O2), for lowest ground state were as: for Pt−O_2-peroxide (−0.84|e|), for Sb2−O_2-peroxide (−0.90|e|) and Sb3−O_2-peroxide (−0.84|e|). It is

clear that the Sb2−O_2 (peroxide) had more negative charge, which was attributed to that both oxygen atoms were bonded to the same Sb2 atom. This indicated that there was more charge gain on the O_2 molecule on Sb2 atoms for peroxide.

Table 4.9: The calculated atomic population (Mulliken) charges of peroxide and bridge O_2 molecule adsorption on $PtSb_2$ (111) surface.

			Mulliken population charges (|e|)				
Adsorption	**Atom**	**Adsorptions state**	**s**	**p**	**d**	**Total**	**Charge**
Pt1–O_2 Peroxide	Sb2	Before adsorption	1.78	2.91	0.00	4.70	+0.30|e⁻|
		After adsorption	1.88	2.56	0.00	4.44	+0.56|e⁻|
	O1	Before adsorption	1.88	4.13	0.00	6.00	0.00|e⁻|
		After adsorption	1.91	4.54	0.00	6.45	–0.45|e⁻|
	O2	Before adsorption	1.88	4.13	0.00	6.00	0.00|e⁻|
		After adsorption	1.90	4.50	0.00	6.39	–0.39|e⁻|
	Sb2	Before adsorption	1.78	2.91	0.00	4.70	+0.30|e⁻|
		After adsorption	1.87	2.55	0.00	4.43	+0.57|e⁻|
Sb2–O_2 Peroxide	Sb2	Before adsorption	1.78	2.91	0.00	4.70	+0.30|e⁻|
		After adsorption	1.79	2.25	0.00	4.04	+0.96|e⁻|
	O1	Before adsorption	1.88	4.13	0.00	6.00	0.00|e⁻|
		After adsorption	1.95	4.50	0.00	4.45	–0.45|e⁻|
	O2	Before adsorption	1.88	4.13	0.00	6.00	0.00|e⁻|
		After adsorption	1.95	4.50	0.00	6.45	–0.45|e⁻|
Sb3–O_2 Peroxide	Sb2	Before adsorption	1.78	2.91	0.00	4.70	+0.30|e⁻|
		After adsorption	1.82	2.51	0.00	4.33	+0.67|e⁻|
	O1	Before adsorption	1.88	4.13	0.00	6.00	0.00|e⁻|
		After adsorption	1.91	4.50	0.00	6.41	–0.41|e⁻|
	O2	Before adsorption	1.88	4.13	0.00	6.00	0.00|e⁻|
		After adsorption	1.91	4.53	0.00	6.43	–0.43|e⁻|
	Sb3	Before adsorption	1.78	2.91	0.00	4.69	+0.31|e⁻|
		After adsorption	1.86	2.51	0.00	4.37	+0.63|e⁻|
Pt1–O_2–Pt1 Bridge	Sb2	Before adsorption	1.78	2.91	0.00	4.70	+0.30|e⁻|
		After adsorption	1.85	2.56	0.00	4.41	+0.59|e⁻|
	O1	Before adsorption	1.88	4.13	0.00	6.00	0.00|e⁻|
		After adsorption	1.92	4.82	0.00	6.75	–0.75|e⁻|
	Sb3	Before adsorption	1.78	2.91	0.00	4.69	+0.31|e⁻|
		After adsorption	1.70	2.34	0.00	4.04	+0.96|e⁻|
	O2	Before adsorption	1.88	4.13	0.00	6.00	0.00|e⁻|
		After adsorption	1.93	4.57	0.00	6.80	–0.80|e⁻|
	Sb2	Before adsorption	1.78	2.91	0.00	4.70	+0.30|e⁻|
		After adsorption	1.85	2.51	0.00	4.36	+0.64|e⁻|

For the bridge bonding in Table 4.9, we observed that the O_2 on Pt1−O_2−Pt1 Bridge dissociated and each oxygen atom bridged on Sb atoms (Sb3−O−Sb2). This was due to the electron transfer from the 5p-orbital of Sb atoms to the oxygen antibonding molecular orbitals, which weakened the bond strength of oxygen molecule and caused dissociation [Rosso et al. 1999]. The charges on each oxygen atom for lowest ground state for Sb2−O−Sb3 were −0.75|e| and −0.80|e|, which showed that there were more charge gains

on each oxygen atom (see Table 4.9). The negative charges on the oxygen atoms was also confirmed by experiment [Lever et al. 1980].

Table 4.8 and 4.9 clearly indicated that there was a greater loss of electrons in the 5p-orbitals of Sb atoms with more gain of electrons in the 2p-orbitals of O_2 molecule. This suggested that there was a strong hybridisation between the 5p-orbital of Sb and 2p-orbital of O_2 molecule. These finding suggested that the 2p-orbital spin-down unoccupied orbital (LUMO) of O_2 was fully occupied as reported by Mkhonto et al. [2015]. These clearly illustrated that the adsorption of O_2 on the surface was initiated by accepting electrons from the mineral surface into the LUMO (π_p*) antibonding orbital. This charge transfer was in the form of back-donation of electrons from the mineral surface of the (π_p*) anti-bonding orbital, which was similar to what was reported by Blyholder [Blyholder et al. 1982].

4.3 Summary

In this chapter, we investigated the oxidation of all the surfaces, where different possible orientations of the oxygen molecules were performed (i.e. peroxide and superoxide). In addition, the multi adsorption of the oxygen, molecules were investigated. The description of the chemistry was analysed from the Mulliken atomic charges. We found that that the oxygen molecules preferred interacting with the Sb atoms than the Pt atoms for all surfaces. We also observed different bonding modes, where bridging and dissociation into atomic bonding occurred. The adsorption energies showed the bonding strength of the oxygen molecules on the surface. For (100) surface we found that the Pt−O2 peroxide initial adsorption site gave the strongest adsorption. For (110) surface we found that the Sb2−O−O−Sb3 bridging gave the most exothermic adsorption. The case of (111) surface showed the Sb2−O−O−Sb2 bridging to give the strongest exothermic adsorption, which resulted in atomic bonding. The atomic charges indicated that the oxygen molecules gained charges from the Pt and Sb atoms. These finding suggested that the 2p-orbital spin-down unoccupied orbital (LUMO) of O_2 was fully occupied. We also observed that the Sb/Pt-bonded oxygen was more negative than the terminal or end-bonded oxygen atom for superoxide bonding modes. Furthermore, based on the charge sum of the O_2 (i.e. charge addition of O1 and O2), we found in all cases that the O_2

interacting with Sb gained more charges, thus showing that the Sb atoms were the preferred sites for oxygen adsorption and hence strong adsorption.

CHAPTER 5

H_2O and OH^- Adsorption on $PtSb_2$ Surfaces

Water is the phase in which the main processes of flotation take place, which begins by usually wet-grinding and for this reason we had to understand the adsorption of water on the ore mineral surface to determine the wettability of the $PtSb_2$ mineral. All minerals react with water to some extent and flotation depends directly on the nature and properties of mineral-water interface [Muzenda et al. 2011]. The processes that affect the surface characteristics of metals in water include dissociation of dissolved species, hydration, the adsorption of ions and flotation reagents.

In this chapter we investigated the adsorption geometries of the water molecules and hydroxide on the three surfaces, i.e. (100), (110) and (111) of the $PtSb_2$. The adsorption energies of the three surfaces were discussed. Firstly, the adsorptions of the water molecule/s on the surfaces were examined i.e. bonding geometry behaviour (bond length and angles). The Mulliken population charges to describe the chemistry of the adsorptions were presented and discussed. Furthermore, the hydroxide adsorption were performed and their charges were analysed. These play a role in understanding the pH required for $PtSb_2$ flotation, in that if a higher pH is used and the OH^- has strong affinity with the surface than the collector it may reduce the recovery of the mineral.

5.1 Hydration adsorption geometries and energies

In order to understand the hydration of the $PtSb_2$ surfaces, we considered two main cases where the water molecule was adsorbed on Pt-top site and Sb-top site. For coverage investigations, we have done adsorption with increasing number of water molecules on the surface until full surface coverage. We calculated the equilibrium geometry of the isolated H_2O molecule and found O–H = 0.974 Å and H–O–H = 104.10˚. These compared well with the experimental equilibrium bond length and angle of H_2O molecule (O–H = 0.957 Å and H–O–H = 104.5˚).
[https://msu.edu/course/css/850/snapshot.afs/teppen/physical_chemistry_of_water.htm]

During the hydration of surfaces, two processes occur, i.e. physisorption or chemisorption. The physisorption is a non-bonding process and is a physical interaction, where weak van der Waal forces dominate and is characterised for formation of multilayers adsorption on the surface. Furthermore, for physisorption the adsorption energies are in the range of E ≈ –19.97 kJ/mol to –40.04 kJ/mol. There have been extensive studies carried out on the hydration of different minerals surfaces which give

relative adsorption energies as compared to our current study on the $PtSb_2$ mineral surfaces. [Cooper et al 2003, Li et al 2016; Zhao et al 2014; Tunega et al 2002]. The chemisorption is a bonding process, where bonds are created and is a chemical interaction where hybridization of orbitals of adsorbate and substrate dominate and is characterized by formation of monolayer adsorption on the surface. The adsorption energies for chemisorption are in the range of E ≈ –49.97 kJ/mol to –400.03 kJ/mol [Li et al 2016; Zhao et al 2014; Tunega et al 2002]. In this section, we seek to understand the reaction of water molecules with $PtSb_2$ mineral surfaces. We further investigated their physisorption and chemisorption on the surfaces.

5.1.1 H_2O adsorptions on $PtSb_2$ (100) surface

We performed water adsorptions on the $PtSb_2$ (100) surface, where H_2O was adsorbed through oxygen on top of the surface Pt and Sb atoms as shown in Figure 5.1, which also presents the optimised output geometry for these systems. The (100) surface was explored by increasing the number of H_2O on the surface and the relaxed strucures are shown in Appendix D. Amongst these, H_2O increment adsorption on the surface, were the Pt half-monolayer (4/8 H_2O/Pt) and full-monolayer (8/8 H_2O/Pt) H_2O adsorption as shown in Figure 5.2. Furthermore the Sb atoms were also investigated in a similar manner; Sb half-monolayer (4/8 H_2O/Sb) and full-monolayer (8/8 H_2O/Sb) H_2O adsorption as shown in Figure 5.3. Lastly, the full-surface coverage (16/16 H_2O/Sb, Pt) was investigated where all Pt and Sb were adsorbed with H_2O (see Figure 5.4). We observed that the H_2O molecules assemble at an angle on the surface and lie horizontal in particular for multi adsorptions. Figure 5.1 shows the adsorption of H_2O on Pt and Sb and we found that in all cases the water molecule/s gave larger bond length between Pt/Sb and water O atoms (Pt–OH_2 and Sb–OH_2). As such, it indicated no bond formation between the surface and water molecules. The H_2O bond angle was slightly larger than the isolated H_2O molecule. Interestingly, for H_2O on Sb atom, we observed a bond formation between the top first surface layer Sb and the fourth surface layer Sb of Sb–Sb = 3.136 Å. This indicated that the top surface Sb relaxed deep into the surface. The calculated adsorption energy of –6.37 kJ/mol was obtained for Pt–OH_2 adsorptions, while the adsorption on Sb–OH_2 gave +10.34 kJ/mol. This showed that there was poor interaction of water on Sb atoms compared to the Pt atoms.

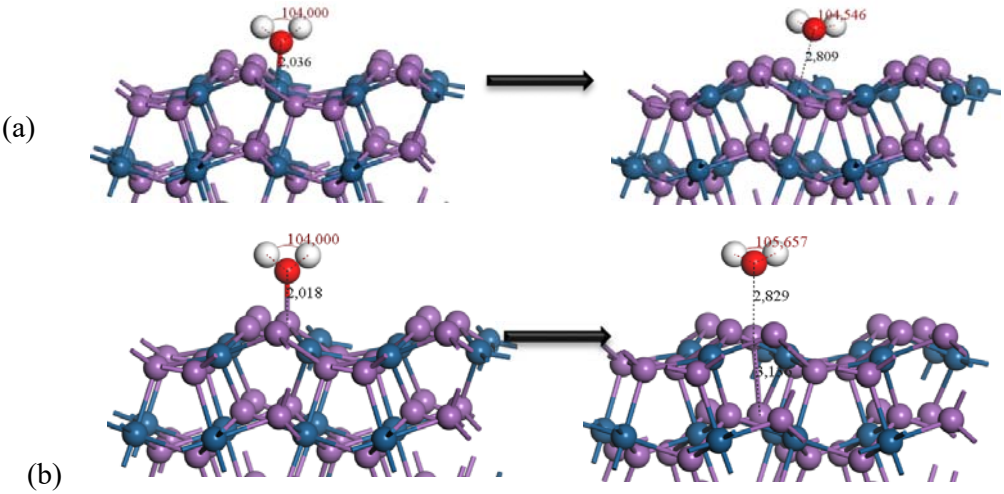

Figure 5.1: The side view of H_2O molecule adsorption on Pt-top and Sb-top of the $PtSb_2$ (100) surface.

The case of multi adsorptions on Pt atoms (i.e 4/8 H_2O/Pt and 8/8 H_2O/Pt) are shown in Figure 5.2 and for Sb atoms (i.e 4/8 H_2O/Sb and 8/8 H_2O/Sb) shown in Figure 5.3. We also observed that in both cases the bond lengths were larger (Pt–OH_2 and Sb–OH_2) indicating no chemisorption. Furthermore, we observed that the water molecules do not bond with the surface atoms and lie horizontal on the surface with the oxygen atoms facing the nearest water H atom as shown in Figure 5.2 and 5.3 the top view.

Table 5.1: The adsorption energies of hydration of $PtSb_2$ (100) surface, calculated according to equation 2.14.

Site	Adsorbate	n_{H2O}	$[S+A]^0$ (eV)	$[A]^0$ (eV)	$[S]^0$ (eV)	Total $E_{ads.}$ (kJ.mol^{-1})	$E_{ads.}$ per H_2O (kJ.mol^{-1})
Pt	H_2O	1	–41335.887	–468.798	–40867.023	–6.37	–
	H_2O	2	–41804.974	–937.596	–40867.023	–34.11	–17.06
	H_2O	3	–42274.197	–1406.394	–40867.023	–75.05	–25.02
	H_2O	4	–42743.175	–1875.192	–40867.023	–92.39	–23.10
	H_2O	5	–43212.240	–2343.99	–40867.023	–118.05	–23.61
	H_2O	6	–43681.471	–2812.788	–40867.023	–159.80	–26.63
	H_2O	7	–44150.409	–3281.586	–40867.023	–173.23	–24.75
	H_2O	8	–44619.207	–3750.384	–40867.023	–173.08	–21.64
Sb	H_2O	1	–41335.714	–468.798	–40867.023	+10.34	–
	H_2O	2	–41804.518	–937.596	–40867.023	+9.90	+4.95
	H_2O	3	–42273.364	–1406.394	–40867.023	+5.29	+1.76
	H_2O	4	–42742.102	–1875.192	–40867.023	+11.21	+2.80
	H_2O	5	–43211.973	–2343.99	–40867.023	–96.26	–19.25
	H_2O	6	–43681.199	–2812.788	–40867.023	–133.52	–22.25
	H_2O	7	–44150.202	–3281.586	–40867.023	–153.24	–21.89
	H_2O	8	–44619.839	–3750.384	–40867.023	–234.11	–29.26
Full	H_2O	16	–48374.137	–7500.768	–40867.023	–611.10	–38.19

This showed the Van der Waals forces interaction of the water molecules. The calculated adsorption energy of –23.10 kJ/mol per H_2O was obtained for Pt half-monolayer (4/8 H_2O/Pt), while the Pt full-monolayer (8/8 H_2O/Pt) adsorption gave –21.64 kJ/mol per H_2O (Table 5.1). The Sb half-monolayer (4/8 H_2O/Sb) adsorption energy was obtained as +2.80 kJ/mol per H_2O, while the Sb full-monolayer (8/8 H_2O/Sb) adsorption gave –29.26 kJ/mol per H_2O molecule. This showed that adsorption of more than $4H_2O$ molecules gave an exothermic reaction on the Sb atoms on the surface.

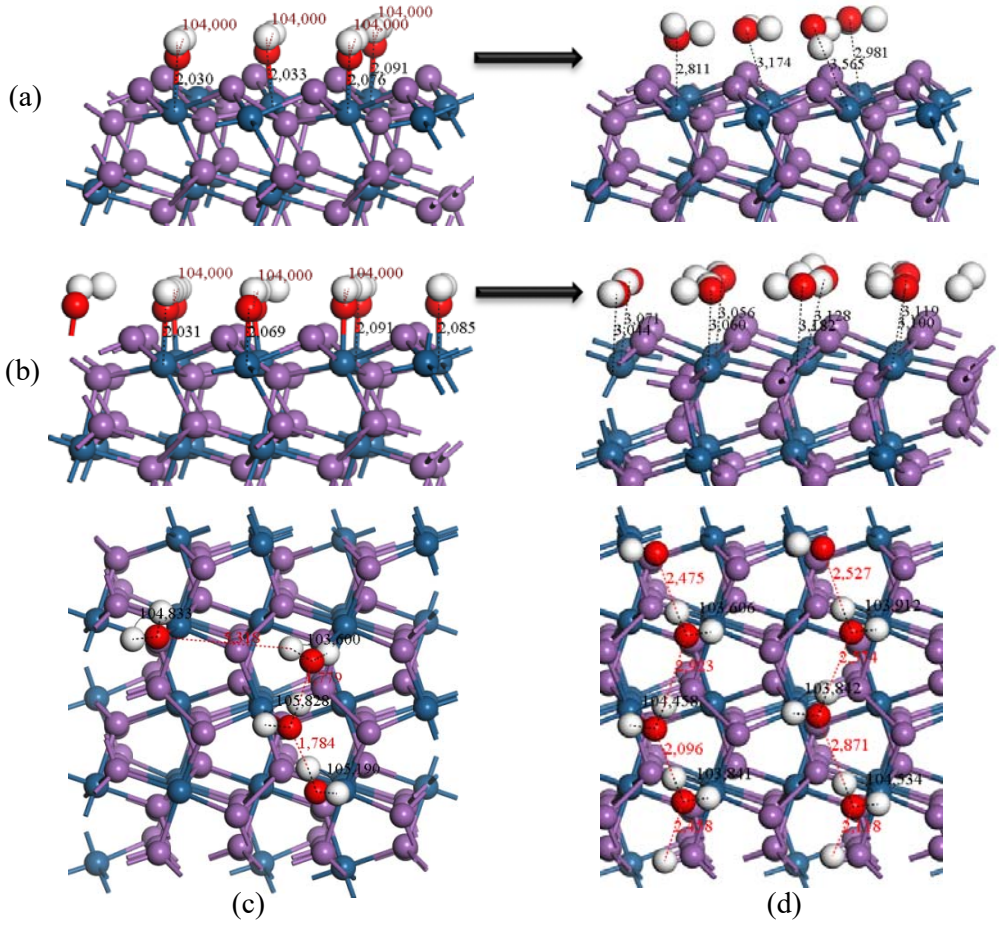

Figure 5.2: The hydration of the $PtSb_2$ (100) surface, side view: (a) Pt half-monolayer and Pt full-monolayer; and top view: (c) Pt half-monolayer and (d) Pt full-monolayer.

Furthermore, we also explored how the adsorption behaves as we increase the water molecule on the surface (see Table 5.1). We observed that for Pt adsorption as more water molecule are adsorbed, the adsorption energies become more exothermic up to 7/8 H_2O/Pt and drops for 8/8 H_2O/Pt. This suggested that the surface was saturated at $8H_2O$

molecules, thus the decrease in adsorption energy. However, for Sb adsorption there was no distinct trend and the adsorptions were endothermic up to 4/4 H_2O/Sb and only showed exothermic from 5/8 H_2O/Sb to 8/8 H_2O/Sb. This showed that for Sb water adsorb stronger in multiple adsorptions.

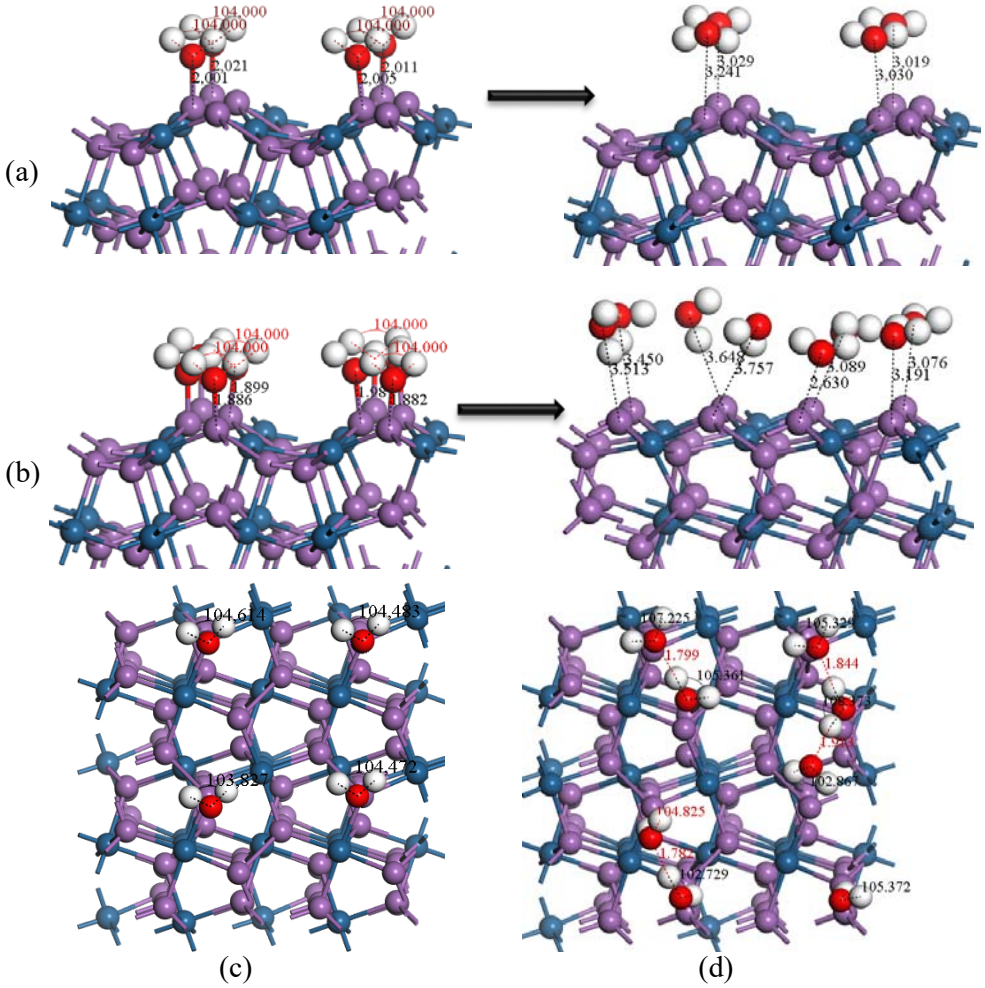

Figure 5.3: The hydration of the $PtSb_2$ (100) surface, side view: (a) Sb half-monolayer and Sb full-monolayer; and top view: (c) Sb half-monolayer and (d) Sb full-monolayer.

The full-surface coverage gave –38.19 kJ/mol per H_2O and we observed only one Sb–OH_2 bond of 2.262 Å on the surface. Moreover, there was a bond formation between the top Sb atoms and the fourth layer (4L) Sb atoms (see Figure 5.4). These findings showed that for (100) surface, the Sb had very poor adsorption of H_2O compared to the Pt atoms. As we had defined the physisorption (E ≈ –19.97 kJ/mol to –40.04 kJ/mol) and

chemisorption (E ≈ –49.97 kJ/mol to –400.03 kJ/mol) energies range, we found that water molecules adsorb through physisorption based on the average adsorption enegies.

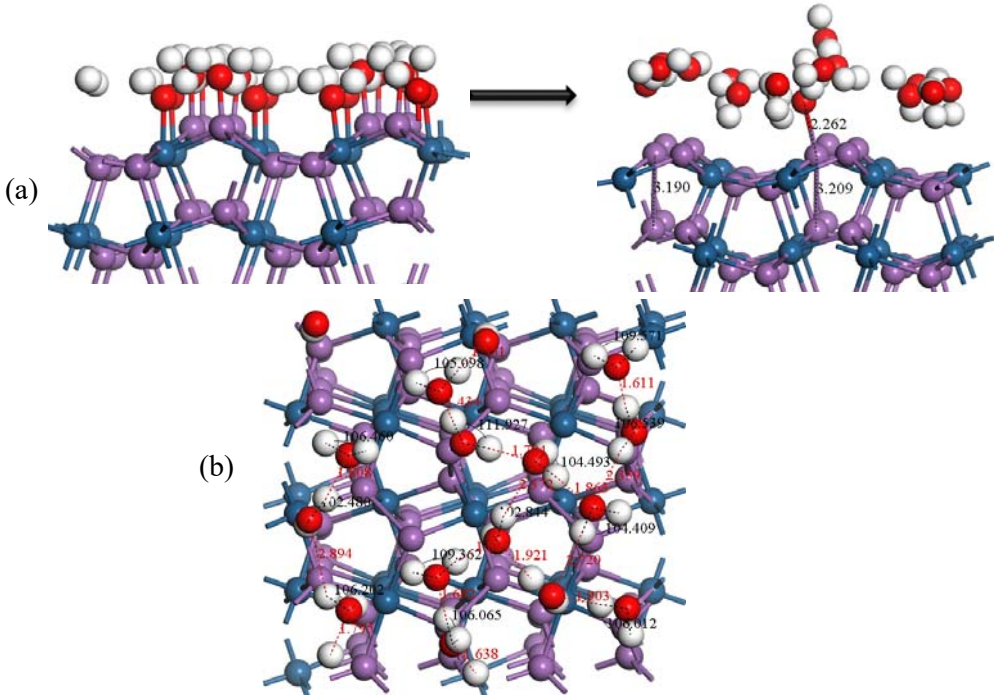

Figure 5.4: The surface full-coverage hydration of the $PtSb_2$ (100) surface: (a) side view and (b) top view.

5.1.2 H_2O adsorptions on $PtSb_2$ (110) surface

The water adsorptions on the $PtSb_2$ (110) surface was also adsorbed through oxygen on top of a surface Pt and Sb atoms as shown in Figure 5.5, which also presents the optimised output geometry for these systems. We have also performed Pt half-monolayer (4/8 H_2O/Pt) and full-monolayer (8/8 H_2O/Pt) H_2O adsorption as shown in Figure 5.7. Furthermore, the Sb atoms were also investigated in a similar manner; Sb2 full-monolayer (4/4 H_2O/Sb2), Sb3 half-monolayer (4/8 H_2O/Sb3) and Sb3 full-monolayer (8/8 H_2O/Sb3) H_2O adsorptions as shown in Figure 5.6. The complete/full surface coverage was investigated, where all Pt and Sb were adsorbed with H_2O (see Figure 5.7c). We observed that the H_2O pack itself in an angle on the surface and lie horizontal in particular for multi adsorptions. In Figure 5.5, the adsorption of H_2O on Pt and Sb in all cases the water molecule/s gave larger distances between Pt/Sb and water O atoms (Pt–OH_2 and

Sb–OH_2). However, the Pt–OH_2 distances were shorter than those of Sb–OH_2. These indicated no bond formation between the surface and water molecules.

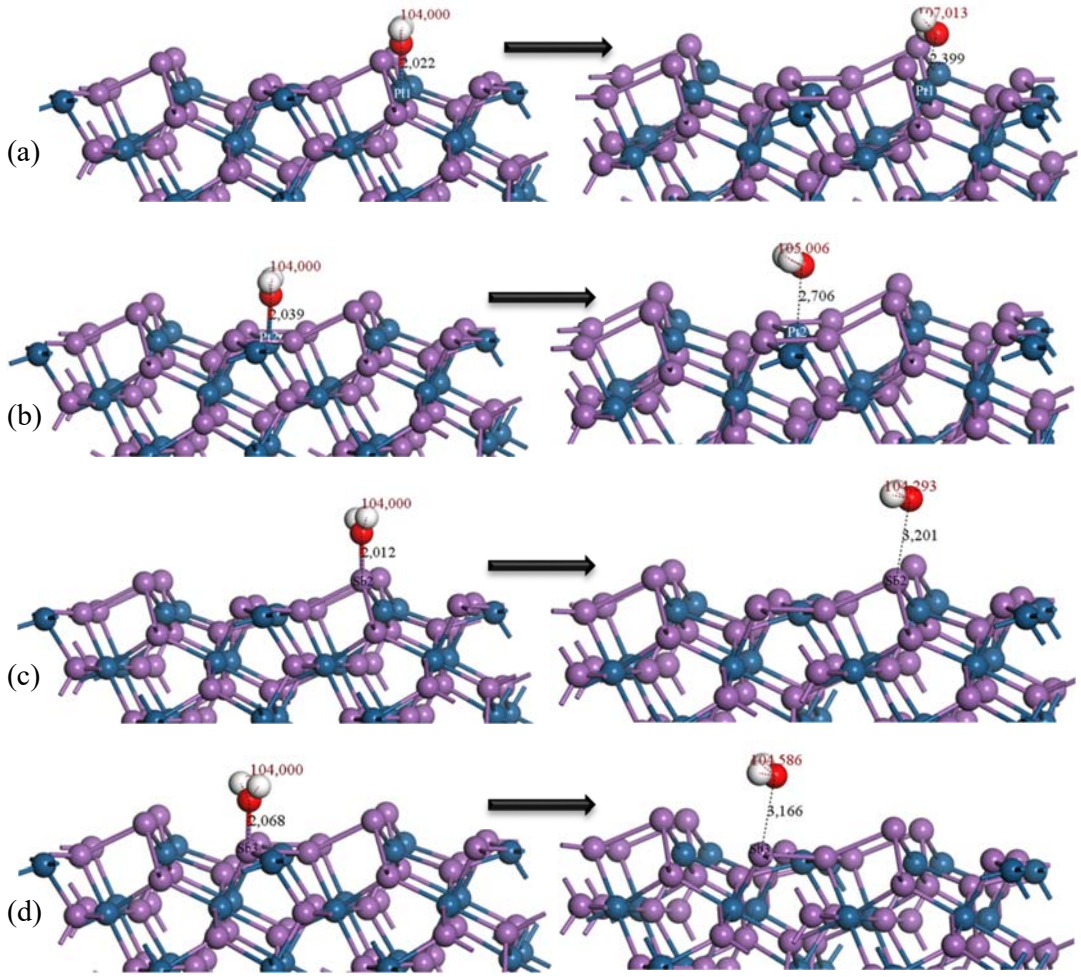

Figure 5.5: The side view of H_2O molecule adsorption on Pt-top and Sb-top on the $PtSb_2$ (110) surface.

The H_2O bond angle was slightly larger than the isolated H_2O molecule. The calculated adsorption energy of –35.60 kJ/mol and –15.99 kJ/mol were obtained for Pt1–OH_2 and Pt2–OH_2 adsorptions, respectively (Table 5.2). The adsorption of H_2O on Sb atom gave +0.55 kJ/mol and –7.04 kJ/mol for Sb2–OH_2 and Sb3–OH_2, respectively. This showed that there was poor interaction of water on Sb atoms compared to the Pt atoms. The case of multi adsorptions on Pt atoms (i.e 4/8 H_2O/Pt and 8/8 H_2O/Pt) are shown in Figure 5.7 and on Sb atoms (i.e 4/8 H_2O/Sb and 8/8 H_2O/Sb) are shown in Figure 5.6. We observed that in both cases the bond lengths were larger (Pt–OH_2 and Sb–OH_2) indicating no chemisorption. Furthermore, we observed that the water molecules lie horizontal on the

surface with the O facing the nearest water H atom as shown in top view in Figure 5.6 and 5.7. This showed that the water molecules interact through Van der Waals forces.

Table 5.2: The adsorption energies of hydration of the $PtSb_2$ (110) surface, calculated according to equation 2.14.

Site	Adsorbate	n_{H2O}	$[S+A]^0$ (eV)	$[A]^0$ (eV)	$[S]^0$ (eV)	Total $E_{ads.}$ (kJ.mol^{-1})	$E_{ads.}$ per H_2O (kJ.mol^{-1})
Pt	Pt1H_2O	1	–49497.776	–468.798	–49028.608	–35.60	–
	Pt2H_2O	1	–49497.573	–468.798	–49028.608	–15.99	–
	H_2O	4	–50904.770	–1875.192	–49028.608	–93.21	–23.30
	H_2O	8	–52780.661	–3750.384	–49028.608	–231.41	–28.93
Sb3	H_2O	1	–49497.480	–468.798	–49028.608	–7.07	–
	H_2O	4	–50903.983	–1875.192	–49028.608	–17.28	–4.32
	H_2O	8	–52781.397	–3750.384	–49028.608	–160.36	–20.05
Sb2	H_2O	1	–49497.401	–468.798	–49028.608	+0.55	–
	H_2O	4	–50903.866	–1875.192	–49028.608	–6.03	–1.51
Full	H_2O	20	–58411.839	–9375.976	–49028.608	–700.06	–35.00

The calculated adsorption energy of –23.30 kJ/mol per H_2O molecule was obtained for Pt half-monolayer (4/8 H_2O/Pt), while the Pt full-monolayer (8/8 H_2O/Pt) adsorption gave –28.93 kJ/mol per H_2O molecule. This indicated that there was an increase in adsorption as more water molecules were adsorbed, as also seen on the (100) surface adsorptions. The Sb2 full-monolayer (4/4 H_2O/Sb2) adsorption energy was obtained as –1.51 kJ/mol per H_2O, while the Sb3 half-monolayer (4/8 H_2O/Sb3) adsorption gave –4.32 kJ/mol per H_2O and the full-monolayer (8/8 H_2O/Sb3) gave –20.05 kJ/mol per H_2O molecule. This showed exothermic adsorption for Sb multi adsorption. The computed adsorption energy for full-surface coverage was –35.00 kJ/mol per H_2O molecule. These findings showed that for (110) surface the Sb atom had weaker adsorption with H_2O compared to the Pt atoms. As we had defined the physisorption (E ≈ –19.97 kJ/mol to –40.04 kJ/mol) and chemisorption (E ≈ –49.97 kJ/mol to –400.03 kJ/mol) energies range, we found that based on the average adsorption energies the water molecule adsorb on the surface through physisorption.

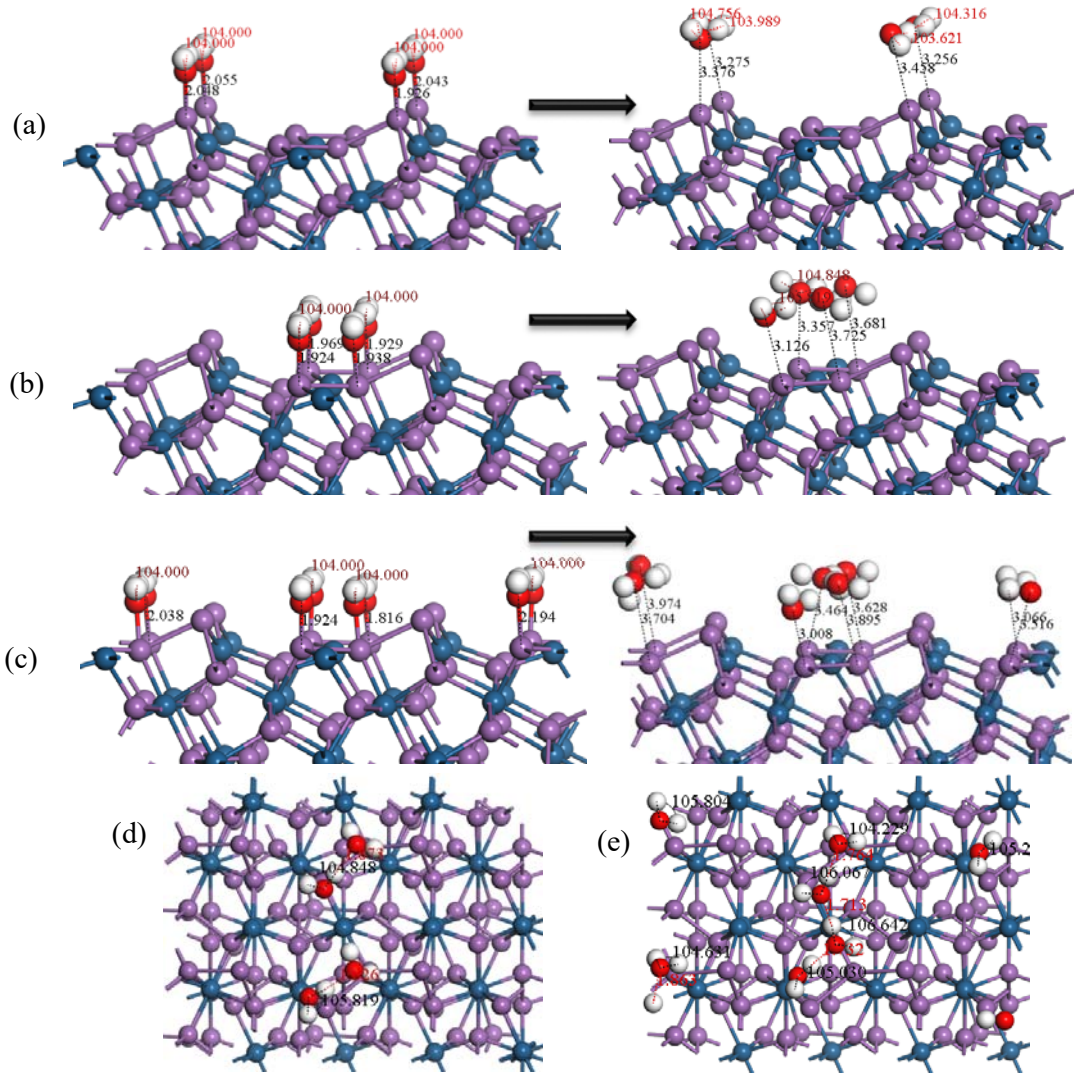

Figure 5.6: The hydration of the $PtSb_2$ (110) surface, side view: (a) Sb2 full-monolayer, (b) Sb3 half-monolayer, (c) Sb3 full-monolayer, (d) Sb3 half-monolayer top view and (e) Sb3 full-monolayer top view.

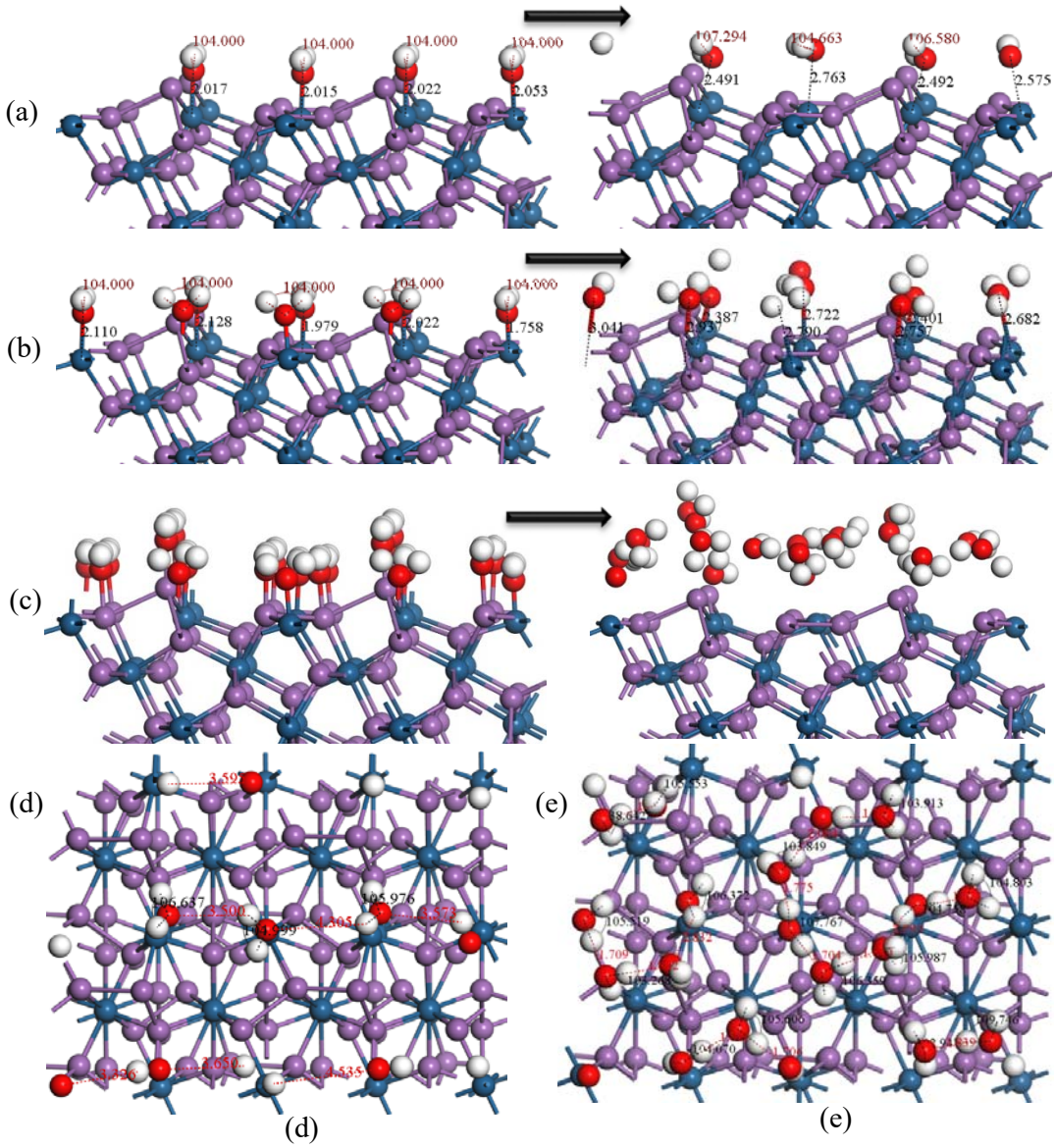

Figure 5.7: The hydration surface coverage of the $PtSb_2$ (110) surface: (a) Pt half-monolayer, (b) Pt full-monolayer, (c) Pt/Sb full surface coverage, (d) Pt full-monolayer top view and (e) Pt/Sb full surface coverage top view.

5.1.3 H_2O adsorptions on $PtSb_2$ (111) surface

The water adsorptions on the $PtSb_2$ (111) surface was also adsorbed through oxygen on top of a surface Pt and Sb atoms as shown in Figure 5.8, which also presents the optimised output geometry for these systems. We have also performed Pt1 full-monolayer (10/10 H_2O/Pt) as shown in Figure 5.10. Furthermore the Sb atoms were also investigated in a similar manner; Sb2 full-monolayer (12/12 H_2O/Sb2) and Sb3 full-monolayer (4/4

H_2O/Sb3) and all Sb full-monolayer (16/16 H_2O/Sb) H_2O adsorption as shown in Figure 5.9. The complete/full surface coverage was investigated where all Pt1 and Sb atoms were adsorbed with H_2O (see Figure 5.10). As in previous surfaces the H_2O sits at an angle on the surface and lie horizontal in particular for multi adsorptions and larger bond length between Pt/Sb and water O atoms (Pt–OH_2 and Sb–OH_2) were noted. These also indicated no bond formation between the surface and water molecules and the H_2O bond angles were slightly larger than the isolated H_2O molecule.

Table 5.3: The adsorption energies of hydration on the $PtSb_2$ (111) surface, calculated according to equation 2.14.

Site	Adsorbate	n_{H2O}	$[S+A]^0$ (eV)	$[A]^0$ (eV)	$[S]^0$ (eV)	Total $E_{ads.}$ (kJ.mol^{-1})	$E_{ads.}$ per H_2O (kJ.mol^{-1})
Pt	Pt1H_2O	1	–49487.909	–468.798	–49015.288	–368.80	–
	Pt2H_2O	1	–49487.832	–468.798	–49015.288	–361.90	–
	Full	10	–53709.343	–4687.988	–49015.288	–585.32	–58.53
Sb3	H_2O	1	–49488.293	–468.798	–49015.288	–405.84	–
	Full	4	–50895.612	–1875.195	–49015.288	–494.84	–123.71
Sb2	H_2O	1	–49487.695	–468.798	–49015.288	–348.13	–
	Full	12	–54648.086	–5625.585	–49015.288	–695.85	–57.99
Sb3(D)	H_2O	1	–49488.253	–9375.976	–49015.288	–344.67	–
Sb2, Sb3	H_2O Full	16	–56525.279	–7500.780	–49015.288	–888.63	–55.54
Pt1, Sb	H_2O Full	26	–61218.865	–12188.77	–49015.288	–1428.80	–54.95

The calculated adsorption energies for these adsorptions are shown in Table 5.3. We found that for Sb3 gave the strongest exothermic adsorption for a single H_2O molecule adsorption (–405.84 kJ/mol). These showed that there was strong interaction of water on Sb and Pt atoms. The case of multi adsorptions on Pt1 atoms (10/10 H_2O/Pt1) shown in Figure 5.10 and Sb atoms (i.e 12/12 H_2O/Sb2 and 4/4 H_2O/Sb3) are shown in Figure 5.9. We observed that in both cases the bond lengths are larger (Pt–OH_2 and Sb–OH_2) indicating no chemisorption. Furthermore, we observed that the water molecules lie horizontal on the surface with the O facing the nearest water H atom as shown in Figure 5.9 and 5.10 the top view. This showed that the water molecules interact through Van der Waals forces.

The calculated adsorption energy of –58.53 kJ/mol per H_2O molecule was obtained for Pt1 full-monolayer (10/10 H_2O/Pt1) and we observed two Sb2–OH_2 bonds for this adsorption (see Figure 5.10). The Sb2 full-monolayer (12/12 H_2O/Sb2) adsorption energy was obtained as –57.99 kJ/mol per H_2O, while the Sb3 full-monolayer (4/4 H_2O/Sb3) adsorption gave –123.71 kJ/mol per H_2O molecule and the all Sb full-monolayer (16/16

H2O/Sb) gave –55.54 kJ/mol per H_2O molecule. The computed adsorption energy for full-surface coverage (all Pt5 and Sb) was –54.95 kJ/mol per H_2O molecule. As we had defined the physisorption (E ≈ –19.97 kJ/mol to –40.04 kJ/mol) and chemisorption (E ≈ –49.97 kJ/mol to –400.03 kJ/mol) energies range, we found that all adsorptions on Pt and Sb showed chemisorption, suggesting that the (111) surface has better interaction with H_2O molecules. The chemisorption was due to the few bonds created for multi H_2O adsorptions.

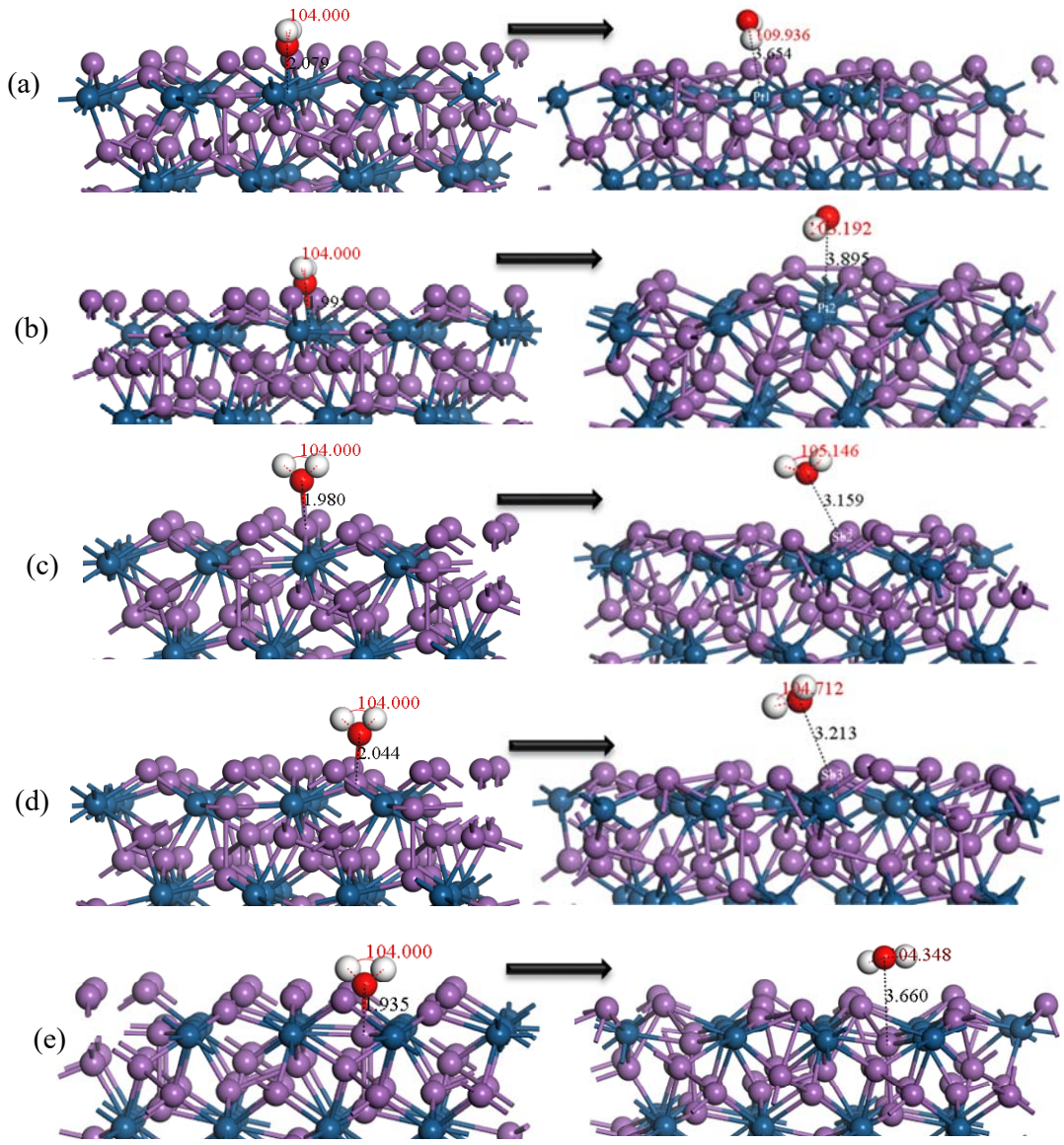

Figure 5.8: The top view and side view of H_2O molecule adsorption on Pt-top and Sb-top of the $PtSb_2$ (111) surface.

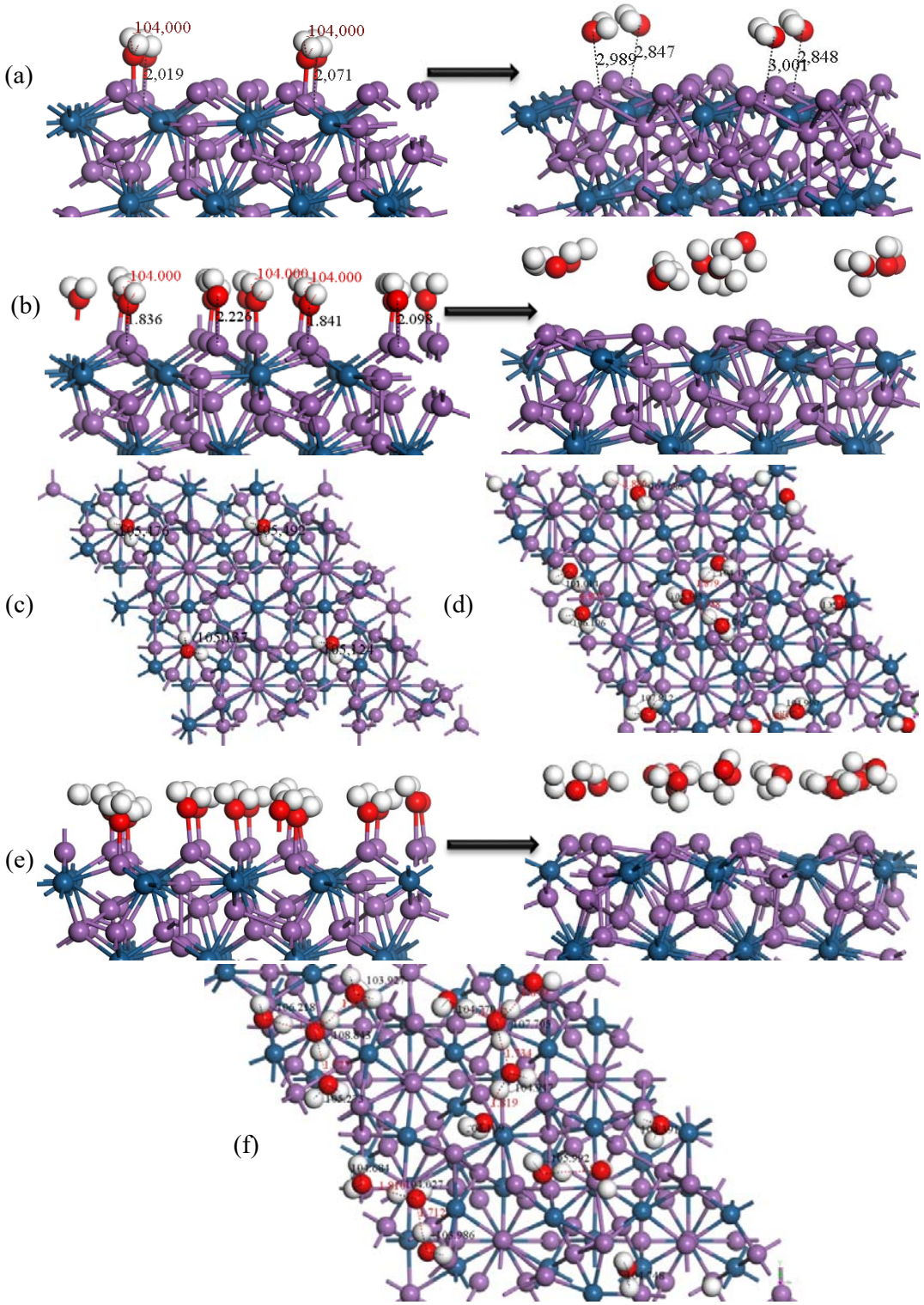

Figure 5.9: The hydration of the $PtSb_2$ (111) surface: (a) side view Sb3 full-monolayer, side view Sb2 full-monolayer, (c) top view of Sb3 full-monolayer, (d) top view Sb2 full-monolayer, (e) side view of all Sb full-coverage and (f) top view of all Sb full-coverage.

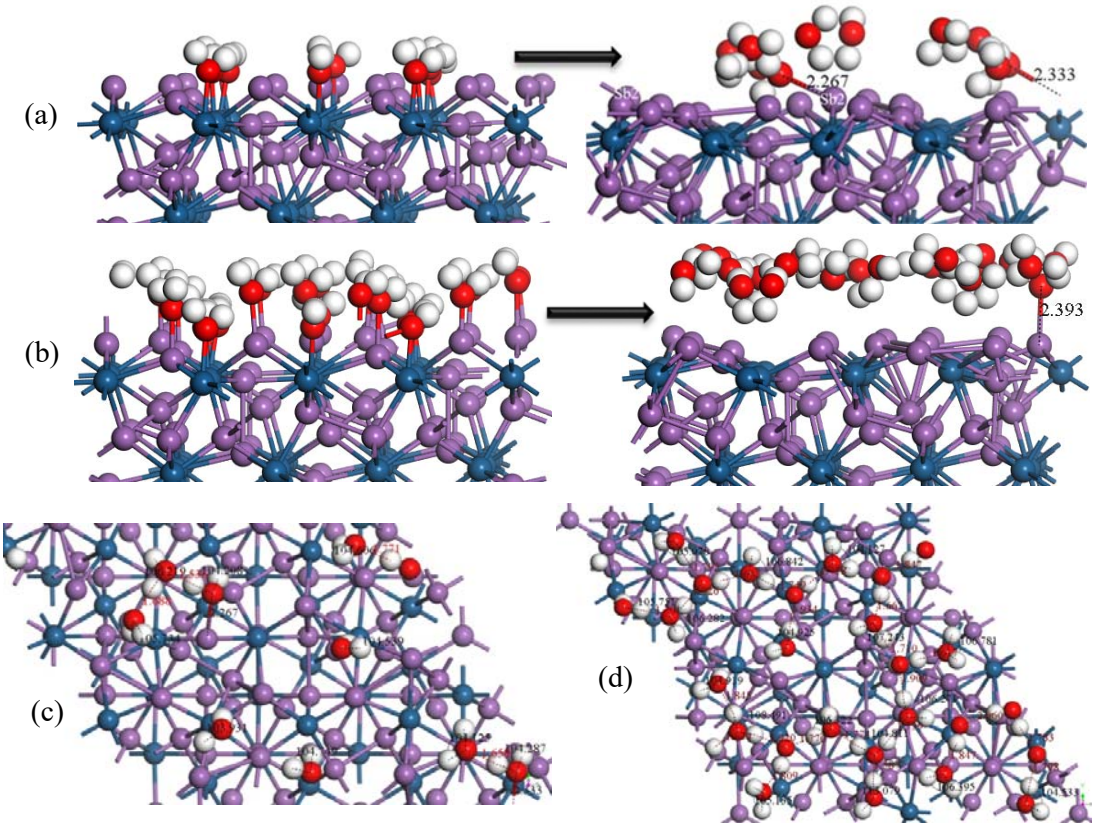

Figure 5.10: The hydration of the $PtSb_2$ (111) surface: (a) side view of Pt1 full-monolayer,(b) side view of surface full-coverage, (c) top view of Pt1 full-coverage and (d) top view of surface full-coverage.

5.2 $PtSb_2$ Hydration Mulliken Population charges

In this section we investigated the electronic properties (Mulliken population charges) for the hydration adsorption on the $PtSb_2$ (100), (110) and (111) surfaces. These properties will give insight into the chemistry bonding of the water molecule on the surfaces. Moreover, the electron accepting and donation character of the surface and oxygen of the water molecule will be analysed.

5.2.1 $PtSb_2$ (100) hydration surface DOS and charges

The adsorption of water on the (100) surface showed that the water molecules did not bond on the surface. Now, we analyse the atomic population charges as shown in Table 5.4, which also shows the occupancy of the s-p-d-orbitals. We found that both the Sb and Pt atoms adopt more positive charge and less negative charge, suggesting loss of charges,

respectively. The water oxygen atoms was found to adopt less negative charge, while the hydrogen atoms adopted less positive charges, suggesting charge loss and gain, respectively. Since there was no chemisorption bond between the Sb or Pt with oxygen of the water, this may imply that the oxygen has transferred charges into the H 1s-orbital from the O 2p-orbital.

Table 5.4: The calculated atomic population (Mulliken) charges of H_2O molecule adsorption on $PtSb_2$ (100) surface.

			Mulliken population charges (|e|)				
Adsorption	**Atom**	**Adsorptions state**	**s**	**p**	**d**	**Total**	**Charge**
$Pt–OH_2$	Pt	Before adsorption	1.00	0.85	9.08	10.97	–0.97|e⁻|
		After adsorption	0.94	0.93	9.03	10.91	–0.91|e⁻|
	H1	Before adsorption	0.47	0.00	0.00	0.47	+0.53|e⁻|
		After adsorption	0.57	0.00	0.00	0.57	+0.43|e⁻|
	O	Before adsorption	1.89	5.16	0.00	7.05	–1.05|e⁻|
		After adsorption	1.86	4.96	0.00	6.82	–0.82|e⁻|
	H2	Before adsorption	0.47	0.00	0.00	0.47	+0.53|e⁻|
		After adsorption	0.58	0.00	0.00	0.58	+0.42|e⁻|
$Sb–OH_2$	Sb	Before adsorption	1.84	2.95	0.00	4.79	+0.20|e⁻|
		After adsorption	1.70	2.88	0.00	4.58	+0.42|e⁻|
	H1	Before adsorption	0.47	0.00	0.00	0.47	+0.53|e⁻|
		After adsorption	0.55	0.00	0.00	0.55	+0.45|e⁻|
	O	Before adsorption	1.89	5.16	0.00	7.05	–1.05|e⁻|
		After adsorption	1.87	5.03	0.00	6.90	–0.90|e⁻|
	H2	Before adsorption	0.47	0.00	0.00	0.47	+0.53|e⁻|
		After adsorption	0.55	0.00	0.00	0.55	+0.45|e⁻|

The Pt atoms were observed to have charge depletion in the s-orbital and d-orbital, with charge accumulation in the p-orbital. This suggested that the mixing of the O 2p-orbital of water with the 5d-orbital, although they did not form bonds, the 6s-orbital and 5d-orbital have transferred charges into the lower-lying regions of the Pt 5p-orbitals manifolds. This was in line with the study on $Ru(H_2O)$ on {0001} surface by Michaelides [Michaelides et al 2003]. The case of Sb atom clearly showed that both 5s-orbital and 5p-orbitals were depleted and may have distributed their charges into neighbouring surface atoms. All these findings suggested that the water molecules adsorb through Van der Waals forces on the surface.

5.2.2 $PtSb_2$ (110) hydration surface Mulliken population charges

The adsorption of water on the (110) surface also showed that the water molecules did not bond on the surface. Now we analyse the atomic population charges as shown in Table 5.5, which also shows the occupancy of the s-p-d-orbitals.

Table 5.5: The calculated atomic population (Mulliken) charges of H_2O molecule adsorption on $PtSb_2$ (110) surface.

Collector	Atom	Adsorptions state	Mulliken population charges (|e|)				
			s	p	d	Total	Charge
Pt1–OH_2	Pt1	Before adsorption	0.99	0.70	9.09	10.78	–0.78|e⁻|
		After adsorption	0.91	0.69	9.03	10.64	–0.64|e⁻|
	H1	Before adsorption	0.47	0.00	0.00	0.47	+0.53|e⁻|
		After adsorption	0.55	0.00	0.00	0.00	+0.45|e⁻|
	O	Before adsorption	1.89	5.16	0.00	7.05	–1.05|e⁻|
		After adsorption	1.85	4.95	0.00	6.80	–0.80|e⁻|
	H2	Before adsorption	0.47	0.00	0.00	0.47	+0.53|e⁻|
		After adsorption	0.58	0.00	0.00	0.58	+0.42|e⁻|
Pt2–OH_2	Pt2	Before adsorption	0.96	0.70	9.11	10.77	–0.77|e⁻|
		After adsorption	1.91	0.72	9.08	10.71	–0.71|e⁻|
	H1	Before adsorption	0.47	0.00	0.00	0.47	+0.53|e⁻|
		After adsorption	0.56	0.00	0.00	0.56	+0.44|e⁻|
	O	Before adsorption	1.89	5.16	0.00	7.05	–1.05|e⁻|
		After adsorption	1.86	4.98	0.00	6.85	–0.85|e⁻|
	H2	Before adsorption	0.47	0.00	0.00	0.47	+0.53|e⁻|
		After adsorption	0.56	0.00	0.00	0.56	+0.44|e⁻|
Sb2–OH_2	Sb2	Before adsorption	1.90	3.04	0.00	4.94	+0.06|e⁻|
		After adsorption	1.72	2.95	0.00	4.67	+0.33|e⁻|
	H1	Before adsorption	0.47	0.00	0.00	0.47	+0.53|e⁻|
		After adsorption	0.54	0.00	0.00	0.54	+0.46|e⁻|
	O	Before adsorption	1.89	5.16	0.00	7.05	–1.05|e⁻|
		After adsorption	1.87	5.05	0.00	6.93	–0.93|e⁻|
	H2	Before adsorption	0.47	0.00	0.00	0.47	+0.53|e⁻|
		After adsorption	0.54	0.00	0.00	0.54	+0.46|e⁻|
Sb3–OH_2	Sb3	Before adsorption	1.85	2.95	0.00	4.80	+0.20|e|
		After adsorption	1.75	2.89	0.00	4.64	+0.36|e⁻|
	H1	Before adsorption	0.47	0.00	0.00	0.47	+0.53|e⁻|
		After adsorption	0.56	0.00	0.00	0.56	+0.44|e⁻|
	O	Before adsorption	1.89	5.16	0.00	7.05	–1.05|e⁻|
		After adsorption	1.87	5.04	0.00	6.91	–0.91|e⁻|
	H2	Before adsorption	0.47	0.00	0.00	0.47	+0.53|e⁻|
		After adsorption	0.56	0.00	0.00	0.56	+0.44|e⁻|

We found that both the Sb and Pt atoms adopt more positive charge and less negative charge, suggesting loss of charges, respectively. The water oxygen atoms was found to adopt less negative charge, while the hydrogen atoms adopted less positive charges, suggesting charge loss and gain, respectively. Since there was no chemisorption bond between the Sb or Pt with oxygen of the water, this may imply that the oxygen has transferred charges into the H 1s-orbital from the O 2p-orbital.

The Pt2 atom was observed to have charge depletion in the s-orbital and d-orbital, with some charge accumulation in the p-orbital. This suggested that the mixing of the O 2p-orbital of water with the 5d-orbitla, although they did not form bonds, the 6s-orbital and 5d-orbital of have transferred charges into the lower-lying regions of the Pt2 5p-

orbitals manifolds. This was also in line with the study on Ru(H_2O) on {0001} surface by Michaelides [Machaelides et al. 2003]. The case of Sb2 and Sb3 atoms clearly showed that both 5s-orbital and 5p-orbitals are depleted and may have distributed their charges into neighbouring surface atoms. Similarly, the Pt1 showed similar behaviour as the Sb atoms, the s-p-d-orbitals have lost some charges to the neighbouring surfaces atoms. All these findings suggested that the water molecules adsorb through Van der Waals forces on the surface.

5.2.3 $PtSb_2$ (111) hydration surface DOS and charges

The case of water adsorption on the (111) surface also showed that the water molecules did not bond on the surface. Now we analyse the atomic population charges as shown in Table 5.6, which also shows the occupancy of the s-p-d-orbitals. We found that both the Sb and Pt atoms adopt more positive charge and less negative charge, suggesting loss of charges, respectively, except for Pt1 which gained charges from the oxygen atom in all s-p-d-orbitals. The water oxygen atoms were found to adopt less negative charge, while the hydrogen atoms adopted less positive charges, suggesting charge loss and gain, respectively. Since there is no chemisorption bond between the Sb or Pt with oxygen of the water, this may imply that the oxygen has transferred charges into the H 1s-orbital from the O 2p-orbital.

The Pt2 atom was observed to have charge depletion in the s-orbital and p-orbital, with some charge accumulation in the d-orbital. This suggested that the mixing of the O 2p-orbital of water with the 5d-orbitla, although they did not form bonds, the 6s-orbital and 5p-orbital of have transferred charges into the lower-lying regions of the Pt2 5d-orbitals manifolds.

Table 5.6: The calculated atomic population (Mulliken) charges of H_2O molecule adsorption on $PtSb_2$ (111) surface.

			Mulliken population charges (|e|)				
Collector	**Atom**	**Adsorptions state**	**s**	**p**	**d**	**Total**	**Charge**
$Pt1–OH_2$	Pt1	Before adsorption	0.96	1.00	9.06	11.02	–1.02|e⁻|
		After adsorption	0.97	1.02	9.07	11.06	–1.06|e⁻|
	H1	Before adsorption	0.47	0.00	0.00	0.47	+0.53|e⁻|
		After adsorption	0.61	0.00	0.00	0.61	+0.39|e⁻|
	O	Before adsorption	1.89	5.16	0.00	7.05	–1.05|e⁻|
		After adsorption	1.85	5.01	0.00	6.87	–0.87|e⁻|
	H2	Before adsorption	0.47	0.00	0.00	0.47	+0.53|e⁻|

		After adsorption	0.58	0.00	0.00	0.58	+0.42|e⁻|
Pt2–OH_2	Pt2	Before adsorption	1.00	1.16	9.03	11.19	–1.19|e⁻|
		After adsorption	0.97	1.01	9.06	11.04	–1.04|e⁻|
	H1	Before adsorption	0.47	0.00	0.00	0.47	+0.53|e⁻|
		After adsorption	0.57	0.00	0.00	0.57	+0.43|e⁻|
	O	Before adsorption	1.89	5.16	0.00	7.05	–1.05|e⁻|
		After adsorption	1.86	5.02	0.00	6.88	–0.88|e⁻|
	H2	Before adsorption	0.47	0.00	0.00	0.47	+0.53|e⁻|
		After adsorption	0.57	0.00	0.00	0.57	0.43|e⁻|
Sb2–OH_2	Sb2	Before adsorption	1.78	2.91	0.00	4.70	+0.30|e⁻|
		After adsorption	1.78	2.80	0.00	4.58	+0.42|e⁻|
	H1	Before adsorption	0.47	0.00	0.00	0.47	+0.53|e⁻|
		After adsorption	0.55	0.00	0.00	0.55	+0.45|e⁻|
	O	Before adsorption	1.89	5.16	0.00	7.05	–1.05|e⁻|
		After adsorption	1.87	5.05	0.00	6.92	–0.92|e⁻|
	H2	Before adsorption	0.47	0.00	0.00	0.47	+0.53|e⁻|
		After adsorption	0.55	0.00	0.00	0.55	+0.45|e⁻|
Sb3–OH_2	Sb3	Before adsorption	1.78	2.91	0.00	4.69	+0.31|e⁻|
		After adsorption	1.89	2.87	0.00	4.76	+0.24|e⁻|
	H1	Before adsorption	0.47	0.00	0.00	0.47	+0.53|e⁻|
		After adsorption	0.56	0.00	0.00	0.56	+0.44|e⁻|
	O	Before adsorption	1.89	5.16	0.00	7.05	–1.05|e⁻|
		After adsorption	1.87	5.04	0.00	6.91	–0.91|e⁻|
	H2	Before adsorption	0.47	0.00	0.00	0.47	+0.53|e⁻|
		After adsorption	0.55	0.00	0.00	0.55	+0.45|e⁻|
Sb3(D)–OH_2	Sb3(D)	Before adsorption	1.62	2.93	0.00	4.55	+0.45|e⁻|
		After adsorption	1.53	2.89	0.00	4.42	+0.58|e⁻|
	H1	Before adsorption	0.47	0.00	0.00	0.47	+0.53|e⁻|
		After adsorption	0.58	0.00	0.00	0.58	–0.42|e⁻|
	O	Before adsorption	1.89	5.16	0.00	7.05	–1.05|e⁻|
		After adsorption	1.86	5.02	0.00	6.88	–0.88|e⁻|
	H2	Before adsorption	0.47	0.00	0.00	0.47	+0.53|e⁻|
		After adsorption	0.59	0.00	0.00	0.59	+0.41|e⁻|

The case of Sb2 atom clearly showed that there is a charge loss only in the 5p-orbital, which may have been distributed their charges into neighbouring surface atom. The Sb3 atom have transferred charges from the 5p-orbital to the 5s-orbital. These were in line with the study on Ru(H_2O) on {0001} surface by Michaelides [Michaelides et al. 2003] All these findings suggested that the water molecules adsorb through Van der Waals forces on the surface.

5.3 $PtSb_2$ OH^- geometries, adsorption energies and population charges

In this section we investigated the adsorption of hydroxide (OH^-) molecules on the $PtSb_2$ (100), (110) and (111) surfaces. This will give more insights in flotation of minerals

mostly adsorbed with hydroxide at elevated pH. We will compute the adsorption energies to examine the strength of hydroxide on the mineral surfaces. This will give clarity if the hydroxides have strong affinities with the mineral compared to the xanthate collectors, a case that determines better flotation. The bonding geometries will also be analysed. We also give the electronic properties (Mulliken population charges) for the hydroxide adsorption on the $PtSb_2$ (100), (110) and (111) surfaces. These properties will give insights into the chemistry bonding of the hydroxide molecule on the surfaces. Moreover, the electron accepting and donation characters of the surface and oxygen of the hydroxide molecule will be analysed.

5.3.1 OH^- adsorption on $PtSb_2$ (100) surface

The OH^- was adsorbed through oxygen on top of a surface Pt and Sb atoms as shown in Figure 5.11, which also presents the optimised output geometry for these systems. The calculated adsorption energy of –443.84 kJ/mol was obtained for Pt–OH adsorptions, while the adsorption on Sb atom gave –516.25 kJ/mol (Table 5.7). This suggested that the OH^- has stronger affinity with Sb atoms than Pt aoms. The complete surface coverage in Figure 5.11(e) and the computed adsorption energy was obtained as –576.65 kJ/mol per OH^- molecule (Table 5.7) indicating strong adsorption of OH^- with the surface at multiple adsorptions.

The Mulliken atomic population charges for the adsorption of OH^- on the (100) surface were analysed as shown in Table 5.8, which also shows the occupancy of the s-p-d-orbitals. We found that the Sb and Pt atoms adopt more positive charge and less negative charge, suggesting charge loss.

Table 5.7: The adsorption energies of OH^- molecule adsorption on $PtSb_2$ (100) surface, calculated according to equation 2.15.

Site	Adsorbate	n_{OH}	$[S+A]^0$ (eV)	$[A]^-$ (eV)	$[S]^0$ (eV)	$\Phi_{[S+A]0}$ (eV)	Total $E_{ads.}$ ($kJ.mol^{-1}$)	$E_{ads.}$ per OH^- ($kJ.mol^{-1}$)
Pt	HO^-	1	–41318.802	–451.647	–40867.023	4.467	–443.84	–
Sb	HO^-	1	–41319.711	–451.647	–40867.023	4.309	–516.25	–
Full	HO^-	16	–48108.066	–7226.352	–40867.023	5.058	–9226.36	–576.65

The hydroxide oxygen atom was found to adopt less negative charge, while the hydrogen atom adopted less positive charges, suggesting charge loss and gain, respectively. The Sb

atom clearly showed that both 5s-orbital and 5p-orbitals were depleted, while for the Pt atom all orbitals were depleted with the oxygen of OH^- 2p-orbital depleted. This may imply that the oxygen has transferred charges into the H 1s-orbital from the O 2p-orbital, while the Sb and Pt atoms formed a back-donation covalent bond through the s-p-orbital and p-d-orbital with the oxygen 2p-orbital atom, respectively.

Table 5.8: **A**tomic population (Mulliken) charges of OH^- molecule adsorption on $PtSb_2$ (100) surface.

			Mulliken population charges				
Adsorption	**Atom**	**Adsorptions state**	**s**	**p**	**d**	**Total**	**Charge (e^-)**
Sb–OH	Sb	Before adsorption	1.84	2.95	0.00	4.79	+0.20|e^-|
		After adsorption	1.71	2.61	0.00	4.31	+0.69|e^-|
	O	Before adsorption	1.93	5.50	0.00	7.43	–1.43|e^-|
		After adsorption	1.90	4.98	0.00	6.88	–0.88|e^-|
	H	Before adsorption	0.57	0.00	0.00	0.57	+0.43|e^-|
		After adsorption	0.59	0.00	0.00	0.59	+0.41|e^-|
Pt–OH	Pt	Before adsorption	1.00	0.85	9.08	10.97	–0.97|e^-|
		After adsorption	0.90	0.94	8.88	10.72	–0.72|e^-|
	O	Before adsorption	1.93	5.50	0.00	7.43	–1.43|e^-|
		After adsorption	1.89	4.87	0.00	6.76	–0.76|e^-|
	H	Before adsorption	0.57	0.00	0.00	0.57	+0.43|e^-|
		After adsorption	0.65	0.00	0.00	0.65	+0.35|e^-|

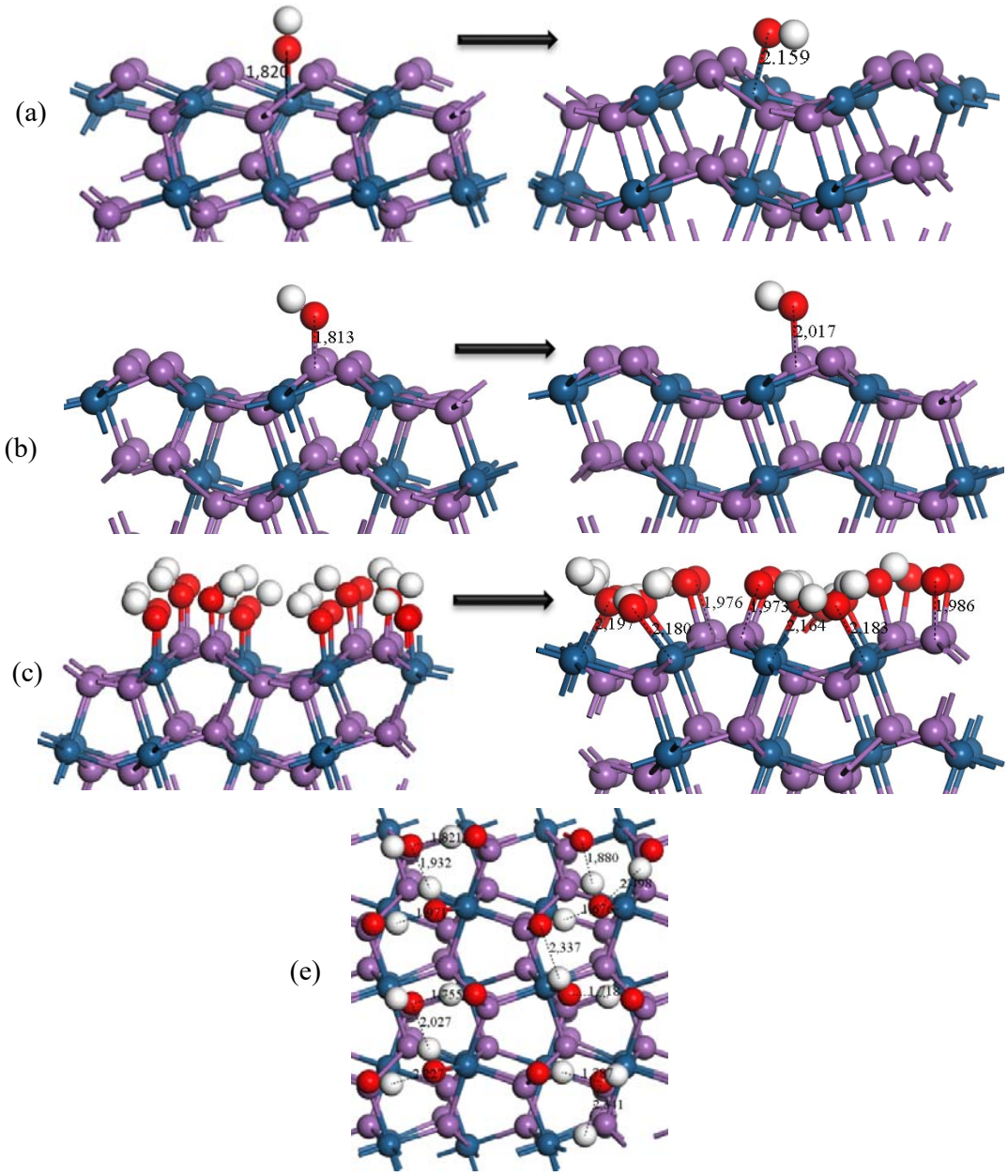

Figure 5.11: The side view of Pt-top site and Sb-top adsorption sites of the hydroxide molecule on the $PtSb_2$ (100) surface.

5.3.2 OH^- adsorption on $PtSb_2$ (110) surface

The (110) surface had different coordinated Sb atoms and as such all these sites interactions with OH^- were investigated as shown in Figure 5.12, which also presents the optimised output geometry for these systems. We observed that the adsorption of OH^- on

Pt resulted in slightly longer bond length than for OH^- on Sb atoms, with the Sb2–OH^- = 2.025 Å bond length being the shortest. The calculated adsorption energy of –497.24 kJ/mol was obtained for Sb2–OH which was weaker than for Sb3–OH (–529.55 kJ/mol). The adsorption energies for Pt–OH were weaker on both cases for Pt1 and Pt2 atoms than for Sb–OH, giving –504.33 kJ/mol and –466.84 kJ/mol, respectively. This showed that the hydroxide adsorbed preferentially on Sb atoms than on Pt atoms. The complete surface coverage computed adsorption energy was obtained as –541.98 kJ/mol per OH^- molecule as shown in Table 5.9.

Table 5.9: The adsorption energies of OH^- molecule adsorption on $PtSb_2$ (110) surface, calculated according to equation 2.15.

Site	Adsorbate	n_{OH}	$[S+A]^0$ (eV)	$[A]^-$ (eV)	$[S]^0$ (eV)	$\Phi_{[S+A]0}$ (eV)	Total $E_{ads.}$ (kJ.mol^{-1})	$E_{ads.}$ per OH^- (kJ.mol^{-1})
Pt1	HO^-	1	–49481.125	–451.647	–49028.608	4.357	–504.33	–
Pt2	HO^-	1	–49480.765	–451.647	–49028.608	4.328	–466.84	–
Sb2	HO^-	1	–49481.189	–451.647	–49028.608	4.220	–497.24	–
Sb3	HO^-	1	–49481.587	–451.647	–49028.608	4.156	–529.55	–
Full	HO^-	20	–58080.745	–9032.933	–49028.608	4.657	–10839.5	–541.98

Table 5.10: Atomic population (Mulliken) charges of OH^- molecule adsorption on $PtSb_2$ (110) surface.

			Mulliken population charges (|e|)				
Adsorption	**Atom**	**Adsorptions state**	**s**	**p**	**d**	**Total**	**Charge**
Pt1–OH	Pt1	Before adsorption	0.99	0.70	9.09	10.78	–0.78|e⁻|
		After adsorption	0.90	0.76	8.87	10.53	–0.53|e⁻|
	O	Before adsorption	1.93	5.50	0.00	7.43	–1.43|e⁻|
		After adsorption	1.89	4.87	0.00	6.75	–0.75|e⁻|
	H	Before adsorption	0.57	0.00	0.00	0.57	+0.43|e⁻|
		After adsorption	0.63	0.00	0.00	0.63	+0.37|e⁻|
Pt2–OH	Pt2	Before adsorption	0.96	0.70	9.11	10.77	–0.77|e⁻|
		After adsorption	1.89	0.78	8.89	10.55	–0.55|e⁻|
	O	Before adsorption	1.93	5.50	0.00	7.43	–1.43|e⁻|
		After adsorption	1.89	4.88	0.00	6.77	–0.77|e⁻|
	H	Before adsorption	0.57	0.00	0.00	0.57	+0.43|e⁻|
		After adsorption	0.61	0.00	0.00	0.61	+0.39|e⁻|
Sb2–OH	Sb2	Before adsorption	1.90	3.04	0.00	4.94	+0.06|e⁻|
		After adsorption	1.78	2.64	0.00	4.42	+0.58|e⁻|
	O	Before adsorption	1.93	5.50	0.00	7.43	–1.43|e⁻|
		After adsorption	1.90	4.99	0.00	6.88	–0.88|e⁻|
	H	Before adsorption	0.57	0.00	0.00	0.57	+0.43|e⁻|
		After adsorption	0.56	0.00	0.00	0.56	+0.44|e⁻|
Sb3–OH	Sb3	Before adsorption	1.85	2.95	0.00	4.80	+0.20|e|
		After adsorption	1.70	2.59	0.00	4.29	+0.71|e⁻|
	O	Before adsorption	1.93	5.50	0.00	7.43	–1.43|e⁻|
		After adsorption	1.89	5.00	0.00	6.89	–0.89|e⁻|
	H	Before adsorption	0.57	0.00	0.00	0.57	+0.43|e⁻|

After adsorption	0.59	0.00	0.00	0.59	+0.41|e⁻|

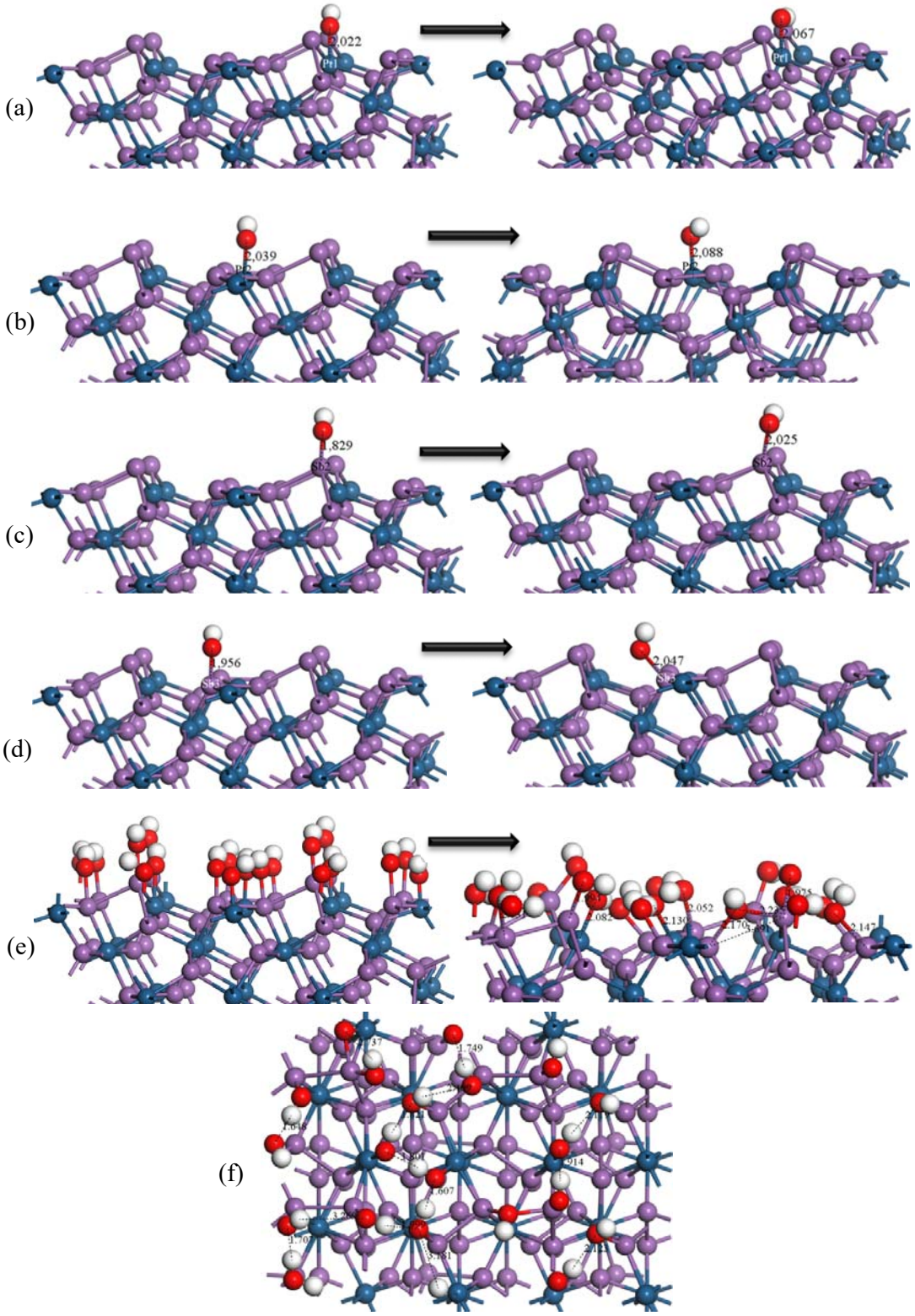

Figure 5.12: The side view and top view of Pt-top site and Sb-top adsorption sites of the hydroxide molecule on the $PtSb_2$ (110) surface.

The Mulliken atomic population charges for the adsorption of OH^- on the (110) surface were analysed as shown in Table 5.10. We found that both the Sb and Pt atoms adopted more positive charge and less negative charge, suggesting charge loss. The hydroxide oxygen atoms was found to adopt less negative charge, while the hydrogen atoms adopted less positive charges, suggesting charge loss and gain, respectively. The Pt1 atom was found to have charge depletion in the 6s-orbital and 5d-orbital, with charge accumulation in the 5p-orbital, which suggested that there was a transfer of charge to the lower-lying region of the 5p-orbital manifold. The Pt2 atoms were different, where only the 5d-orbital was depleted, with charge accumulation in the 6s-orbital and 5p-orbital, which also showed that there was a transfer of charge to the lower-lying region of the s-p-orbital manifold. The Sb2 and Sb3 atoms clearly showed that both 5s-orbital and 5p-orbitals were depleted, while only the oxygen of OH^- 2p-orbital was depleted. This may imply that the oxygen atom had transferred charges into the H 1s-orbital from the 2p-orbital, while the Sb and Pt atoms formed a back-donation covalent bond with the oxygen 2p-orbital. Furthermore, we noted a greater charge loss on OH^- oxygen atom for the Sb3-OH adsorption, which showed that this adsorption was stronger and was in line with the adsorption energy (–289.99 kJ/mol).

5.3.3 OH^- adsorption on $PtSb_2$ (111) surface

In the case of (111) surface we also tested all the different coordinated Sb and Pt atoms on their interactions with OH^- molecule as shown in Figure 5.13, which also presents the relaxed output geometry for these systems. We observed that the adsorption of OH^- on both Pt1 and Pt2 resulted in migration of OH^- to Sb atoms, where the ^-OH migrated from Pt1 to Sb3 atoms and from Pt2 to Sb2 atoms. A similar behaviour was perceived on the (100) surface. This indicated that these Pt atoms have poor interactions with OH^- molecule. In addition, since the 4-coordinated Pt on (110) surface interacted with OH^-, it showed that the 5,6-coordinated Pt atoms had poor interaction as perceived on (100) and (111) surface. The Sb2–OH bond which resulted from the migration of OH^- from Pt2 gave the shortest bond length (2.027 Å) as shown in Figure 5.13b. Furthermore, after surface relaxation we observed that there were new bonds formed between the surface Sb atoms. These are shown in Figure 5.13b and 5.13c, where Sb2–Sb3 and Sb3–Sb3 bonds were formed.

Table 5.11: The adsorption energies of OH^- molecule adsorption on $PtSb_2$ (111) surface, calculated according to equation 2.15.

Site	Adsorbate	n_{OH}	$[S+A]^0$ (eV)	$[A]^-$ (eV)	$[S]^0$ (eV)	$\Phi_{[S+A]0}$ (eV)	Total $E_{ads.}$ (kJ.mol^{-1})	$E_{ads.}$ per OH (kJ.mol^{-1})
Pt1	OH^-	1	–49470.985	–451.647	–49015.288	4.212	–797.18	–
Pt2	OH^-	1	–49472.021	–451.647	–49015.288	4.216	–897.51	–
Sb2	OH^-	1	–49472.333	–451.647	–49015.288	4.238	–929.75	–
Sb3	OH^-	1	–49472.517	–451.647	–49015.288	4.209	–944.72	–
Sb3(D)	OH^-	1	–49467.497	–451.647	–49015.288	4.249	–464.18	–
Full	OH^-	26	–60796.721	–11742.81	–49015.288	4.521	–15167.7	–579.53

In Table 5.11, the calculated adsorption energy of –929.75 kJ/mol was obtained for Sb2–OH, which was weaker than for Sb3–OH (–944.72 kJ/mol). The adsorption on Sb3(D) was very weak and gave –464.18 kJ/mol. Note that for Pt1 and Pt2 adsorption cases the OH^- migrated to Sb atoms (see Figure 5.13). The adsorption energies for Pt–OH^- were weaker on both cases for Pt1 and Pt2 atoms than for Sb–OH, giving –797.18 kJ/mol and –897.51 kJ/mol, respectively. The complete surface coverage showed similar behaviour where the Pt had weaker interaction with the OH^- molecules, where only one Pt1 atom bonded with OH^- molecule, while the other OH^- migrate to bond with Sb atoms (see Figure 5.14a). The computed adsorption energy for the full-coverage was obtained as –579.53 kJ/mol per OH^- molecule, suggesting that the adsorption energy for OH^- on (111) surface was best described through multi OH^-adsorption.

The Mulliken atomic population charges for the adsorption of OH^-on the (111) surface were analysed as shown in Table 5.12, which also shows the occupancy of the s-p-d-orbitals. Note that all Pt adsorptions resulted in migration of OH^- to Sb atoms. We found that all Sb atoms adopted more positive charge, suggesting charge loss. The hydroxide oxygen atoms were found to adopt less negative charge, while the hydrogen atoms adopted less positive charges, suggesting charge loss and gain, respectively. The Sb3 atom adsorption after migration from Pt1 was found to have charge depletion in the 5p-orbital, with charge accumulation in the 5s-orbital, which suggested that there was a

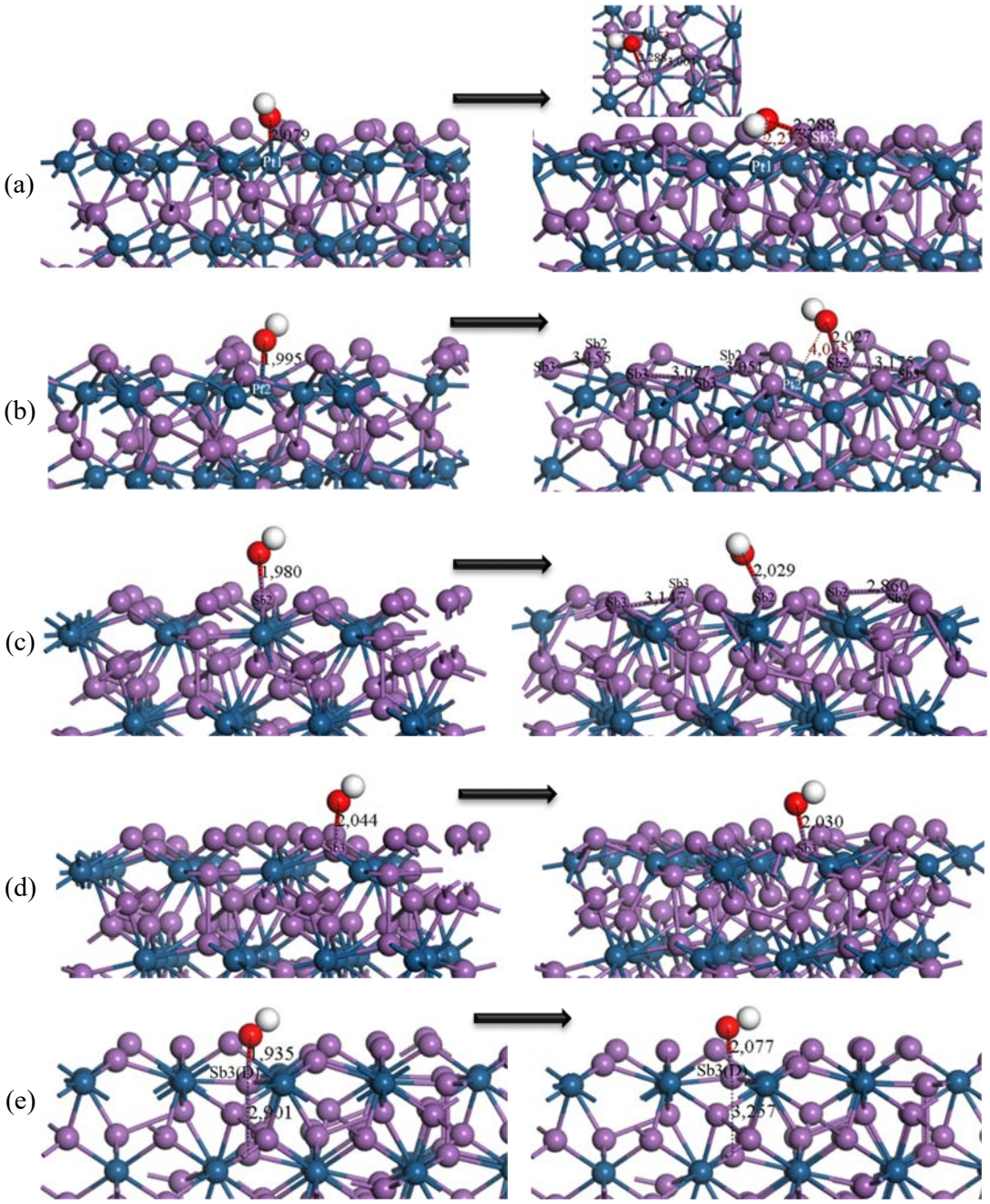

Figure 5.13: The side view of Pt-top site and Sb-top adsorption sites of the hydroxide molecule on the $PtSb_2$ (111) surface.

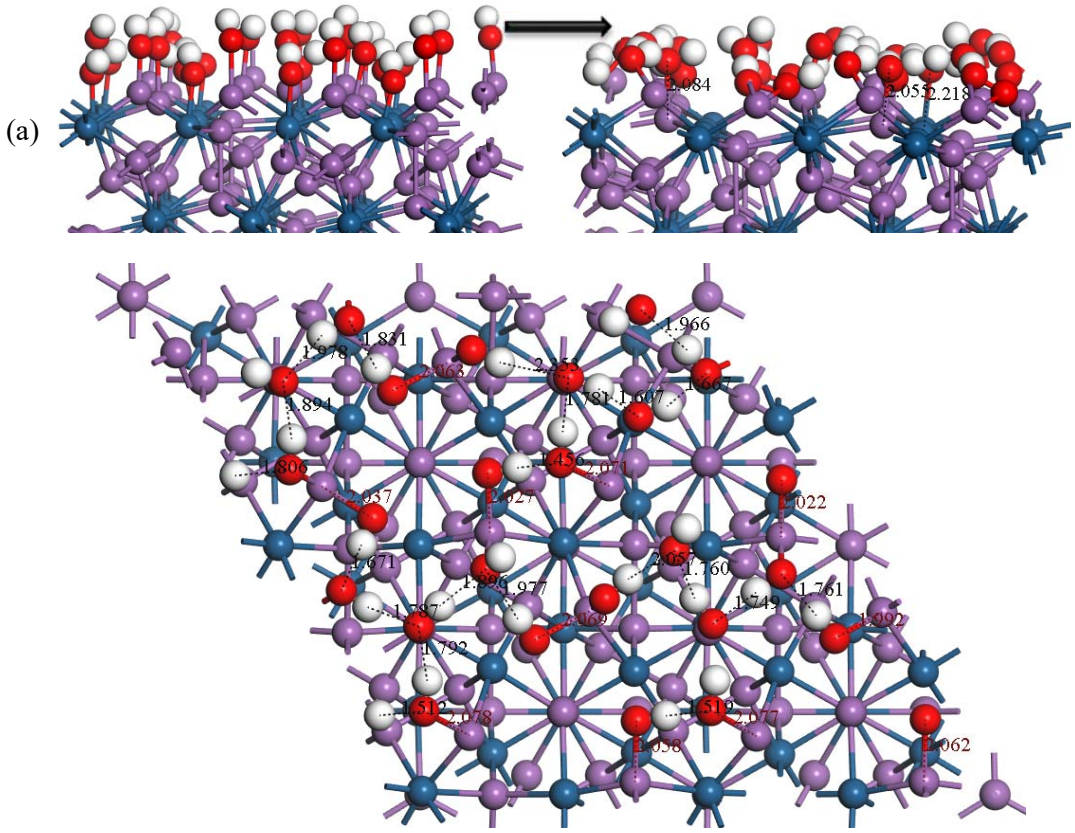

Figure 5.14: Full coverage adsorption of OH^- on the $PtSb_2$ (111) surface: (a) Side view and (b) Top view after relaxation.

transfer of charge to the lower-lying region of the 5s-orbital manifold. The Sb2 atoms adsorption after migration from Pt2 was different, where the 5p-orbital was depleted, with only 0.01|e^-| charge accumulation in the 6s-orbital, which also showed that there was a transfer of charge to the lower-lying region of the 5s-orbital manifold. The Sb2 atom was observed to have only the 5p-orbital losing charges, while the 5s-orbital remained unchanged. The Sb3 atom clearly showed that both 5s-orbital and 5p-orbitals lost charges. Since the oxygen of OH^- lost charges, with charge gain on H atom, it may imply that the oxygen had transferred charges into the H 1s-orbital from the O 2p-orbital. The Sb atoms were viewed to have formed a back-donation covalent bond with the oxygen 2p-orbital atom

Table 5.12: Atomic population (Mulliken) charges of OH^- molecule adsorption on $PtSb_2$ (111) surface.

			Mulliken population charges (|e|)				
Adsorption	**Atom**	**Adsorptions state**	**s**	**p**	**d**	**Total**	**Charge**
Pt1–OH	Sb3	Before adsorption	1.78	2.91	0.00	4.69	+0.31|e⁻|
		After adsorption	1.87	2.66	0.00	4.53	+0.47|e⁻|
	O	Before adsorption	1.93	5.50	0.00	7.43	–1.43|e⁻|
		After adsorption	1.89	4.88	0.00	6.77	–0.77|e⁻|
	H	Before adsorption	0.57	0.00	0.00	0.57	+0.43|e⁻|
		After adsorption	0.62	0.00	0.00	0.62	+0.38|e⁻|
Pt2–OH	Sb2	Before adsorption	1.78	2.91	0.00	4.70	+0.30|e⁻|
		After adsorption	1.79	2.50	0.00	4.29	+0.71|e⁻|
	O	Before adsorption	1.93	5.50	0.00	7.43	–1.43|e⁻|
		After adsorption	1.89	4.98	0.00	6.87	–0.87|e⁻|
	H	Before adsorption	0.57	0.00	0.00	0.57	+0.43|e⁻|
		After adsorption	0.57	0.00	0.00	0.57	+0.43|e⁻|
Sb2–OH	Sb2	Before adsorption	1.78	2.91	0.00	4.70	+0.30|e⁻|
		After adsorption	1.78	2.46	0.00	0.00	+0.77|e⁻|
	O	Before adsorption	1.93	5.50	0.00	7.43	–1.43|e⁻|
		After adsorption	1.89	4.98	0.00	6.87	–0.87|e⁻|
	H	Before adsorption	0.57	0.00	0.00	0.57	+0.43|e⁻|
		After adsorption	0.58	0.00	0.00	0.58	+0.42|e⁻|
Sb3–OH	Sb3	Before adsorption	1.78	2.91	0.00	4.69	+0.31|e⁻|
		After adsorption	1.71	2.55	0.00	4.26	+0.74|e⁻|
	O	Before adsorption	1.93	5.50	0.00	7.43	–1.43|e⁻|
		After adsorption	1.89	4.98	0.00	6.87	–0.87|e⁻|
	H	Before adsorption	0.57	0.00	0.00	0.57	+0.43|e⁻|
		After adsorption	0.58	0.00	0.00	0.58	+0.42|e⁻|
Sb3(D)–OH	Sb3(D)	Before adsorption	1.62	2.93	0.00	4.55	+0.45|e⁻|
		After adsorption	1.51	2.63	0.00	4.15	+0.85|e⁻|
	O	Before adsorption	1.93	5.50	0.00	7.43	–1.43|e⁻|
		After adsorption	1.89	4.98	0.00	6.87	–0.87|e⁻|
	H	Before adsorption	0.57	0.00	0.00	0.57	+0.43|e⁻|
		After adsorption	0.60	0.00	0.00	0.60	+0.40|e⁻|

5.4 Summary

We have investigated the adsorption of water and hydroxide molecule/s on the three $PtSb_2$ mineral surfaces (100), (110) and (111). For the adsorption of H_2O we observed that the water molecules did not form bonds on the surface. Interestingly, for multi adsorption we observed that the water interacted on the surface through van der Waals' forces, where the H interacted with the neighbouring O atom of the water molecules. For (100) surface we found that the H_2O–Pt was exothermic, while the H_2O–Sb was endothermic for 1-4/8 H_2O/Sb and showed exothermic adsorption from 5-8/8 H_2O/Sb. The full-coverage on the surface gave stronger adsorption of –38.19 kJ/mol per H_2O molecule. Interestingly, 8/8 H_2O/Sb showed much stronger exothermic adsorption than the 8/8 H_2O/Pt. The case of

(110) surface showed strong adsorption of H_2O on Pt than on Sb atoms, with the Sb2 being the weakest. The full-coverage gave –35.00 kJ/mol per H_2O molecule, which was slightly weaker than on (100) surface. The adsorption of single water adsorption on (111) surface showed stronger adsorption on Sb3 and weaker on Sb2. We found that for full-monolayer on Sb2 (–57.99 kJ/mol per H_2O) gave a strong adsorption than for Pt1 and Sb3-full-monolayer. Furthermore, the full-monolayer adsorption on Sb2 and Sb3 gave even stronger adsorption (–55.54 kJ/mol per H_2O). A strong interaction of the water molecules with the mineral surface is an indication of a hydrophilic reaction. The full-coverage on the surface (i.e. on Pt1 and all Sb atoms) gave adsorption energy of –54.95 kJ/mol per H_2O molecule.

The adsorption of hydroxide on the surfaces showed stronger affinity than the water molecules. This suggested that OH^- would bind preferentially over the water molecules. We found that the OH^- was preferred more on the Sb atoms for the (100) surface, with a greater adsorption energy of –576.65 kJ/mol per OH^- for full-coverage. The (110) surface was observed to give the order of Sb3 > Sb2 > Pt1 > Pt2, which showed strong adsorption on Sb3 atoms. An adsorption energy of –541.98 kJ/mol per OH molecule (deleted) was found for full-coverage. The (111) surface also displayed a strong exothermic adsorption for Sb3 atom and the order followed as: Sb3 > Sb2 > Pt2 > Pt1 > Sb3(D). The surface full-coverage gave adsorption energy of –579.53 kJ/mol per OH molecule.(deleted)

The atomic charges of both hydration and hydroxide adsorption showed that there was charge depletion on both Pt/Sb and O atoms of the H_2O and OH^-. This had shown that there was a charge transfer into other regions of the orbitals.

CHAPTER 6

Adsorption of Xanthates Collectors on $PtSb_2$ Surfaces

In this chapter, we investigated the adsorption geometries of the xanthates collectors of different chain lengths (C_2, C_3, C_4 and C_5) on the three surfaces ((100), (110) and (111)) of the $PtSb_2$. The thiol collectors are important during flotation for maximum extraction of the concentrate mineral, and their abilities render the mineral of interest become hydrophobic. We began by examining the molecular geometries in isolation to gain understanding on how these collectors might behave prior to adsorption. We then adsorbed these collectors on the surfaces and examined their bonding behaviours in terms of bond length and bond angles. The adsorption orientation of these organic compounds was critical, since they determined how the molecule would relax on the surface. The vertical orientation allowed easy interaction of the sulphur atoms with the metals, while the hydrocarbon chain facilitates attachment to the air bubble during flotation. More importantly, these interactions suggested ways in which the collectors render the $PtSb_2$ (geversite) mineral hydrophobic, an important factor during flotation.

6.1 Xanthates adsorption geometries and energies

The Thiol collectors are generally used to enhance mineral recovery in mineral processing, since they render hydrophobicity to the desired minerals. In order to understand the process of mineral recovery we considered adsorption of the xanthates organic collectors on the three surfaces, the thiol collectors considered for the study are $C_2H_5OCS_2$ (EX), $C_3H_7OCS_2$ (nPX), $C_4H_9OCS_2$ (nBX), $C_5H_{11}OCS_2$ and (AX). The use of these surfactants will also give an understanding on the effect of the thiol collector chain length when adsorbed on $PtSb_2$ minerals and more importantly, the preferential adsorption site.

6.1.1 Molecular geometry of organic collectors

The collectors were first optimized employing ultrasoft pseudopotential, cut-off energy and other precision parameters as in the surface system, with k-points parameters at gama point (1x1x1). Each molecule (EX, nPX, nBX and AX) was placed in a cubic cell of 25 Å. The optimized collector geometries are shown in Figure 6.1 and their geometric parameters for the head group are given in Table 6.1. The bond lengths for EX were in

good agreement with the available experimental values reported in previous study [Winter, 1980].

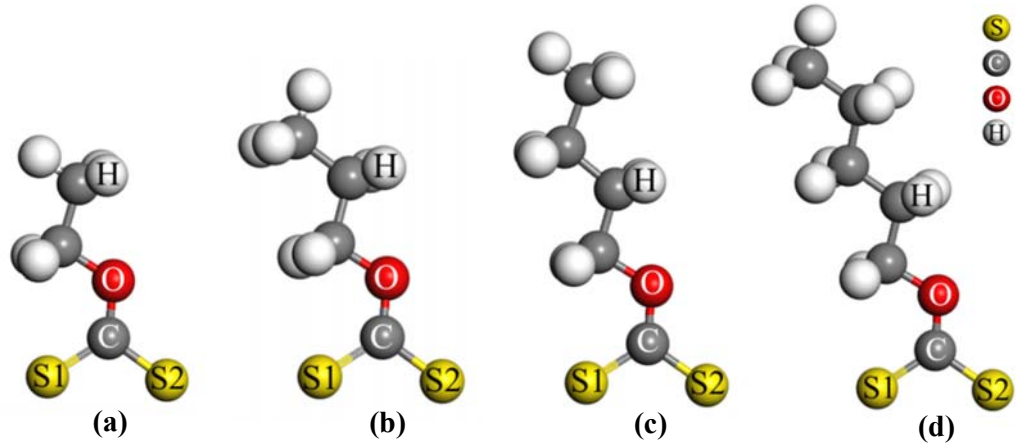

Figure 6.1: Relaxed molecular geometries of organic collectors: (a) ethyl xanthate (EX^-), (b) normal propyl xanthate (nPX^-), (c) normal butyl xanthate (nBX^-) and (d) amyl xanthate (AX^-).

The xanthate collectors were characterised by head group (S_2CO), and are different depending on the chain length of hydrocarbon. Note that we described the selected parameters (bond length and bond angles) for the polar head group since they contain sulphur atoms that are the centres of interaction. Table 6.1 shows that the C–S group bond distance (*R*) for EX, nPX, nBX and AX ranged at about the same bond length of 1.690 Å for double bond (C–S1) and 1.683 Å for single bond (C–S2). However, the C–S2 group bond length on nBX on the average appeared to be shorter which suggests that it was more stable than the other collectors. The differences that are realized derives from the energy landscape that the molecules have as depicted in the bar graphs Figure 6.4 and Figure 6.5. Note that the double bond on these collectors was on S1 (C=S1), with S2 possesing a negative charge. The EX^- head group bond lengths were also comparable to those of EX^- reported by Winter [Winter, 1980], where bond length and angles of C–O = 1.35 Å, C–S1 = 1.67 Å, C–S2 = 1.70 Å and S1–C–S2 = 124° were reported. Table 6.1 indicated that the selected torsion/dihedral bond angles in EX, nPX, nBX and AX molecules and were nearly 180º or 0º, which meant that the atoms in (O–C3(=S1)–$S2^-$) group lied almost in the same plane. Comparison of the current study to the study by Liu et al. (Liu et al. 2012], suggested that the planar configuration favoured formation of conjugated π– or π*–bond

Table 6.1: Calculated bond lengths (*R*, in Å), bond angles (θ, in deg.) and torsion/dihedral angle (ϕ, in deg.). The theoretical/experimental values are shown in parenthesis for comparison.

Xanthate collectors				
Bonds	**EX**	**nPX**	**nBX**	**AX**
R(C=S1)	1.692 (1.670)[a]	1.689	1.690	1.690
R(C–S2)	1.683 (1.700)[a]	1.683	1.685	1.684
R(C–O)	1.401 (1.350)[a]	1.400	1.401	1.400
θ(S1=C–S2)	128.02 (124.0)[a]	128.24	128.28	128.35
ϕ(S1=C–S2–O)	179.93	179.81	179.69	179.55
ϕ(S2–C=S1–O)	–179.94	–179.82	–179.71	–179.58

a – Experimental values of ethyl xanthate (EX^-) by Winter (1980) (Winter G., 1980).

Further geometry optimizations of the collectors were also performed with $DMol^3$ [Delley 2000] to calculate the highest occupied molecular orbital (HOMO) and lowest un-occupied molecular orbital (LUMO) energies. These were performed using GGA-PBE functional. The convergence tolerance for energy, force and displacement were $2.0x10^{-5}$ Ha, 0.004 Ha/Å and 0.005 Å, respectively. The double numerical plus polarisation (DNP) basis set with 4.4 Basis file was set using the DFT Semi-core Pseudopotentials. The atomic charges were calculated using CASTEP as discussed in the methodology, section 2.6. Table 6.2 shows the obtained results and we noted that for Mulliken charges, the S atoms have the same charges for all the collectors.

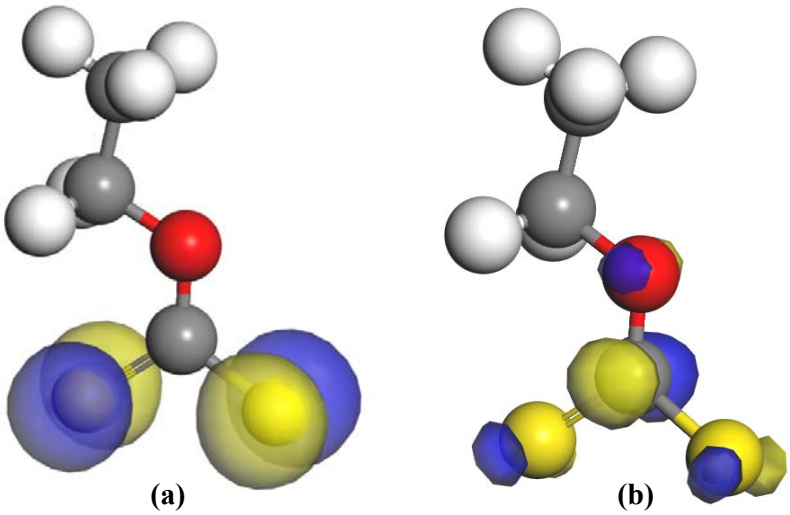

Figure 6.2: Xanthates HOMO-LUMO isosurfaces ($DMol^3$): (a) HOMO isosurfaces and (b) LUMO isosurfaces.

The HOMO and LUMO energies described the reactivity of these collectors prior to adsorption. The chemical bonds between the molecules and the surface were created by the valence electrons as such the spatial distribution of these electrons was determined by the HOMO orbital. In Figure 6.2, we showed the isosurfaces for the HOMO and LUMO orbitals. We observed that for all xanthate molecules the HOMO isosurface was concentrated on the S atoms, suggesting that electron donation could occur from these atoms. The LUMO isosurface was dominant on the C atom, indicating that electron acceptance ability was on the carbon atom.

Table 6.2. Calculated HOMO and LUMO energies and atomic population (Mulliken) charges.

	DMol^3 (eV)		Atomic charges (|e$^-$|) (CASTEP)			
Collector	**HOMO**	**LUMO**	**S1**	**S2**	**C**	**O**
EX	–5.092	–2.096	–0.37	–0.33	–0.11	–0.43
nPX	–5.049	–2.053	–0.36	–0.33	–0.11	–0.43
nBX	–5.061	–2.056	–0.36	–0.33	–0.11	–0.43
AX	–5.039	–2.043	–0.36	–0.33	–0.11	–0.43

The atomic sites with high density of the HOMO orbital can be correlated to electrophilic attacks [Merape 2010, Yekeler et al. 2004, 2006]. The behaviour of these collectors on the mineral surface, (i.e. which collector has greater electron donor and electron acceptor capacity), was predicted based on previous reports that a molecule with highest HOMO energy has the strongest ability to donate its electrons, while the molecule with the lowest LUMO energy has the strongest ability to accept electrons from the mineral surface [Wang 2000, Liu et al. 2012]. Base on this we depicted that the order of electron donating was as: AX > nPX > nBX > EX, while for electron accepting was as: EX > nBX > nPX > AX. This clearly shows that AX has a stronger capacity to donate electrons, while the EX has a stronger capacity to accept electrons. Interestingly, we noted that the electron accepting was the reverse order for electron donating. This suggested that the weakest electron donor has the strongest electron acceptor. However, these did not indicate which collector would be more reactive on the mineral surface which will be determined on the adsorption systems.

6.2 Xanthate adsorption geometries and energies

In this section, we investigated the adsorption of organic collectors on the $PtSb_2$ surfaces. Different adsorption sites were tested and the most exothermic adsorption determined by

the most negative adsorption energy for each collector, was considered as shown in Appendix E. The relaxed geometries of the collectors on the surface, their reactivity and bonding mode will also be discussed. Note that the four collectors (EX, nPX, nBX and AX) were adsorbed in order to determine the effect of chain length on xanthate adsorption on the mineral surface. The calculations were performed with the collector double bond being on the S1 atom.

6.2.1 $PtSb_2$ (100) surface xanthates adsorptions

After the adsorption of xanthates collectors onto $PtSb_2$ (100) surface, we observed that the bridging adsorption on Pt and Sb was the most exothermic and thus would be the most stable adsorption site on (100) surface. We also noted that for EX, nPX and nBX the Pt–S1 and Sb–S2 bridge bonding was preferred, while for AX the Pt–S2 and Sb–S1 bridge bonding was the most stable as shown Figure 6.3. These bonding mechanisms suggested that the xanthate collectors preferred to interact with the $PtSb_2$ mineral surface through both Pt and Sb atoms. In addition, it indicated how the xanthates render $PtSb_2$ mineral hydrophobic during flotation on (100) surface dominated mineral. Furthermore, we noted conjugation of the double bond for nBX and AX, where the double bond moved from C–S1 to C–S2, which did not occur for EX and nPX collectors.

Table 6.3: Relaxed bond lengths (*R*, in Å) and bond angles (θ, in deg.) for xanthate adsorptions onto $PtSb_2$ (100) surface.

Bonds	EX	nPX	nBX	AX
Pt–S1	2.401	2.381	2.388	–
Sb–S2	2.520	2.550	2.531	–
Pt–S2	–	–	–	2.390
Sb–S1	–	–	–	2.556
C–S1	1.686	1.689	1.689	1.722
C–S2	1.727	1.724	1.724	1.690
S1–C–S2	131.33	130.74	131.13	131.36

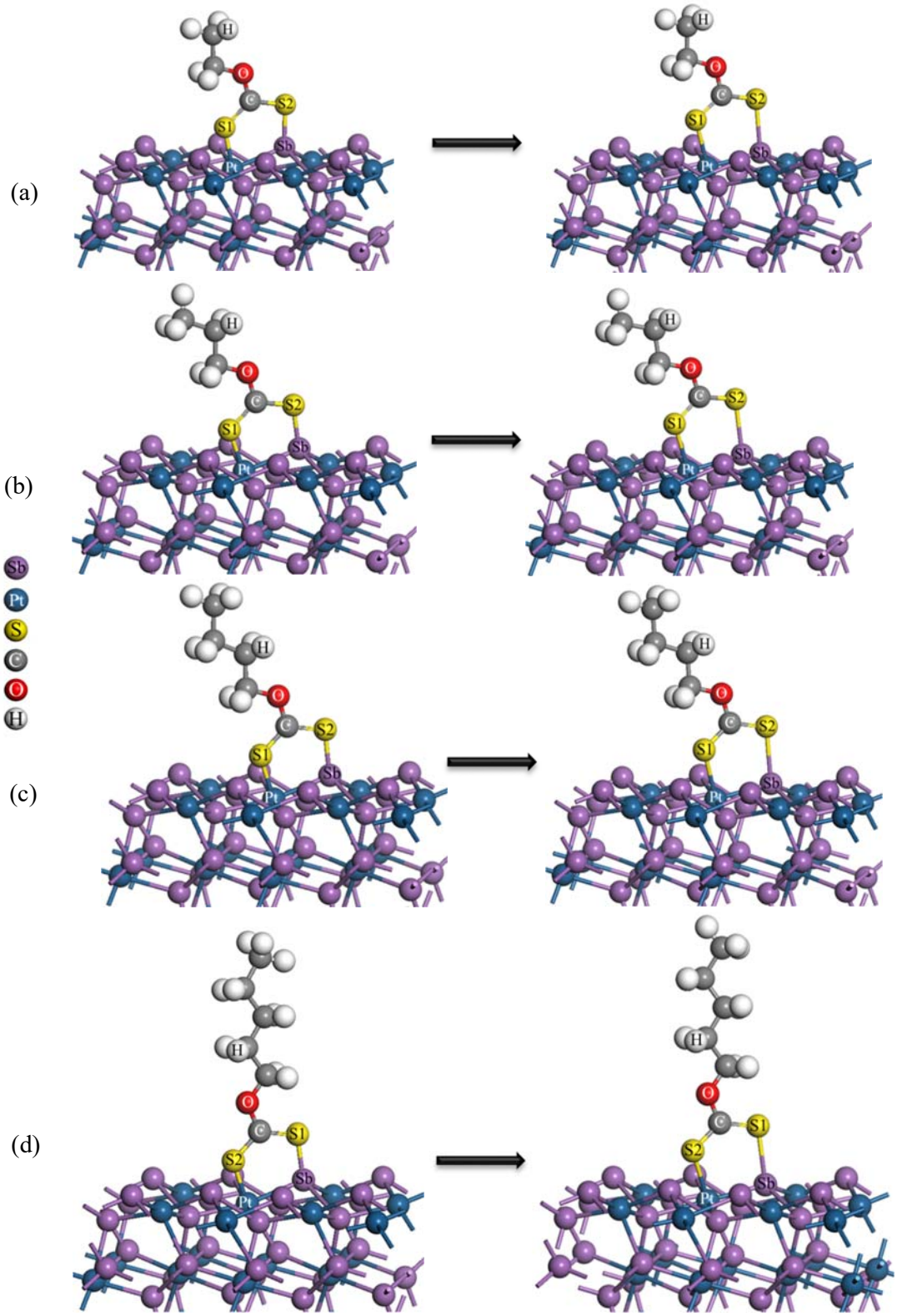

Figure 6.3: Xanthates collector adsorption onto $PtSb_2$ (100) surface after relaxation: (a) EX, (b) nPX, (c) nBX and (d) AX adsorptions.

The bond length and angles for the bonding geometries of xanthates have been computed and given in Table 6.3. We observed that the Pt–S bonds were shorter than the Sb–S bonds and in addition the C–S bond for S atom interacting with Sb atom was longer than the S atom interacting with the Pt atom. This suggested that the Sb atom had a weaker bonding with the collector than the Pt atoms. Moreover, it suggested that there could be some charge transferred into the S atoms interacting with Sb that weakens the C–S bond. This will be discussed in detail in section 6.3. The bond angles (S1–C–S2) of the collectors were also greater than the isolated collectors (±128.2°).

Table 6.4: Adsorption energies for most exothermic EX, nPX, nBX and AX collector on $PtSb_2$ (100) surface, calculated according to equation 2.15.

Adsorbate (A)	Adsorption mode	$[S+A]^0$ (eV)	$[A]^-_{corr}$ (eV)	$[S]^0$ (eV)	$\Phi_{[S+A]0}$ (eV)	$E_{ads.}$ (kJ.mol^{-1})
EX	Pt-S1, Sb-S2_N	–42405.064	–1538.634	–40867.023	3.974	–326.30
nPX	Pt-S1, Sb-S2_N	–42592.318	–1725.943	–40867.023	3.985	–322.03
nBX	Pt-S1, Sb-S2_N	–42779.622	–1913.252	–40867.023	4.016	–324.52
AX	Pt-S2, Sb-S1_N	–42967.037	–2100.552	–40867.023	3.912	–325.65

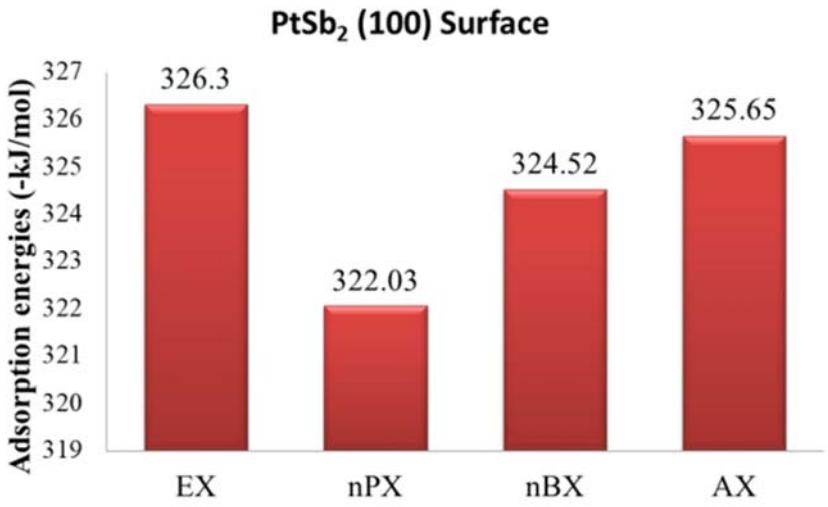

Figure 6.4: Bar graph for adsorption energies of xanthates collector adsorption onto $PtSb_2$ (100) surface.

Now the adsorption strengths for the xanthates were calculated and the adsorption energies for the most stable sites are shown in Figure 6.4 and also displayed in Table 6.4. We depicted that EX showed strong adsorption and the order followed as: EX ≈ AX > nBX > nPX. Its interesting to note that the nPX, nBX and AX are weaker than the EX,

this may imply that the presence of water may change the affinity of the collector, as it was not considered in this study. Previously, the investigation of $PtAs_2$ the (100) surface with EX was conduction, where the mono (Pt–S) and bridging (Pt–S, Pt–S) adsorptions were explored by Waterson et al. (2015) and their adsorption energies were found as –299.5 kJ/mol and –371.3 kJ/mol, respectively. It was found that the bridging was more exothermic than the mono adsorption. In comparison with our work (see Appendix E), we found that all the four xanthates for mono adsorptions are in agreement with the finding by Waterson et al. (2015). However, for bridging we found that our values were lower than those reported. These indicated that the there are similarities between $PtAs_2$ and $PtSb_2$ minerals.

6.2.2 $PtSb_2$ (110) surface xanthates adsorptions

In the case of xanthates collectors adsorption onto $PtSb_2$ (110) surface we observed that the bridging adsorption on Pt and Sb for EX adsorption and Pt-bridging was the most exothermic, hence the most stable adsorption site for (110) surface. We noted that nPX and nBX the Pt1–S1 and Pt2–S2 bridge bonding was preferred as shown Figure 6.5b and 6.5c. The case of EX and AX was different from the nPX and nBX, where the Pt1–S2 and Pt2–S1 was the most stable adsorption. These bonding mechanisms suggested that the xanthate collectors preferred to interact with the $PtSb_2$ mineral (110) surface through both Pt atoms (Pt-bridging) for EX, nPX, nBX and AX. In addition, it indicated how the xanthates float the $PtSb_2$ mineral during flotation on (110) surface liberated mineral. Furthermore, we noted conjugation of the double bond for EX and nBX, where the double bond moved from C–S1 to C–S2, which did not occur for nPX and AX collectors.

Table 6.5: Calculated bond lengths (R, in Å), bond angles (θ, in deg.) for xanthate adsorptions onto $PtSb_2$ (110) surface.

Bonds	EX	nPX	nBX	AX
Pt1–S1	–	2.432	2.392	–
Pt1–S2	2.404	–	–	2.384
Pt2–S2	–	2.368	2.383	–
Pt2–S1	2.362	–	–	2.419
C–S1	1.698	1.706	1.703	1.715
C–S2	1.717	1.712	1.714	1.707
S1–C–S2	131.41	132.74	134.58	132.91

The bond length and angles for the bonding geometries of xanthates have been computed and given in Table 6.5. We observed that the Pt2–S1 bonds were shorter than

the Pt1–S2 bonds for EX adsorption, while for nPX, nBX and AX, the Pt1–S1 was longer than for Pt2–S2 bond. The C–S1 bonds were found to be shorter than the C–S2 for EX, nPX and nBX, while for AX the opposite was depicted, where C–S2 was shorter than C–S1 bond. This suggested that the Pt–S2 bond was weaker than Pt–S1 for EX, while for nPX, nBX and AX the Pt–S1 was weaker than Pt–S2 bonds.

Table 6.6: Adsorption energies for most exothermic EX, nPX, nBX and AX collector on $PtSb_2$ (110) surface, calculated according to equation 2.15.

Adsorbate (A)	Adsorption mode	$[S+A]^0$ (eV)	$[A]^-_{corr}$ (eV)	$[S]^0$ (eV)	$\Phi_{[S+A]0}$ (eV)	$E_{ads.}$ (kJ.mol^{-1})
EX	Pt-S1, Pt-S2	–50566.864	–1538.634	–49028.608	4.124	–361.41
nPX	Pt-S1, Pt-S2	–50754.283	–1725.943	–49028.608	4.128	–372.40
nBX	Pt-S1, Pt-S2	–50941.624	–1913.252	–49028.608	4.130	–375.66
AX	Pt-S1, Pt-S2	–51128.918	–2100.552	–49028.608	4.093	–371.56

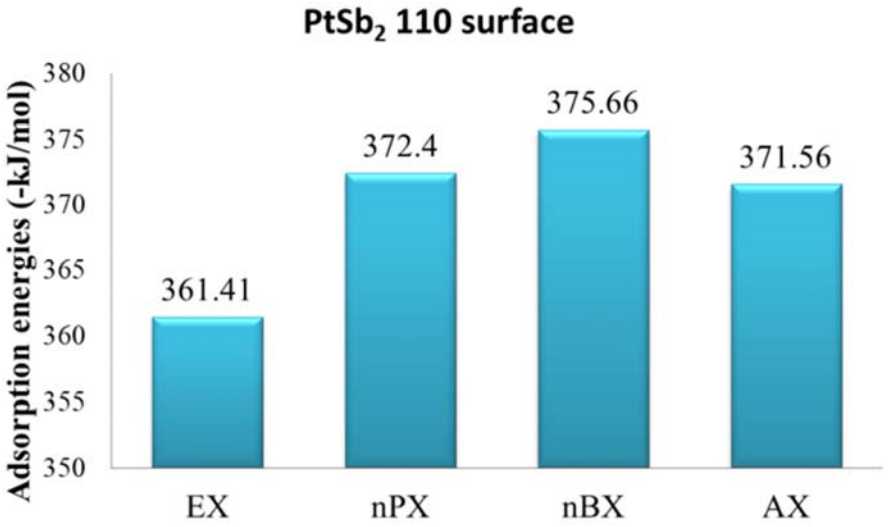

Figure 6.5: Bar graph for adsorption energies of xanthates collector adsorption onto $PtSb_2$ (110) surface.

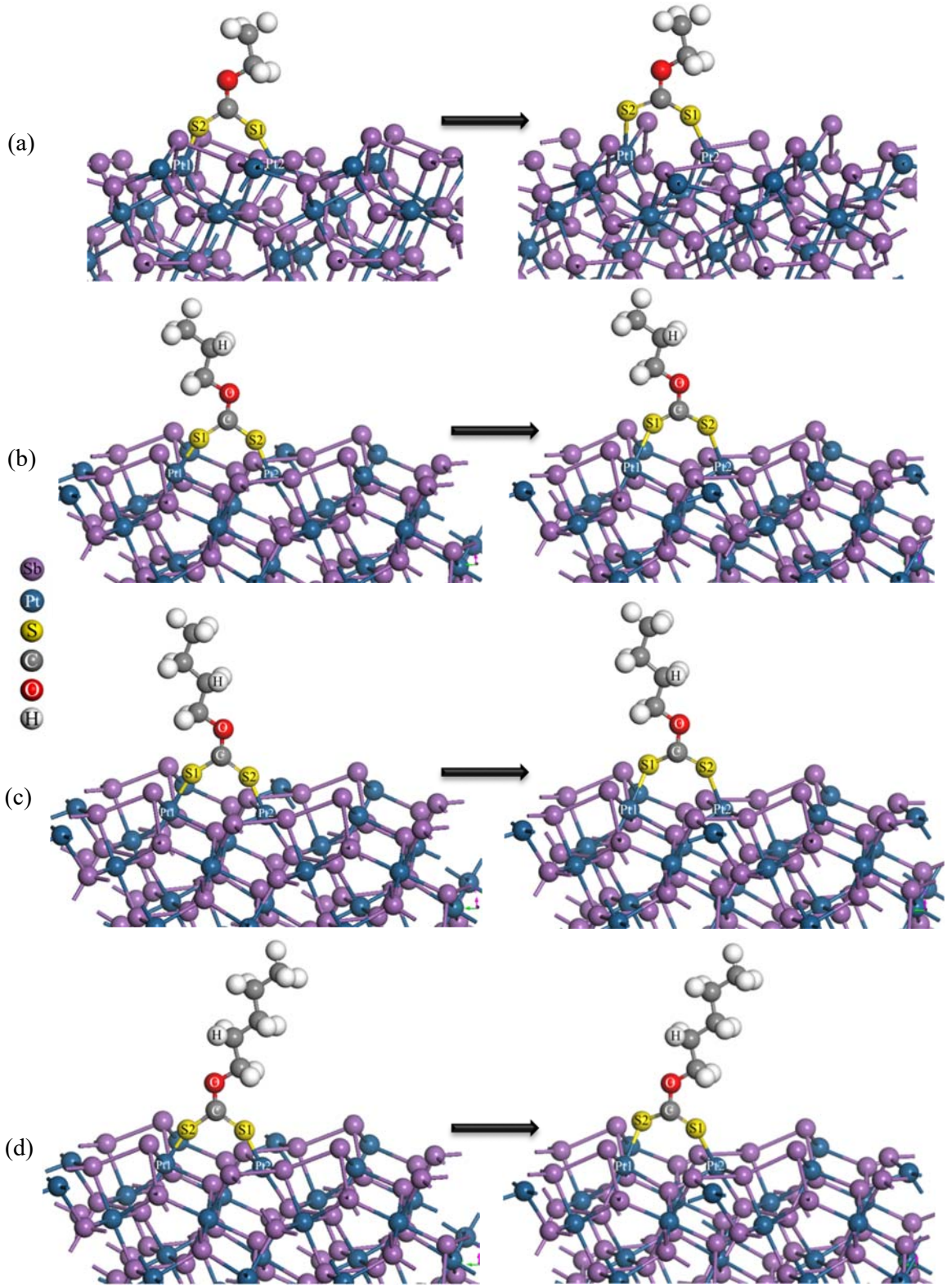

Figure 6.6: Xanthates collector adsorption onto $PtSb_2$ (110) surface after relaxation: (a) EX, (b) nPX, (c) nBX and (d) AX adsorptions.

Now the adsorption strengths for the xanthates were calculated and the adsorption energies for the most stable sites are shown in Figure 6.6 as displayed in Table 6.6. We depicted an increasing trend from EX to nBX and the order followed as: nBX > nPX ≈ AX > EX. This suggested that nBX has a stronger adsorption amongst the xanthate collectors adsorbed on $PtSb_2$ (110) surface. It is interesting to note that AX was weaker than the nPX and as such may suggest that effect of chain length may be perceived in the presence water.

6.2.3 $PtSb_2$ (111) surface xanthates adsorptions

We have also investigated the adsorption of xanthates collectors onto $PtSb_2$ (111) surface. The initial and relaxed geometries for the most stable adoptions are shown in Figure 6.8. We observed that the bridging adsorption on Sb2 and Sb3 for EX, nBX and AX was the most exothermic, while for nPX the bridge adsorption on Pt1 and Sb3 was more exothermic as shown in Figure 6.8. This indicated that these sites were the most preferred adsorption sites for the xanthate collectors on $PtSb_2$ mineral. Interestingly, we found that the Sb atoms were active and played a significant role in the flotation recovery of the $PtSb_2$ mineral. Note that for Sb2 and Sb3 bridge bonding, the xanthate S1 interacted with Sb2 atom (Sb2–S1), while the Sb3 interacted with S2 atom (Sb3–S2). The case of nPX was different, where the Pt1–S1 and Sb3–S2 was the most stable adsorption. These bonding mechanisms suggested that the xanthate collectors preferred to interact with the $PtSb_2$ mineral surface through both Pt and Sb atoms for nPX and with Sb-bridging for EX, nBX and AX. Furthermore, we noted conjugation of the double bond for nBX, where the double bond moved from C–S1 to C–S2, which did not occur for EX, nPX and AX collectors.

Table 6.7: Calculated bond lengths (*R*, in Å), bond angles (θ, in deg.) for xanthate adsorptions onto $PtSb_2$ (111) surface.

Bonds	EX	nPX	nBX	AX
Sb2–S1	2.690	–	2.750	2.753
Sb3–S2	2.526	2.551	2.521	2.511
Pt1–S1	–	2.381	–	–
C–S1	1.688	1.695	1.681	1.682
C–S2	1.721	1.715	1.728	1.727
S1–C–S2	128.85	129.54	129.59	129.56

The bond length and angles of the bonding geometries for xanthates have been computed and shown in Table 6.7. We observed that the Pt1–S1 bond was shorter than

the Sb3–S2 bond for nPX adsorption, while for EX, nBX and AX, the Sb2–S1 was longer than for Sb3–S2 bond. This was due to the twisting of the molecule as it relaxed to its preferential position. The C–S1 bonds were found to be shorter than the C–S2 for all xanthate collectors.

Table 6.8: Adsorption energies of the most stable EX, nPX, nBX and AX collector adsorbed on $PtSb_2$ (111) surface, calculated according to equation 2.15.

Adsorbate (A)	Adsorption mode	$[S+A]^0$ (eV)	$[A]^-_{corr}$ (eV)	$[S]^0$ (eV)	$\Phi_{[S+A]0}$ (eV)	$E_{ads.}$ (kJ.mol^{-1})
EX	Sb3-S2, Sb2-S1	–50557.866	–1538.634	–49015.288	4.073	–773.50
nPX	Pt5-S1, Sb3-S2	–50745.380	–1725.943	–49015.288	4.093	–795.18
nBX	Sb3-S2, Sb2-S1	–50932.639	–1913.252	–49015.288	4.084	–789.45
AX	Sb3-S2, Sb2-S1	–51119.950	–2100.552	–49015.288	4.021	–784.55

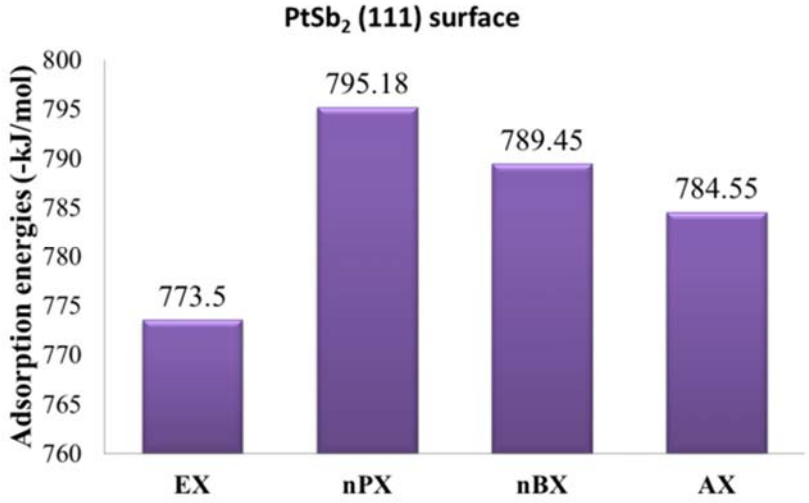

Figure 6.7: Adsorption energies for xanthates collector adsorption onto $PtSb_2$ (100) surface.

Now the adsorption strengths for the xanthates were calculated and the adsorption energies for the most stable sites are shown in Figure 6.7 as perceived in Table 6.8. The order followed as: nPX > nBX > AX > EX. This suggested that nPX has a stronger adsorption amongst the xanthate collectors adsorbed on $PtSb_2$ (111) surface. This indicated that in the absence of water the effect of chain length cannot be examined.

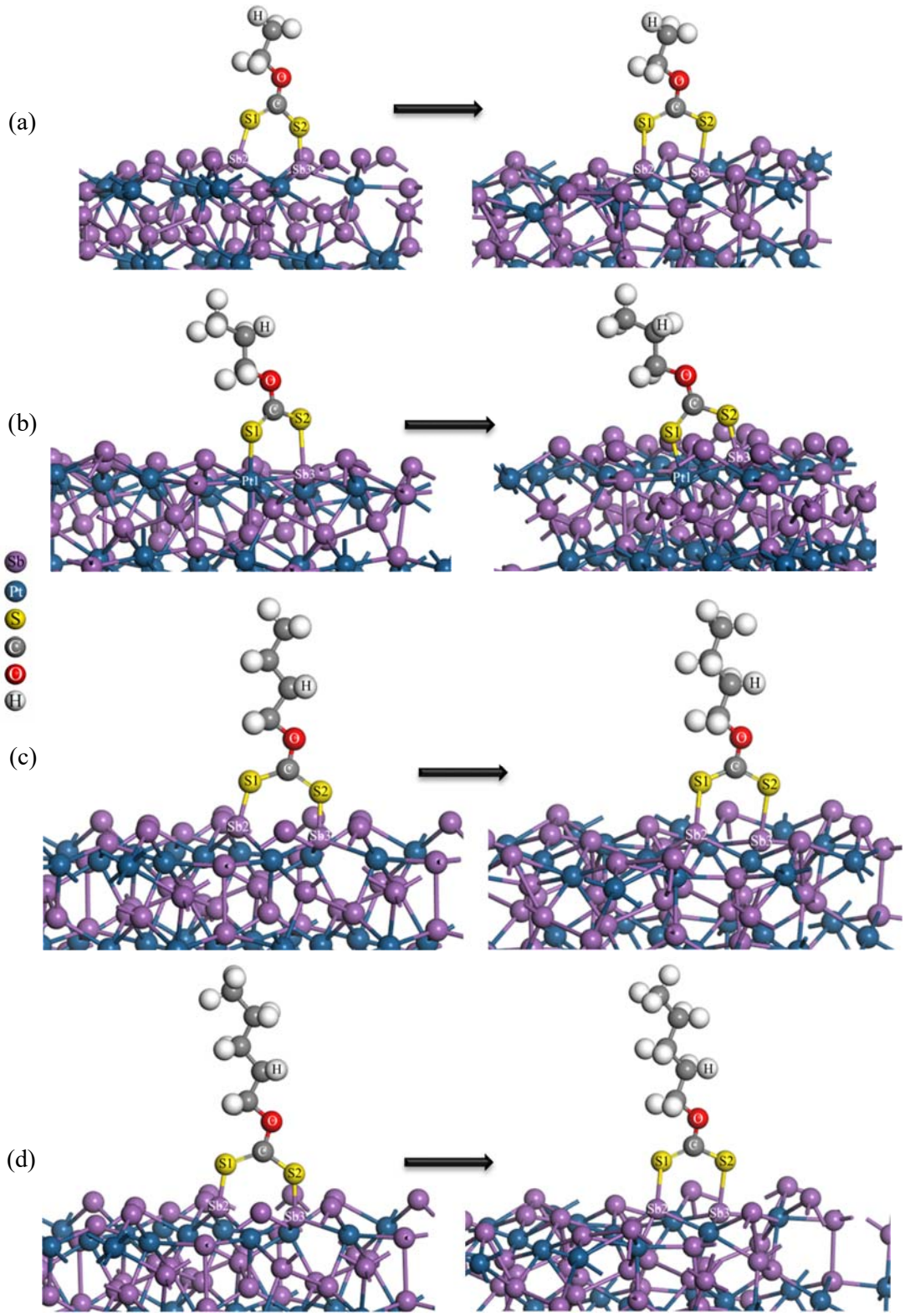

Figure 6.8: Xanthates collector adsorption on the $PtSb_2$ (111) surface before relaxation and after relaxation: (a) EX, (b) nPX, (c) nBX and (d) AX adsorptions.

6.3 Xanthates adsorption density of states and Mulliken charges

In this section we presented and analysed the electronic structures for the adsorption of xanthate collectors on the $PtSb_2$ surfaces. We focused on the exothermic adsorption sites and describe their chemistry of bonding. We have analysed the density of states (DOS) and Mulliken atomic charges. The valence electrons for the surface species considered were as: Pt [Xe]$4f^{14}5d^{9}6s^{1}$ and Sb [Kr]$4d^{10}5s^{2}5p^{3}$, and for the collectors species were: S [Ne]$3S^{2}3p^{4}$. Note that we only report for the atoms that were involved in interaction (i.e. between the surface and collector).

6.3.1 $PtSb_2$ (100) surface xanthates adsorption DOS and charges

Note that all the four collectors interacted with the surface in a similar manner and their DOS trends were similar as well. The Sb atoms interacted with S1, while the Pt interacted with S2 atoms of the xanthates. In the case of Pt interaction, we observed that the 5d-orbital (d1) peak splits into two peaks and we noted a small peak (d2) just above the E_F which was absent for clean surface (Figure 6.9a). This indicated that the Pt 5d-orbital had direct interaction with the S2 of the collector and suggested that the $6s^{1}$-orbital lost its electron and the 5d-orbital electrons depleted to the collector S 3p-orbitals. Moreover, we observed that the E_F fell deep into the pseudo-gap (pg) for S atoms, suggesting stability. Furthermore, in the case of Sb interaction, there was a shift in the E_F to the higher energy, where it fell deep into the pseudo-gap (pg1) and suggested stability. Further examinations of the peaks, showed that the d1 peak was reduced in states and split into small peaks (Figure 6.9a).

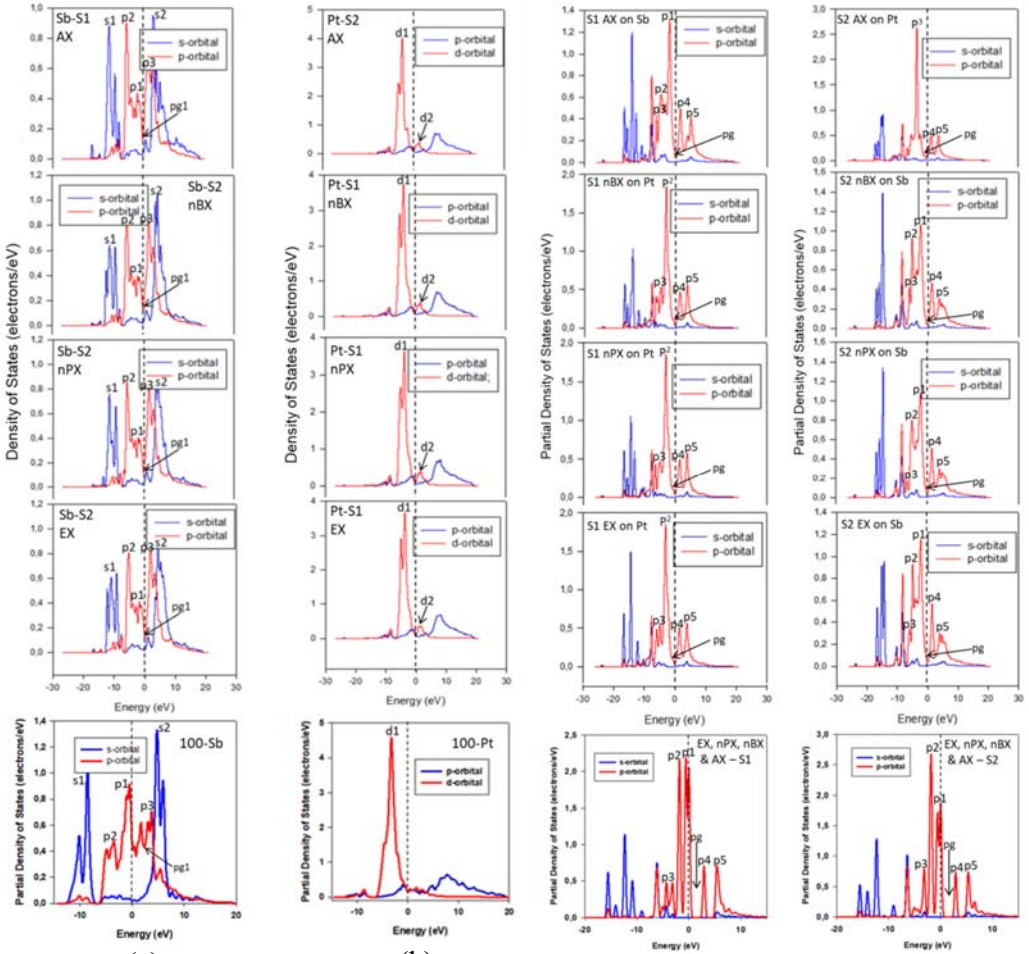

Figure 6.9: Partial density of states (PDOS) for $PtSb_2$ (100) surface adsorption: (a) and (b) Pt PDOS; and (c) and (d) xanthates S atoms PDOS, before and after adsorption.

Now, in the case of collectors, we examined the S 3p-orbital as they have direct interaction with the minerals surface (Figure 6.9b). We also observed that all collectors have similar behaviour, where the S 3p-orbital shifted down in energy as a result the E_F fell deep into the pseudo gap (pg) and suggested stability. We noted that the S1 and S2 atoms have distinct behaviour, in that those that interacted with Pt atoms behaved differently from those that interacted with Sb atom. Firstly, for S1 atom, we noted that p1 and p2 peaks merged to form p^2 peak, while for S2 atom, the p2 peak reduced states and was observed to be shorter than p1 peak. Secondly, the p5 peak on S1 remained unchanged, while for S2 atom it was reduced and split into small peaks. Furthermore, we observed that p3 peak merged with p2 peak (see Figure 6.9b). These behaviours suggested

electron gain from the mineral surface, which were examined from the Mulliken atomic charges.

Table 6.9. Calculated atomic population (Mulliken) charges of collectors on $PtSb_2$ (100) surface.

			Mulliken population charges (|e|)				
Collector	**Atom**	**Adsorptions state**	**s**	**p**	**d**	**Total**	**Charge**
EX	Pt	Before adsorption	1.00	0.85	9.08	10.97	–0.97
		After adsorption	0.94	1.08	8.97	10.99	–0.99
	Sb	Before adsorption	1.84	2.95	0.00	4.79	+0.20
		After adsorption	1.77	2.84	0.00	4.62	+0.38
	S1	Before adsorption	1.83	4.54	0.00	6.37	–0.37
		After adsorption	1.81	4.11	0.00	5.92	+0.08
	S2	Before adsorption	1.82	4.51	0.00	6.33	–0.33
		After adsorption	1.85	4.17	0.00	6.01	–0.01
nPX	Pt	Before adsorption	1.00	0.85	9.08	10.97	–0.97
		After adsorption	0.94	1.08	8.97	10.99	–0.99
	Sb	Before adsorption	1.84	2.95	0.00	4.79	+0.20
		After adsorption	1.79	2.84	0.00	4.62	+0.38
	S1	Before adsorption	1.83	4.53	0.00	6.36	–0.36
		After adsorption	1.80	4.12	0.00	5.92	+0.08
	S2	Before adsorption	1.82	4.51	0.00	6.33	–0.33
		After adsorption	1.85	4.17	0.00	6.02	–0.02
nBX	Pt	Before adsorption	1.00	0.85	9.08	10.97	–0.97
		After adsorption	0.94	1.08	8.97	10.99	–0.99
	Sb	Before adsorption	1.84	2.95	0.00	4.79	+0.20
		After adsorption	1.78	2.84	0.00	4.62	+0.38
	S1	Before adsorption	1.83	4.53	0.00	6.36	–0.36
		After adsorption	1.81	4.12	0.00	5.92	+0.08
	S2	Before adsorption	1.82	4.51	0.00	6.33	–0.33
		After adsorption	1.85	4.17	0.00	6.01	–0.01
AX	Pt	Before adsorption	1.00	0.85	9.08	10.97	–0.97
		After adsorption	0.94	1.08	8.97	10.98	–0.98
	Sb	Before adsorption	1.84	2.95	0.00	4.79	+0.20
		After adsorption	1.71	2.84	0.00	4.54	+0.46
	S1	Before adsorption	1.83	4.53	0.00	6.36	–0.36
		After adsorption	1.84	4.21	0.00	6.06	–0.06
	S2	Before adsorption	1.82	4.51	0.00	6.33	–0.33
		After adsorption	1.81	4.08	0.00	5.89	+0.11

Now, the atomic charges were compared before and after adsorption in order to examine the change (Table 6.9). We observed that Sb adopted more positive charge, while the Pt adopted more negative charge, suggesting charge depletion and charge gain, respectively. The collector S atoms were all noted to adopt less negative charges, indicating charge loss, which suggested a back donation covalent bond by Sb atoms and normal covalent bonding by S atoms to Pt atoms. As discussed in section 6.2.1, there was

a greater stretch of the C–S2 bond for EX, nPX and nBX and on C–S1 for AX, this is due to charge donation from the surface Sb into collector S atoms, which weakens the C–S bond.

6.3.2 $PtSb_2$ (110) surface xanthates adsorption DOS and charges

In the case of the (110) surface we observed that for all collectors adsorption, the Pt1 atoms d2 peak shifted to the CB just above the E_F, and was reduced, while for Pt2 had more peak states (Figure 6.10a). These suggested that the Pt donated electrons to the collector S atoms. Now, in the case of collectors, we also examine the S 3p-orbital since they have direct interaction with the minerals surface as shown in Figure 6.10b. We observed that in all collectors S atoms PDOS showed similar behaviour, where the S 3p-orbital shifted down in energy as a result the E_F fell deep into the pseudo gap (pg) and suggested stability. Further examination, we showed that for EX, the S1 and S2 had distinct behaviour, the S2 interacting with Pt1 behaved differently from the S1 interacting with Sb2. We showed that for EX, S1 and S2 PDOS, the p1 and p2 peaks merged to form p^2 peak. Furthermore, we observed that p3 peak merged with p^2 peak for all four collectors (see Figure 6.10b). These behaviours suggested electron gain from the mineral surface. Interestingly for AX, the S2 p4 peak was reduced.

Now for the case of atomic charges, we have compared the before and after adsorption in order to examine the change as shown in Table 6.10. We observed that Sb2 adopt more positive charge, while the Pt atoms adopted more negative charge. Except on Pt2 for nPX and AX, where the charge remained the same and it adopted less negative charge, respectively. This clearly showed that Sb2 lost charges, while Pt1 gained charges. For the collector S atoms, we noted that for all collector the S1 atoms adopted less negative charge (Table 6.10).

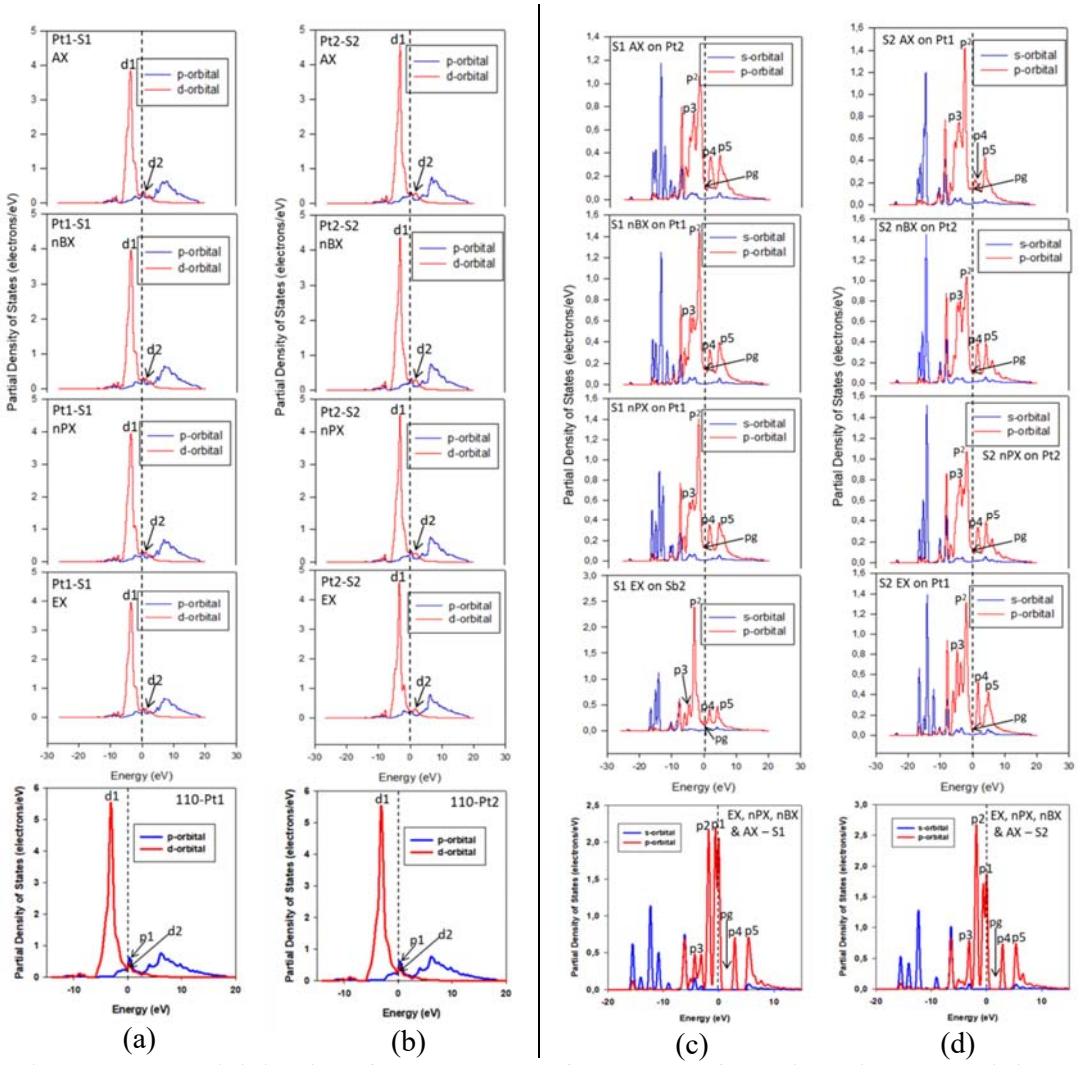

Figure 6.10: Partial density of states (PDOS) for (110) surface adsorption: (a) and (b) Pt PDOS; and (c) and (d) xanthates S atoms PDOS, before and after adsorption.

In the case of S2 atoms for all collectors, we noted that there was large charge loss, (Table 6.10). These indicated a charge loss on S atoms from the surface Pt and Sb2 atoms and also suggested a back-donation covalent bonding.

Table 6.10. Calculated atomic population (Mulliken) charges of collectors on $PtSb_2$ (110) surface.

			Mulliken population charges (|e⁻|)				
Collector	**Atom**	**Adsorptions state**	**s**	**p**	**d**	**Total**	**Charge**
EX	Pt1	Before adsorption	0.99	0.70	9.09	10.78	–0.78
		After adsorption	0.91	0.85	9.01	10.78	–0.78
	Sb2	Before adsorption	1.90	3.04	0.00	4.94	+0.06
		After adsorption	1.87	2.90	0.00	4.77	+0.23
	S1	Before adsorption	1.83	4.54	0.00	6.37	–0.37
		After adsorption	1.84	4.23	0.00	6.07	–0.07
	S2	Before adsorption	1.82	4.51	0.00	6.33	–0.33
		After adsorption	1.81	4.11	0.00	5.92	+0.08
nPX	Pt1	Before adsorption	0.99	0.70	9.09	10.78	–0.78
		After adsorption	0.92	0.86	9.01	10.79	–0.79
	Pt2	Before adsorption	0.96	0.70	9.11	10.77	–0.77
		After adsorption	0.93	0.83	9.03	10.78	–0.78
	S1	Before adsorption	1.83	4.53	0.00	6.36	–0.36
		After adsorption	1.80	4.20	0.00	6.00	+0.00
	S2	Before adsorption	1.82	4.51	0.00	6.33	–0.33
		After adsorption	1.81	4.12	0.00	5.93	+0.07
nBX	Pt1	Before adsorption	0.99	0.70	9.09	10.78	–0.78
		After adsorption	0.93	0.85	9.01	10.79	–0.79
	Pt2	Before adsorption	0.96	0.70	9.11	10.77	–0.77
		After adsorption	0.92	0.85	9.02	10.79	–0.79
	S1	Before adsorption	1.83	4.53	0.00	6.36	–0.36
		After adsorption	1.80	4.18	0.00	5.98	+0.02
	S2	Before adsorption	1.82	4.51	0.00	6.33	–0.33
		After adsorption	1.82	4.13	0.00	5.95	+0.05
AX	Pt1	Before adsorption	0.99	0.70	9.09	10.78	–0.78
		After adsorption	0.93	0.81	9.03	10.77	–0.77
	Pt2	Before adsorption	0.96	0.70	9.11	10.77	–0.77
		After adsorption	0.92	0.86	9.01	10.80	–0.80
	S1	Before adsorption	1.83	4.53	0.00	6.36	–0.36
		After adsorption	1.81	4.20	0.00	6.01	–0.01
	S2	Before adsorption	1.82	4.51	0.00	6.33	–0.33
		After adsorption	1.81	4.11	0.00	5.93	+0.07

6.3.3 $PtSb_2$ (111) surface xanthates adsorption DOS and charges

The DOS and population charges of the (111) surface were computed and analysed. Note that for this surface the nPX bridged on Pt1 and Sb3 through S1 and S2, while the EX, nBX and AX bridged on Sb2 and Sb3 through S1 and S2, respectively. We observed that for nPX adsorption, the Sb3 atoms DOS change was very interesting, where the E_F shifted to lower energy from pg1 to cut the peak at its top point, while p1 peak reduced states and

split into two peaks. More interestingly, we noted that pg3 closed due to p3 and p4 merging into p5 peak, which had more states (Figure 6.11). For Pt1 PDOS with nPX examinations, we noted that there was a decrease in states of d1 peak and a new small peak (d2) was formed just above the E_F after adsorption (see Figure 6.11). These suggested that there was electron loss from the Sb3 and Pt1 to the nPX S2 and S1 atom, respectively.

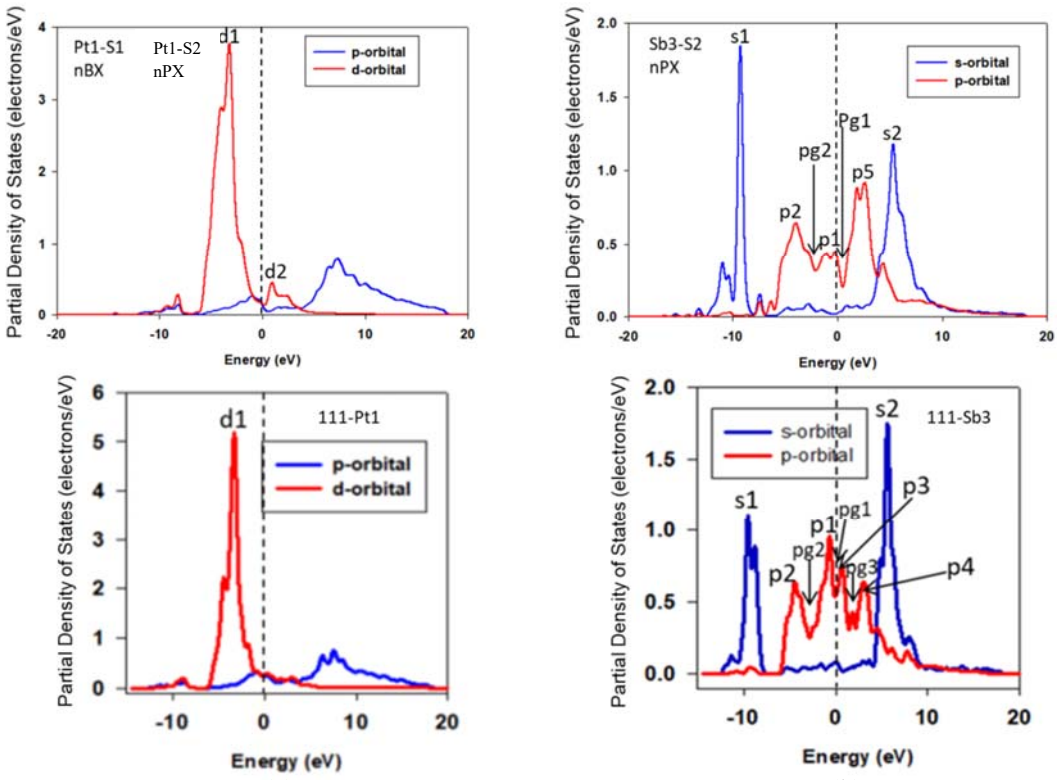

(a) (b)

Figure 6.11: Partial density of states (PDOS) for (111) surface: (a) Pt and (b) Sb PDOS with nPX collector.

The PDOS for EX, nBX and AX adsorption was observed to effect similar behaviour on both Sb2 and Sb3 atoms. The Sb2 atoms were very interesting as we observed a shift in E_F to lower energy where p1 peak shifted to the conduction band and has reduced states. Furthermore, a new pseudo gap (pg1) was observed to form just above the E_F.

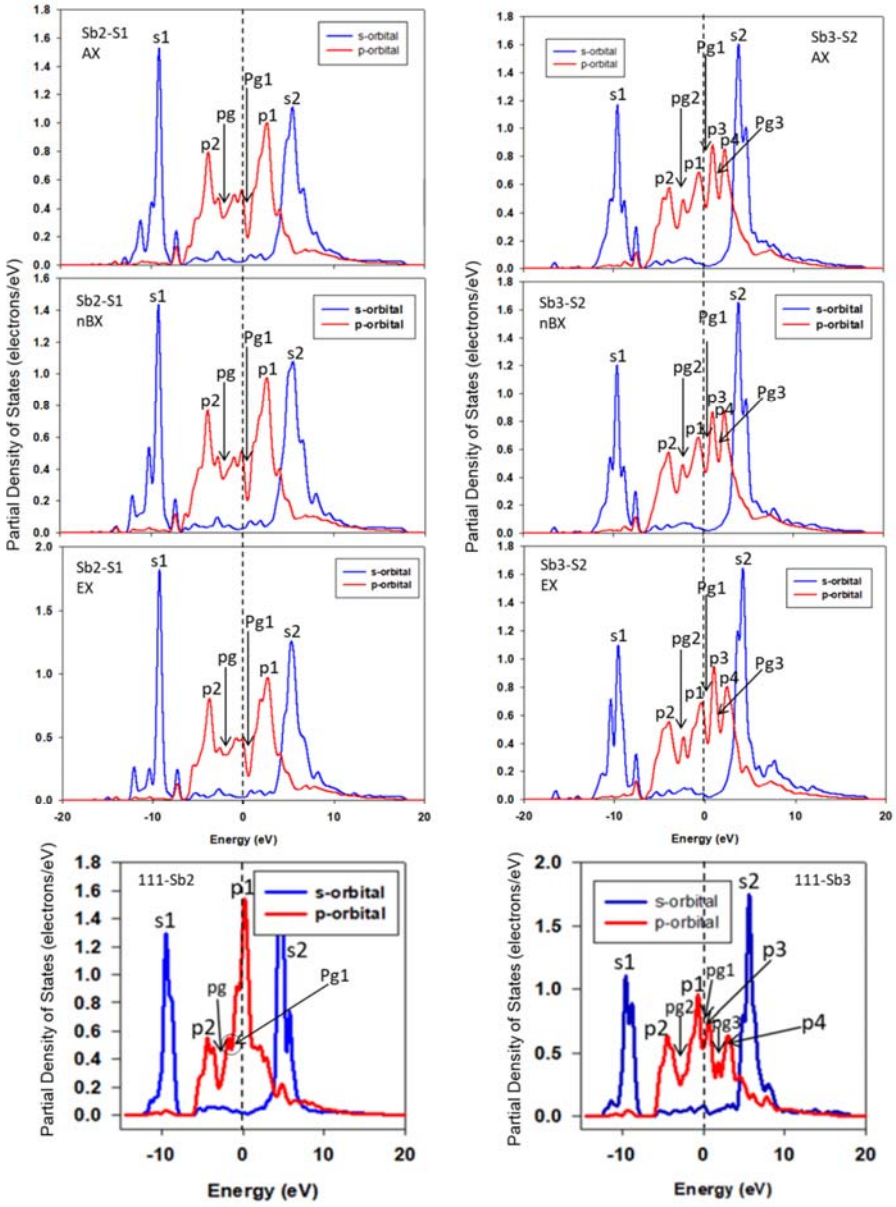

Figure 6.12: Partial density of states (PDOS) for (111) surface: (a) Pt and (b) Sb PDOS with EX, nBX and AX collector.

This was formed due to the opening of the small peak below the p1 peak, (see Figure 6.12). The Sb3 atom analysis showed a small shift of E_F to the lower energy as the p1 peak reduced states, while the p3 and p4 peaks increased states, suggesting electron loss. Interestingly, we observed a small peak forming in the pseudo gap (pg2), see Figure 6.12. All these effects indicated electron transfer from the surface Sb and Pt atoms to the collector S atoms.

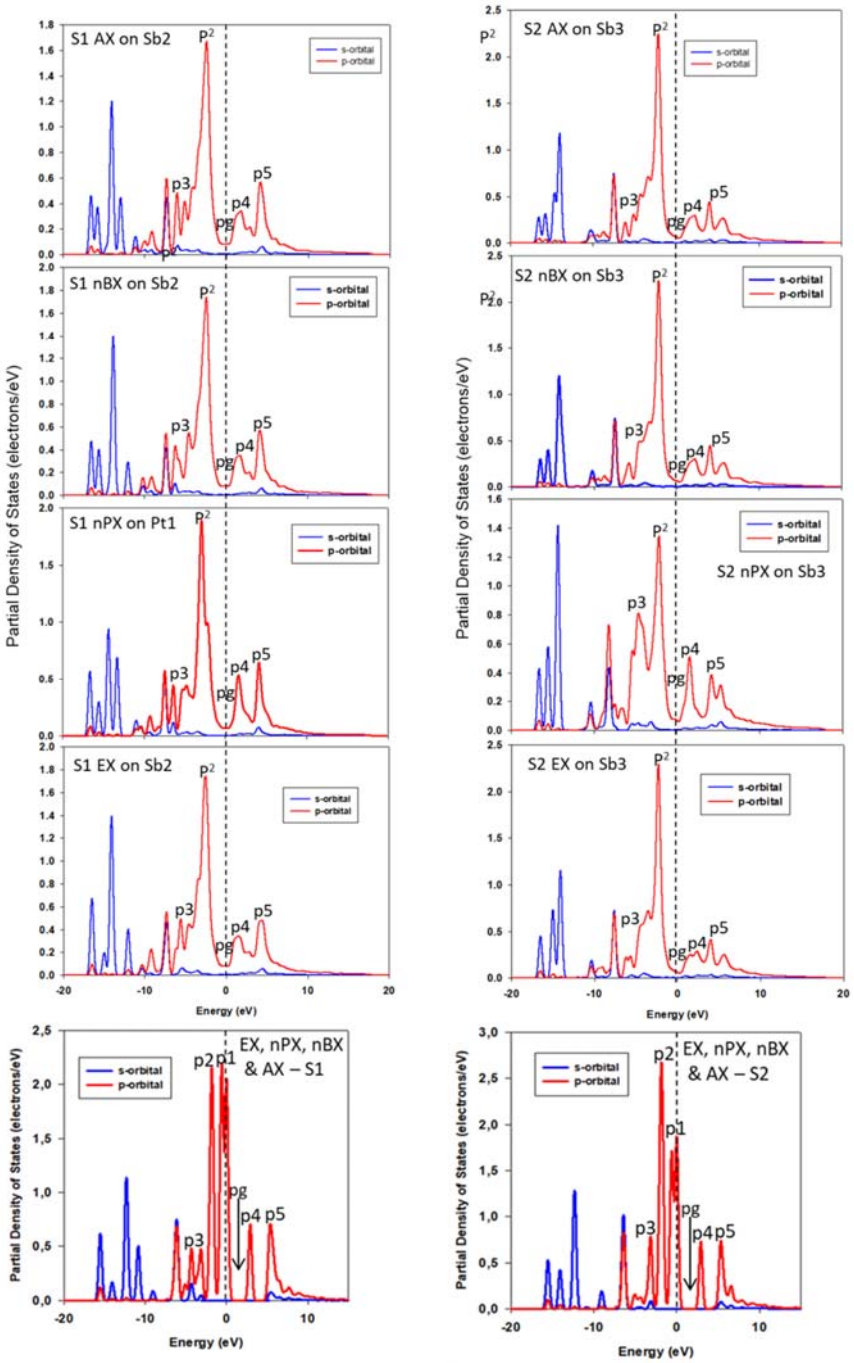

Figure 6.13: Partial density of states (PDOS) for (111) surface: (a) Pt and (b) Sb PDOS with EX, nPX, nBX and AX collector.

Now, in the case of collectors, we also examined the S 3p-orbital as they have direct interaction with the minerals surface as shown in Figure 6.13. We observed that all collectors' S atoms PDOS had similar behaviour, where the S 3p-orbital shifted down in

energy as a result, the E_F fell deep into the pseudo gap (pg) and suggested stability. During further examination, we noted that for all collectors the p1 and p2 peaks merged to form p2 peak, see Figure 6.13. Moreover, we observed that the p3 peak splitting peaks merge with p^2 peak for all four collectors. Interestingly, for nPX we observed that S p4 peaks were reduced and more reduced for EX, nBX and AX collectors. These behaviours suggested electron gain from the mineral surface.

Table 6.11. Calculated atomic population (Mulliken) charges of collectors on $PtSb_2$ (111) surface.

			Mulliken population charges (|e⁻|)				
Collector	**Atom**	**Adsorptions state**	**s**	**p**	**d**	**Total**	**Charge**
EX	Sb2	Before adsorption	1.78	2.91	0.00	4.70	+0.30
		After adsorption	1.76	2.77	0.00	4.52	+0.48
	Sb3	Before adsorption	1.78	2.91	0.00	4.69	+0.31
		After adsorption	1.75	2.78	0.00	4.53	+0.47
	S1	Before adsorption	1.83	4.54	0.00	6.37	–0.37
		After adsorption	1.83	4.25	0.00	6.08	–0.08
	S2	Before adsorption	1.82	4.51	0.00	6.33	–0.33
		After adsorption	1.84	4.15	0.00	6.00	0.00
nPX	Pt1	Before adsorption	0.96	1.00	9.06	11.02	–1.02
		After adsorption	0.93	0.99	8.97	10.89	–0.89
	Sb3	Before adsorption	1.78	2.91	0.00	4.69	+0.31
		After adsorption	1.79	2.77	0.00	4.55	+0.45
	S1	Before adsorption	1.83	4.53	0.00	6.36	–0.36
		After adsorption	1.84	4.16	0.00	6.01	–0.01
	S2	Before adsorption	1.82	4.51	0.00	6.33	–0.33
		After adsorption	1.81	4.14	0.00	5.94	+0.06
nBX	Sb2	Before adsorption	1.78	2.91	0.00	4.70	+0.30
		After adsorption	1.81	2.77	0.00	4.58	+0.42
	Sb3	Before adsorption	1.78	2.91	0.00	4.69	+0.31
		After adsorption	1.76	2.77	0.00	4.53	+0.47
	S1	Before adsorption	1.83	4.53	0.00	6.36	–0.36
		After adsorption	1.83	4.26	0.00	6.09	–0.09
	S2	Before adsorption	1.82	4.51	0.00	6.33	–0.33
		After adsorption	1.84	4.16	0.00	6.01	–0.01
AX	Sb2	Before adsorption	1.78	2.91	0.00	4.70	+0.30
		After adsorption	1.81	2.77	0.00	4.57	+0.43
	Sb3	Before adsorption	1.78	2.91	0.00	4.69	+0.31
		After adsorption	1.76	2.77	0.00	4.53	+0.47
	S1	Before adsorption	1.83	4.53	0.00	6.36	–0.36
		After adsorption	1.83	4.26	0.00	6.09	–0.09
	S2	Before adsorption	1.82	4.51	0.00	6.33	–0.33
		After adsorption	1.84	4.16	0.00	6.01	–0.01

For the computed atomic charges as displayed in Table 6.11, we observed that Sb2 and Sb3 adopted a more positive charge, while the Pt1 atoms adopted less negative

charge. This clearly showed that the surface Sb and Pt atoms transferred charges to the collector S atoms. For the collector S atoms, we noted that for all collectors (EX, nPX, nBX and AX) the S atoms lost charges to the surface. Furthermore, Table 6.11 clearly showed that the Sb atoms lost charges largely from their p-orbitals, while the Pt1 lost from their d-orbitals. The collector S atoms were observed to lose charges from their p-orbitals. This indicated that there was a hybridisation of the p-orbitals of Sb atoms with p-orbitals of the collectors S atoms. Similarly for nPX adsorption, there was a mixing between the d-orbital of Pt1 and p-orbital of S atoms. These hybridisations were also observed from the PDOS to occur between –5.0 eV and 3.0 eV around the E_F.

6.4 Adsorption of H_2O, OH^- and xanthates comparison

We have adsorbed water, hydroxide and xanthates on the mineral surfaces. Note that for xanthates and water mixed adsorption, we considered the most exothermic collector adsorption for each surface. We compared the adsorption energies of H_2O, OH^- and xanthate collector to examine which had stronger adsorption. Note that for OH^- and H_2O we used the adsorption energy per molecule(deleted) obtained from the full surface coverage. The results indicated that OH^- had a stronger adsorption than the H_2O and xanthates, suggesting that the mineral surface had the probability of being covered by OH^- molecules at elevated pH. This behaviour hinders the adsorption on collector during flotation, thus a strong collector would be required to displace these OH^- molecules.

Table 6.12. The adsorption energies for OH^-, H_2O and xanthate collectors on (100), (110) and (111) surfaces: A comparison of adsorption strength.

Surface models	Adsorption energies (kJ/mol)		
	OH^-	**H_2O**	**Collectors**
(100)	–576.65	–38.19	EX = –326.30
(110)	–541.98	–35.00	nBX = –375.66
(111)	–579.53	–54.95	nPX = –795.18

The H_2O adsorption as a binding competitor, it was clear that xanthate would easily be able to displace H_2O, as the binding energy of xanthates were far stronger and more exothermic by ~288.11 kJ/mol for EX on (100) surface, ~340.66 kJ/mol for nBX on (110) surface and ~740.23 kJ/mol for nPX on (111) surface. However, the collectors bind poorly compared to the OH^- molecule, where the OH^- molecule was stronger than xanthates by ~250.35 kJ/mol for OH^- on (100) surface and ~166.32 kJ/mol for OH^- on

(110) surface. However, for (111) surface we found that the xanthates were stronger than the OH^- by ~215.65 kJ/mol. Since the (100) surface is most dominant plane of the platinum antimony mineral, the competition of the OH^- with xanthate can be overcome by the pH change that will not favour the hydroxide attachment or presence on the surface during flotation. Under the hydroxide favouring conditions or elevated pH, we found that the OH^- will also bind much stronger than the H_2O on the surface by ~538.46 kJ/mol for OH^- on (100) surface, ~506.98 kJ/mol for OH^- on (110) surface and ~524.58 kJ/mol for OH^- on (111) surface. This suggested that the pH control would be crucial in the flotation of the $PtSb_2$ and that neutral or lower pH would be required to avoid the formation of hydroxide on the surface.

6.5 Summary

We have carried out collector adsorption on the $PtSb_2$ surfaces to investigate the effect of their affinity with surfaces. We firstly analysed the isolated collectors and their head group bond lengths were found to be similar and were compared with experiments where available. Furthermore, their HOMO and LUMO energies were computed and indicated that the order of electron accepting ability decreased as: EX > nBX > nPX > AX, while the electron donating order decreased as AX > nPX > nBX > EX. Their adsorptions on the surfaces were performed, considering different adsorption sites in order to find the most stable exothermic preferred site. For (100) surface, we found that the bridging on Pt and Sb through collector S atoms was preferred for all xanthate collectors. Their adsorption energies showed that EX has strong affinity with the surface and the order decreased as: EX ≈ AX > nBX > nPX.

The (110) surface was found to have the bridging on Pt atoms and it was the most preferred site for EX, nPX, nBX and AX. The adsorption energies were found to have an increasing trend from EX to nBX, then dropped for AX. The order was observed to decreased as nBX > nPX ≈ AX > EX. The (111) surface was observed to have the bridging on Sb2 and Sb3 atoms and most exothermic for EX, nBX and AX, while the nPX showed the bridging on Pt1 and Sb3 more exothermic compared to the other adsorption sites. The adsorption energies were found to have the nPX more stronger on the surface, with EX weaker and the order decreased as: nPX > nBX > AX > EX. These observations showed that the collectors' adsorption was dependent on surface, in that one collector may show

strong affinity on one surface plane and weaker on the other surface plane. This gave insights into the recovery of the minerals during flotation. Thus, the most dominant surface was mostly considered.

The electronic structures of the collector on the surface were analysed and we found that the density of states (DOS) showed stability bonding of the collector on the surface. We further found that the adsorptions were stable, since we observed that after adsorption the E_F fell deep into the pseudo gap for both collector S atoms and surface Pt and Sb PDOS. For (100) surface, we noted that S1 interacted with Pt1, while S2 interacted with Sb, and the atomic charges computed indicated that there was charge depletion on S1 and charge accumulation for Pt. For S2 and Sb, we observed charge depletion on Sb and charge accumulation on S2 atom. These showed that the collector behaves as electron donor and acceptor to the Pt and Sb on the surface, respectively. Interestingly for (110) surface we observed that the surface Pt atoms lost charges, with a loss of charges on the collector S atoms. These observations suggested that the collectors S atoms offer its HOMO electrons to Pt atoms to form normal covalent bond and simultaneously the Pt atoms donate their d-orbital and p-orbitals electrons to the LUMO of the collectors to form a back donation covalent bond. The (111) surface clearly showed that the surface Pt and Sb atoms lose charges to the collector S atoms, suggested a back donation covalent bonds.

CHAPTER 7

Summary and Conclusion

Geversite ($PtSb_2$) platinum group mineral (PGMs) was investigated using density functional theory CASTEP code. We investigated the bulk and surface properties and also the adsorption of all low-index surfaces: (100), (110) and (111) surfaces. The oxidation, hydration, hydroxide adsorptions and xanthate collectors' adsorption were performed to understand the $PtSb_2$ mineral surface reactivity that is directly related to its extraction during flotation. In order to attain accurate calculations, the cut-off energies were varied for the bulk $PtSb_2$, which were also transferred to the surfaces. The cut-off energy of 500 eV was chosen as the energy change was converged. In addition, the k-points were sampled for the Brillion zone space for both the bulk and surfaces. The k-points grid of 6x6x6 for the bulk and 4x4x1 for surfaces were employed. The bulk relaxation gave a final lattice parameter of 6.531 Å. The DOS indicates that the $PtSb_2$ had a metallic character, even though previous studies suggested that it has a pseudo-gap, thereby insinuating semiconducting behaviour.

The relaxed bulk structure was used to cleave the low-index surfaces, namely (100), (110) and (111). In cleaving the surfaces, all possible terminations were considered and the slab thickness was varied. The relaxed (2x2) super cell surface energies were 0.807 $J.m^{-2}$, 1.077 $J.m^{-2}$ and 1.074 $J.m^{-2}$ for (100), (111) and (110), respectively. This indicated that the (100) surface was the most stable and most dominant plane of the $PtSb_2$ mineral. The DOS showed stability with the E_F falling deep into the pseudo gap for all surfaces. The valence electrons on the surface were the $5d^9 6s^1$ for Pt and $5s^2 5p^3$ for Sb and these electrons were actively involved in the hybridisation. The atomic charges clearly displayed these effects in the presence of 6p-orbital for Pt atoms, due to the strong hybridisation of the Pt 5d-orbitals with the 5s-orbital and 5p-orbitals of Sb atoms. Interestingly, we observed that on all surfaces the 5d-orbital of Pt had the nine electrons ($5d^9$ filled), suggesting that these orbitals were occupied unlike in the bulk model. These effects occurred in order to form a stable surface.

The oxidation showed that the oxygen molecules preferred interacting with the Sb atoms than the Pt atoms for all surfaces. We observed different bonding modes, where bridging and dissociation into atomic bonding occurred. For the (100) surface we found that the Pt-O_2 peroxide initial adsorption site gave the strongest adsorption. In the case of the (110) surface the Sb2-O-O-Sb3 bridging yielded the most exothermic adsorption. The (111) surface showed the Sb2-O-O-Sb2 bridging as the strongest exothermic adsorption,

which dissociated and resulted in atomic bonding. The atomic charges indicated that the oxygen molecules gain charges from the Pt and Sb atoms. These findings suggested that the 2p-orbital spin-down un-occupied orbital (LUMO) of O_2 was fully occupied. We also observed that the Sb/Pt-bonded oxygens were more negative than the terminal or end-bonded oxygen atom for superoxide bonding modes. Furthermore, based on the charge sum of the O_2, i.e. charge addition of O1 and O2, we found that in all cases the O_2 interacting with Sb gained more charges, thus showing that the Sb atoms were the preferred sites for oxygen adsorption.

The case of H_2O molecules adsorption on the three $PtSb_2$ mineral surfaces indicated that H_2O adsorbed through van der Waals forces, in particular for multi adsorptions by physisorption process for (100) and (110) surfaces. However, for the (111) surface we observed chemisorption. For the (100) surface the H_2O-Pt was exothermic, while the H_2O-Sb was endothermic and only exhibited exothermic tendency from 5/8-8/8 H_2O/Sb. The (110) surface showed stronger adsorption of H_2O on Pt than on Sb atoms, with the Sb2 being the weakest. The full-coverage gave –35.00 kJ/mol per H_2O molecule, which was close to the full-coverage on the (100) surface (–38.19 kJ/mol per H_2O molecule). The adsorption of a single water molecule on the (111) surface is stronger on Sb3 and weaker on Sb2 atoms. Furthermore, the full-monolayer adsorption on Sb2 and Sb3 gave even stronger adsorption (–55.54 kJ/mol per H_2O). The full-coverage on the (111) surface (i.e. on Pt1 and all Sb atoms) yielded adsorption energy of –54.95 kJ/mol per H_2O molecule.

The adsorption of hydroxide on the $PtSb_2$ surfaces was generally stronger than that of the water molecules. This suggested that they will bind preferentially over the water molecules. We found that the OH^- preferred the Sb atoms on the (100) surface, with a greater adsorption energy of –576.65 kJ/mol per OH^- molecule for full-surface coverage. The adsorption energies of OH^- on the (110) surface depicted the following order : Sb3-OH > Sb2-OH > Pt1-OH > Pt2-OH, which reflected preferential adsorption on Sb3 atoms. The adsorption energy of full-surface coverage was reported as –541.98 kJ/mol per OH molecule. The (111) surface also displayed a strong exothermic adsorption on the Sb3 atom and the order followed as: Sb3 > Sb2-OH > Pt2-OH > Pt1-OH > Sb3(D)-OH. The surface full-coverage gave adsorption energy of –579.53 kJ/mol per OH^- molecule. The atomic charges of both hydration and hydroxide adsorption showed that there was a

charge depletion on both Pt/Sb and O atoms of the H_2O and OH^-. This suggested that there is a charge transfer into other regions within the orbitals.

We now consider the adsorption of collectors on the $PtSb_2$ surfaces. Firstly, analysing the isolated collectors and in particular their head group bond lengths. These were found to be consistent with available experimental results. Furthermore, their HOMO and LUMO energies were computed and indicated that the order of electron accepting ability decreased as: EX > nBX > nPX > AX, while the electron donating order decreased as: AX > nPX > nBX > EX. Their adsorptions on the surfaces were performed considering different adsorption sites in order to find the most stable exothermic preferred site. For (100) surface, the bridging on Pt and Sb through collector S atoms was preferred for all xanthate collectors. Their adsorption energies followed the order : EX ≈ AX > nBX > nPX, which indicated that EX has strong affinity for the (100) surface.

The case of the (110) surface was found to have the bridging on Pt atoms most preferred sites for EX, nPX, nBX and AX. The order was observed as nBX > nPX ≈ AX > EX. The (111) surface was observed to have the bridging on Sb2 and Sb3 atoms most exothermic for EX, nBX and AX, while the nPX showed the bridging on Pt1 and Sb3 more exothermic compared to the other adsorption sites. The adsorption energies were were similar to the (110) surface, the EX was weaker and the order decreased as: nPX > nBX > AX > EX. These gave insights into the recovery of the minerals during flotation. Since the (100) surface plane was the most stable phase cleavage of the platinum antimonide it suggested that the EX and AX may be a best collectors to float the platinum antimonide, amongst the studied xanthate of different chain length.

Experimentally, it has been found that the recovery and the enthalpy of adsorption increases with an increase in carbon chain for xanthates. However, the trends observed in this study did not show the increasing trend with increase in carbon chain. Recently, it has been shown on pyrite that the presence of Na or K on the xanthate collector makes a difference in adsorption, where the increasing trend was perceived and agreed well with microcalorimentry enthalpy of adsorption [McFadzean et al. (2018)]. As such it is proposed that the presence of Na or K ions are crucial in order to obtain similar behaviour as experiments for collectors such as xanthates that possess a negative charges when the Na or K dissociates in solution. Furthermore, our results for xanthate adsorption on $PtSb_2$ (100) were found to have some agreement with the work by Waterson et al. (2015) for

$PtAs_2$ (100) surface. This showed that there are some similaries between the two minerals compounds.

The electronic structures of the collectors on the surface were analysed. We noted the partial density of states (DOS) showed stability when the collectors bond on the surface, since the E_F fell deep into the pseudo gap for both collector S atoms and surface Pt and Sb PDOS. For the (100) surface, S1 interacted with Pt1, while S2 interacted with Sb, the computed atomic charges indicated a charge depletion on S1 and charge accumulation for Pt atom. For S2 and Sb, we observed charge depletion on Sb and charge accumulation on S2 atom. These results show that the collector behaved as electron donor and acceptor to the Pt and Sb on the surface, respectively. Interestingly for the (110) surface both the surface Pt and Sb atoms lost charges, as the collector S atoms lose charges. These observations suggested that the collector S atoms offered their HOMO electrons to Pt and Sb atoms to form bonds and simultaneously the Pt and Sb atoms donate their d-orbital and p-orbitals electrons to the LUMO of the collectors to form a back donation covalent bond, respectively. The (111) surface clearly showed that the surface Pt and Sb atoms lost charges to the collector S atoms, which suggested a back donation covalent bonds.

We have compared the adsorption energies for water, hydroxide and xanthates on the mineral surfaces. The results indicated that OH^- has a stronger adsorption than H_2O and xanthates, hence suggesting that the mineral surface has a probability of being covered by OH^- molecules at elevated pH. This behaviour may hinder the interaction of collector with mineral surface during flotation, thus a strong collector would be required to displace these OH^- molecules.

Recommendations and future work

It is recommended that new collectors with stronger affinity for the $PtSb_2$ surface than the OH^- are required in order to improve the flotation at elevated pH or lower pH. The EX and AX collectors were found suitable to float the platinum antimonide.

In the future, the xanthates will be adsorbed in the presence of water and explore the effects of Na (sodium) and K (potassium) on xanthate collectors. We will also test other collectors and design new ones that can improve the flotability of the $PtSb_2$ mineral.

References

Aneesuddin M., Char P. N., Raza Hussain M. and Saxena E.R., 1983, Studies on thermal oxidation of chalcopyrite from Chitradurga, Karnataka State, India, *Journal of Thermal Analysis*, ***26***, 205–216.

Bader R. (1990). *Atoms in Molecules: A Quantum Theory.* New York: Oxford University Press.

Bartell L. S. (1968). Molecular Geometry: Bonded Versus Nonbonded interactions. *Journal of Chemical Education,* ***45***, 754–766.

Blyholder G., Head J. and Ruette F. (1982). Semi empirical Calculation of Iron-Oxygen Interactions. *Inorganic Chemistry,* ***21***, 1539–1545.

Brese N. E. and Schnering H. G., (1994). Bonding trends in pyrites and a reinvestigation of the structures of $PdAs_2$, $PdSb_2$, $PtSb_2$ and $PtBi_2$, *Zeitschrift für Anorganische und Allgemeine Chemie,* ***620***, 393.

Chadi D. J. and Cohen M. L. (1973). Special Points in the Brillouin Zone. *Physical Review B,* ***8***, 5747–5753.

Chandra A. P. and Gerson A. R. (2010), The mechanisms of pyrite oxidation and leaching: A fundamental perspective, *Surface Science Reports*, **65**, 293–315.

Clark S. J., Segall M. D., Pickard C. J., Hasnip P.J., Probert M., Refson K. and Payne M.C. (2005). First principles methods using CASTEP. *Z. Kristallography,* ***220***, 567–570.

Cooper T.G. and de Leeuw N.H. (2003). A combined ab initio and atomistic simulation study of the surface and interfacial structures and energies of hydrated scheelite: introducing a $CaWO_4$ potential model. *Surface Science* ***531*** 159–176

Delley B. (2000). Density Functional Theory Electronic Structure Program. *Journal of Chemical Physics,* ***113***, 7756–7764.

Dong J. and Xu M. (2011). Evaluation of environmentally friendly collectors for xanthate replacement. *Proceedings of the 43rd Annual Canadian Mineral Processors Conference.*, CIM, ottawa, ON, Canada, 289–302.

Edelbro R., Sandstrom A. and Paul J. (2003). Full potential calculations on the electrons of spalerite, pyrite and chalcopyrite. *Applied Surface Science,* ***206***, 300–313.

Eisenberg D. and Kauzmann W. (1969). *The Structure and Properties of Water.* Oxford University Press.

Emtage P. R., (1965) Band Structure of Platinum Antimonide, *Physical Review*, ***138***, A246–A259.

Evarestov R. A. and Simirnov V. P. (1983). Special Points of the Brillouin Zone and Their Use in the Solid State Theory. *Physical Status Solidi A,* ***119***, 9–40.

Ferihan G. (2002). Effect of pH on pulp potential and sulphide mineral flotation. *Turkish Journal Engineering Enviromental Science,* ***26***, 309–318.

Flotation. (2010, 05). Retrieved 11 2012, from ranjit.rds.net.in/wp-content/uploads/2010/05/FLOTATION.pptx

Froth flotation is one of the most versatile and flexible of all mineral separation processes. Retrieved 11 2012, from www.jmeech.mining.ubc.ca/MINE290/Froth%20Flotation.pdf

Godel B., Barnes S. and Maier W. D. (2007). Platinum group elements in sulphide minerals and whole rock of the merensky reef (Bushveld Complex, South Africa): Implications for the formation of the reef. *Journal of Petrology,* ***48***, 1569–1604.

Gutsev G. L., Rao B. K. and Jena P. (2000). Systematic Study of Oxo, Peroxo, and Superoxo Isomers of 3d-Metal Dioxides and Their Anions. *Journal of Physical Chemistry A,* ***104***, 11961–11971.

Herzberg G. (1950). *Spectra of Diatomic Molecules 2nd ed.* D. Van Nostrand & Company, Inc. Princeton N.J.

Heyd J., Scuseria G. E. and Ernzerhof M. (2003). *Journal of Chemical Physics,* ***118***, 8207.

Hohenberg P. and Kohn W. (1964). Inhomogeneous electron gas. *Physical Review B,* ***136***, 864–871.

Housecroft C. E., Shape A. G. (2008). *Inorganic chemistry (3rd ed).* Prentice Hall.

http://science.marshall.edu/castella/chm448/chap11.pdf. (2016, March 15).

http://www.everyscience.com/Chemistry/Inorganic/Crystal and Ligand Field Theories/b.1013.php. (2016, March 15).

http://www.nano-ou.net/files/3D%20Density%20of%20States.doc. Retrieved 05 15, 2013.

http://www2.uncp.edu/home/mcclurem/ptable/o.htm. (2015, October 26).

https://en.wikipedia.org/wiki/Crystal_field_theory. (2016, February 17).

https://msu.edu/course/css/850/snapshot.afs/teppen/physical_chemistry_of_water.htm (2020 February 04).

https://people.ifm.liu.se/thoed/water/water-1.pdf.

Hung A, Muscat J, Yarovsky I, Russo S. P. (2002) Density-functional theory studies of pyrite FeS_2 (100) and (110) surfaces. *Surface Science,* ***513(3)***, 511–524.

Hung A, Muscat J, Yarovsky I, Russo S. P. (2002) Density-functional theory studies of pyrite FeS_2 (111) and (210) surfaces. *Surface Science,* ***520(1-2)***, 111–119.

Hung A., Yarovsky I. and Russo S. P. (2003). Density-functional theory studies of xanthate adsorption on the pyrite FeS_2 (110) and (111) surface. *Journal of Chemical Physics,* ***118***, 6022–6029.

Kleinman L. and Bylander D. M. (1982). Efficacious form for model pseudopotentials. *Physical Review Letter,* ***48***, 1425–1428.

Kohn W. and Sham L. J. (1965). Self-consistent equations including exchange and correlation effects. *Physical Review,* ***140***, 1133–1138.

Komsa H. -P, Rantala T. T. and Pasquarello A., *Physical Review B*, 2012, ***86***, 045112.

Kresse G. and Furthermuller J. (1996). Efficient iterative schemes for ab-initio total-energy calculations using a plane-wave basis set. *Physical Review B,* ***54***, 11169–11186.

Kresse G. and Furthmuller J. (1996). Efficiency of ab-initio total energy calculations for metals and semiconductors using a plane-wave basis set. *Computational Material Science,* ***6***, 15–50.

Kresse G. and Joubert D. (1999). From ultrasoft pseudopotentials to the projector augmented-wave method. *Physical Review B,* ***59***, 1758–1775.

Kudoh Y. and Takeda A. H. (1986). local density approximation for the exchange-correlation energy of an electronic system. *Physical Chemical Mineral,* ***13***, 233–237.

Legrand D. L., Bancroft G. M. and Nesbitt H. W. (2005), Oxidation/alteration of pentlandite and pyrrhotite surfaces at pH 9.3: Part 1. Assignment of XPS spectra and chemical trends, *American Mineralogist,* ***90***,1042–1054.

Legrand D. L., Bancroft G. M. and Nesbitt H. W. (2005), Oxidation of pentlandite and pyrrhotite surfaces at pH 9.3: Part 2. Effect of xanthates and dissolved oxygen, *American Mineralogist,* ***90***, 1055–1061.

Lever A. B. P., Ozin G. A. and Gray H. B. (1980). Electron transfer in metal–dioxygen adducts. *Inorganic Chemistry,* ***19***, 1823–1824.

Li Q., Qin W., Sun W. and Qiu G. (2007) Calculation of electron structure by density function theory and electrochemical process of surface (100) of FeS_2. *Journal Central South University of. Technololgy* ***14*****,** 618–622.

Li X.and Paier J, (2016) Adsorption of Water on the Fe3O4(111) Surface: Structures, Stabilities, and Vibrational Properties Studied by Density Functional Theory, *J. Phys. Chem. C*, 120, 1056−1065.

Liang Qi, Xiaofeng Qian and Ju Li. (2008). Near neutrality of an oxygen molecule adsorbed on a Pt(111) surface. *Physical Riview Letters,* ***101***, 1–4.

Liu G., Wang Y., Yuan L., Xu Z., Lu Y., Zeng H and Zhong H. (2012). A DFT study on the flotation performance of thiol collectors for copper sulphide flotation. *International Mineral Processing Congress, proceeedings/ new delhi, India*, 2947–2958.

Liu H., Xiang H. and Gong X. G. (2011). First principles study of adsorption of O2 on Al surface with hybrid functionals. *Journal of Chemical Physics, **135***, 1–5.

Loewenberg M. and Davis R. H. (1994). Flotation rates of fine, spherical particles and droplets. *Chemical Engineering Science, **49***, 3923–3941.

Makanza A. T., Vermaak M. K. G and Davidtz J. C. (2008). The flotation of auriferous pyrite with mixture of collectors. *International Journal of Minerals Processing, **86***, 85–93.

Makov G and Payne M. C., (1995) Periodic boundry conditions in ab-initio calculations, *Physical Review B, **51***, 4014–4022.

Manyeruke T. D. (2003). The petrography and geochemistry of the platreef on the farm Townlands, near Potgiestersrus, northern Bushveld Complex*, MSc Thesis.* Pretoria, South Africa: University of Pretoria.

Marston R. J., Groves D. I., Hudson D. R. and Ross J. R. (1981). Nickel sulfide deposits in Western Australia: a review. *Economic Geology, **76***, 1330-1363.

Matsuda A., Sugita S., Fujii T. and Watanabe T. (2001). Study of Pseudogap Phenomena by STM and Other Probes. *Journal of Physics and Chemistry Solids, **62***, 65–68.

Matsuda T., Ohara I., Satoi H., Ohashi S. and Mizutani U. (1989). Electronic Properties for Icosahedral and Amorphous Phases in the Mg-Zn-Al Alloy System. *Journal of Physics Condensed Matter, **1***, 4087–4098.

Mehlape A. M., Ngoepe P. E and Parker S. C. (2013). Computational modeling studies of cobalt pentlandite (Co_9S_8). Polokwane, South Africa: University of Limpopo.

Marape G. Fundamental Electrochemical Behaviour of Pentlandite. Masters in Engineering, University of Pretoria, Pretoria South Africa, August 2010.

McFadean B., Mkhonto P. P. and Ngoepe P. E. (2018). Intergrating computational modelling with experimental enthalpy of adsorption: A xanthate-pyrite system. XXIX International Minerals Processing Congress conference procedings, Moscow, Russia.

Meyer B. (2006). The Pseudopotential Plane Wave Approach. *Computational Nanoscience,* ***31***, 71–83.

Michaelides A., Alavi A. and King D. A. (2003). Differnt surface chemistries of water on Ru{0001}: From monomer adsorption to partially dissociated bilayer. *Journal of American Chemical Society,* ***125***, 2746–2755.

Milmann V., Winkler B., White J. A., Pickard C. J., Payne M. C., Akhmatskaya E. V. and Nobes R. H. (2000). Electronic structure properties and phase stability of inorganic crystals: A pseudopotential plane-wave study. *International Journal of Quantum Chemistry,* ***77***, 895–910.

Mkhonto D., Ngoepe P. E. Cooper T. G. and de Leeuw N. H. (2006). A computer modelling study of the interaction of organic adsorbates with fluorapatite surfaces. *Physical Chemistry of Minerals,* ***33***, 314–331.

Mkhonto P. P., Chauke H. R. and Ngoepe P. E., (2015) *Ab-initio* Studies of O_2 Adsorption on (110) Nickel-Rich Pentlandite ($Fe_4Ni_5S_8$) Mineral Surface, *Minerals*, ***5***, 665–678.

Monkhorst H. F. and Park J. D. (1976). Special points for Brillouin-Zone integrations. *Physical Review B,* ***13***, 5188–5192.

Mostert A. B. (1982). *A mineralogical and Petrological investigation of the Platreef on Drenthe 778 LR, northwest of Potgietersrus, MSc thesis.* Pretoria, South Africa: University of Pretoria.

Muzenda E., Afolabi A. S., Abdulkareem A. S. and Ntuli F. (2011). Effect of pH on the Recovery and Grade of Base Metal Sulphides (PGMs) by Flotation. *Proceedings of the world congress on Engineering and Computer science,* ***2***, 609–612.

Neugebauer J. and Scheffler M., (1992), Adsorbate-substrate and adsorbate-adsorbate interactions of Na and K adlayers on Al(111), *Physical Review B,* ***46***, 16067–16080.

Ngobeni W. and Hangone G. (2013). The effect of using pure thiol collectors on the froth floataion od pentlandite containing ore. *South African Journal of Chemical Engineering,* ***18***, 41–50.

O'Connor C. T. and Shackleton N. J., (2013), Investigations into the Recovery of Platinum Group Minerals from the Platreef Ore of the Bushveld Complex of South Africa, *Platinum Metals Review*, ***57(4)***,302–309.

Payne M. C., Teter M. P., Allan D. C., Arias T. A. and Joannopoulos J. D. (1992). Iterative minimization techniques for ab initio total-energy calculations: molecular dynamics and conjugate gradients. *Review of Modern Physics,* ***64***, 1045–1097.

Pentlandite - Wikipedia, the free encyclopedia. (n.d.). Retrieved from http://en.wikipedia.org/wiki/Pentlandite (25 May 2015).

Perdew J., Burke K. and Ernzerhof M. (1996). Generalized gradient approximation made simple. *Physical Review Letters,* ***118***, 3865–3868.

Perdew J. P. and Wang Y. (1986). Generalized gradient approximation for the exchange-correlation hole of a many-electron system. *Physical Review B,* ***33***, 8800–8822.

Perdew J. P. and Wang Y. (1996). Generalized gradient approximation for the exchange-correlation hole of a many-electron system. *Physical Review B,* ***45***, 13 244–13 249.

Pierce F. S., Basov D. N., Volkov P., Poon S. J. and Timusk T. (1994). Optical Conductivity of Insulating Al-Based Alloys: Comparison of Quasiperiodic and Periodic Systems. *Physical Review Letters,* ***73***, 1865–1868.

Rimstidt, J. D.; Vaughan, D. J. (2003). Pyrite oxidation: A state-of-the-art assesment of the reaction machanism. *Geochim. Cosmochim. Acta,* ***67***, 873–880.

Rosso K. M., Becker U. and Hochella M. F. (1999b). The interaction of pyrite (100) surfaces with O2 and H2O: Fundamental oxidation mechanisms. *American Mineralogist,* ***84***, 1549–1561.

Sanville E., Kenny S. D., Smith R. and Henkelman G. (2007). Improved grid-based algorithm for Bader charge allocation. *Journal Computational Chemistry,* ***28***, 899–908.

Scoon R. N. and Mitchell A. A., (2004) The platiniferous dunite pipes in the eastern limb of the Bushveld Complex: Review and comparison with unmineralized discordant ultramafic bodies, *South African Journal of Geology,* ***107****,* 505–520.

Slater J. and Verma H. C. (1929) The Theory of Complex Spectra. *Physical Review,* ***34***, 1293–1322.

Stirlinga A.,Bernasconi M. and Parrinello M., (2003), *Ab initio* simulation of water interaction with the (100) surface of pyrite, *J. Chem. Phys*.**118**, 8917

Stumpfl E. F., (1961) Some new platinoid-rich minerals, indentified with the electron microanalyser. *Journal of the Mineralogical Society*, ***32(254)***, 833–847.

Sun, W., Hu, Y., Qiu, G., (2004) Oxygen adsorption on pyrite (100) surface by density functional theory, *Journal Central South University of Technology,* ***11***, 385–390.

Tasker P. W., (1979), The stability of ionic crystal surfaces., *Journal of Physics. C: Solid State Physics,* ***12***, 4977–4984.

Todd E. C., Sherman D. M., and Purton J. A. (2003), Surface oxidation of chalcopyrite ($CuFeS_2$) under ambient atmospheric and aqueous (pH 2-10) conditions: Cu, Fe L- and O K-edge X-ray spectroscopy, Geochimica et Cosmochimica Acta, ***67(12)***, 2137–2146.

Tunega D., Haberhauer G., Gerzabek M. and Lischka H. (2002) Theoretical Study of Adsorption Sites on the (001) Surfaces of 1:1 Clay Minerals, *Langmuir***,** ***18****,* 139-147

Uzunova, E. L.; Mikosch, H.; Nikolov, G. St. (2008). Electronic structure of oxide,peroxide, and superoxide clusters of the 3d elements: A comparative functional study. *Journal of Chemical Physics., **128***, 094307-1–094307-8.

Vanderbilt D. (1990). Soft self-consistent pseudopotentials in a generalized eigenvalue formalism. *Physical Review B., **41***, 7892–7895.

Vignale R. G. (1979). DFT in magnetic fields. *Physical Review Letter, **59***, 2360–2363.

Walker G. W., Walters C. P. and Richardson P. E. (1986). Hydrophobic effects of sulfur and xanthate on metal and mineral surfaces. *International Journal of Mineral Processing, **18***, 119–137.

Wang, L. S. (2000) Photodetachment Photoelectron Spectroscopy of TransitionMetal Oxide Species. InPhotoionization and Photodetachment; Ng, C. Y.,Ed.; *Advanced Series in Physical Chemistry*; World Scientific:Singapore, ***10***, 854–957.

Waterson C. N., Sindt J. O., Cheng J., Tasker P. A. and Morrison C. A. (2015). First-principle study on ligand binding and positional disorder in pentlandite. *Journal of Physical Chemistry. C, **119***, 25457–25468.

Waterson C. N, Tasker P. A., Farinato R., Nagaraj D. R., Shackleton N. and Morrison C. A., (2016). A Computational and Experimental Study on the Binding of Dithio Ligands to Sperrylite, Pentlandite, and Platinum. *Journal Physical Chemistry C*, ***120(39)***, 22476–22488.

Watson G. W., Kelsey E. T., de Leeuw N. H., Harris D. J. and Parker S. C., (1996) Atomistic simulation of dislocations, surfaces and interfaces in MgO, *Journal of the Chemical Society Faraday Transactions, **92***, 433–438.

Weast R. (1985). *CRC Handbook of Chemistry and Physics.* FL, USA: CRC, Boca Raton.

Weia Z., Li Y., Gao H., Zhu Y., Qian G., Yao J. (2019). New insights into the surface relaxation and oxidation of chalcopyrite exposed to O_2 and H_2O: A first-principles DFT study, Applied Surface Science, ***492***, 89–98.

Winter G. (1980). Inorganic xanthates. *Reviews in Inorganic Chemistry,* ***2***, 253–342.

Wulff, G. (1901). XXV. Zur Frage Der Geschwindigkeit Des Wachstums Und Der Auflö sung Der Krystallflagen. *Zeitschrift für Kristallographie,* ***34***, 449−480.

www.chem.uky.edu/courses/che510/exam2k-05.pdf. (2014, July 15).

www.jmeech.mining.ubc.ca/MINE290/Froth%20Flotation.pdf. (2012, october 20).

Yekeler H. and Yekeler M. (2004). Reactivities of some thiol collectors and their interactions with Ag (+1) ion by molecular modelling. *Applied Surface Science ,* ***236***, 435–443.

Yekeler M. and Yekeler H. (2006). A density functional study on the efficencies of 2-mercaptobenzoxazole and its derivatives as chelating agents in flotation processes. *Colloids and Surfaces A: Physiocochemical Engineering Aspects,* ***186***, 121–125.

Zhanga K., Wang X, Zheng P. Y., Huang K. K., Hua C. Q., Feng S. H., Wen M., Zheng W. T. (2017),The investigation of magneto-transport properties of $PtSb_2$ single crystal synthesized by sb-flux method, *Journal of Alloys and Compounds* **694**, 935–938.

Zhao C., Chen J., Long X. and Guo J. (2014), Study of H_2O adsorption on sulfides surfaces and thermokinetic analysis, *Journal of Industrial and Engineering Chemistry,* ***20*** 605–609.

Appendix A: Project flow chat

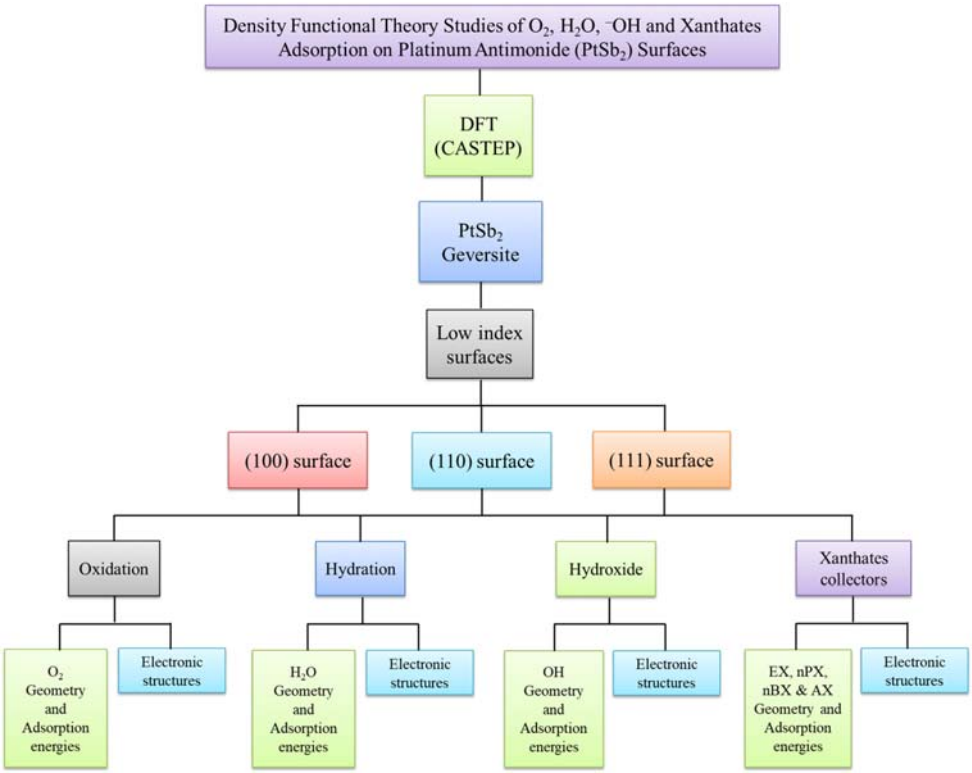

Figure A.1: Flow chart of the project and the connection of all calculations performed.

Explanation of terms:

Project	– Density Functional Theory Studies of O_2, H_2O, OH^- and Xanthates Adsorption on Platinum Antimonide (PtSb2) Surfaces.
DFT (CASTEP)	– Density functional theory method implemented in CASTEP code used to study the $PtSb_2$ mineral surfaces and their interactions with O_2, H_2O, OH^- and xanthates collectors.
$PtSb_2$ Mineral	– The bulk structure was used to study the low index (100), (110) and (111) surfaces.
Low index surfaces	– The investigation of the (100), (110) and (111) surfaces before adsorption and their oxidation, hydration and thiol

collectors interactions. Their electronic properties (DOS and Mulliken charges) are also evaluated to describe the bonding behaviour.

Appendix B: Papers presented at conferences

1 SAIP, University of Limpopo, 2008, Oxidation studies on $PtSb_2$ (100) surface.

2 SAIP, University of KwaZulu Natal, (2009), Studies of oxygen adsorption on $PtSb_2$ surfaces

2 SAIP, CSIR (2010), Oxidation of $PtSb_2$ using ab-initio techniques, (Poster)

3 SAIP, Saint George Hotel, (2011), Oxygen adsorption on (110) surfaces of Pyrolusite MnO_2 and Anatase TiO_2 (Poster)

Appendix C: Publications

1. Mangwejane S.S., Mkhonto P.P. and Ngoepe P.E., Computational Modelling Study of H_2O, OH^- and O-, N-, S-bearing Collectors Adsorption onto (100) Surface of Platinum Antimonide ($PtSb_2$), Journal name, volume, pages (*to be published*).

Appendix D: Relaxed structures for hydration of (100) surface

In this section we show the relaxed structures for the hydration for different numbers of H_2O molecules adsorbed on the (100) surface as depicted in the adsorption energies in the main text.

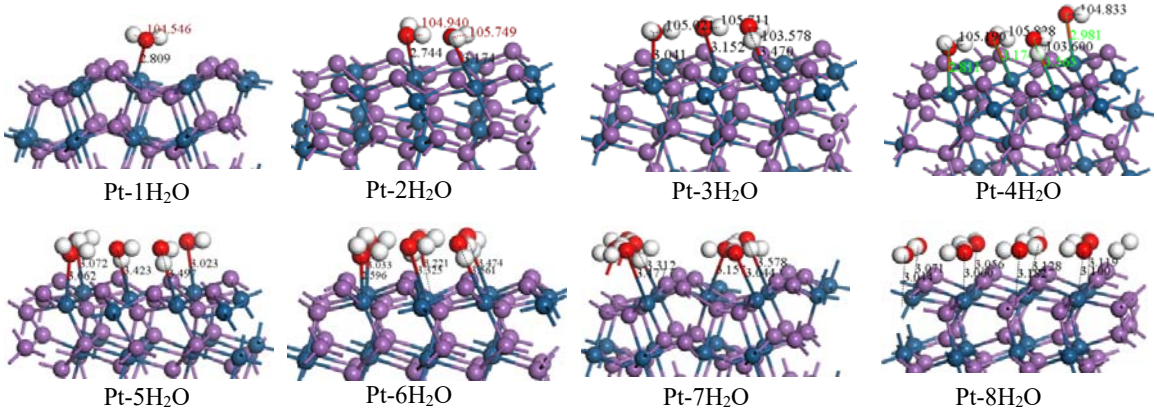

Figure D.1: Relaxed geometries for H_2O adsorptions on Pt atom sites of (100) surface.

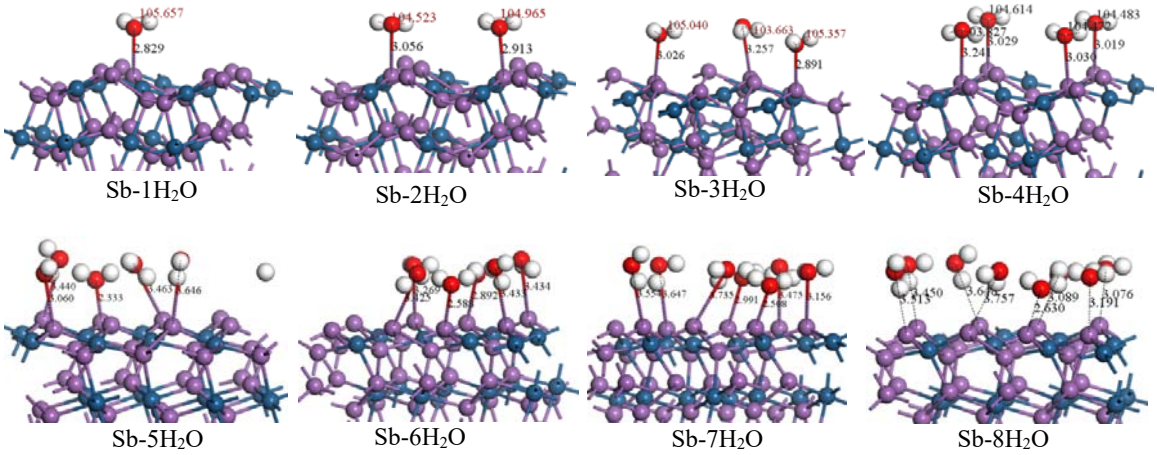

Figure D.2: Relaxed geometries for H_2O adsorptions on Sb atom sites of (100) surface.

Appendix E: Data for Xanthate Adsorption on Surface

In this section we show the different adsorption sites considered for the xanthate adsorption. This is mostly influenced by the fact that as the collector come in contact with a minerals surface it has a freedom to select and attach on any position on the surface. The most active stable site for the xanthate would give the most exothermic heat of adsorption (adsorption energy). Note that we did not consider the mononuclear adsorption for (111) surface as this has not shown to give the most exothermic adsorption. For a $PtSb_2$ it was paramount to explore the Sb interaction as well with the Pt atoms interaction with the xanthate. And as we have shown in Chapter 6, the Sb really has a significant role in the adsorption of the collector. We have shown in Figure E.1, E.2 and E.3 some initial

adsorption geometries. In these positions, after surface relaxation the xanthate may move to its preferential positions. However, we did not show these final relaxation as we were more concerned with the adsorption energies that will show the most active and preferred site by the collector.

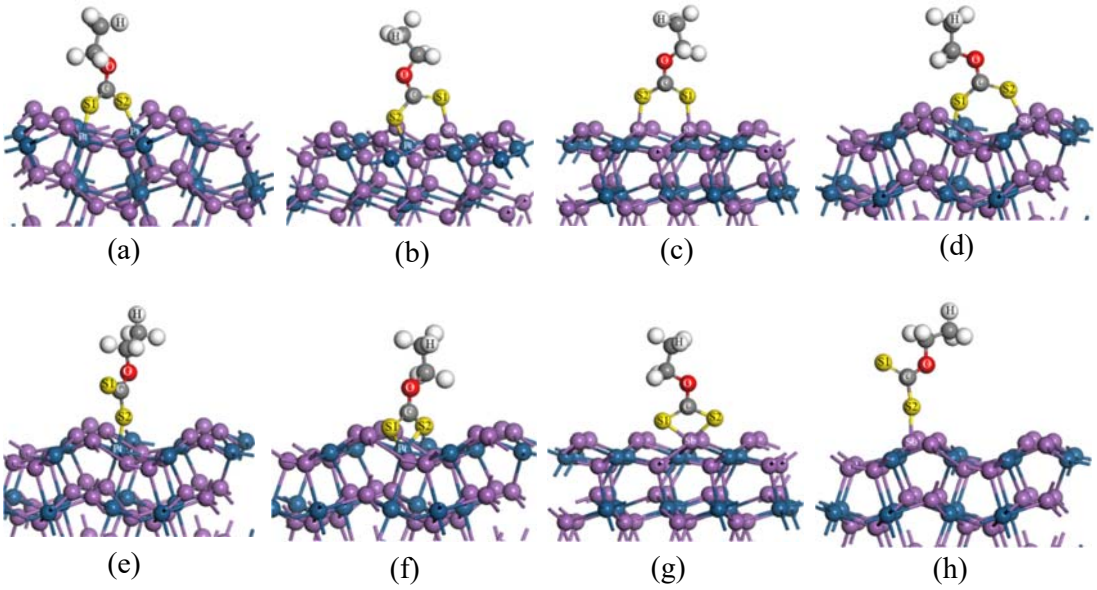

Figure E.1: Unrelaxed different adsorption sites considered for EX, nPX, nBX and AX on $PtSb_2$ (100) surface

Table E.1: Adsorption energies for all adsorption sites considered for $PtSb_2$ (100) surface.

Structure	Adsorption sites	Adsorption Energy (kJ/mol)			
		EX	nPX	nBX	AX
(a)	Pt–S1, Pt–S2	–311.05	–310.32	–304.14	–296.19
(b)	Pt–S2, Sb–S1_N	–314.87	–309.50	–304.43	**–325.65**
	Pt–S1, Sb–S2_N	**–326.30**	**–322.03**	**–324.52**	–314.01
(c)	Sb–S1, Sb–S2	–282.57	–277.40	–287.85	–269.66
(d)	Pt–S1, Sb–S2_F	–293.14	–276.92	–293.79	–290.20
	Pt–S2, Sb–S1_F	–291.21	–284.13	–286.40	–267.57
(e)	Pt–S2	–305.86	–299.36	–303.51	–300.86
(f)	S1–Pt–S2	–279.21	–314.34	–310.23	–248.01
(g)	S1–Sb–S2	–299.72	–248.18	–271.94	–285.50
(h)	Sb–S2	–242.85	–251.88	–252.77	–214.88

Values in **bold** shows the most exothermic adsorption sites

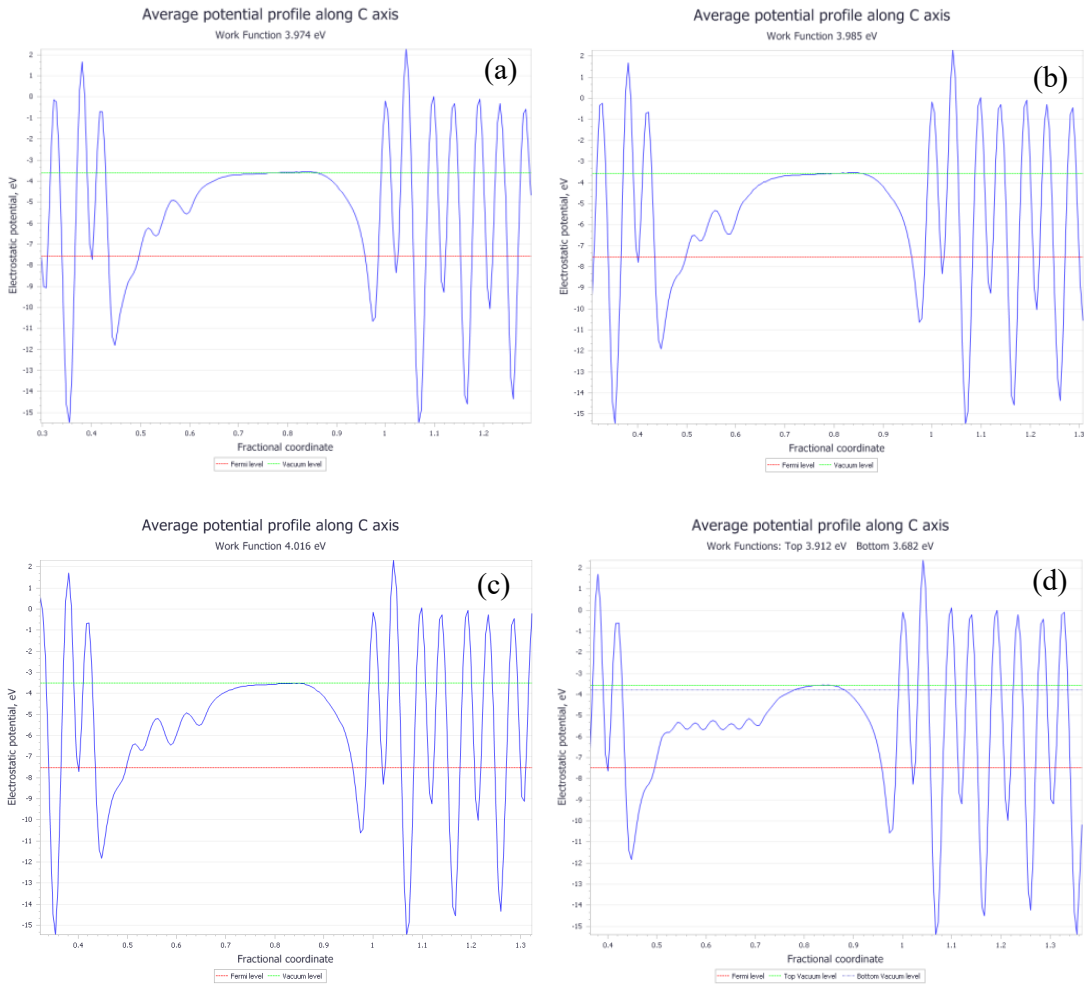

Figure E.2: Average electrostatic potential for most stable adsorption for each xanthate collector in absence of the Neugebauer and Scheffler dipole correction: (a) EX, (b) nPX, (c) nBX and AX adsorption on $PtSb_2$ (100) surface.

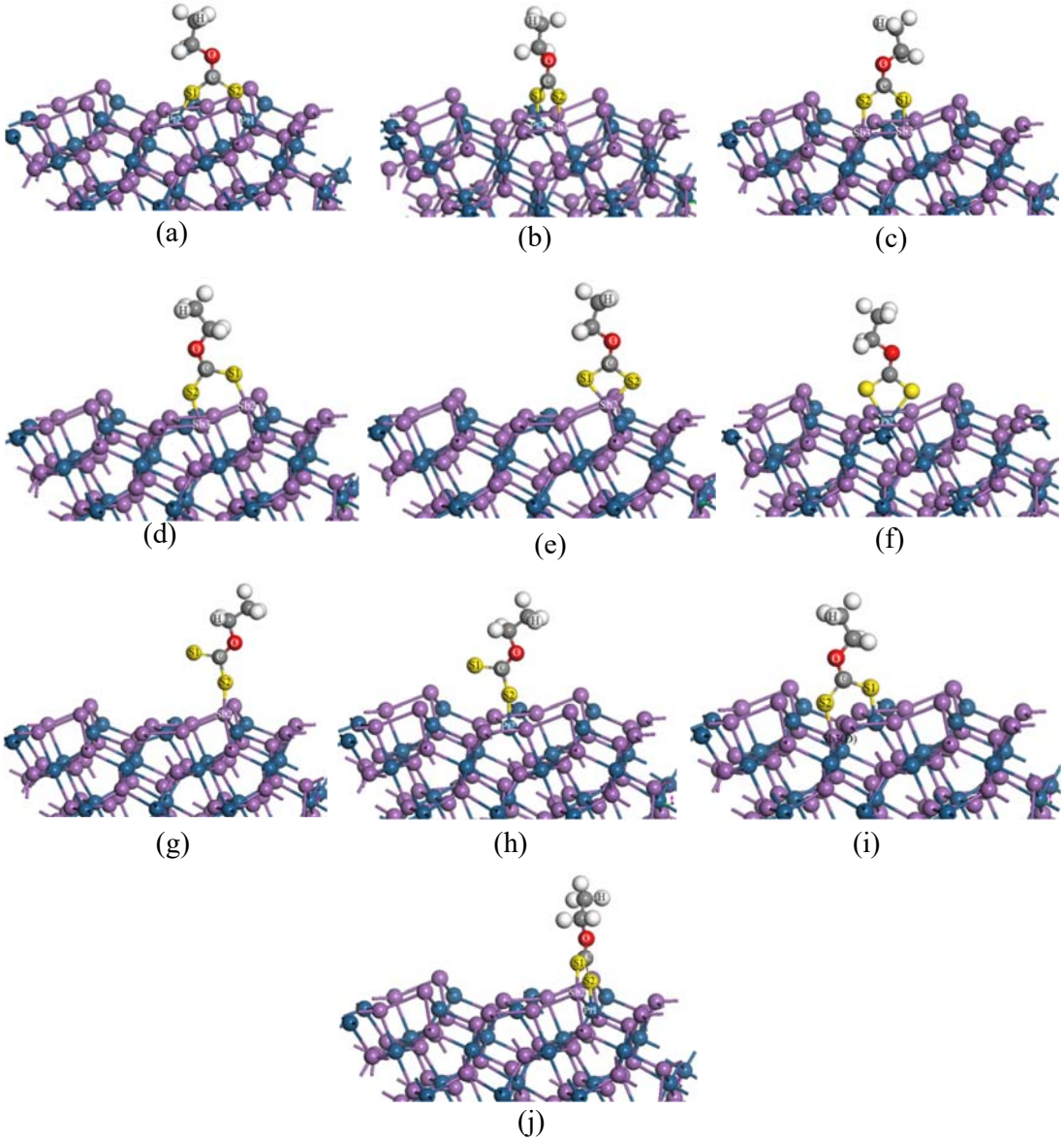

Figure E.3: Unrelaxed different adsorption sites considered for EX, nPX, nBX and AX on $PtSb_2$ (110) surface

Table E.2: Adsorption energies for all adsorption sites considered for $PtSb_2$ (110) surface.

Structure	Adsorption sites	Adsorption Energy (kJ/mol)			
		EX	nPX	nBX	AX
(a)	Pt1–S1, Pt2–S2	**–361.41**	**–372.40**	**–375.66**	**–371.56**
(b)	Pt2–S1, Sb3–S2	–324.87	–324.31	–331.11	–320.40
	Pt2–S2, Sb3–S1	–322.19	–321.68	–327.17	–323.50
(c)	Sb3–S1, Sb3–S2	–278.45	–277.43	–277.03	–274.11
(d)	Sb3–S2, Sb2–S1	–255.67	–255.83	–255.77	–256.26
	Sb3–S1, Sb2–S2	–263.87	–259.72	–259.22	–257.94
(e)	S1–Sb2–S2	–285.67	–252.20	–270.91	–276.12
(f)	S1–Pt2–S2	–360.56	–356.28	–360.87	–352.85
(g)	Sb2–S2	–280.05	–270.51	–271.86	–258.17
(h)	Pt2–S2	–317.09	–315.07	–307.20	–314.28
(i)	Pt1–S2, Sb3(D)–S1	–328.07	–323.93	–321.50	–323.63
	Pt1–S1, Sb3(D)–S2	–299.61	–285.13	–295.92	–318.33
(j)	Pt1–S1, Sb2–S2	–364.53	–362.76	–362.55	–365.26
	Pt1–S2, Sb2–S1	–359.72	–351.36	–362.48	–361.67

Values in **bold** are the most exothermic adsorption sites

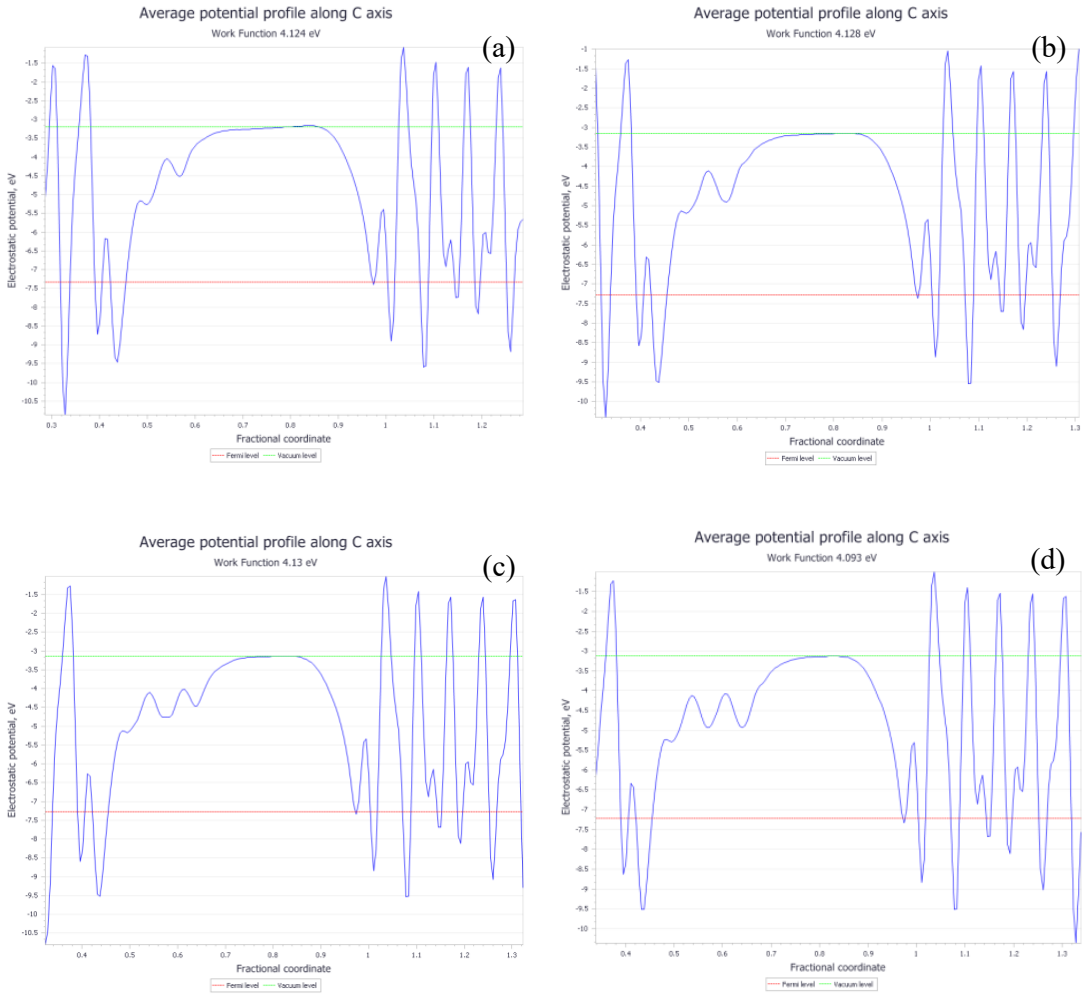

Figure E.4: Average electrostatic potential for most stable adsorption for each xanthate collector in absence of the Neugebauer and Scheffler dipole correction: (a) EX, (b) nPX, (c) nBX and AX adsorption on $PtSb_2$ (110) surface.

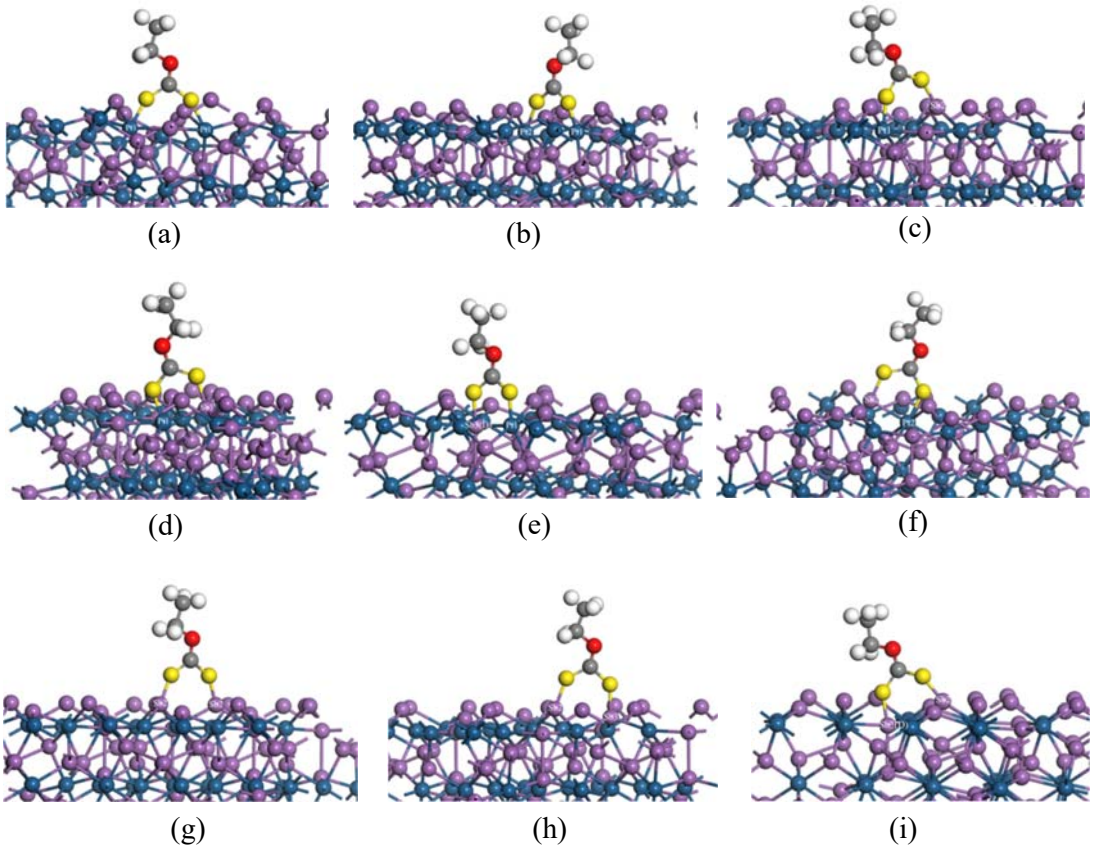

Figure E.5: Unrelaxed different adsorption sites considered for EX, nPX, nBX and AX on $PtSb_2$ (111) surface

Table E.3: Adsorption energies for all adsorption sites considered for $PtSb_2$ (111) surface, as calculated in equasion 2.15.

Structure	Adsorption sites	Adsorption energies (kJ/mol)			
		EX	nPX	nBX	AX
(a)	Pt5–S1, Pt5–S2	–696.12	–697.21	–685.88	–703.97
(b)	Pt6–S1, Pt5–S2	–714.23	–717.44	–674.28	–670.12
	Pt6–S2, Pt5–S1	–718.08	–716.79	–673.76	–697.75
(c)	Pt5–S2, Sb2–S1	–690.79	–698.47	–581.07	–667.27
	Pt5–S1, Sb2–S2	–704.79	–719.28	–643.65	–724.07
(d)	Pt5–S1, Sb3–S2	–708.60	**–795.18**	–738.44	–741.61
	Pt5–S2, Sb3–S1	–760.39	–760.42	–700.95	–721.12
(e)	Pt5–S2, Sb3(D)–S1	–690.78	–743.28	–734.32	–733.23
	Pt5–S1, Sb3(D)–S2	–681.36	–687.03	–726.43	–717.56
(f)	Pt6–S1, Sb2–S2	–629.93	–694.49	–728.65	–726.52
	Pt6–S2, Sb2–S1	–724.85	–703.24	–722.68	–721.36
(g)	Sb2–S1, Sb2–S2	–471.14	–691.25	–598.07	–694.13
(h)	Sb3–S1, Sb2–S2	–772.11	–774.48	–772.28	–769.68
	Sb3–S2, Sb2–S1	**–773.50**	–788.49	**–789.45**	**–784.55**
(i)	Sb2–S2, Sb3(D)–S1	–702.18	–671.45	–688.31	–654.49
	Sb2–S1, Sb3(D)–S2	–479.21	–574.34	–690.48	–621.15

Values in **bold** shows the most exothermic adsorption sites

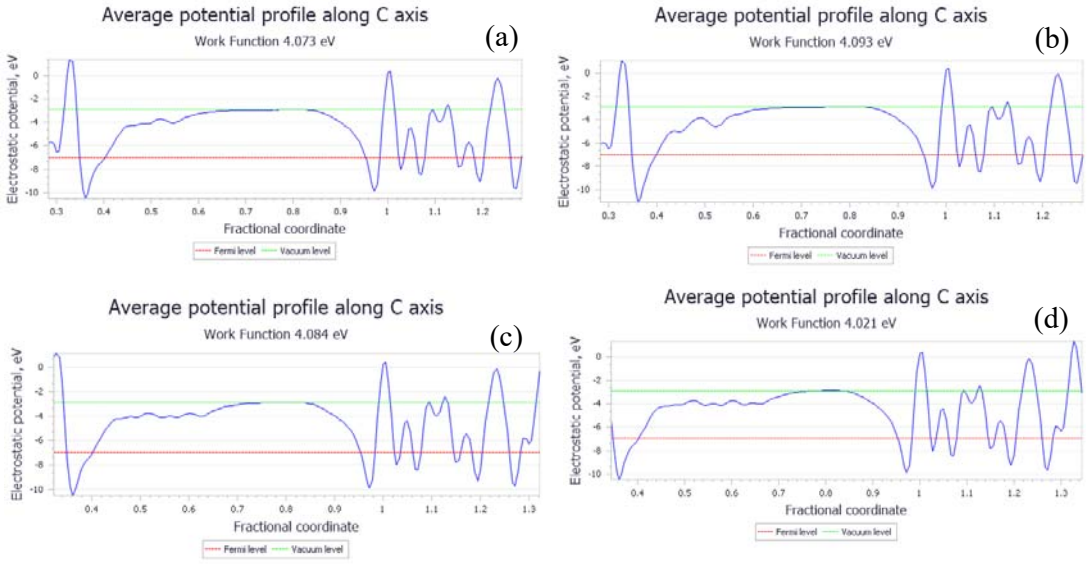

Figure E.6: Average electrostatic potential for most stable adsorption for each xanthate collector in absence of the Neugebauer and Scheffler dipole correction: (a) EX, (b) nPX, (c) nBX and AX adsorption on $PtSb_2$ (111) surface.